De novo designed metallopeptides with a type 2 copper center: a structural and functional model for copper nitrite reductase

by

Fangting Yu

A dissertation submitted in partial fulfillment
of the requirements for the degree of
Doctor of Philosophy
(Chemistry)
in the University of Michigan
2014

Doctoral Committee:
Professor Vincent L. Pecoraro, Chair
Associate Professor Nicolai Lehnert
Associate Professor Bruce A. Palfey
Professor James E. Penner-Hahn

To my mom

Acknowledgements

I owe thanks to many people in the process of completing my degree. I cannot express enough gratitude to my thesis advisor, Professor Vincent Pecoraro, for his patient guidance, enthusiastic encouragements, constructive critiques, and his constant support for my projects. I am very grateful for everything that I learnt working with Vince, the passion and curiosity towards the unknowns and the wisdom of life. I especially enjoyed the numerous discussions we had in his office, when we bounced ideas back and forth to tackle a problem. I appreciate that Vince really respects independent thinking, which fostered my growth as a scientist. Graduate school is not always an easy path. Having a great advisor like Vince, who always got your back and whom you can always look up to, definitely makes it better. I am very lucky in that regard.

I wish to thank my other committee members, Professor Nicolai Lehnert, Professor James Penner-Hahn, and Professor Bruce Palfey. They have provided useful insights along the progression of my thesis project. I am also grateful for the conversations about career development with Professor Mi Hee Lim (UNIST) and Professor Nicolai Lehnert. They mentorship has played an important role to shape my career. Special thanks should be given to Dr. Matteo Tegoni, who started this copper-peptide project and taught me the relevant techniques. I also appreciate his continuing support and friendship. I wish to acknowledge the members in the bioinorganic community at the University of Michigan. Three years ago, Mi Hee and Nicolai started the Bio-Inorganic Group (BIG) meeting that features monthly presentations from scientists in the bioinorganic community. I have learnt a lot from these presentations and discussions, which deepened my interest in bioinorganic chemistry. I would like to thank my collaborators: Professor James Penner-Hahn, Professor Kevin Kubarych, Dr. Jennifer Meagher, Dr. Jeanne Stuckey, and Professor David Britt, for their contribution to the projects. I would also like to extend my thanks to the staff members and technicians at the Department of Chemistry.

I wish to thank the Pecoraro lab members, who are not only great co-workers, but also good friends. I thank the past lab members Dr. Ted Boron, Dr. Joe Jankolovits, Dr. Melissa Zastrow, Dr. Saumen Chakraborty, and Dr. Ginny Cangelosi for their comments at my group meetings and practice talks, the helpful discussions, and laughers we shared at numerous lab outings. I would like to offer my thanks to the current group members Evan (Professor Evan Trivedi), Cathy, Alison, Jeff, Leela, David, Casey, and Jake for their constant support and friendship. I wish to thank Dr. Victoria Campbell, Dr. Cedric Tard, Manuela Bersellini, and other visitors in the lab.

I want to give special thanks to my friends in Michigan. I am very lucky to be able to share my graduate school experience with all these wonderful people. I thank them for the enjoyable times by the lake, happy hours, dinner parties, tailgating, and the great conversations and company. I wish to thank the GradTONES (Graduate Troupe of Needlessly Educated Singers). My time here would not have been this much fun without them. I thank them for sharing my passion for music, the inspiring conversations, and all the fun activities (karaoke nights, board game nights, laser tag, random hangouts, and four successful concerts) in the past two years.

Last but not least, I give my deepest gratitude to my family. My parents have always been very supportive of me pursuing a career in science. I have not visited them much during the past five years, but they have been extremely understanding. My heartfelt thanks are given to my fiancé Sunny and his family. Sunny has always been there for the most important steps of my time in graduate school, providing constant care and support. I could not have completed my degree without him.

Table of Contents

List of Tables

List of Figures

Abstract

The *de novo* design of three generations of copper-peptides as structural and functional models for the type 2 copper center (T2Cu) in copper nitrite reductase (CuNiR) is described. Using an α-helical coiled coil scaffold, a tris-histidine site is introduced in the TRI peptide, yielding TRIW-H [sequence: Ac-G WKALEEK $(LKALEEK)_2$ HKALEEK G-NH_2].

While the protein scaffold is completely different from that in native CuNiR, copper binds with high affinity in both cuprous and cupric forms, with a three-coordinate cuprous state [$Cu(I)(His)_3^+$] and likely a five-coordinate cupric state [$Cu(II)(His)_3(OH_2)_{1-2}^{2+}$]. Redox chemistry is demonstrated *for the first time* in a *de novo* designed copper-peptide system. Although the reduction potential of $Cu(II)/(I)(TRIW\text{-}H)_3^{2+/+}$ is 150–200 mV higher than that of the native T2Cu in CuNiR, it is still capable of catalyzing nitrite reduction in the presence of sodium ascorbate as a reductant with multiple turnovers. The first generation model establishes the minimal requirements to confer NiR activity in this system.

To understand the fundamental structure-function relationship of this $Cu(His)_3$ center with the ultimate goal of improving the catalytic activity, two more generations of models are described, with designs based on the modifications of the charged residues at the helical interface (second generation) and the interior (third generation) of the helical coiled coils, respectively. The second generation peptides have a key glutamate residue replacing the lysine residue at the 22nd position (TRIW-EH sequence: Ac-G WKALEEK LKALEEK LKALEEE HKALEEK G-NH_2). By systematically modifying the charged residues to the C-terminus of the copper site (the 24th and 27th positions), a series of peptides with modifications at the helical interface are designed. These changes lead to modulated copper-binding affinities, deprotonation equilibria, and reduction potentials. While trends in reduction potential and rates correlate with the total charge of the

peptides, it is believed that modification of H-bonding to the histidine site causes the observed changes. The NiR rate is influenced to a small extent (4–fold at pH 5.8) with these modifications.

Two strategies are used for the third generation models: mutating the leucine at 19th position into an alanine and changing the histidine to N-methyl histidine. The interior modifications, with a maximum 1300-fold observed rate enhancement, are far more effective in tuning the NiR rates than the second generation alterations.

This thesis lays the groundwork for the incorporation of metal centers in *de novo* designed peptide scaffolds to carry out redox catalysis.

Chapter I . Protein design: toward functional metalloenzymes

Protein design is a valuable tool for understanding the fundamental factors that dictate protein structure and function. The field of protein design has seen significant progress over the past 30 years, with a growing range of applications in areas of research from fundamental biochemistry to biotechnology and medicine. Protein design is no trivial task. It is an ultimate test of our understanding of structure–function relationships and requires a combined knowledge of physics, chemistry, and biology. Evolution is nature's method of designing proteins, which has been very effective in producing scaffolds with exquisite structural details, breath-taking efficiency, and high selectivity. Rapid advancement of computer applications in biotechnology now enables one to model the evolution of a particular protein on a human time scale, instead of an evolutionary time scale; however, it is still quite a challenge to select an optimal solution from the enormous amount of mutations and to understand how these selective factors relate to the function of the protein. From the early examples of designing polypeptides or proteins that are stable in aqueous environments to today's novel functional metalloproteins, protein design has advanced to a stage where it is possible to create structures never before seen in nature, with functions not found in nature and novel sequences not derived from nature while exhibiting desired properties.

The main goal of this thesis is to design a structural and functional model for copper nitrite reductase (CuNiR) using *de novo* protein design approach. It is important to realize that the progress toward designing functional metalloenzyme mimics is built upon many previous endeavors of constructing a stable metal-binding site in a peptidic/protein scaffold. Here, I will highlight a few representative cases of designed proteins to illustrate the strategies for incorporating functional metal-binding sites into designed protein/peptide scaffolds based on a recently published review article authored by me and

coworkers.[1] I will discuss the general considerations of constructing a metal-binding site and introduce protein redesign and *de novo* design in section 1. Section 2 will focus on selected designed non-heme iron proteins that are capable of catalyzing oxidation/oxygenation reactions. Section 3 will describe the design of functional zinc-binding proteins that have hydrolytic activities. Section 4 will describe the design of copper centers. Section 5 will outline this thesis.

1. Introduction

1) General considerations

Before delving into specific cases of designed protein systems, I will delineate some general considerations as a foundation for both protein redesign and *de novo* design. The fundamental interactions that play important roles in determining protein structures are hydrophobic, electrostatic, hydrogen bond (H-bond), and van der Waals interactions. Conceptually, creating a stable protein scaffold is a trade-off between the unfavorable entropy and favorable enthalpy upon protein folding, in addition to the entropic term of the surrounding water molecules,[2] all of which eventually lead to the notion of positive and negative design that distinguishes the unique, native fold versus other folded states.[3] Accordingly, in the process of designing a stable protein construct, one needs to consider how to utilize hydrophobic interactions as a driving force for folding, electrostatic interactions to build salt bridges, H-bonds to create secondary structures, and van der Waals interactions for packing. Additionally, when designing helix bundles, the helical dipole is an important factor to take into account because it will contribute to the alignment of helices. When it comes to incorporating a metal-binding site, it is critical to consider whether the site is a pre-organized ligand environment or if the metal ions would direct the ligand coordination.[4] There are reported examples where metal ions are responsible for protein folding, in which case the binding of metal ions is the major force for overcoming the unfavorable entropy upon protein folding.[5–7] Moreover, ligand recognition, metal specificity, and substrate specificity (if applicable) are the next level of design goals.

Rational protein design has been aided by the development of automated algorithms, despite the tremendous complexity associated with protein structures and sequences and the degrees of freedom of the calculation. Several strategies have been developed to reduce the degrees of freedom and improve search algorithms for energy minimization, which are widely used in the construction of suitable metal-binding sites (see later sections in this chapter). One of the earliest programs enlisted for protein design is InsightII/Discover (MSI), which was applied to the development of helical bundle proteins.[8–13] This program uses molecular mechanics to achieve energy minimization. The rational design algorithm Dezymer, for example, searches proteins of known structure for locations where side chain rotamers can be introduced to form a site of known coordination.[14,15] This program is particularly useful in the redesign of metalloproteins because it can identify a novel metal-binding site based on user-defined geometry in a protein of known structure. On the other hand, the numerical computer method, Rosetta, developed in the laboratory of David Baker, takes short fragments of proteins and assembles them by a Monte Carlo strategy to form a native-like protein conformation.[16] The prerequisite for Rosetta design is a library of fragments representing all of the possible local structures of various native proteins. After the Monte Carlo assembly, the folding and stability of the designed sequences are evaluated based on the comparison between conformational parameters and known protein structures. Metal Search, developed by Clarke and Yuan, is written specifically for designing tetrahedral metal-binding sites in proteins.[17]

2) Protein redesign and de novo design

The effort of protein design can be categorized into redesign, which is to rationally engineer desired functionality into an existing protein scaffold,[18–26] and *de novo* design, which is to build a peptidic or protein system that is not directly related to any sequence found in nature yet folds into a predicted structure and/or carries out desired reactions.[1,27–29] Each functional designed metalloprotein system requires both a stable protein scaffold or "ligand" and an incorporated metal-binding site. Part of the previous literature addressed how protein scaffolds are designed in terms of fundamental physical properties such as the energy landscape associated with folding and packing of a protein

from a biophysical perspective, which is the foundation of designing functional models.[28–35] Knowledge of the critical factors that govern protein stability and other properties allows researchers to begin incorporating cofactors to pursue better performance or novel functions of designed proteins. Previous reviews on this topic elaborated the strategies of certain metal cofactor functionality and characterization of designed metalloproteins.[1,18,20,27,36–42]

Metalloproteins are essential biomacromolecules that play important roles ranging from structural stabilization to chemical signaling and catalysis in metabolic processes necessary to sustain life on the planet. Over millions of years, nature has evolved a set of metalloenzymes that function as electron transfer or catalytic centers. Biochemists, biophysicists, and chemists are intrigued by the fundamental molecular transformations that occur within various metalloenzymes. One approach to studying these functions is to design and engineer new metal-binding sites into existing native proteins: protein redesign.[18,43,44] The ultimate goal of protein redesign is to impart improved or novel properties, for example, new activities, inverted stereoselectivity, or new substrate specificity, into existing proteins, that is, to teach the old enzyme new "tricks".[44,45] What protein design teaches us about the structure–function relationship will eventually allow us to harness the richness of native protein structures and the diverse functions of metalloproteins to construct new proteins for biomedical and pharmaceutical applications.

To create novel artificial metalloenzymes, a fundamental understanding of the structure–function relationship is necessary to predict and control the active site properties of a particular system. More often than previously believed, native proteins exhibit intrinsic catalytic promiscuity, using a single active site to catalyze more than one chemical transformation.[46,47] The microenvironment modification of active sites can allow a wider range of chemical transformations to occur within naturally existing scaffolds. Moreover, metalloenzymes have been evolved to exhibit optimal catalytic efficiencies in the context of their metabolic transformations; however, the activity of a single isolated metalloenzyme is not necessarily the "best". This leaves chemical space for protein redesign to achieve modified activity and/or specificity. The advantage of a protein redesign strategy is that it can bypass the problem of developing a stable protein fold

because many native proteins have remarkable adaptability for changes. Protein redesign strategy has proven to be one of the most effective approaches in the design and engineering of artificial metalloenzymes. Although biochemical and biophysical studies generally focus on features that result in the modification of functions, design allows us to incorporate only those features that are believed to be necessary for reactivity. By applying a minimal number of changes to convert a known protein to a metalloprotein with a specific cofactor and activity, the basic requirements for a certain activity can be examined in the absence of complications from the limits of stability and symmetry of the scaffold. One can also seek to improve upon the native function of a metalloprotein by making systematic changes, favoring greater stability, altering inhibition profiles, or affecting reactivity as needed for a particular purpose.

Arguably more challenging than protein redesign, *de novo* or "from scratch" design has helped to disentangle structure–function relationships on a fundamental level and to create novel properties and functions in peptidic/ protein systems that are not necessarily related to native protein sequences. Designing proteins from scratch was considered a bold endeavor in its infancy; however, the challenges did not prevent researchers from trying. As Richard Feynman expressed, "What I cannot create I do not understand."[48] Indeed, *de novo* design is the ultimate test of our understanding of the fundamental factors that dictate protein folding, structure, and function using a minimalist approach.[29] It involves constructing a peptide sequence that spontaneously folds into a unique, predictable three-dimensional structure while retaining sufficient complexity and functionality to provide an adequate model for a protein.[10,27,29,49,50] What distinguishes de novo design from other types of protein design or engineering strategies is that it is based on first principles,[51] which refer to the postulation that the primary amino acid sequence determines the three-dimensional structure of a protein. Richardson presented a vivid analogy of the protein folding problem at the Biophysical Society National Lecture in 1992: the folded protein can be thought of as an origami canary with the amino acid sequence being the creased piece of paper from which it is folded.[32] Thus, protein redesign amounts to modifying the wings or the tail of the folded origami canary, while *de novo* design starts with a flat piece of paper to figure out the crease patterns needed to fold it into a three-dimensional origami canary.

The goal of *de novo* design is to create stable peptidic/ protein constructs with desirable functions and properties comparable to or better than those of native proteins. Combined with the knowledge learned from synthetic model complex studies and protein redesign work, *de novo* design should eventually lead to novel applications in biocatalysis and pharmaceuticals. Ever since the first reported *de novo* designed peptides,[49,52] this approach has been utilized to understand the interplay between protein structure and function, heavy metal toxicity, electron transfer, and structural and catalytic sites in metalloproteins.

Rather than designing each new protein from scratch, previous *de novo* scaffolds can serve as a starting point for the design of metalloproteins (much as natural proteins are the starting points in protein redesign). Although there are fewer *de novo* designed scaffolds to choose from as compared to the number of natural proteins, the existing ones cover the most important and common structural motifs found in nature. Choosing a starting scaffold is a critical first step of *de novo* metalloprotein design because the scaffold provides the protein environment and orients the residue side chains, which have a profound impact on metal coordination. There are a few excellent and exhaustive reviews discussing the *de novo* design of turns, β-sheets, and other motifs.[53–58] Since most of the functional metalloenzyme mimics are associated with α-helical coiled coils, I will focus on the design based on α-helical coiled coils. Finally, it is worth mentioning that computational protein design has contributed greatly to the establishment and expansion of the field. The major goal of computational design is to identify amino acid sequences compatible with a stable, folded, three-dimensional structure or to find the lowest free-energy structure for a specific amino acid sequence. I will omit a detailed discussion on computational design because the effort of this approach in the past few decades has already been reviewed extensively.[34,40,59–71]

2. Design of catalytic non-heme iron proteins

Iron is the most abundant trace metal in the human body and it plays important roles in an array of metalloenzymes.[72] Some of the earliest and most successful protein design efforts are focused on creating an iron-binding site, which warrants a discussion of selected designed iron proteins. Since the goal of this thesis is to design a catalytic center,

I will omit detailed descriptions of electron transfer iron sites. Interested readers can refer to Ref [1].

Nonheme iron centers are defined as those in which iron is coordinated by ligands other than polydentate tetrapyrroles (e.g., porphyrins). Figure I-1 illustrates the six general types of nonheme iron centers including mononuclear, binuclear, and iron–sulfur centers. Nonheme iron centers exhibit a broad range of functions, including electron transfer, substrate oxidation and reduction, and metal ion transport.[73] The redesign of nonheme iron proteins aims to explore the factors that govern the redox properties and reactivity of the iron center, elucidate the influence of interactions between different key amino acid residues, and construct a novel functional nonheme iron site into another nonheme iron protein. Besides electron transfer, nonheme iron centers can also serve different reaction purposes including oxygenation (protocatechuate 3,4-dioxygenase,[74,75] catechol 2,3-dioxygenase[76]), peroxidation (rubrerythrin[77]), oxidation (ribonucleotide reductase (RnR),[78] 1–aminocyclopropane carboxylic acid oxidase[79]), superoxide dismutation [iron superoxide dismutase (SOD)[80]], hydroxylation (phenylalanine hydroxylase,[81,82] calavaminate synthase[83]), and H-abstraction (iron-bound bleomycin[84–86]). Several comprehensive reviews cover the structures, functions, and mechanistic perspectives of these native nonheme iron centers, so we will omit a detailed description of each enzyme.[73,87–89] There are several examples of redesigned nonheme iron proteins that use iron as a catalytic center to control the redox properties and reactivity of the protein.

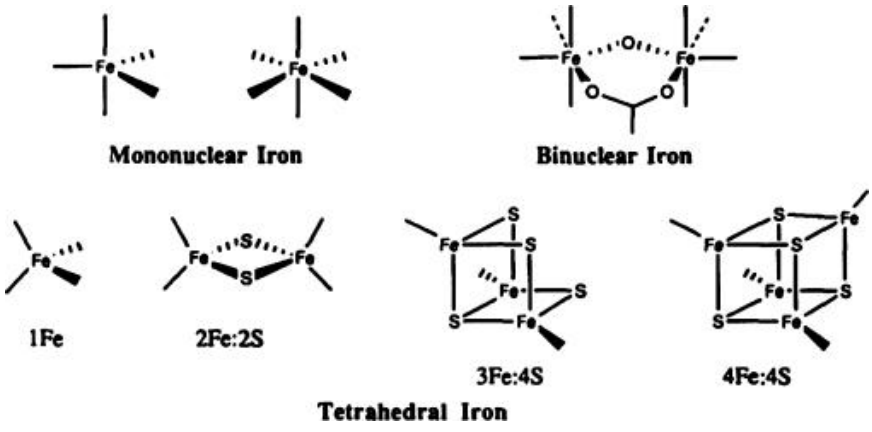

Figure I-1. Nonheme iron centers. Reproduced with permission from ref [73]. Copyright 1991 Elsevier.

SOD catalyzes the disproportionation of superoxide into molecular oxygen and hydrogen peroxide, an important gating mechanism for controlling cellular oxidative stress.[90] Three types of SODs have been discovered in a variety of organisms: NiSOD in certain fungi and bacteria,[91] CuZnSOD in eukaryotic cells,[92] and Fe/MnSOD in bacteria, some plant chloroplasts, and mitocondria.[80,93,94] FeSOD and MnSOD share a high sequence homology, including the same amino acid ligand set, and, therefore, are considered as one general type. Metal ion substitutions result in a loss of activity,[95–97] likely a reflection of the different midpoint potentials of FeSOD and MnSOD.[98,99] In FeSOD, iron is bound in a trigonal bipyramidal geometry with two His and One Asp on the trigonal plane and one water/hydroxide and one additional His as axial ligands.[80,93,100] This coordination environment was constructed into Trx using the rational protein design program, Dezymer.[101] The mutations Leu7His, Phs27Asp, Ile60His, and Asp63His constructing the FeSOD active site, together with several other mutations for structural stability, yielded Trx-SOD. Fe-Trx-SOD exhibits spectroscopic features similar to those observed in WT FeSOD and readily catalyzes superoxide dismutation. Although the rate of Fe-Trx-SOD is ~10^4-fold lower than that of the WT enzyme, it remains an excellent model toward elucidating the chemical details in native proteins.

Using Dezymer, Benson *et al*. introduced a mononuclear $(His)_3$ iron-binding site and an oxygen-binding pocket into Trx,[24] with the goal of creating an empty binding site on the iron center for facilitating substrate access. The oxygen-binding center was created by examining the locations that could sterically accommodate a molecular oxygen. Six locations were selected, including three sites in a groove (G1– G3), two sites in a shallow pocket (S1 and S2), and one site in a deep pocket (D1). The reduction potentials of this $Fe(His)_3$ center are location-dependent: the relatively buried G3 and D1 sites have significantly lower reduction potentials (+28 ± 2 and +10 ± 2 mV, respectively), whereas the more exposed S1 site has a higher potential (+440 ± 2mV). Fenton, SOD, and Udenfriend reactions were tested for these mutants, demonstrating that the stabilization of surface electrostatics, transition states, and the elimination of nonspecific electron transfer processes all contribute to the specificity of the catalytic reaction.

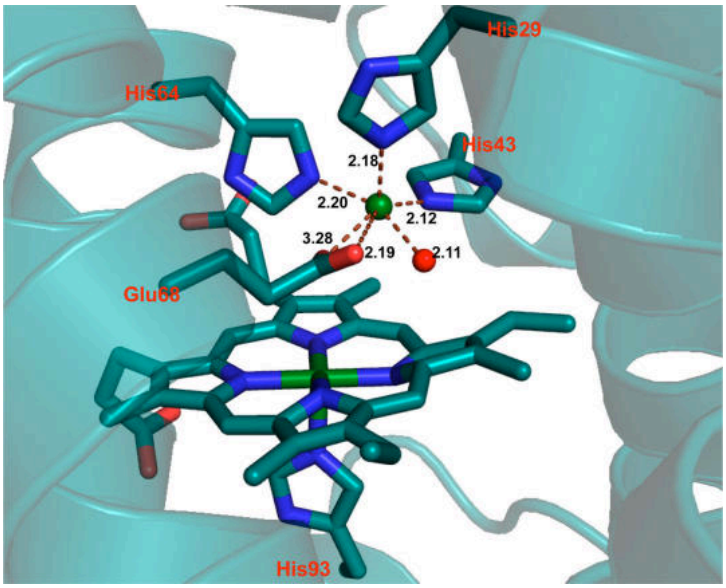

Figure I-2. The active site of Fe(II)-Fe_BMb. $Fe(II)_B$ is represented by a green sphere. The Fe(II)-bound water is represented by a red sphere. PDB code: 3K9Z. Bond lengths in the figure are in angstroms.

In nitric oxide reductase (NOR), a nonheme iron center, Fe_B, is coupled to a heme center, which promotes the two-electron reduction of NO, producing N_2O and water.[102,103] On the basis of a previously reported Cu_BMb construct, where a $(His)_3$ site was introduced close to the heme center in Mb for copper binding,[104] Yeung *et al*. successfully designed a NOR mimic by coupling a nonheme iron center [$Fe(His)_3$] to the heme center in Mb.[105] Specifically, the Val68Glu mutation was chosen in addition to the two preexisting mutations in Cu_BMb (Leu29His and Phe43His). The resulting Fe_BMb protein contains a nonheme iron coordinated to three His residues (His29, His43, and His64) and Glu68 revealed by its crystal structure (Figure I-2). The presence of the Fe_B site dramatically increases the reduction potential of the heme center, from −158 to −46 mV (vs NHE), which, along with EPR data, supports the coupling of two iron centers. Fe(II)-Fe_BMb is also a functional model of NOR to catalyze NO reduction into N_2O.

To design a model closer to native NOR, Lin *et al*. introduced a second Glu residue in close proximity to the Fe_B-heme site.[106] Previous reports indicated that a few Glu residues are critical for retaining NOR activity;[107,108] however, because of the complexity of the native protein, the precise functional role of each Glu remains unknown. An Ile residue on the second coordination sphere of Fe_B was mutated to Glu in

the simplified model, Fe_BMb, to elucidate its function. The crystal structure of Fe(II)-I107E-Fe_BMb was solved, showing that Fe(II) is coordinated to three His residues, Glu68, and a water molecule situated between Fe(II) and Glu107. Glu107 was proposed to facilitate proton uptake. Under single turnover conditions, after ~20 h, the yield of N_2O catalyzed by Fe(II)-I107E-Fe_BMb is 24%, more than twice that catalyzed by Fe(II)-Fe_BMb (~10%), reflecting the important functional role of Glu107. Moreover, the introduction of Glu107 does not alter the reduction potential of the heme center, showing that the effect of the conserved Glu residues is not additive, but rather depends on the location of the Glu residue. Metal ion substitutions were carried out to confirm the role of the nonheme metal center. Structural differences such as altered H-bonding networks and coordination geometries are observed in the crystal structures when Fe(II) was substituted with Cu(II) and Zn(II), showing that Fe_B site is involved in the structural fine-tuning.

Several proteins contain di-iron oxo active sites that carry out various reactions. For example, both hemerythrin and methane monooxyganse contain a di-iron oxo site, which functions as an O_2 carrier center in hemerythrin[109] and a methane hydroxylation site in methane monooxygenase (MMO).[110] One of the major goals of protein redesign is to investigate whether it is possible to swap similar active sites from proteins that exhibit dissimilar functions, which may lead to a more in-depth understanding of how structure relates to activities in metalloprotein active sites. DeMaré *et al*. redesigned the di-iron site in rubrerythrin (Rr) to mimic that of RnR R2.[111] Although the physiological function of Rr is yet to be determined, this study contributes to improving the understanding of the functional aspect of the di-iron center. Specifically, the authors created Rr mutants aiming to probe the possibility of forming a tyrosyl radical near the active site (Leu60Tyr) and to determine the role of a coordinating Glu residue (Glu97Ala). The X-ray crystal structures for both Leu60Tyr and Glu97Ala mutants show minimal structural perturbation as compared to WT-Rr. Leu60Tyr is located in a position similar to the stable tyrosyl radical-forming position in native RnR R2; however, EPR and UV−vis spectroscopies do not show any tyrosyl radical feature in Leu60Tyr-Rr. Ferroxidase reactions were carried out with the mutants. Only the Glu97Ala mutant, in which the directly coordinating Glu ligand is removed, shows decreased activity, while the distal mutation in L60Y-Rr does not result in variation of the activity. These results suggest that

the physiological reaction of Rr involves ferroxidase-like activity. In L60Y-Rr, Tyr does not form an H-bond with an iron-coordinating carboxylate, as would have been required to form the tyrosyl radical during the ferroxidase reaction.

Moreover, a di-iron center with activity resembling that of MMO was introduced into RnR R2 through a series of mutations.[112] The crystal structures of RnR R2 from different species show similar di-iron sites as well as the conserved residues Phe208, Phe212, and Ile234, which form a hydrophobic patch. Tyr122 forms a radical to initiate the catalytic cycle for ribonucleotide reduction.[113,114] To investigate the role of Phe208 and how it may influence Tyr122 radical formation, Örmo *et al*. mutated Phe208 to Tyr, yielding an RnR R2 mutant that does not have a tyrosyl radical, based on the absence of a characteristic 410 nm feature in the absorption spectrum. The Raman spectrum shows the presence of a ferric bidentate catecholate species, likely derived from the protein rather than an exogenous ligand. The authors postulated that the Tyr108 could be the precursor of the dihydroxyphenylalanine ligand, the formation of which is proposed. Scheme I-1 (Reproduced from ref [112] with permission. Copyright 2012 American Society for Biochemistry and Molecular Biology) shows the self-hydroxylation activity of this di-iron center, which involves the formation of a ferric-peroxide that transforms to a high-valent Fe(IV)–oxo species.

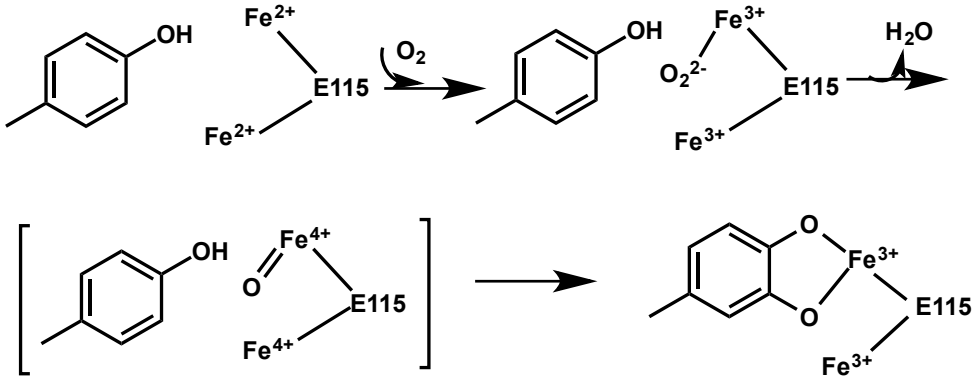

Scheme I-1

Di-iron center has also been incorporated into *de novo* designed scaffolds. DeGrado and co-workers have used retrostructural analysis of the active sites of several carboxylate-bridged di-iron proteins to design a family of artificial metalloproteins as

models for enzymes such as RnR and bacterioferritin.[115–120] Despite a low sequence identity (<5%) and overall complex protein folds, the active sites of these proteins are all found within a simple antiparallel D_2-symmetric four-helix bundle.[117] The Due Ferri (two-iron, DF) proteins, designed to understand how solvent accessibility, polarity, and electrostatic environment influence the properties, are comprised of a binuclear metal site with two chelating Glu residues, two His residues, and two bridging Glu residues. These primary ligands are buried in the interior of the scaffold with metal geometries stabilized by a network of hydrogen bonds to second-shell ligands. The parent model, DF1, is an antiparallel dimer of noncovalently associated HLH motifs, each 48 residues in length.[117] The design was approached by first carefully defining the above-described dimetal coordinating site and second shell residues and then incorporating mainly hydrophobic core residues for packing and hydrophilic interfacial residues to define the topology. The design was first structurally characterized as a di-Zn(II) complex (but also binds Fe(II) and Co(II) in solution), confirming the presence of the dimetal cofactor near the center of the dimer.[117] The subsequent apo-DF1 NMR structure demonstrated that the metal site is largely preorganized.[121] Each metal is five-coordinate with a sixth vacant site lying on adjoining faces of the two metal ions to provide a potential binding site for small molecules. Complete characterization of DF1 was not possible due to low solubility and extreme stabilization (the scaffold had to be unfolded and refolded to bind metal). Further, Leu residues 13 and 13′ were found to block dimetal site access.

Table I-1. Designed metalloenzymes mimicking native protein metal active sites

Designed protein	Reaction	k_{cat}/s^{-1}	$k_{cat}/K_M/M^{-1}s^{-1}$	$k_1, k_2/$ $M^{-1}s^{-1}$	Metal coordination and spectroscopic parameters	Other notes	Ref
PT3.3	DECP hydrolysis	351 (± 26) × 10^{-3}	9,750 ± 1,534	-	$Zn(His)_3Asp(OH_2/OH^-)$ PDB code: 3T1G	*1.* k_{cat}, k_{cat}/K_m values at pH 7.5 2. The crystal structure is for PT3.1. Same active site.	[122]
MID1-zinc	*p*NPA hydrolysis	0.30	$630_{(max)}$*		$Zn(His)_3(OH_2/OH^-)$ PDB code: 3V1C	1. pK_a = 8.2 ± 0.1 2. The crystal structure shows tartrate binding but the activity supports water/hydroxide binding	[123]
$Hg(II)_sZn(II)(H_2O/OH^-)_N$(**TRI**L9CL23H)$_3$	*p*NPA hydrolysis	~ 0.053	31 ± 4 $_{(max)}$*		$Zn(His)_3(OH_2/OH^-)$ PDB code: 3PBJ	1. pK_a = 9.0 ± 0.1 2. $k_{cat}/K_{m(max)}$ determined by fitting the $k_{cat}/K_{m(max)}$ values *vs*. pH	[124,125]
$Hg(II)_sZn(II)(H_2O/OH^-)_N$(**TRI**L9CL23H)$_3$	CO_2 hydration	1.8 (± 0.4) × 10^3	1.8 (± 0.5) × 10^5		$Zn(His)_3(OH_2/OH^-)$ PDB code: 3PBJ	k_{cat}, k_{cat}/K_m values at pH 9.5	[125]
Cu(II)/(I)(**TRI**W-H)$_3^{2+/+}$	Nitrite reduction	-	-	k_{1Asc} = 12 ± 3 ×10^{-4}	Cu(I)$(His)_3$ trigonal planar ($R_{(Cu-N)}$ = 1.93 Å); Cu(II) $\lambda_{d\text{-}dmax}$ = 640 nm (ε = 138 $M^{-1}cm^{-1}$); g_{II} = 2.27 (A_{II}= 186 G)	1. pH-dependent rates 2. k_{1Asc} at pH 5.3 3. Spectroscopic parameters at pH 7.4	[126]

di-Fe^{III}-DF3	3, 5-DTBC oxidation	0.22 ± 0.02		105	di-iron center with an oxo-bridge; $\varepsilon_{350\ nm}$ = 5270 $M^{-1}cm^{-1}$	pH 7.0 , 25 ºC	[127]
di-Fe^{III}-DF3	4AP oxidation	0.045 ± 0.003		23.0		pH 7.0 , 25 ºC	[127]
G_4DF_{tet}	4AP oxidation	0.022 ± 0.002		25.7		pH 7.0 , 25 ºC	[128]

* Maximal efficiency from the fitting of k_{cat}/K_M values versus pH (assuming 100% active enzyme complex is present)

DF2 was subsequently designed to increase solubility (more surface hydrophilic residues were incorporated, and, in a similar model DF2t, a longer interhelix loop was introduced for stabilization and minimization of aggregation) and to allow for access of small molecules to the metal site (by replacing Leu residues with Ala and Gly).[118,120,121,129–131] The crystal structures of di-Mn(II)-L13A-DF1976 and di-Mn(II)-L13G-DF1981 confirm the presence of the designed cavity (which increases in size going from the larger Ala to Gly) filled with ordered water molecules. Notably, the asymmetric unit of di-Mn(II)-L13G- DF1 has four independent dimers, three of which have bridging water molecules and intermetal distances of 3.6 Å and one with two terminal water molecules and an intermetal distance of 4.2 Å.[130] Superimposition of the structures revealed that two copies of the N-terminal helices have shifted in opposite directions, leading to the increased metal–metal bond length. Dubbed the sliding-helix mechanism, it is postulated that this mechanism could occur in native systems for signal transduction, but it would be difficult to observe this effect experimentally.

Having developed a construct with improved properties and a larger active site cavity, a combinatorial approach was undertaken to search for a functional assembly. To this end, DFtet, a noncovalent assembly of four separate helices that could easily be varied, was designed.[132] One of the resulting heterotetramers, DFtet A_2B_2,[132] with all Gly residues replacing the Leu and Ala residues in the active site cavity (G4-DFtet), could perform the rapid two-electron oxidation of 4-aminophenol to benzoquinone monoamine with a k_{cat}/K_M of 25.7 $M^{-1}s^{-1}$ and a rate enhancement of ~1000-fold relative to the background reaction (and no detectable intermediates).[128] Further, this *de novo* design approach also demonstrates that the activity is sensitive to changes of the size of a methyl group in the active site cavity (substituting Gly for Ala decreased the rate up to 5-fold). The diferrous form of another resulting heterotetramer, DFtet AA'B_2, reacts with oxygen to form a peroxo-bridged diferric species similar to an important reactive intermediate found in many native proteins.[133] Given difficulties involving complex stoichiometry and unwanted ligand-exchange reactions with G4-DFtet, DF3 was designed on the basis of the original DF1 sequence with all Gly residues around the active site to accommodate the substrate and with modified loop residues to stabilize the resulting fold.[127] Like DFtet, DF3 is a phenol oxidase for the substrates 4–aminophenol (k_{cat}/K_M of 23 $M^{-1}s^{-1}$), 3,5-di-

tert-butyl-catechol (3,5-DTBC, k_{cat}/K_M of 100 $M^{-1}s^{-1}$), and *p*-phenylenediamine (k_{cat}/K_M of 14 $M^{-1}s^{-1}$) (Table I-1). No phenol oxidase activity was observed for *o*-phenylenediamine. These results are consistent with crystallographic analysis of the size of the cavity. The active site cleft created by the Gly mutations, at its narrowest, matched the width of the phenyl ring and, in wider sections, substitutions at the 3 and 5 positions could be accommodated.

A single chain DF protein, DFsc (with Ala residues around the active site), was also designed, and the NMR structure of di-Zn(II)-DFsc was obtained.[134,135] While rapid oxidation of the diferrous center was observed, it was due to an off-pathway iron-tyrosinate complex and not the important diferric intermediate observed for the other diferrous DF proteins.[136,137] Substitution of the four Ala residues to Gly (G4-DFsc) led to the minimization of this complex and a scaffold, which could also catalyze 4-aminophenol oxidation on the same order of magnitude as DFsc was obtained.[138] Most recently, the DeGrado group has shown that a single mutation (from Ile) provides an additional coordinating His residue at the dimetal center of G4-DFsc and results in a protein that can now catalyze the N-hydroxylation of arylamines such as *p*-anisidine, an activity not detected for G4-DFsc.[138] Only three additional mutations outside of the coordination sphere were made to counterbalance the steric clashes and unfavorable electrostatic interactions introduced by the His residue. The design does not fold well in the absence of metal, but does adopt a fold similar to those of the other DF proteins in the presence of divalent metals. It is particularly striking that addition of a single metal-coordinating residue can result in complete loss of one activity, phenol oxidation, and generate another, N-hydroxylation. This work is an excellent example of how *de novo* design can be utilized to directly correlate structure with function by removing much of the complexity of native proteins.

3. Design of hydrolytic zinc proteins

Following iron, zinc is the second most abundant trace metal in the human body. The major roles of zinc in proteins are catalytic (including cocatalytic) and structural. The major difference between structural zinc sites, as in zinc fingers (ZFs), and catalytic sites, as in carbonic anhydrase (CA), is that structural sites have saturated coordination spheres,

with amino acid ligands His and/or Cys bound to the zinc ion, whereas catalytic centers have at least one vacant site allowing for solvent (water) or substrate coordination.[139] Bound water is a feature of catalytic zinc centers, as it can be activated for ionization, polarization, or displaced by another ligand, such as an alcohol substrate.[140] I will discuss herein the redesign of a structural ZF site into a catalytic site, and the design of a zinc site for phosphate hydrolysis. Then I will introduce a few *de novo* designed zinc-binding peptides that have carbonic anhydrase activities. One of the *de novo* designed zinc-peptide, in particular, is an important foundation to this thesis work.

3) Redesign of zinc fingers for catalysis

ZFs are ubiquitous, small protein domains that bind to DNA to regulate gene expression. ZFs are now classified into at least 14 different classes, based on the metal-coordinating ligand as well as the protein fold, if known.[141] ZFs utilize four Cys and/or His residues for tetrahedral metal binding, forming a $Zn(Cys)_x(His)_{4-x}$ coordination site. Three commonly studied ZF proteins are those with Cys_4, $Cys_2HisCys$, and Cys_2His_2 sites.[142] Cys_4 ZFs constitute one class, which are usually found in nuclear receptors and play important roles in developmental biology.[143–161] Another class of ZFs is the nucleic acid binding proteins that have $Cys_2HisCys$ binding site.[162–174] The third, best-known, and most common ZF motif in eukaryotes is the His_2Cys_2 metal-binding site.[141,168,175–180] The secondary structure of ZF proteins consists of an α-helix packed against a two-stranded antiparallel β-sheet. The opposite side of the α-helix with respect to β-sheet packing associates to DNA for gene regulation, whereas the β-hairpin region does not interact with DNA but instead is a structural component of the domain.[181–183] For all three types of ZF domains, Zn(II) is almost always necessary for protein folding yet is not directly involved in the DNA-binding activity.[177,184]

Based on a wild-type (WT) ZF protein ZF(CCHH), Nomura *et al*. incorporated an unsaturated Zn(II) binding site by mutating the coordinating His and Cys residues into an Ala or a Gly.[185] CD spectroscopy shows that Zn(II) still induces α-helix formation for some of the mutants. Because of the unsaturation of the coordination at the Zn(II) ion, all of the mutants exhibit *p*NPA hydrolysis activity. Furthermore, increasing the number of ligating His residues leads to higher catalytic activity, due to the increased Lewis acidity

of Zn(II). Inhibition studies were carried out to confirm the catalytic role of the Zn(II)-bound protein complex. Interestingly, the Zn(II)-bound complex of ZF(HHHH) exhibits enantioselective esterase activity toward Boc-glutamine 4-nitrophenyl ester (Gln-ONp), indicating that the Zn(II) active site in this protein is situated in an asymmetric environment.

Follow-up studies using the ZF protein derivative ZF(HHHH) (Zn·1) and a previously reported three-tandem ZF protein[186] derivative Zn·2 (where two Cys residues were mutated to two His) showed that these Zn–protein complexes could hydrolytically cleave DNA.[187] A supercoiled plasmid DNA, pUC19GC, was used as a substrate to examine the nuclease activity. Because of preferred binding of Zn·2 to the GC box of the DNA duplex, selective hydrolytic cleavage of DNA could be achieved with moderate activity. To improve the DNA cleavage activity, Negi *et al*. combined ZF structural sites with a nuclease site into one design, yielding ZWH4.[188] ZWH4 contains four Zn(II)-binding sites, three of which are Cys_2His_2 ZF sites and the fourth a His_4 hydrolytic site. Zinc-bound ZWH4 catalyzes DNA cleavage with a clear production of different forms of products depending on the protein concentration. Specifically, at 25, 50 equiv. of ZWH4/ DNA, the cleavage reaction produced form II (a nicked circular form), a mixture of form II and form III (a linear form) products, respectively. This report shows how further control of the specificity of artificial nucleases can be achieved.

Many designed ZF nucleases have been developed to obtain alternative methods to gene therapy. Porteus and Baltimore analyzed gene targeting with homodimers consisted of an artificial ZF binding domain, QQR, to create a DNA double-stranded break in a genomic target.[189] Nakatsukasa *et al*. also placed a ZF protein on either side of a functional DNA cleavage linker.[190] Ideally, these new systems will be capable of unique and specific DNA cleavage and could ultimately be used to manipulate genetic information to precisely alter or replace damaged or disease-correlated DNA sequences. However, off-target site cleavage induced by ZF nucleases could result in cytotoxicity that must be mitigated for these systems to be useful as routine medicinal nucleases.

4) Designed zinc enzymes for phosphate hydrolysis

The Baker group has developed a computational method for redesigning metalloenzymes to catalyze noncognate reactions, and computationally redesigned a Zn(II)-containing mouse adenosine deaminase for organophosphate hydrolysis.[122] The approach harnesses *de novo* enzyme computational design methods.[191–193] Scaffolds are selected that contain backbones that can support active sites for the target reaction, and then the binding pocket sequence is optimized for the transition state. Applying this approach to existing metalloenzymes will address only the geometric compatibility of the site with the transition state and not the reactivity of WT functional groups. This is a valuable consideration as most enzymatic redesign involves altering substrate specificity or stereoselectivity, enhancing a preexisting promiscuous activity,[194] or relies on having structural homologues that already have the desired activity (in the case of introducing mechanistically related activities) as a starting point.[195] One example involved the redesign of the Zn(II)-containing glyoxalase II enzyme into a β-lactamase through extensive modifications made through insertion, deletion, and substitution of several active site loops and subsequent point mutations.[196] This redesign alters both the metal-binding geometry and the substrate-binding pocket, yet both glyoxalase II and metallo β-lactamase enzymes contain binuclear metal ions essential to the hydrolysis reaction.

In this study, organophosphate hydrolysis was chosen as a target reaction and Zn(II) metalloenzymes as templates for supporting this activity, given that Zn(II) ions serve as powerful catalysts in many hydrolase enzymes with diverse mechanisms. Several mononuclear Zn(II) enzymes were examined for their geometric compatibility with the transition state of the target reaction (using methyl paraoxon and diethyl 7-hydroxycoumarinyl, or DECP, as substrates). Residues were introduced for both H-bonding interactions and shape complementarity leading to a set of 12 possible designed proteins for experimental characterization. One of these hydrolyzed DECP with a modest efficiency of ~4 $M^{-1}s^{-1}$. The template enzyme for this model was adenosine deaminase, which, although also a hydrolytic enzyme, is distinct in terms of its transition state geometry, leaving group character, and inherent reactivity at the substrate electrophilic center. Eight mutations relative to the parent WT complex were made in the

computational design model, seven for shape complementary interactions and one for an H-bond interaction to the nucleophile in the model. The Zn(II)-coordinating residues, Asp and three His residues (in a trigonal bipyramidal geometry with one open coordination site), and the catalytic residues, Glu217 and His238, were all retained from the WT enzyme (Figure I-3A). The WT enzyme showed no acceleration for DECP hydrolysis over buffer at <20 mM enzyme. Using the initial velocity, the substrate concentration at which it was measured, and 20 μM enzyme concentration, a $k_{cat}/K_M \approx 10^{-3}$ $M^{-1}s^{-1}$ was estimated. Mutation of Glu217, a residue involved in proton shuttling in the WT enzyme, to Gln results in complete loss of activity, indicating that this residue is crucial for organophosphate hydrolysis.

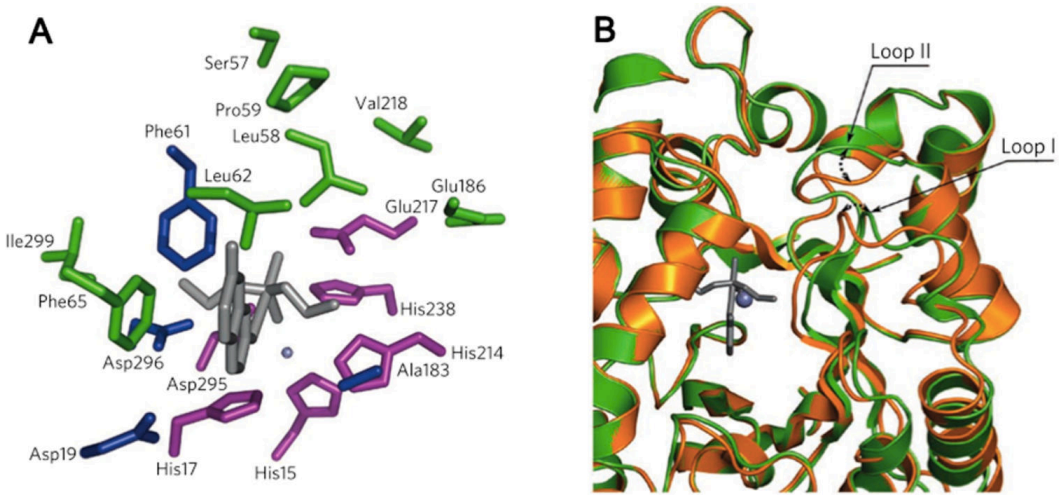

Figure I-3. (A) Spatial clustering of WT and activity-enhancing residues in a Zn(II)-containing mouse adenosine deaminase. Residues in which computationally designed simultaneous substitutions were essential for the emergence of organophosphate hydrolysis activity are highlighted in blue. Deaminase residues retained in the most active variant of PT3 (purple), and positions in which activity-enhancing mutations occur during directed evolution (green) form two separate spatial clusters. Residue side chain identities are from the deaminase crystal structure (PDB code: 1A4L), and the transition state model is shown in gray sticks. (B) Superposition of the PT3.1 design model (gold) and the crystal structure (green, PDB code: 3T1G) shows that, although the overall backbone similarity is high (backbone rms deviation = 0.65 Å), there are small shifts in two active site-proximal loops. Reproduced with permission from ref [122]. Copyright 2012 Nature Publishing Group.

Directed evolution, a method used in protein engineering for evolving proteins through an iterative process of preparing mutants and selecting those with the desired

properties,[197] was undertaken to gain a better understanding of the missing elements in this computational design method. Three rounds were performed, the first in which a set of selected residues around the active site was considered and three new mutations were incorporated, leading to a 40-fold increase in efficiency. Two subsequent rounds were carried out, the second by introducing random mutations, and the third considering a single residue identified to be in a suboptimal position by crystallography. These led to four more mutations, and another 10-fold increase in efficiency for each round, resulting in a total 2500-fold improvement over the initial computational design model. The biggest contributor to the increase came from the first round of directed evolution, and involved mutation of Val to the bulkier Phe, resulting in increased hydrophobicity around the catalytic residue Glu217 (Figure I-3). The authors propose that, although Zn(II) in the WT enzyme activates the hydroxyl nucleophile, Zn(II) in the design model is more likely to polarize the P–O bond, along with the side chain of His238, and Glu217 is the general base that activates the nucleophile (although a crystal structure with a bound substrate or transition state analogue is required to prove this). These results indicate that the redesigned protein may operate with a mechanism different from that of the WT enzyme.

Analysis of the computational design protocol revealed some of its shortcomings. Most of the mutations that result in an improved efficiency are due to an increase in k_{cat}. The biggest increase came from the Val218Phe mutation in the first round of directed evolution. This residue does not directly contact the transition state, but it does increase the bulk around the catalytically critical side chain of Glu217, probably modulating its pK_a and reactivity. Analysis of the apo-PT3.1 (from the first round of directed evolution) crystal structure reveals that, although much of the backbone and other elements of the structure match the design model, some conformational shifts in the loop backbone structure proximal to the active site were observed (Figure I-3). These acted to accommodate the bulkier side chain that came from the Val218Phe mutation. Notably, the design was carried out on a fixed WT backbone so this mutation would have caused clashes in the design model. The authors' future efforts will be in developing computational enzyme design methodology to allow more backbone flexibility and incorporate pK_a effects with more accurate electrostatic interaction models. Although the primary coordination environment around the metal has not been changed in this enzyme

redesign, this study demonstrates an effective approach to harnessing the inherent catalytic power of metal ions and introducing new reactivity into an existing metalloenzyme in a way that does not rely on preexisting activity. This study demonstrates the importance that the surrounding protein structure can have on the activity of the "same" metal site, given that both the substrate and the reaction mechanism are different. As a result, this approach can be one way of generating powerful metalloenzymes to catalyze novel reactions for a variety of biocatalyst applications. The catalytic efficiency of this enzyme is compared to other designed system in Table I-1. More recently, the Baker group has expanded the realm of computational protein design by incorporating an unnatural amino acid (2,2'-bipyridine-5yl)alanine (2,2'-bpy-Ala) into native proteins.[198] RosettaMatch and RosettaDesign were used to search for the backbone location for the bpy-Ala residue and introduce additional interactions to stabilize the protein, respectively. The resulting protein scaffolds bind to divalent metal ions with a relatively high affinity, laying a solid foundation for the future design of unnatural amino acid-containing hydrolases.

Many native nucleases contain metal ions such as Mg(II), Ca(II), Cu(II), and Zn(II),[199–204] which enhance catalytic activity by acting as Lewis acid catalysts or activators for either the nucleophilic attack or the leaving group departure.[199–202,205–214] Early attempts to incorporate a Zn(II) binding moiety in a peptidic scaffold to carry out hydrolytic phosphate cleavage reactions were performed by the Scrimin group.[215,216] They installed 2 equiv of an azacrown functionalized amino acid, (*S*)-2-amino-3-[1-(1,4,7-triazacyclononane)]propanoic acid (ATANP), into a water-soluble heptapeptide chain that adopts a 310-helix structure. This peptide binds up to 2 equiv of Zn(II) at the azacrown sites, which cooperatively catalyze the cleavage of an RNA model substrate 2-hydroxypropyl-*p*-nitrophenol phosphate (HPNP) (Scheme I-2, Figure I-4). This represents the first example of a short, water-soluble 310-helix peptide with catalytic activity. Further studies involved binding other divalent metal ions such as Cu(II) and Ni(II) to the azacrown site of the same scaffold with minor adjustments to the amino acid side chains and examination of their reactivity toward HPNP cleavage. Although all three metal-bound peptides exhibit catalytic activity, the Zn(II)-peptide has the highest activity, more than 3-fold faster than the Ni(II)- and Cu(II)-peptides. It was shown that the

dinuclear metallopeptide complex with a 310-helix structure has higher activity than the smaller dipeptide without any secondary structure due to the proper positioning of the substrate. Only upon binding two metal ions 6.3 Å apart, as is the case occurring in a 310-helix peptide, could an HPNP molecule be properly activated and subsequently cleaved.[216] With the incorporation of an interchelating moiety (an acridine ring) at the N-terminus for DNA binding, the dinuclear Zn(II)-peptide was able to perform hydrolytic cleavage of plasmid DNA pBR322.[217]

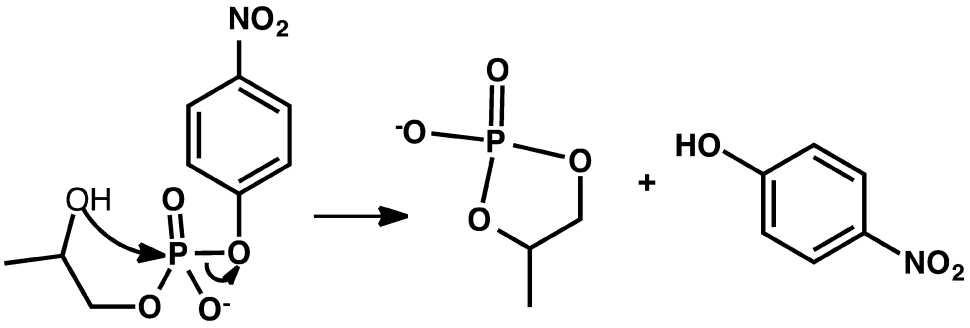

Scheme I-2

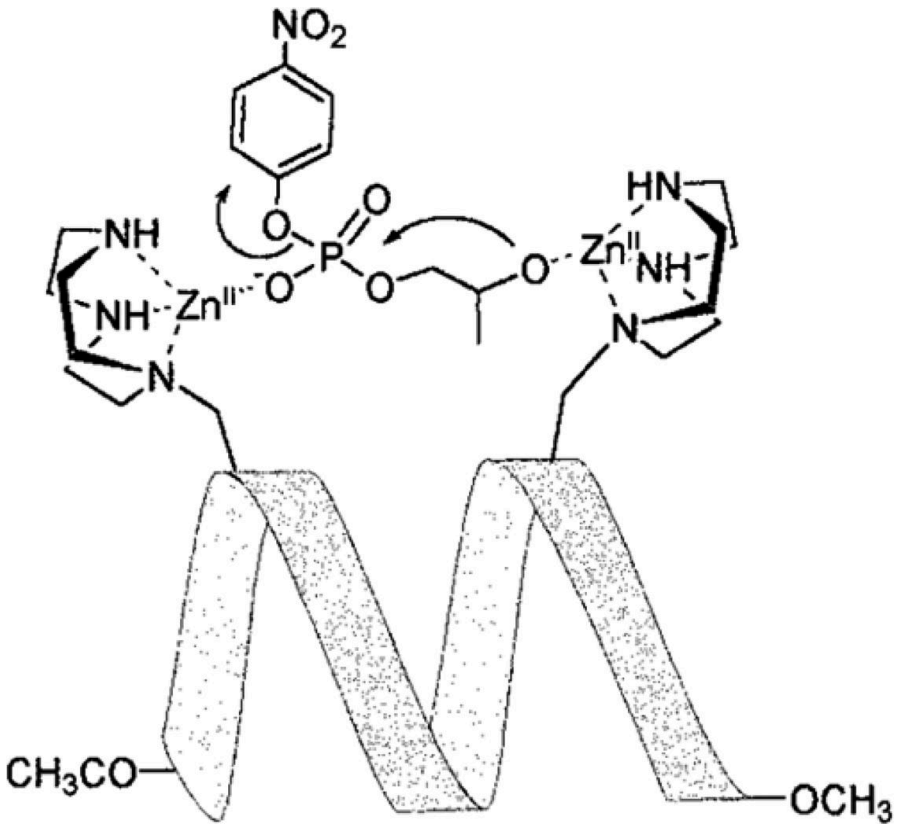

Figure I-4. Proposed cleavage mechanism of HPNP. Reproduced with permission from ref [215]. Copyright 1999 American Chemical Society.

On the basis of the same principle, Scarso *et al*. designed a peptide template $T(P1)_3$ that is capable of binding 4 equiv of Zn(II).[218] This peptide template consists of three copies of P1a, which is a designed 310-helix heptapeptide chain that has one azacrown Zn(II) binding moiety (Figure I-5A), and a tris(2-aminoethyl)amine (Tren) moiety as a platform onto which three peptide strands were attached. Because Tren can bind 1 equiv of Zn(II) itself, the fully Zn(II)-bound complex contains 3 equiv of Zn(II) bound to the peptide and 1 equiv of Zn(II) at the Tren center (Figure I-5B). This complex was able to carry out the transphosphorylation of HPNP (Scheme I-2) with the highest rates when 4 equiv of Zn(II) were bound. In addition, allosteric control of Zn(II) binding to Tren was observed for $T(P1)_3$, which led to the cooperative interactions between the Zn(II)-azacrown moieties, previously demonstrated to be critical to the rates of the cleavage reaction.[215,216] Oligomeric RNA cleavage was also attempted with $Zn(II)_4(T-(P1)_3)$, but proved to be less efficient than the more flexible apo-$(T(P1)_3)$.

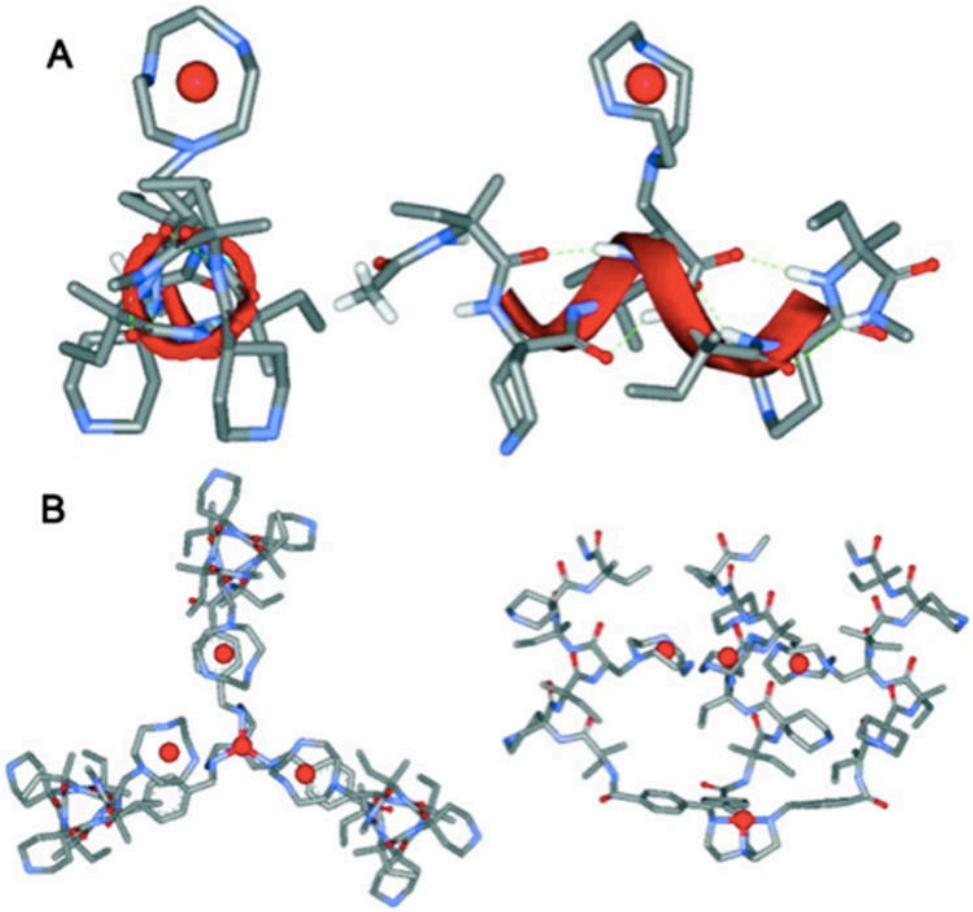

Figure I-5. Molecular models of (A) P1a-Zn(II) complex top view and side view; and (B) $Zn(II)_4(T(P1)_3)$ complex top view and side view. Reproduced with permission from ref [218]. Copyright 2002 National Academy of Sciences.

The same Zn(II)(1,4,7-triazacyclononane) moiety was also integrated into a *de novo* designed helix–loop–helix (HLH) motif.[219] The 42-residue peptides PR I–III were designed on the basis of the sequence of SA-42 and KO-42 that Baltzer and co-workers previously reported.[220–222] PRI has two ATANP on each helical strand at the *i*/(*i*+4) positions, assuming the peptide adopts an α-helical conformation, yielding four Zn(II) binding sites. PRII has two ATANP on one helical strand at the *i*/(*i*+4) positions, and PRIIII has one ATANP on each strand. All three peptides adopt predicted HLH conformations at a neutral pH range. The apparent second-order rate constant of $Zn(II)_4$-PRI toward HPNP cleavage was improved by 3-fold as compared to the first Zn(II)-peptide with the aridine ring (k_2 = 0.16 $M^{-1}s^{-1}$ for $Zn(II)_4$-PRI and 0.05 $M^{-1}s^{-1}$ for $Zn(II)_2$-310).[215,216] $Zn(II)_2$-PRII and $Zn(II)_2$-PRIII show comparable second-order rate constants

(k_2 = 0.094 and 0.084 $M^{-1}s^{-1}$, respectively), both smaller than that of $Zn(II)_4$-PRI. Rossi *et al*. also showed cooperativity between at least two Zn(II) ions in the metal-loaded peptides. They proposed two possible pathways for the hydrolysis reaction to proceed coorperatively, both of which involve two Zn(II) ions acting together to interact with the substrate hydroxyl or Zn(II)-bound water molecules.[219] Overall, the efforts on designing zinc phosphate hydrolase demonstrate the utilization of the Lewis acidity of Zn(II), which is also an important feature entailed in the next section.

5) Design of carbonic anhydrase mimics

CA is a Zn(II)-containing enzyme that is found in almost all plants, algae, and mammals, whose function is fundamental to many eukaryotic biological processes such as respiration, ion transport, and acid–base balance.[223–225] The physiological reaction catalyzed by CA is the interconversion between CO_2 and HCO_3^-; however, the catalytic promiscuity of CA allows for the rational design of the active site to exhibit increased activity toward ester hydrolysis.

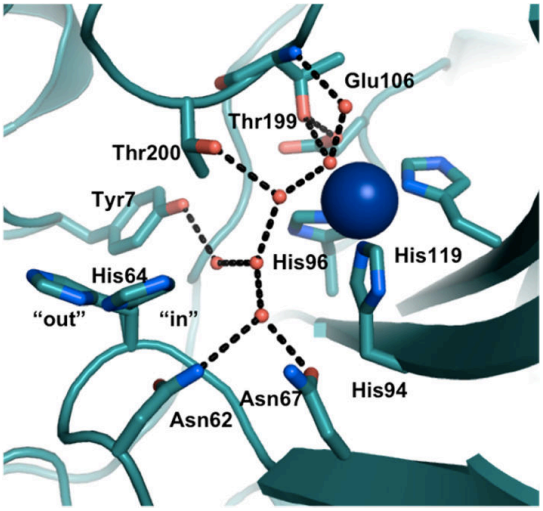

Figure I-6. CA H-bonding network based on the crystal structure of CA (PDB code: 3KS3[226]). Reproduced from Ref [1]. Copyright American Chemical Society 2014.

High-resolution crystal structures of CA reveal that Zn(II) is coordinated to three His residues (His94, 96, 119) and a water molecule/hydroxide ion, that is H-bonded to the hydroxyl side chain of a nearby residue, Thr199, which, in turn, forms an H-bond with Glu106 (Figure I-6).[227–230] The active site is contained in a twisted beta-sheet. The

redesign of the active site of CA involves modification of the first or outer coordination spheres. Fierke, Christianson, and co-workers pioneered studies mutating both coordinating and noncoordinating residues around the Zn(II) center in CA.[231–237] Specifically, one or more of the Zn(II)-coordinating His residues (His94, 96, 119) were substituted with a neutral, nonpolar, noncoordinating amino acid residue (Ala), carboxylate-containing residues (Asp, Glu), a thiolate-containing residue (Cys), and carboxyamide-containing residues (Gln, Asn), and observed varied Zn(II)-binding affinities and catalytic rates and efficiencies.[232–234,238] The substitution of any coordinating His residue decreased the Zn(II)-binding affinity by ~10^4–10^5-fold. The pK_a of Zn(II)-bound water, representing conversion to the active Zn(II)-hydroxide species, increased by at least one pH unit when His residues were replaced with other residues (p$K_{a(WT–CAII)}$ = 6.8 ± 0.1,[239] p$K_{a(mutants)}$ ≥ 8.4). In addition to catalyzing physiological CO_2 hydration, CAII can also catalyze ester hydrolysis, which is another important hallmark of its activity. The catalytic efficiency of both *p*NPA hydrolysis and CO_2 hydration decreased significantly with the substitutions described above. Although these studies were reviewed in an earlier contribution,[231] it is important to revisit them briefly here because they have provided important insight into the role of coordinating His residues, outer-sphere residues, and the mechanistic aspects of CO_2 hydration, which are relevant for the *de novo* designed CA models.

The studies on native CA illustrate that the coordinating His residues are essential in maintaining the Zn(II)-binding affinity, the pK_a of Zn(II)-bound water, the stability of Zn(II)-bound hydroxide, and the negatively charged transition state for CO_2 hydration. Moreover, these His residues might also play a role in forcing the tetrahedral coordination geometry, found in native CAII, over trigonal bipyramidal geometry.[231]

The modification of the second coordination sphere of the Zn(II) site in CA focuses on the alteration of hydrogen bonding (H-bonding) interactions, particularly by substituting Thr199, Thr200, and Gln92 residues that were shown to be important in maintaining the H-bonding network around the active site.[235–237,240,241] In WT-CAII, Thr199 accepts an H-bond from Zn(II)-bound hydroxide and donates an H-bond to Glu106, building a proton transfer chain to facilitate CO_2 hydration.[230] The crystal structure of Co(II)-substituted Thr199Cys-CAII reveals that the substitution of Thr199

with a Cys residue leads to the displacement of the Zn(II)-bound water by the thiolate ligand.[240,242] The additional coordinating ligand, Cys, results in a Zn(II) affinity increase in of 4-fold; however, the catalytic efficiency of CO_2 hydration is compromised substantially. Similarly, Thr199 is replaced with Glu, Asp, or His residues.[237] Both mutants with residues containing carboxylate groups (Thr199Glu and Thr199Asp) show displacement of Zn(II)-bound water by the carboxylate ligand in their crystal structures, although the O(carboxylate)– Zn(II) distances are different. For the Thr199Asp mutant, the two oxygens from the carboxylate of Asp bind Zn(II) in a bidentate fashion with a Zn(II)–O distance of 2.5 Å, whereas the carboxylate in the Thr199Glu mutant displaces a water molecule and adopts a unidentate binding mode with a Zn(II)–O distance of 2.2 Å. Only Thr199Glu exhibits a significant increase in the Zn(II)-binding affinity (200-fold), demonstrating the influence of metal–ligand separation and side chain torsion angles on protein–metal affinity. In contrast to Thr199Asp and Thr199Glu, Thr199His does not coordinate Zn(II). The Zn(II) affinity of the Thr199His mutant decreased by as much as 20-fold as compared to that of the WTCAII [$K_d = 7.7(\pm1.3) \times 10^{-11}$ M for Thr199His, $K_d = 4(\pm1) \times 10^{-12}$ M for WTCAII]. In addition to Thr199, residues at the 200 position are also polar residues (Thr, Asn, or His) that influence the catalytic efficiency of CO_2 hydration for different CA isozymes.[243] Krebs *et al*. substituted Thr200 with a Ser residue in CAII, with little to no change in the catalytic efficiency for CO_2 hydration, but a 4-fold increase in the catalytic efficiency for *p*NPA hydrolysis was observed.[241] The crystal structure of the Thr200Ser mutant shows that this substitution results in relocation of His64, which was thought to change the solvent structure around the active site and to modify the proton transfer chain. Moreover, two additional important second-sphere residues, Gln92 and Glu117, H-bonded to the imidazoles of His94 and His119, respectively, were mutated to examine alteration of the H-bond length (Gln92Asn, Glu117Asp) or charge (Gln92Glu) of the H-bond acceptor.[235,237] These studies illustrate the importance of these H-bonding residues for maintaining proper Zn(II) affinity, but also suggest that changing the length or charge of donor residues does not alter the affinity significantly (≤3-fold decrease in Zn(II) affinity). More importantly, these second-sphere residues indirectly influence the stability of the pentacoordinate transition state during CO_2 hydration, altering the catalytic efficiency.

The substitution of residues on the secondary coordination sphere, Thr200Cys/His and Asn67His, results in increased catalytic efficiency for *p*NPA hydrolysis.[241,244] Additionally, the substitution of Thr200 by His, Leu, Ile, Lys, Arg, Ser, *etc*., led to a variation of substrate specificity, which might be explained by the dissimilar van der Waals volume of the side chains and their interactions with different substrates. Furthermore, a directed evolution method was used to produce an esterase toward a less active, bulkier substrate 2-naphthyl acetate (2NA).[245] The most successful variant with Thr200Ala and Ala65Val mutations, where the Ala to Val substitution was thought to increase the "affinity" of the hydrophobic substrate, raised the catalytic efficiency toward large aromatic substrates. Later, variants of human carbonic anhydrase II (hCAII) were designed by Höst *et al*. with the goal of modulating the size and increasing the shape of the hydrophobic pocket for ester binding.[194,195] The hydrophobic pocket close to the Zn(II) site in hCAII is defined by four amino acids: Val121, Val143, Leu198, and Trp209.[239] In this work, increasing the size of the pocket was achieved by Val121Ala/Val143Ala mutations, which showed a significant increase in the catalytic efficiency toward larger substrates with longer acyl chains.[194] Moreover, a Thr200Ala mutation was introduced in addition to the two Val mutations, creating a hCAII derivative with a catalytic efficiency 5 orders of magnitude better than that of the WT-hCAII toward *p*NPA hydrolysis.[195] These efforts provide the foundation for elucidating the structure–function relationship of the active site of CA, shedding light on the *de novo* design of Zn(II) hydrolytic sites (*vide infra*).

Designed zinc metalloprotein systems have shown modest activity until recently. Notably, a few successful examples of hydrolytic zinc centers have been reported based on redesigns of native proteins. There has been no precedent of incorporating an efficient zinc hydrolytic center in a novel peptide sequence until Dr. Melissa Zastrow from our group reported her CA mimic based on the TRI family peptides.[125] It is important to introduce the basis of this construct and the design of CA mimic here because my copper-peptides share the same scaffold and similar sequences.

A well-defined coiled coil scaffold based on the heptad repeat approach is used as a basic construct for this thesis. Using the program InsightII/Discover,[246] DeGrado applied negative design principles[3,27,33] to prepare the 29 amino acid peptide CoilSer

(CS)[8,9] (Table I-2), which was acetylated at the N-terminus and amidated at the C-terminus, with the intention of generating an antiparallel four-stranded coiled coil (4SCC). However, X-ray analysis demonstrates that the resulting aggregate is an antiparallel (two "up" C-termini and one "up" N-terminus) three-stranded coiled coil (3SCC).[9] The basis of this approach is to exploit the heptad repeat, known to induce α-helix formation. Simply, the concept is that a peptide assembly will form through "hydrophobic collapse"[247–250] based on the exclusion of hydrophobic residues from the aqueous phase. Control of strand number is achieved by matching the packing of the hydrophobes into the desired aggregates (2SCC, 3SCC, or 4SCC). Orientational control (parallel vs antiparallel) and solubility are conferred by hydrophilic, charged residues placed at the interhelical interface. These charged residues form salt bridges at appropriate pH conditions.

A heptad is composed of seven amino acid residues, denoted as *abcdefg*, where *a* and *d* positions are usually hydrophobic residues, and *e* and *g* positions are salt-bridging residues.[251,252] The connectivities between helices and overlapping hydrophobes are often represented as helical wheel diagrams (Figure I-7). For heptads containing Leu, the addition of each 7 amino acid repeat confers ~9 kcal/mol of stability to the system.[253,254] It should be noted that the intrinsic nature of the heptad places the *a* residue of the first heptad slightly (~20°) out of phase with the *a* residue of the following heptad. To optimize packing of the hydrophobes, the resultant α-helices twist or supercoil around one another. This is where the name "coiled coil" comes from as α-helices (coils) supercoil around each other to form the stable aggregate.

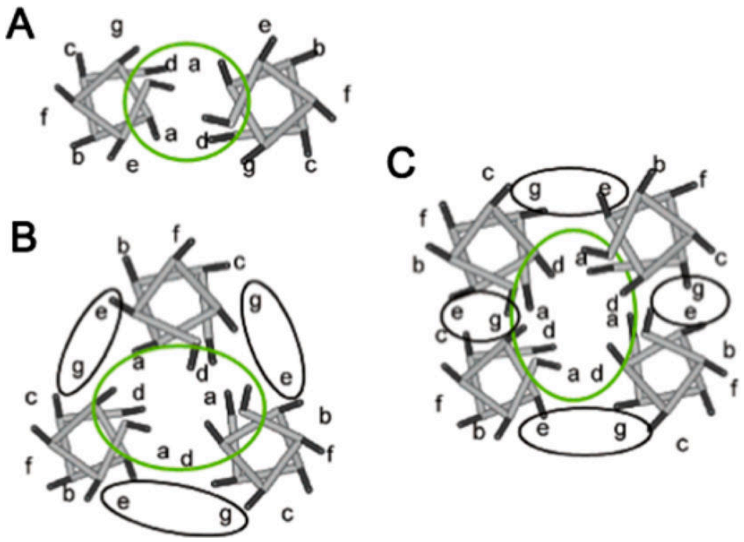

Figure I-7. Helical wheel diagram of (A) 2SCC, (B) 3SCC, and (C) 4SCC. Reproduced with permission from ref [251]. Copyright 2004 American Chemical Society.

Because of the high symmetry of these systems, one must determine whether a single protein fold exists in a "native-like fold", or has multiple similar energy conformations, which is then termed a "molten globule".[255–257] Usually, increasing the number of heptads or increasing the asymmetry in the sequence will lead to native-like folds. DeGrado demonstrated that a parallel 3SCC can be achieved by preparing Coil-V_aL_d.[11] This sequence alternates Val and Leu residues at the *a* and *d* positions, respectively, assuring that all helices are aligned by commensurate matching of the amino acid side chains in each layer.

Table I-2. CoilSer and TRI peptide sequences

Peptide[1]	N-terminus 1	*a b c d e f g* 2 8	*a b c d e f g* 9 12 15	*a b c d e f g* 16 19 22	*a b c d e f g* 23 26 29	*a b c d e f g* (30 36)	C-terminus 30(37)
BABY	Ac-G	LKALEEK	LKALEEK	LKALEEK			G-NH_2
TRI	Ac-G	LKALEEK	LKALEEK	LKALEEK	LKALEEK		G-NH_2
TRIL9C	Ac-G	LKALEEK	CKALEEK	LKALEEK	LKALEEK		G-NH_2
TRI-H	Ac-G	LKALEEK	LKALEEK	LKALEEK	HKALEEK		G-NH_2
TRIW-H	Ac-G	WKALEEK	LKALEEK	LKALEEK	HKALEEK		G-NH_2
TRIL9CL23H	Ac-G	LKALEEK	CKALEEK	LKALEEK	HKALEEK		G-NH_2
TRIL9CL19H	Ac-G	LKALEEK	CKALEEK	LKAHEEK	LKALEEK		G-NH_2
TRIL9HL23C	Ac-G	LKALEEK	HKALEEK	LKALEEK	CKALEEK		G-NH_2
CoilSer (CS)	Ac-E	WEALEKK	LAALESK	LQALEKK	LEALEHG		-NH_2
CSL9C	Ac-E	WEALEKK	CAALESK	LQALEKK	LEALEHG		-NH_2
CSL16C	Ac-E	WEALEKK	LAALESK	CQALEKK	LEALEHG		-NH_2
CSL12AL16C	Ac-E	WEALEKK	LAAAESK	CQALEKK	LEALEHG		-NH_2
CSL16P_n	Ac-E	WEALEKK	LAAAESK	P_nQALEKK	LEALEHG		-NH_2
CSL19C	Ac-E	WEALEKK	LAALESK	LQACEKK	LEALEHG		-NH_2
Grand (GR)	Ac-G	LKALEEK	LKALEEK	LKALEEK	LKALEEK	LKALEEK	G-NH_2

1. Metal-binding residues are in red
2. P_n = Pen

On the basis of these early studies, DeGrado and Pecoraro designed the amphipathic peptide scaffold known as the TRI family of peptides, so named because a parallel 3SCC scaffold was desired. This scaffold utilizes the generic heptad repeat, LKALEEK, and is capped by Gly residues at either end.[10,12,13] The peptides in this group are BABY, TRI, and GRAND, which have three, four, and five heptad repeats, respectively (Table I-2). The N-termini are acetylated and C-termini amidated to align the helical dipole, facilitating the assembly of the coiled coils.[10,12,252]

The TRI-family peptides self-assemble upon dissolving in water into 2SCCs at low pH (< 5) and 3SCCs at higher pH (> 5.5).[10,12] The Leu residues in the interior of the helix bundle can be substituted for heavy or transition metal-binding residues such as Cys or His. The locations of the mutations included in this chapter are described in Table I-2. At physiological pH, these peptides adopt a 3-fold symmetry, which is an excellent framework to generate trigonal, tetrahedral, or trigonal pyramidal metal coordination environments.[39]

Despite the prevalence of multisite metalloproteins in nature, there are few reports of designed two-site metalloproteins in which two different metals exist in separate binding sites.[7,124,125,258] Of these, only one has reported catalytic activity (Table I-1).[124,125] This *de novo* designed 3SCC contains two metal sites, one for structural stabilization (HgS_3) and the second for hydrolytic activity (ZnN_3O) within just a few hundred-fold of the native CA. To design a 3SCC, which discriminates two different metals in two different sites, the peptide TRIL9CL23H was used together with a metal ion with high affinity for thiolate ligands but low affinity for His (Hg(II)). Previous work demonstrated that Hg(II) can be used to induce folding in unfolded peptides and increase thermodynamic stability in prefolded peptides (as demonstrated by CD denaturation studies).[13,124,125] Additionally, Hg(II) provides a well-studied spectroscopic tag for the formation of a 3SCC (UV–vis and ^{199}Hg NMR differentiate between linear HgS_2 found in a 2SCC and trigonal HgS_3).[259] In the presence of this highly stable Hg(II)pep_3 complex, Zn(II) then binds solely to the His_3 site.

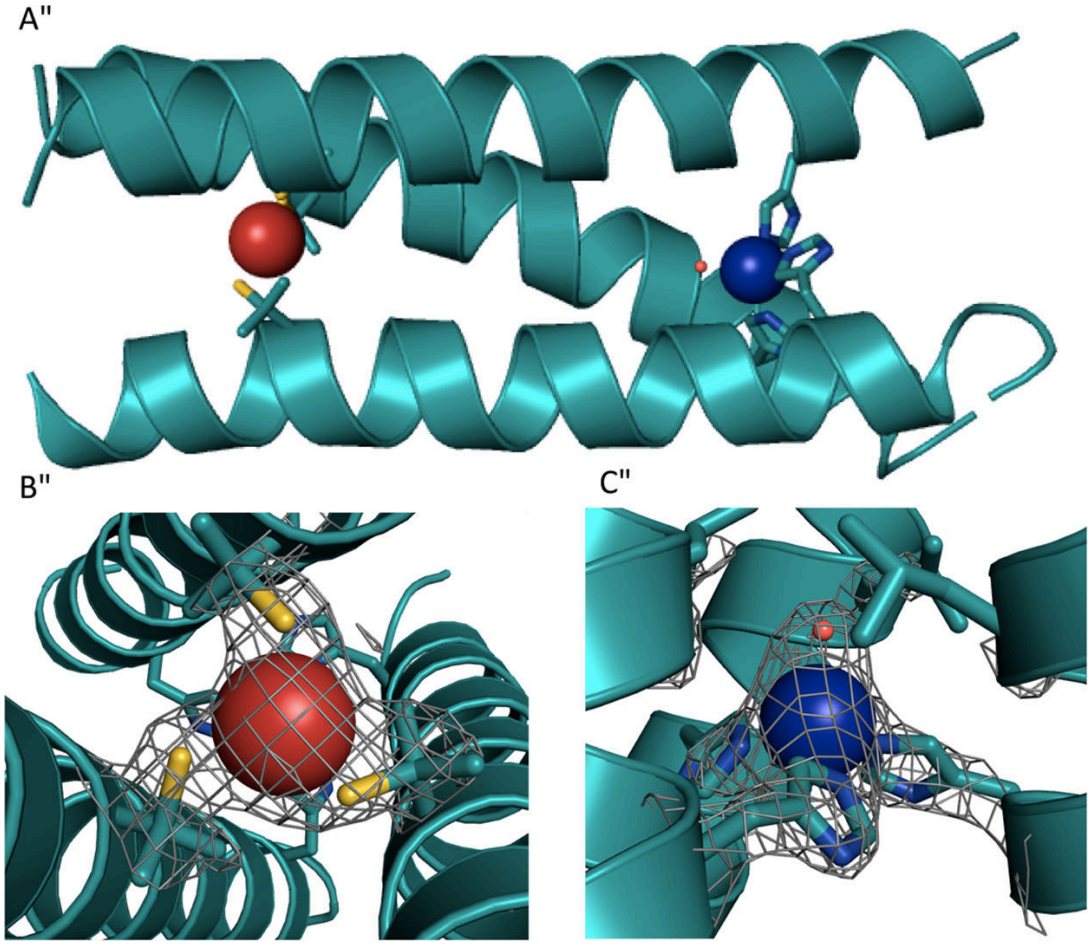

Figure I-8. Ribbon diagrams of the $[Hg(II)]_S[Zn(II)(H_2O/OH^-)]_N(CSL9PenL23H)_3^{n+}$ parallel 3SCC (one of two different 3-helix bundles present in the asymmetric unit) at pH 8.5. Shown are the main chain atoms represented as helical ribbons (cyan) and the Pen and His side chains in stick form (sulfur = yellow, nitrogen = blue, oxygen = red). (A) One of two trimers found in the asymmetric unit of the crystal structure; (B) a top down view of the structural trigonal thiolate site, $Hg(II)S_3$, confirming the proposed structure of Hg(II) in Cys-containing TRI peptides.[10] This metal site should mimic well the structural site in the metalloregulatory protein MerR.[260] (C) A side view of the tetrahedral catalytic site, $Zn(II)N_3O$, which closely mimics CA and matrix metalloproteinase active sites.[261] All figures are shown with 2Fo – Fc electron density contoured at 1.5σ overlaid. Reproduced with permission from Ref [1]. Copyright 2014 American Chemical Society.

One motivation behind the development of a $Zn(II)N_3$ site was to model the active site of CA, which catalyzes the reversible hydration of carbon dioxide and is one of the fastest known and most well-studied zinc metalloenzymes, making it an excellent system for *de novo* design mimicry studies. X-ray crystallographic studies on the Hg(II)Zn(II) complex of the related peptide sequence CSL9PenL23H (the CS sequence has properties

similar to those of TRI in solution) confirmed the presence of Hg(II) in the sulfur site (fully trigonal in one of the 3SCCs in the asymmetric unit and T-shaped in the second) and a Zn(II)N_3X site in both 3SCCs in the asymmetric unit, analogous to that found in CA (Figure I-8).[125]

This X-ray structure was significant for two reasons. First, it demonstrated that the proposed trigonal Hg(II) center for Hg(II)(TRIL16C)$_3^-$ existed as was predicted (*vide supra*) and provided the first structural model for the Hg(II) binding site in the metalloregulatory protein MerR.[260,262–264] Second, this work demonstrated that the native protein fold of CA was not necessary to achieve a closely similar structural model for the first coordination sphere of the Zn(II)$(His)_3(H_2O)$ center. One can conclude that for the first coordination sphere, this type of center can be accommodated in protein structures as varied as a twisted β-sheet with a long water channel as found in the native enzyme or in the hydrophobic interior of an α-helical coiled coil as shown for $[Hg(II)]_S[Zn(II)(OH_2/OH^-)]_N(TRIL9CL23H)_3^{n+}$.

Finding that the structural similarity of the Zn(II) site to that in CA is limited to the first coordination sphere (Figure I-9) allowed, for the first time, to begin to address what is the minimal unit required for catalytic activity in this type of system. To do this, Pecoraro and co-workers initially looked at whether the construct could catalyze the hydrolysis of *p*NPA, the non-physiological substrate of CA often used for analysis of its reactivity as compared to mutants and small molecule model complexes. Analysis of these reactivity studies demonstrates that hydrolysis of *p*NPA by $[Hg(II)]_S[Zn(II)(OH_2/OH^-)]_N(TRI\text{-}L9CL23H)_3^{n+}$ follows enzyme-like saturation kinetics with a maximal k_{cat}/K_M of 31 ± 4 $M^{-1}s^{-1}$, about 550-fold more efficient than comparable small molecule model complexes.[124,125,265–267] Further, it is within ~100-fold of the maximum efficiency of CAII and has a similar pH-dependent profile (increasing with increasing pH), yet the pK_a is shifted ~2 units higher (9.0 ± 0.1 versus 6.8 for CAII).[268,269] Importantly, the model compares even more favorably with CA mutants such as Thr199Ala in which the Thr residue that forms a hydrogen bond to the Zn(II)-bound solvent is replaced by Ala and as a result loses ~100-fold of its catalytic efficiency along with an increase in pK_a of about 2 units.[231,270,271] Therefore, it is reasonable to assume that the design of further secondary interactions similar to those found in CA is needed to

bridge the differences between this design and the native enzyme (assuming it is possible in this alternate scaffold). One other designed Zn(II)N_3 site (*vide infra*) catalyzes *p*NPA with a k_{cat}/K_M ~20-fold faster than $[Hg(II)]_S[Zn(II)(OH_2/OH^-)]_N(TRIL9CL23H)_3^{n+}$ and has a pK_a of 8.2 ± 0.1.[123] CA's physiologically relevant reaction, CO_2 hydration, was also examined, which yields an efficiency of ~1.8×10^5 $M^{-1}s^{-1}$ (pH 9.5) that is within ~500-fold of that of CA and faster than any reported small molecule complex.[125,272–279] There are no reports of CO_2 hydration by other designed protein systems.

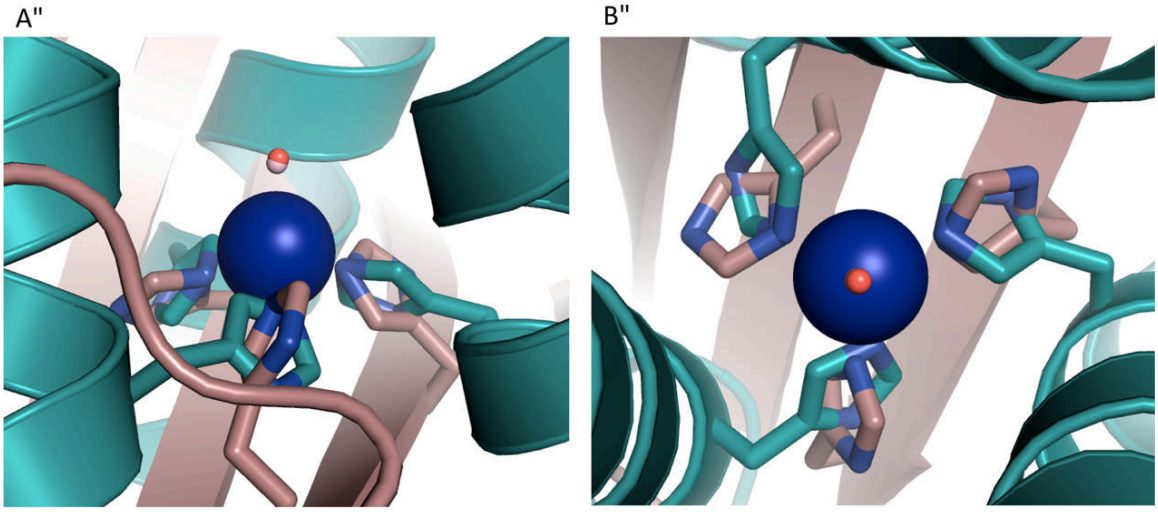

Figure I-9. Overlay of the Zn(II)N_3O site in $[Hg(II)]_S[Zn(II)(H_2O/OH^-)]_N(CSL9PenL23H)_3^{n+}$ with the active site of human CAII. $[Hg(II)]_S[Zn(II)(H_2O/OH^-)]_N(CSL9PenL23H)_3^{n+}$ is shown in cyan (PDB code: 3PBJ) and CAII in tan (PDB code: 2CBA). (A) Top-down view of the overlay with CAII. The solvent molecule associated with $[Hg(II)]_S[Zn(II)(H_2O/OH^-)]_N(CSL9PenL23H)_3^{n+}$ is shown in red, and that associated with CAII lies underneath. (B) Side-on view of the overlay with CAII. The model displays an excellent structural overlay for the first coordination sphere atoms with CAII; however, the orientation of the imidazoles differs between the two proteins. Another subtle difference is that the present structure has three ε amino nitrogens bound to the Zn(II) ion, whereas CAII has a mixed two ε and one δ coordination sphere. Overlay was performed manually in PyMol. Reproduced with permission from Ref [1]. Copyright 2014 American Chemical Society.

Having demonstrated that a significant amount of hydrolytic activity can be achieved simply by removing an active site from its native scaffold and placing it into a 3SCC, the next major aim was to incorporate secondary interactions to modulate the properties of this site (activity, pK_a, binding affinity). As mentioned above, the design of H-bonding channels so often found in native proteins is likely necessary. However, this

advanced design will likely require changes to the location of the active site within the 3SCC to retain stability and potentially allow for improved substrate access. To this end, Pecoraro and co-workers recently reported the systematic variation of the Zn(II) active site along the TRI sequence.[124] It is important to note that, although the properties of the Zn(II) site remain roughly the same in the absence of the $Hg(II)S_3$ site, they chose to retain the structural site when moving the active site along the linear sequence to take advantage of the $Hg(II)S_3$ chromophore's utility as a spectroscopic tag to ensure that the oligomeric state (trimer) remained. The first variation in sequence involved switching the locations of the two different metal sites to generate $[Zn(II)(OH_2/OH^-)]_N[Hg(II)]_S(TRIL9H\text{-}L23C)_3^{n+}$. Assuming that the general orientation of the Zn(II) site remains constant (with the Zn(II)-bound solvent molecule oriented toward the N-terminus), it was expected and found that the substrate access was improved. This was further confirmed through inhibition studies using one of the products, acetate, and fitting the *p*NPA kinetic data for competitive inhibition. The K_I's for the Zn(II) sites in $(TRIW\text{-}H)_3$ and $[Hg(II)]_S(TRIL9CL23H)_3^-$ are similar (0.34 ± 0.01 and 0.32 ± 0.01 M, respectively), while that for $[Hg(II)]_S(TRIL9HL23C)_3^-$ is 0.20 ± 0.01 M.[124] Despite the improved substrate access, however, the catalytic rate is decreased relative to the original model. Overall, the maximal catalytic efficiency is about the same as the original model with and without the structural site (24 ± 3 $M^{-1}s^{-1}$).

The second variation in sequence involves moving the His_3 site from the 23rd position closer to the N-terminus of the coiled coil and into a *d* site to yield TRIL9CL19H. It is worth considering why *a* and *d* sites might be different. If one considers the sequence LKALEEKLKALEEK, one realizes that going from an *a* position to a *d* position requires a spacer of two amino acids **L**<u>KA</u>**L**, whereas proceeding from *d* to *a* requires three amino acids, **L**<u>EEK</u>**L**. This sequence difference requires that layers be separated asymmetrically within the helical core. Second, because of the rotation of the peptide backbone around the helix, it is expected that the side chain of an *a* position hydrophobe or metal ligand will be oriented slightly differently from that of a *d* position side chain. Thus, either steric effects based on the layer above a metal or the positioning of a metal ligand will be different depending on the choice between an *a* or a *d* position for the metal-binding site. Analysis of the hydrolysis of *p*NPA by the metal-bound

complex of this peptide showed that while maximal catalytic efficiency is approximately the same as for those previously described, the substrate access is slightly worse, while the maximal catalytic rate is improved. The most drastic difference with this sequence, however, is that the kinetic pK_a shifted up to 9.6 (all of the others are approximately the same within error, ~9–9.2). It is unclear whether this is due to the altered orientation of the His ligands (from *a* site to *d* site) or simply the change in location. The K_I of acetate inhibition for L19H is approximately the same as for the L23H peptides, 0.36 ± 0.01 M. The apparent dissociation constants of Zn(II) to the His_3 site for all of the above-described complexes vary from ~0.2 μM (L23H sites) to 0.4 μM (L19H) to 0.8 μM (L9H) at pH 9, demonstrating some location-dependence. Generally, these binding affinities indicate that the designs bind Zn(II) well and are in the same range as for similar designs with three binding ligands; however, they remain weak as compared to native Zn(II) enzymes (K_d ~ nanomolar to picomolar).[6,36,231,280–288]

In summary, despite drastic variation in the location of the active site along this 3SCC, significant catalytic efficiency for hydrolysis is retained, suggesting that this may represent the "baseline" activity in this type of model. Further, Pecoraro and co-workers have shown that location can be used to control binding affinity, pK_a, catalytic rate, and substrate and solvent access (and selectivity). Although there are very few studies examining the effects of the protein matrix on the active site in this way,[24] such a systematic approach is very important to future design endeavors, especially when deciding on the placement of the active site. As a whole, these studies demonstrated that replicating the exact protein fold of the native system was unnecessary to achieve a structural and functional model; however, maximal catalysis may still be critically dependent on the native protein structure as the incorporation of water channels, H-bonds for activation or stabilization of the substrate or intermediates, and H-bonds to metal coordinated amino acids may be best facilitated by β-sheet structure rather than α-helices.

Although most designed enzymes rely on monomeric structures with metal sites inserted into their cores, Der and co-workers serendipitously discovered that a designed Zn(II) site at the interface of a homodimer (MID1-Zn) could effectively catalyze *p*NPA and p-nitrophenyl phosphate (*p*NPP) hydrolysis (Table I-1).[123,289] The motivation behind

the design was to use metal-binding sites at a designed protein interface to improve computational design protocols for protein–protein interactions. Given that metals form stronger interactions with the side chains of residues such as His, Cys, Asp, and Glu than do protein–protein hydrogen bonds or van der Waals contacts, it is reasonable to postulate that metal-binding interactions should overcome suboptimal hydrogen-bonding patterns or packing at the interface in a design.

The design was based on a two-residue Zn(II) binding site on a monomeric protein (derived from the Rab4-binding domain of rabenosyn), which was then dimerized and computationally optimized to form what was intended to be two $ZnHis_4$ binding sites at the interface of a homodimer.[289] The design model, which also included interactions between Met38, Tyr41, and Phe42 on both chains for forming a hydrophobic core at the interface, was named MID1 (metal interface design 1). As intended, MID1 forms a dimer at high micromolar concentrations both with and without Zn(II) present, but the dissociation constant in the presence of Zn(II) is more than 100-fold stronger than it is in its absence (K_d < 30 nM). X-ray crystallography demonstrates that MID1-Zn closely resembles the model, although with some key differences (Figure I-10). One difference is that only three His residues coordinate each Zn(II) ion at the interfaces. The coordination sphere is completed either by carboxylate groups from the C-terminal Asp or by a symmetry-related molecule or tartrate from the crystallization buffer. A small deviation in the binding orientation and in the protein–protein interface contacts was also observed. Despite these differences, a high affinity metal-mediated homodimer site was prepared using only computational design without any optimization by directed evolution.

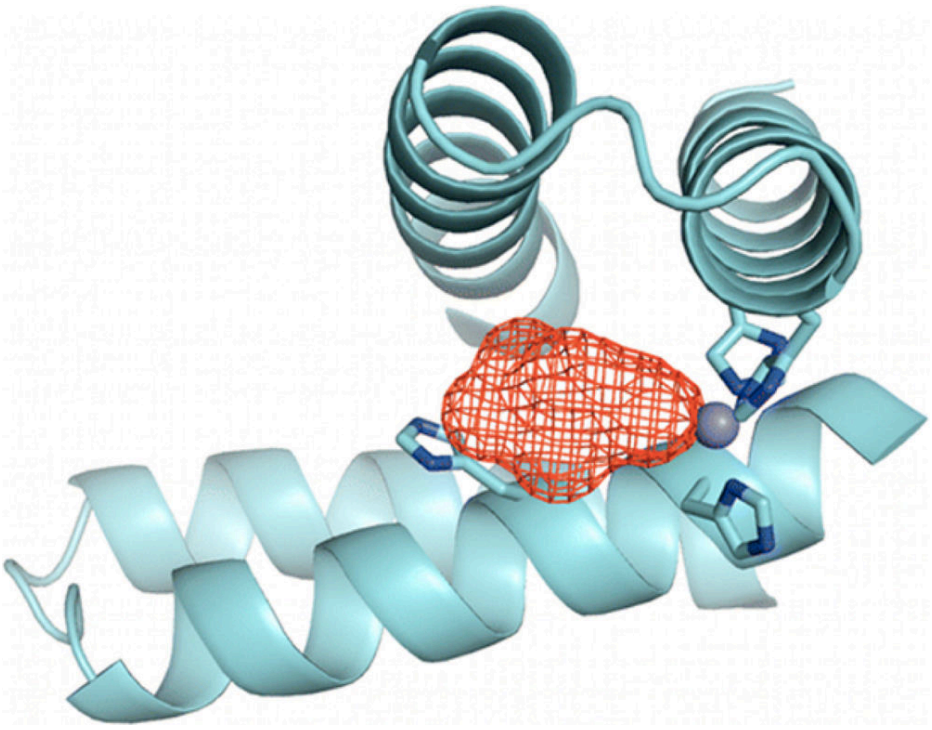

Figure I-10. X-ray crystal structure of MID1-zinc, a designed protein with a metal-mediated protein interface. The red mesh represents the active site cleft above the open coordination site of the $ZnHis_3$ metal site. Reproduced with permission from Ref [1]. Copyright 2012 American Chemical Society.

Although the original intention was to obtain a $ZnHis_4$ site, Der *et al*. observed that the presence of tartrate in the $ZnHis_3$ represented a small binding pocket (~6 Å wide and 4 Å deep), suggesting that the interface metal site may display esterase activity toward substrates like *p*NPA and *p*NPP. Indeed, MID1-Zn effectively catalyzes *p*NPA hydrolysis with more than 50 turnovers and a rate of 0.22 s^{-1} and K_M = 0.47 mM at pH 8.5.[123] The reaction is pH-dependent (increasing efficiency with increasing pH) and has a kinetic pK_a of 8.2 ± 0.1 and a maximal efficiency of 630 ± 90 $M^{-1}s^{-1}$. Control experiments using the apo version of the homodimer, a mutated version with no His binding residues, the WT monomer on which the design was based mutated with His residues, and free zinc all demonstrated no significant activity above the background, confirming that the interface pocket and Zn(II)-binding site are both required for catalysis. Further, mutation of some of the surrounding His residues to Glu demonstrated a loss of activity because the open coordination site was closed (His12Glu and His35Glu). Despite the original design intention of two Zn(II) sites, only one active site is

observed in the crystal structure (only one tartrate is bound to one Zn(II) site), and the dimer is fully formed with 1 equiv of Zn(II) for 2 equiv of monomer (no additional activity is observed with more Zn(II) present). Although *p*NPP is intrinsically less reactive, MID1-Zn still effectively catalyzes its hydrolysis with an efficiency of 14 $M^{-1}s^{-1}$ at pH 8.5. The K_M for this reaction, 12 μM, is 40 times lower than that for *p*NPA because of favorable electrostatic interactions between the negative phosphate group and positive Zn(II) active site.

The authors discuss the importance of the binding cleft in achieving these efficiencies. However, while enhancing efficiencies, it is expected that such an open catalytic site is likely to exhibit significant product inhibition, which has been a bane to small molecule model compounds. Synthetic models are relatively ineffective given that they have no binding cleft, although this can be improved somewhat in apolar solvents, which can simulate the apolarity of an active site cleft.[290] Further discussions and comparisons will be made in a later section where the de novo design of a $ZnHis_3O$ site in a 3SCC is described. Regardless, this study of a minimalist engineered enzyme demonstrates that cleft formation at protein interfaces provides another effective strategy for the rational engineering of new catalytic activities.

4. Design of copper proteins

Copper proteins play an important role in maintaining the redox poise and catalyzing oxidoreductase chemistry. The two major functions of copper centers are electron transfer and catalysis, both of which have been the target for protein redesign and *de novo* design efforts. Over the past two decades, the redesign of copper centers has seen considerable successful examples that involve the modulation of copper electron transfer capacity, tuning the catalytic activity, and the incorporation of copper centers with novel reactivity into foreign proteins. These studies address important issues such as the function of each copper-coordinating ligand, the role of protein secondary or tertiary structure, possible electron transfer pathways, *etc*. *De novo* designed copper centers, however, were still scarce at the time that this thesis began. Although there were a few reports of copper-binding peptides that share spectroscopic features of either a

cupredoxin site or a type 2 copper (T2Cu) center, no reactivity was demonstrated. Since the focus of this thesis is to design a functional model for a copper enzyme nitrite reductase (NiR), I will only summarize the effort of designing an electron transfer center. I will then discuss a few examples of designed type 2 centers. For a more detailed discussion on designing copper electron transfer proteins, readers can refer to Ref [1].

The design of copper electron transfer centers

Copper electron transfer centers encompass cupredoxin (type 1 copper, T1Cu), Cu_A, and some T2Cu centers. They function in electron transfer chains or in chemical reactions by relaying electrons to the catalytic centers.[291–295] Both cupredoxin and Cu_A centers are found in an overall Greek β-barrel fold, with the metal-binding ligands in a pocket between loops, protected from solvent access. T1Cu centers are mononuclear copper centers coordinated to two imidazole N atoms from His residues and the thiolate from a Cys residue in a trigonal plane ($CysHis_2$).[296,297] In addition, one or two weak axial ligands can be bound to the copper center, resulting in a distorted tetrahedral geometry that is not preferred by either Cu(II) or Cu(I) metal ions.[298] This unique structural feature provides cupredoxins with unusual spectroscopic and redox properties. The contribution of the copper electronic structure to its function and spectroscopic properties has been thoroughly studied.[296–312] Cu_A is a binuclear copper center with a diamond shaped [2Cu-2S(Cys)] core structure and N_{His}, S_{Met}, and $O_{backbone}$ ligands bound to the copper ions (Figure I-11). Cu_A centers have a unique structural feature, the Cu–Cu bond, which is not commonly observed in biological systems for first row transition metals.[313,314] The electronic and spectroscopic characteristics of Cu_A centers have been previously reported and reviewed.[291,297,301–303,308,309,315–318]

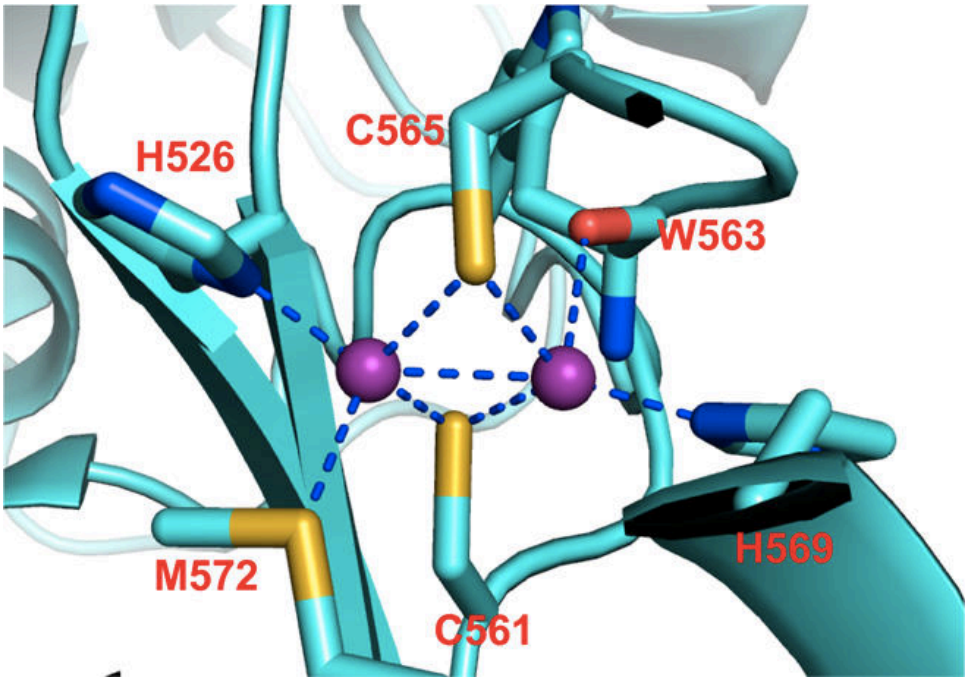

Figure I-11. CuA center in N_2OR from *Pseudomonas nautica*. The purple spheres are copper ions. PDB code: 1QNI.[319]

Azurin (Az), a native T1Cu protein, has been widely used in studies intended for modulating the redox and electron transfer properties of the copper center. Az is a small protein with a T1Cu center that shuttles electrons in certain types of denitrifying bacteria.[320–322] At its T1Cu site, copper is coordinated to two His (His47, 117) and a Cys (Cys112) in a trigonal plane, while weakly interacting with two axial ligands, Met121 and a carbonyl oxygen from Gly45.[323] The electron transfer function of Az was proposed to be related to cellular redox stress.[324] Extensive studies have been carried out to probe the roles of each ligand to the spectroscopic features, redox properties, and the impact of certain substitutions on the driving force and the reorganization energy of the electron transfer process.[325–339] In particular, Lu and co-workers carried out a series of studies aiming to address the roles of the Cys ligand,[340,341] the axial Met ligand,[342–344] and secondary coordination sphere interactions.[345] In these studies, a semisynthetic method that allows the fusion of a recombinantly expressed protein with a synthetic peptide containing the desired substitutions was used to incorporate unnatural amino acids into Az.[346] The impact of these residues on the spectroscopic and redox properties of T1Cu in Az highlights the power in using protein redesign to deepen our understanding of the

factors that influence redox properties. Furthermore, these designs show varied intraprotein electron transfer capability, which is indicative of variation of the reorganization energy with rational design.[347]

A Cu_A center was first introduced into the CyoA subunit of *E. coli* cytochrome *o* quinol oxidase complex, a scaffold that is devoid of a copper binding site.[348,349] Mutagenesis studies on the Cu_A-CyoA hybrid protein demonstrate that at least five residues, two His, two Cys, and one Met, are essential to construct a Cu_A site.[349] A Cu_A center was then incorporated into an Az, taking the place of the T1Cu center.[350–359] The roles of each coordinating ligand were examined.[351,352,356,358,359] Electron transfer activities were also demonstrated for the Cu_A–Az hybrid protein.[353] Moreover, several groups have incorporated a Cu_A center into another T1Cu protein, amicyanin, a cupredoxin found in methylotrophic bacteria,[360,361] and showed the electron transfer capability in these designed systems.[360,361]

The examples introduced above all have the copper electron transfer center in the loop region of a Greek β-barrel fold. By creating a copper electron transfer center in α-helical bundles, people can start to address the question of whether β-sheets are necessary to facilitate electron transfer. In addition, the *de novo* design of copper electron transfer centers provides critical insight into how the geometric constraints influence the spectroscopy.

Schnepf *et al*. were the first to report a T1Cu center embedded in an antiparallel four-helix bundle using a template-assembled synthetic protein (TASP) approach.[362,363] TASP is a *de novo* design approach that entails a combinatorial assembly of peptides that are linked to a preorganized template.[364–368] As a result, this strategy bypassed the entropically unfavorable nucleation step in the assembly of secondary structures, producing the desired peptidic scaffold for further functionalization.[366–368] Topological templates on the surface were used to covalently attach peptide strands to a predetermined packing arrangement. By designing and synthesizing a library of proteins, the modification on the first and second coordination sphere was demonstrated by changing the coordinating ligands, altering the sterics, polarity, and flexibility of amino acid side chains.

Also taking a *de novo* design approach, Tanaka and co-workers incorporated a His_2Cys core motif in a four-stranded α-helical coiled coil scaffold to adopt a T1Cu site.[369,370] Likewise, the amino acid sequence was based on a heptad approach, containing Lys and Glu residues to form electrostatic interactions and nonpolar residues such as Ala and Leu to establish a hydrophobic interior. The His_2Cys residues replace Leu residues in three of the four helices, forming a preorganized trigonal planar binding site.[369] A few exogenous axial ligands were introduced, which gives the copper center a gradual change of colors from blue to green, indicative of the change of copper coordination from trigonal planar to tetrahedral. Using the same protein scaffold, they modified certain residues to accommodate a Cu_A center.[371] Similar to their T1Cu construct, the coordinating ligands in the new protein include four His residues and two Cys residues as equatorial and bridging ligands, respectively, but are devoid of axial (S_{Met} and Oxx) ligands. XAS studies support a Cu_A coordination environment in this scaffold with typical ligand–metal and metal–metal distances similar to those of the native Cu_A centers.[372]

Copper catalytic centers by protein redesign

Design of a Cu_B site

Heme-copper oxidases (HCOs) are a class of important terminal oxidases that catalyze the reduction of molecular oxygen to water, coupled to proton translocations, which drive the synthesis of ATP in eukaryotic mitochondria and bacteria.[373–378] HCOs contain a bimetallic iron–copper center with a Cu_B site located above the heme porphyrin plane, and coordinated by three His residues and a hydroxide ion in a tetrahedral geometry.[379] Because native HCOs are large membrane proteins that contain other metal-binding sites, it is challenging to isolate the Cu_B-heme site for biochemical studies.

Lu and co-workers introduced a Cu_B center into myoglobin (Mb), a small globular oxygen-binding protein that does not contain a copper site in its native state.[104,380,381] With the guidance of molecular modeling of sperm whale myoglobin (swMb), two mutations were introduced, Leu29His and Phe43His, which, combined with the distal His64 residue, form a $(His)_3$ copper binding site.[104] The double-mutation does not perturb the structure of the protein or the integrity of the heme center. The difference spectrum

before and after Cu(II) addition indicates a single Cu(II)-binding site. An important method to characterize the Cu_B-heme site in HCOs is to examine the binding of a small bridging ligand. Cyanide was titrated into a solution of Cu_BMb, leading to changes in the UV–vis spectra from a high- to low-spin heme. In the presence of copper, the change required less cyanide. These results indicate that cyanide interacts with both Cu_B and heme iron, which is further supported by EPR studies. Moreover, the disappearance of the Fe(III)-heme EPR signal upon addition of copper to Cu_BMb indicates a spin coupling between the iron and the copper center, another important feature of HCOs.

The kinetics of oxygen binding and its reduction at the Cu_BMb site was investigated by Sigman *et al*.[380] In the absence of copper, the oxygen-binding ability of Cu_BMb decreases in comparison to WTMb. However, once a redox-inactive metal was added (*e.g*., Ag(I)), the oxygen affinity was enhanced. Kinetic studies of oxygen reduction suggest that the copper ion facilitates the reduction of oxygen, which then converts heme to verdoheme. Protons are necessary for maintaining the integrity of the heme center by inhibiting the conversion from heme to verdoheme.[380] The redox properties of Cu_BMb were examined using UV–vis spectroelectrochemistry, showing that the reduction potential of the heme iron center is strongly dependent on the surrounding environment and electrostatics at the distal site.[381] Specifically, the reduction potentials were determined for Cu_BMb in the presence and the absence of the bridging ligand cyanide, Cu(II), and a redox-inactive Zn(II). The cyanide free complexes generally have higher reduction potentials than the cyanide-bound complexes. Most importantly, in the absence of cyanide, the reduction potential of the heme center remains the same (+77 to +80 mV, vs NHE) whether or not a divalent cation is present. However, in the presence of CN^-, the reduction potential of Cu(II)–Cu_BMb is 16 mV higher than that of Cu_BMb; the reduction potential of the Zn(II)–Cu_BMb was even higher, an effect attributed to the addition of positive charge close to the heme center. These studies provide important insight into the role of Cu_B and proton coupled redox processes in native HCOs.

X-ray crystallography and relevant biophysical studies reveal a cross-link between the copper-coordinating His24 and a Tyr244 residue, an important feature of native HCOs. A covalent bond is formed between the carbon C6 of the Tyr residue and nitrogen N_ε of the His residue. This covalent link is responsible for the decreased pK_a

values of both the phenol and the imidazole groups.[382–385] The importance of the Tyr residue at the active site was also demonstrated for the engineered HCO system Cu_BMb. Miner *et al*. introduced a Tyr residue at two different positions close to the copper-coordinating His of the Cu_B site, aiming to examine whether this functionality would lead to higher efficiency in reducing oxygen to water.[386] A Phe four residues away from the copper-coordinating His29 was substituted with a Tyr to mimic the native HCO, leading to F33Y-Cu_BMb. The second design was based on the crystal structure of a cbb_3 HCO,[387] and resulted in the G65Y-Cu_BMb mutant. This second mutant exhibited higher product selectivity than F33Y-Cu_BMb and could cleanly reduce oxygen to produce water with a higher TON that was attributed to the better positioning of the Tyr residue.

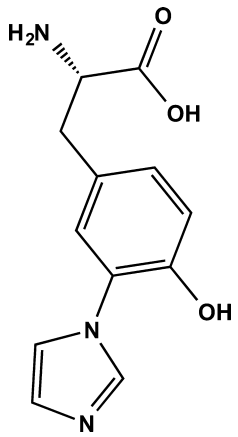

Scheme I-3

Having demonstrated the importance of the Tyr residue in close proximity to the copper-coordinating His, to further investigate the role of this cross-linked Tyr-His functionality, Liu *et al*. introduced an unnatural amino acid imiTyr (Scheme I-3) into the engineered Cu_BMb protein, yielding imiTyrCu_BMb.[388] Cu(II) binds to imiTyrCu_BMb with a K_d of 1.6 μM, with a perturbation of the Soret band of heme. The rate of oxygen reduction was measured in the presence of a reductant and a redox mediator; and catalase and SOD were introduced to distinguish between the formation of water and reactive oxygen species. The oxygen reduction assay shows that imiTyrCu_BMb carries out an efficient and selective oxygen reduction to produce water only when Cu(II) is bound to the protein. More importantly, the turnover number of Cu(II)-imiTyrCu_BMb is almost 3 times that of Cu(II)-F33YCu_BMb (a mutant lacking the Tyr-His cross-link). These studies

demonstrated the functional significance of the Tyr-His cross-link in maintaining sufficient catalytic activity.

Diels-Alder catalysts

A series of Cu(II) centers in protein matrices that are capable of catalyzing enantioselective Diels–Alder reactions have been reported. Aqueous solutions of Cu(II) complexes with amino acids,[389,390] Cu(II) DNA intercalating agents,[391–393] and Cu(II)–phthalocyanine anchored noncovalently to serum albumins[394] were shown to carry out stereoselective Diels–Alder reactions using (aza)chalchones and cyclopentadiene as the reactants (Scheme I-4). Here, I introduce examples of redesigned proteins as catalysts for the benchmark reaction described in Scheme I-4.

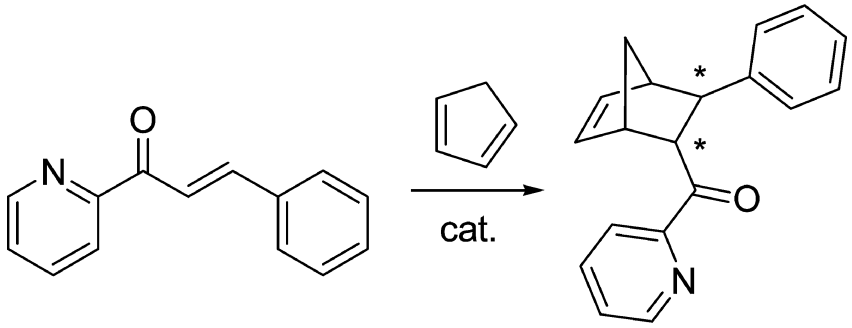

Scheme I-4

The imidazole glycerol phosphate synthase (tHisF) from *Thermotoga maritime* is a thermostable enzyme essential in the biosynthesis of His residue,[395] which has a typical TIM barrel structure with a narrow bottom and a wide top. This scaffold has been used to engineer a His_2Asp Cu(II) binding site in proximity to the wide top rim.[396] The selective mutation of two noncoordinating residues close to Asp at position 11 yielded the mutant tHisFL50H/I52H, where the copper binding site is accessible by relatively large substrates (Figure I-12). Furthermore, to avoid nonspecific Cu(II) binding, surface Cys and His residues were mutated to Ala. An extensive EPR characterization reveals that Cu(II) is coordinated to Asp11/His50/His52 residues, matching the proposed model. When the reaction reported in Scheme I-4 was carried out, the conversion was 73%, with 46% *ee* and an endo/exo ratio of 13:1. The mutation of either the Asp or the His into an Ala of the His2Asp site results in lower conversion values and almost negligible

enantiomeric excess values, demonstrating the necessity of a stable Cu(II)N_2O center to catalyze this enantioselective reaction. As reported in the literature, to obtain a significant stereoselectivity in Diels–Alder reactions, the substrate must bind to Cu(II) through a carbonyl oxygen and a pyridine nitrogen to activate this reaction.[394,397] This type of activation is required also for the Cu(II)-tHisF protein. The chalcones (an aromatic ketone and an enone that form the central core for a variety of important biological compounds) lacking the pyridine nitrogen in the *ortho* position with respect to the carbonyl did not react with significant conversion values.[396]

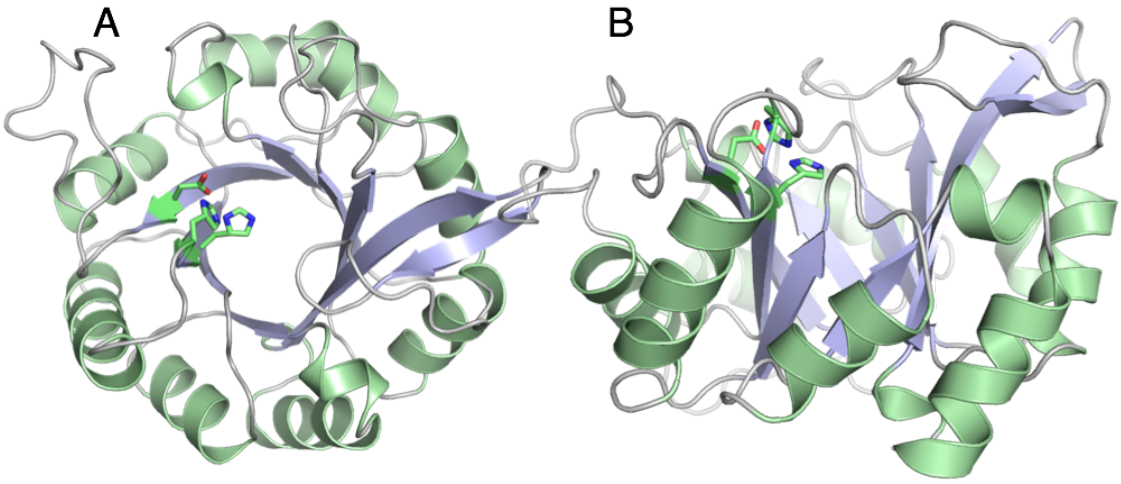

Figure I-12. Putative Cu(II) binding site in tHisF mutant. (A) top view. (B) side view. Models are made based on the crystal structure of tHisF (PDB code: 1THF).[398]

The bovine pancreatic polypeptide (bPP) is a 36 amino acid peptide that contains a poly-Pro type II helix (residues 1–8), a turn (9–12), and a helix (13–31).[399–401] The poly-Pro helix is backfolded on the α-helix, and the construct dimerizes in solution. A 31-amino acid truncated sequence (1–31) of bPP was designed, where Tyr7 was mutated into a His, a L-3-pyridylalanine, or a L-4-pyridylalanine residue, while an Asp or Glu residue in the loop (position 10) provided additional donor atoms.[402] Upon dimerization, a His_2 or $pyridyl_2$ copper-binding site forms within the intrahelical space of the dimer. Further mutations were introduced at the interface between the dimers with an attempt to make the interior less sterically crowded. Unfortunately, these mutants were found to exist predominantly in their monomeric Cu(II)-peptide form. The best results for the reaction shown in Scheme I-4 (complete conversion of the substrate and up to 83% *ee*)

were obtained with the L-3-pyridylalanine mutant (bPPc). As observed for tHisF, the coordination of the substrate to the Cu(II)-bound protein is a prerequisite for having the highest activity.[402] Moreover, Cu(II) or WT bPP 1–31 alone does not show significant catalytic activities, neither does the His-containing mutant of bPP. Overall, these results demonstrate that the nature of the coordinating groups (pyridyl vs imidazolyl, and their diastereoisomers) has a profound impact on regulating the stereoselectivity and the activity of these reengineered protein catalysts. Moreover, it has been previously shown that the presence of a cavity in the construct is not a strict requirement to achieve control of the stereoselectivity. These bPP mutants were also examined as catalysts for the Michael addition reaction, exhibiting significant stereoselectivity.[402]

An effective strategy for incorporating a metal cofactor into a protein is to incorporate a metal complex to the protein scaffold by a covalent linking approach, instead of binding a metal ion directly to the protein amino acid side chains as its ligands. Lactococcal multidrug resistance Regulator (LmrR) protein, a dimeric protein of ~13.5 kDa per subunit, was engineered to catalyze the Diels–Alder reaction shown in Scheme I-4.[403] LmrR consists of a typical β-winged helix-turn-helix domain with an additional C-terminal helix.[404,405] The large flat hydrophobic core in this dimer was functionalized with two phenanthroline- or bpy-based chelating moieties per dimer (one per monomer) (Figure I-13).[403] Cys residues, which are not present in the WT protein, were incorporated into the protein monomers as anchor points for these copper-binding moieties. By reacting bromoacetamide-substituted 1,10-phenanthroline (1,10-Phen) or 2,2′-bpy with the Cys residues, mutants were generated with the copper-chelating moieties in the hydrophobic core.

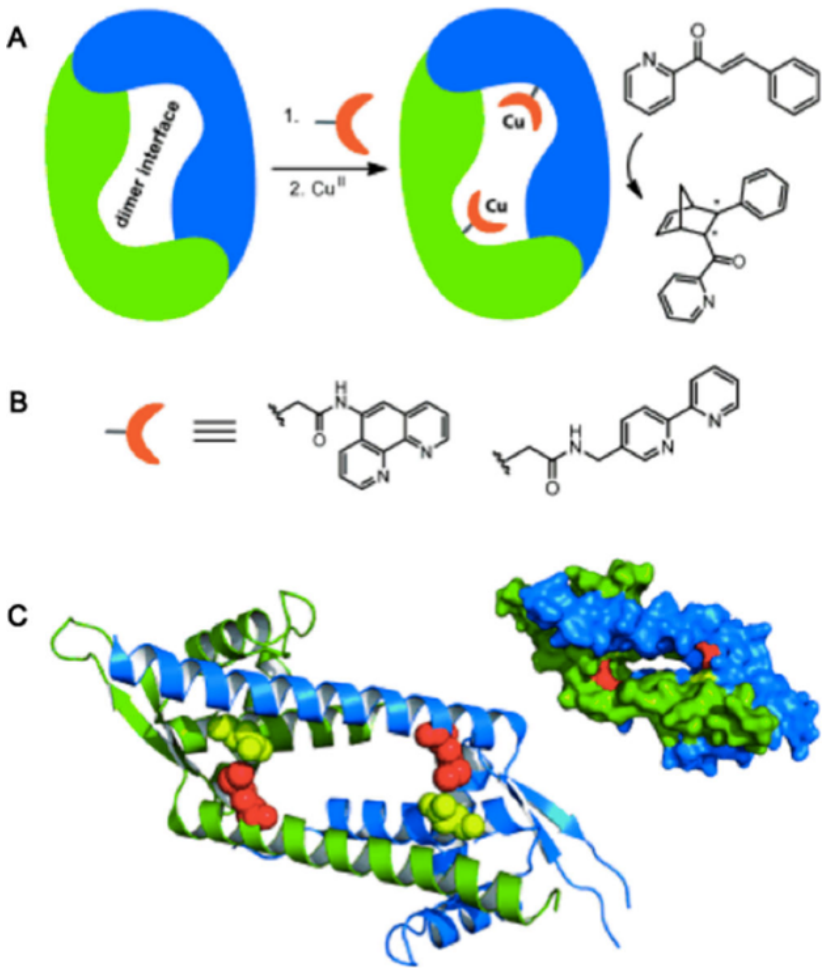

Figure I-13. (A) Schematic representation of the proposed artificial metalloenzyme in which a Cu(II) complex is grafted on the dimer interface of a protein scaffold. (B) Ligands used for grafting on the dimer interface. (C) Pymol representations of dimeric LmrR in a ribbon and a space-filling model (PDB code: 3F8B). Either position 89 (red) or position 19 (yellow) was used for the covalent attachment of the copper-chelating ligands. Reproduced with permission from ref [403]. Copyright 2012 Wiley.

The final constructs can bind two Cu(II) ions and still retain their dimeric form. The catalytic activity of the Cu(II)(1,10-Phen)-LmrR-M89C for the reaction described in Scheme I-4 (monitored after 3 days of reaction) is remarkable: the reaction yields 98% conversion of the substrate and 95% *ee* of the (+)-endo isomer at room temperature. Interestingly, an even higher enantiomeric excess (97%) was achieved when the reaction was carried out at 4 °C, albeit with a lower conversion (93%). Conversely, the Cu(II)(2,2′-bpy)-LmrR-M89C mutant yielded 66% *ee* of the opposite (–)-endo isomer of the Diels–Alder product. This demonstrates that these constructs can be tuned for a

desired stereoselectivity through a proper choice of the position and the nature of the Cu(II) sites. The design of these constructs was prompted by the observation that in DNAzymes, copper(II) sites close to a chiral environment have the ability to catalyze Diels–Alder or Michael reactions with a high degree of selectivity.[391–393] The chiral scaffold, even quite distant from the copper site, could therefore provide efficient secondary sphere interactions to induce significant stereoselectivity.

De novo designed type 2 copper centers

One of the challenges to obtain a stable catalytic copper center is to design a peptide with a coordination environment suitable to stabilize copper on both oxidation levels. The coordination geometry of Cu(I) is usually linear, trigonal (T-shaped), or tetrahedral, while for Cu(II), distorted square planar, tetrahedral, pyramidal, and octahedral geometries are commonly observed.[406] However, in copper proteins, coordination numbers of four or higher (involving weak interactions between the copper ion and distal ligands) are prevalent.[407] At the same time, the two principal oxidation states (+1 and +2) of copper have different hard–soft behaviors: while Cu(I) is a soft metal, Cu(II) has a more intermediate-to-hard character. The general strategy to design a defined copper binding site is to mutate the hydrophobic residues into coordinating residues such as His, Met, Cys, Asp, or Glu in the interior of the two- to four- stranded coiled coils. T2Cu centers, in particular $Cu(His)_3$ centers, play multiple roles in native proteins. Their functions span from electron transfer to cofactor-assisted oxygen activation to nitrite reduction.[408–416] For example, in peptidylglycine α-hydroxylating monooxygenase (PHM), the Cu_H center [$Cu(His)_3$] is involved in shuttling electrons to a Cu_M copper center 12.5 Å away where oxygen activation occurs.[411,417,418]

The first case of *de novo* designed 3SCCs with a T2Cu center $CuHis_3$ was reported in 1993.[258] The construct consists of a 19-amino acid peptide based on the heptad repeat approach. It contains a 4,4′-bpy moiety at the N-terminus, a His residue for Cu(II) binding at the C-terminus, and a Tyr residue adjacent to His as a spectroscopic probe (sequence: 4,4′-bpy-GELAQKLEQALQKLAAAHYNH$_2$).[258] When reacted with $Ru_5Cl_{12}^{2-}$, three helices assemble into a homotrimeric α-helix bundle from the template created by the *fac*-$[Ru(bpyPep)_3]^{2-}$ unit at the N-terminus (Figure I-14).[419,420] The

presence of this stable Ru(II)(bpyPep)$_3$ unit assists the formation of an α-helix apo-(peptide)$_3$ construct, which contains a preorganized (His)$_3$ site at the C-terminus available for copper binding. Indeed, the addition of Cu(II) to the Ru(II)(peptide)$_3$ leads to Cu(II)Ru(II)(peptide)$_3$ with a dissociation constant of ~3 × 10^{-7} M determined by the change of Tyr emission. Ru(II)(peptide)$_3$ possesses a high degree of helical content; the addition of Cu(II) to the Ru(II)(peptide)$_3$ does not change the CD spectrum even when Cu(II) is 20-fold in excess compared to Ru(II)(peptide)$_3$. Spectroscopic studies reveal that the Cu(II)Ru(II)(peptide)$_3$ complex has a ligand-field band centered at 495 nm (ε = 300 $M^{-1}cm^{-1}$) and an $A_{||}$ value of 173 G, fully consistent with the presence of a tetrahedral or square planar T2Cu site in a (His)$_3$ environment.[258] This work represents the first example of a stable T2Cu center in a *de novo* designed α-helical coiled coil scaffold, laying a solid foundation for the development of catalytic T2Cu centers.

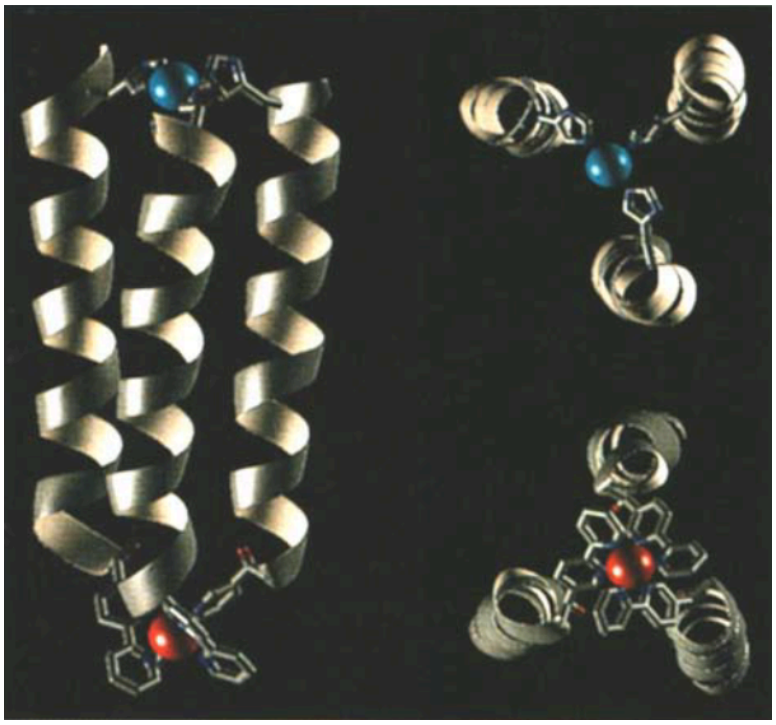

Figure I-14. A model of Cu(II)Ru(II)-peptide complex. Reproduced with permission from ref [258].

Tanaka *et al*. reported the design of a parallel 3SCC (in the presence of metal ions) Ile-zipper peptide (IZ) (sequence YGG-(IEKKIEA)$_4$).[421] Similar to the TRI peptide introduced earlier, the design of this peptide is also based on a heptad repeat approach.[8]

Ile residues are constructed in the interior of the helical coiled coils and Glu and Lys residues are on the helical interface. Substitution of the Ile residue on the third heptad with a His yields IZ-3aH and with two His substitutions, IZ-3adH.[422] In the presence of Cu(II), Zn(II), Co(II), or Ni(II), the peptides are converted from random coils to 3SCCs. Interestingly, Cu(II) only induces α-helical formation at a concentration below 100 μM; excess Cu(II) destabilizes the helices. Cu(II) binds to IZ-3adH with a dissociation constant of 17(1) μM. EPR studies show that Cu(II)(IZ-3adH) likely has a T2Cu with N_3O coordination in a tetragonal geometry.[6] An elongated version of IZ-3adH with additional His residues was then designed to impart more stability with an additional heptad repeat and to incorporate two metal ions in the same peptide scaffold.[7] IZ(5)-2a3adH has three His residues placed along the helix at 2*a*, 3*a*, and 3*d* positions, out of which, 2*a* and 3*a* are at *i* and *i* + 3 positions while 3*a* and 3*d* are at *i* and *i* + 4 positions. Spectroscopic studies indicate that Cu(II) binds at the 2*a* position to three His residues and a solvent water molecule and Ni(II) binds at the 3*a* and 3*d* positions.

These examples of incorporating copper centers into *de novo* designed systems have laid a solid foundation for imparting catalysis. Nonetheless, in most cases, no redox chemistry has been shown, nor are the copper centers very well characterized. Before the beginning of this thesis, there was no report of functional copper centers embedded in *de novo* designed proteins. However, such efforts are necessary to evaluate whether a simplified protein construct can incorporate copper into a desired coordination environment and impart catalytic activity as seen in native copper centers. When I started working on this project, Dr. Melissa Zastrow demonstrated hydrolytic activity with zinc-bound TRI family peptides. Based on the similarity between the zinc center in CA and the T2Cu center in CuNiR,[423] one asks the question of whether the same construct is capable of carrying out redox-active catalytic activities as seen in many T2Cu centers in native proteins.

5. Thesis outline

This thesis is focused on designing a structural and functional model for the T2Cu in CuNiR. As shown above, the design of metalloenzyme mimics has seen a significant progress, however, the *de novo* design of a catalytic copper center was essentially non-

existent before this thesis was begun, which emphasizes the novelty of the work described in this thesis.

In Chapter II, I describe the design and characterization of the first generation model Cu(II)/(I)(TRIW-H)$_3^{2+/+}$, the sequence of which contains a Trp at the 2nd position as a spectroscopic tag and a His at the 23rd position for copper binding. Detailed spectroscopic studies are carried out the probe the coordination environment for both oxidation states. Cu(I) and Cu(II) affinities to (TRIW-H)$_3$ are determined using competitive chelation assays and Trp fluorescence spectroscopy, respectively. Reduction potentials of Cu(II)/(I)(TRIW-H)$_3^{2+/+}$ are calculated based on the affinities using the Nernst equation. This system has a reduction potential that is ~100 to 150 mV higher than that of the T2Cu in native CuNiR, possibly due to the stabilization of a trigonal Cu(I). Small molecule binding studies are carried out to evaluate the possibility of forming substrate-enzyme and product-enzyme complexes. The rates of nitrite reduction catalyzed by Cu(II)/(I)(TRIW-H)$_3^{2+/+}$ with sodium ascorbate as a sacrificial reductant are reported. I then discuss the possibility of going through a different reaction mechanism with this model from the native enzyme. This peptide, as a starting point of my thesis work, has pronounced advantages over some of the synthetic small molecule models, however, the rates are not ideal, which gave me an incentive to design a better model.

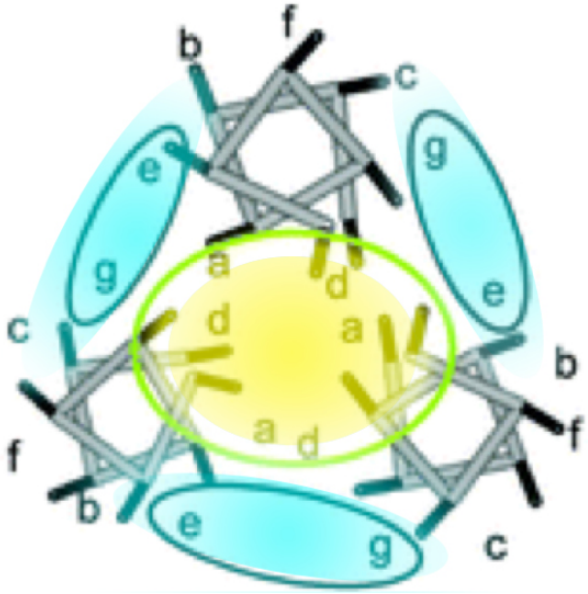

Figure I-15. Helical wheel diagram showing the helical interface region (blue) and the interior of the coiled coils (yellow).

In Chapter III of this thesis, I present the modulation of reduction potentials and NiR rates by modifying the charged residues at the helical interface (Figure I-15), yielding a series of peptides (the TRIW-EH series). The intention of this design is to add negative charge close to the copper-binding site to stabilize Cu(II), thus lowering the reduction potentials. I show that the reduction potentials are lowered by this design strategy not from the stabilization of Cu(II) but the destabilization of Cu(I). pH conditions also influence the affinities, more so for Cu(II) than for Cu(I). Detailed analysis of how charged residues influence both oxidation states is presented. These modifications do not abolish the reactivity of the peptides. The peptides of the TRIW-EH series all have NiR activity with varied rates. The increase in rate is directly correlated with the decrease in reduction potential within the series, which, however, does not mean that the electron transfer step is the rate-limiting step in the catalytic cycle. This chapter describes the first systematic study on how charged residues influence the copper binding affinities, reduction potentials, protonation equilibria, and NiR rates for a T2Cu center, showcasing the strength of *de novo* design in deepening our understanding of the structure-function relationship with a highly modular scaffold.

In Chapter IV, I describe the modification of the interior of the helical coiled coils (Figure I-15) to improve the NiR rates. The TRIW-EH series described in Chapter III only varies the rates by as much as four-fold at pH 5.8. In this chapter, I describe the design and characterization of a few peptides with rates up to three orders of magnitude higher than the initial design. Two strategies are employed in these designs: 1) substituting the Leu residue one hydrophobic layer above the copper-binding His residues to increase the solvent/substrate access; 2) replacing the natural His with an N-methyl-His to change the electronics of the imidazole ring and the sterics around the binding site, hoping to force Cu(I) into a tetrahedral coordination to lower the reorganization energy upon oxidation. I show the design and characterization of a series of peptides that contain these features combined with certain charged residue modifications. Michaelis-Menten kinetic studies are carried out for selected peptides in this series. Mechanistic insight based on the spectroscopic and kinetics data is presented.

X-ray absorption spectroscopy (XAS) is a powerful tool for understanding the coordination environment of non-crystallographically characterized metal sites in

metalloproteins. It is used in all of my previous data chapters to probe the Cu(I) coordination environment. In Chapter V, I introduce XAS in more details and describe the protocol that I have been using to fit EXAFS data. In addition, I present two short stories on a Cu(I)-thiol/thiolate site and a Zn(II)$(His)_3(OH_2/OH^-)$ center to demonstrate the application of XAS in characterizing spectroscopically silent systems.

In the last chapter, I conclude the major achievements in this thesis and propose future directions for this project.

References

(1) Yu, F.; Cangelosi, V. M.; Zastrow, M. L.; Tegoni, M.; Plegaria, J. S.; Tebo, A. G.; Mocny, C. S.; Ruckthong, L.; Qayyum, H.; Pecoraro, V. L. *Chem. Rev.* **2014**, *114*, 3495–3578.

(2) Robson, B.; Vaithilingam, A. *Protein folding revisited.*; 1st ed.; Elsevier Inc., 2008; Vol. 84, pp. 161–202.

(3) Woolfson, D. N. In *Advances in Protein Chemistry*; Elsevier, 2005; Vol. 70, pp. 79–112.

(4) Doerr, A. J.; McLendon, G. L. *Inorg. Chem.* **2004**, *43*, 7916–7925.

(5) Li, X.; Suzuki, K.; Kanaori, K.; Tajima, K.; Kashiwada, A.; Hiroaki, H.; Kohda, D.; Tanaka, T. *Protein Sci.* **2000**, *9*, 1327–1333.

(6) Kiyokawa, T.; Kanaori, K.; Tajima, K.; Koike, M.; Mizuno, T.; Oku, J. J.-I. I.; Tanaka, T. *J. Pept. Res.* **2004**, *63*, 347–353.

(7) Tanaka, T.; Mizuno, T.; Fukui, S.; Hiroaki, H.; Oku, J.-I.; Kanaori, K.; Tajima, K.; Shirakawa, M. *J. Am. Chem. Soc.* **2004**, *126*, 14023–14028.

(8) O'Neil, K. T.; Degrado, W. F. *Science* **1990**, *250*, 646–651.

(9) Lovejoy, B.; Choe, S.; Cascio, D.; Mcrorie, D. K.; William, F.; Eisenberg, D.; Degrado, W. F. *Science* **1993**, *259*, 1288–1293.

(10) Dieckmann, G. R.; McRorie, D. K.; Tierney, D. L.; Utschig, L. M.; Singer, C. P.; O'Halloran, T. V; Penner-Hahn, J. E.; Degrado, W. F.; Pecoraro, V. L. *J. Am. Chem. Soc.* **1997**, *119*, 6195–6196.

(11) Ogihara, N. L.; Weiss, M. S.; Degrado, W. F.; Eisenberg, D. *Protein Sci.* **1997**, *6*, 80–88.

(12) Dieckmann, G. R.; McRorie, D. K.; Lear, J. D.; Sharp, K. A.; DeGrado, W. F.; Pecoraro, V. L. *J. Mol. Biol.* **1998**, *280*, 897–912.

(13) Farrer, B. T.; Pecoraro, V. L. *Proc. Natl. Acad. Sci. U. S. A.* **2003**, *100*, 3760–3765.

(14) Hellinga, H. W.; Richards, F. M. *J. Mol. Biol.* **1991**, *222*, 763–785.

(15) Hellinga, H. W.; Caradonna, J. P.; Richards, F. M. *J. Mol. Biol.* **1991**, *222*, 787–803.

(16) Rohl, C. A.; Strauss, C. E. M.; Misura, K. M. S.; Baker, D. In *Methods in enzymology*; 2004; pp. 66–93.

(17) Clarke, N. D.; Yuan, S. M. *Proteins Struct. Funct. Genet.* **1995**, *23*, 256–263.

(18) Lu, Y.; Berry, S. M.; Pfister, T. D. *Chem. Rev.* **2001**, *101*, 3047–3080.

(19) Lu, Y. *Inorg. Chem.* **2006**, *45*, 155–158.

(20) Lu, Y.; Yeung, N.; Sieracki, N.; Marshall, N. M. *Nature* **2009**, *460*, 855–862.

(21) Harris, K. L.; Lim, S.; Franklin, S. J. *Inorg. Chem.* **2006**, *45*, 10002–10012.

(22) Ringenberg, M. R.; Ward, T. R. *Chem. Commun. (Camb).* **2011**, *47*, 8470–8476.

(23) Steinreiber, J.; Ward, T. R. *Coord. Chem. Rev.* **2008**, *252*, 751–766.

(24) Benson, D. E.; Wisz, M. S.; Hellinga, H. W. *Proc. Natl. Acad. Sci. U. S. A.* **2000**, *97*, 6292–6297.

(25) Hellinga, H. W. *Fold. Des.* **1998**, *3*, R1–8.

(26) Ward, T. R. *Acc. Chem. Res.* **2011**, *44*, 47–57.

(27) DeGrado, W. F.; Summa, C. M.; Pavone, V.; Nastri, F.; Lombardi, A. *Annu. Rev. Biochem.* **1999**, *68*, 779–819.

(28) Bryson, J. W.; Betz, S. F.; Lu, H. S.; Suich, D. J.; Zhou, H. X.; O'Neil, K. T.; DeGrado, W. F. *Science* **1995**, *270*, 935–941.
(29) Degrado, W. F.; Wasserman, Z. R.; Lear, J. D. *Science* **1989**, *243*, 622–628.
(30) Cohen, C.; Parry, D. A. D. *Proteins Struct. Funct. Genet.* **1990**, *7*, 1–15.
(31) Beasley, J. R.; Hecht, M. H. *J. Biol. Chem.* **1997**, *272*, 2031–2034.
(32) Richardson, J. S.; Richardson, D. C.; Tweedy, N. B.; Gernert, K. M.; Quinn, T. P.; Hecht, M. H.; Erickson, B. W.; Yan, Y.; Mcclain, R. D.; Donlan, M. E.; Surles, M. C. *Biophys. J.* **1992**, *63*, 1186–1209.
(33) Baltzer, L.; Nilsson, H.; Nilsson, J. *Chem. Rev.* **2001**, *101*, 3153–3163.
(34) Saven, J. G. *Chem. Rev.* **2001**, *101*, 3113–3130.
(35) Schneider, J. P.; Lombardi, A.; DeGrado, W. F. *Fold. Des.* **1998**, *3*, R29–40.
(36) Regan, L. *Trends Biochem. Sci.* **1995**, *20*, 280–285.
(37) Baltzer, L. *Curr. Opin. Struct. Biol.* **1998**, *8*, 466–470.
(38) Reedy, C. J.; Gibney, B. R. *Chem. Rev.* **2004**, *104*, 617–649.
(39) Zastrow, M. L.; Pecoraro, V. L. *Coord. Chem. Rev.* **2013**, 1–24.
(40) Samish, I.; MacDermaid, C. M.; Perez-Aguilar, J. M.; Saven, J. G. *Annu. Rev. Phys. Chem.* **2011**, *62*, 129–149.
(41) Barker, P. D. *Curr. Opin. Struct. Biol.* **2003**, *13*, 490–499.
(42) Lu, Y.; Chakraborty, S.; Miner, K. D.; Wilson, T. D.; Mukherjee, A.; Yu, Y.; Liu, J.; Marshall, N. M.; Champaign, U. In *Comprehensive Inorganic Chemistry II*; Elsevier Ltd., **2013**; pp. 565–593.
(43) Lu, Y.; Valentine, J. S. *Curr. Opin. Struct. Biol.* **1997**, *7*, 495–500.
(44) Toscano, M. D.; Woycechowsky, K. J.; Hilvert, D. *Angew. Chem. Int. Ed. Engl.* **2007**, *46*, 3212–3236.
(45) Ghirlanda, G. *Nature* **2008**, *453*, 164–166.
(46) Kazlauskas, R. J. *Curr. Opin. Chem. Biol.* **2005**, *9*, 195–201.
(47) Khersonsky, O.; Roodveldt, C.; Tawfik, D. S. *Curr. Opin. Chem. Biol.* **2006**, *10*, 498–508.
(48) Feynman, R. *Phys. Today* **1989**, *42*, 88.
(49) Hecht, M. H.; Richardson, J. S.; Richardson, D. C.; Ogden, R. C. *Science* **1990**, *249*, 884–891.
(50) Hill, R. B.; Raleigh, D. P.; Lombardi, A.; DeGrado, W. F. *Acc. Chem. Res.* **2000**, *33*, 745–754.
(51) Onuchic, J. N.; Wolynes, P. G. *Curr. Opin. Struct. Biol.* **2004**, *14*, 70–75.
(52) Regan, L.; DeGrado, W. F. *Science* **1988**, *241*, 976–978.
(53) Rose, G. D.; Gierasch, L. M.; Smith, J. A. In *Advances in Protein Chemistry*; Academic Press, Inc, 1985; Vol. 37, pp. 1–110.
(54) Hecht, M. H. *Proc. Natl. Acad. Sci. U. S. A.* **1994**, *91*, 8729–8730.
(55) Nesloney, C. L.; Kelly, J. W. *Bioorg. Med. Chem.* **1996**, *4*, 739–766.
(56) Smith, C. K.; Regan, L. *Acc. Chem. Res.* **1997**, *30*, 153–161.
(57) Hughes, R. M.; Waters, M. L. *Curr. Opin. Struct. Biol.* **2006**, *16*, 514–524.
(58) Pantoja-Uceda, D.; Santiveri, C. M.; Jiménez, M. A. *Methods Mol. Biol.* **2006**, *340*, 27–51.
(59) Kim, D. E.; Chivian, D.; Baker, D. *Nucleic Acids Res.* **2004**, *32*, W526–31.
(60) Kuhlman, B.; Dantas, G.; Ireton, G. C.; Varani, G.; Stoddard, B. L.; Baker, D. *Science* **2003**, *302*, 1364–1368.

(61) Bradley, P.; Misura, K. M. S.; Baker, D. *Science* **2005**, *309*, 1868–1871.
(62) Saven, J. G. *Curr. Opin. Struct. Biol.* **2002**, *12*, 453–458.
(63) Park, S.; Yang, X.; Saven, J. G. *Curr. Opin. Struct. Biol.* **2004**, *14*, 487–494.
(64) Saven, J. G. *Curr. Opin. Chem. Biol.* **2011**, *15*, 452–457.
(65) Hecht, M. H.; Das, A.; Go, A.; Bradley, L. H.; Wei, Y. *Protein Sci.* **2004**, *13*, 1711–1723.
(66) Moffet, D. A.; Hecht, M. H. *Chem. Rev.* **2001**, *101*, 3191–3203.
(67) Smith, B. a; Hecht, M. H. *Curr. Opin. Chem. Biol.* **2011**, *15*, 421–426.
(68) Bradley, L. H.; Thumfort, P. P.; Hecht, M. H. *Methods Mol. Biol.* **2006**, *340*, 53–69.
(69) Butterfoss, G. L.; Kuhlman, B. *Annu. Rev. Biophys. Biomol. Struct.* **2006**, *35*, 49–65.
(70) Floudas, C. A.; Fung, H. K.; McAllister, S. R.; Mönnigmann, M.; Rajgaria, R. *Chem. Eng. Sci.* **2006**, *61*, 966–988.
(71) Kang, S.; Saven, J. G. *Curr. Opin. Chem. Biol.* **2007**, *11*, 329–334.
(72) Reilly, C. *The Nutritional Trace Metals*; John Wiley & Sons, 2008; p. 356.
(73) Howard, J. B.; Rees, D. C. *Adv. Protein Chem.* **1991**, *42*, 199–280.
(74) Arciero, D. M.; Lipscomb, J. D.; Huynh, B. H.; Kent, T. A.; Münck, E. *J. Biol. Chem.* **1983**, *258*, 14981–14991.
(75) Sugimoto, K.; Senda, T.; Aoshima, H.; Masai, E.; Fukuda, M.; Mitsui, Y. *Structure* **1999**, *7*, 953–965.
(76) Kita, A.; Kita, S.; Fujisawa, I.; Inaka, K.; Ishida, T.; Horiike, K.; Nozaki, M.; Miki, K. *Structure* **1999**, *7*, 25–34.
(77) Sieker, L. C.; Holmes, M.; Le Trong, I.; Turley, S.; Liu, M. Y.; LeGall, J.; Stenkamp, R. E. *J. Biol. Inorg. Chem.* **2000**, *5*, 505–513.
(78) Smith, P.; Zhou, B.; Ho, N.; Yuan, Y.-C.; Su, L.; Tsai, S.-C.; Yen, Y. *Biochemistry* **2009**, *48*, 11134–11141.
(79) Zhang, Z.; Ren, J.; Clifton, I. J.; Schofield, C. J. *Chem. Biol.* **2004**, *11*, 1383–1394.
(80) Muñoz, I. G.; Moran, J. F.; Becana, M.; Montoya, G. *Protein Sci.* **2005**, *14*, 387–394.
(81) Erlandsen, H.; Fusetti, F.; Martinez, A.; Hough, E.; Flatmark, T.; Stevens, R. C. *Nat. Struct. Biol.* **1997**, *4*, 995–1000.
(82) Fusetti, F.; Erlandsen, H.; Flatmark, T.; Stevens, R. C. *J. Biol. Chem.* **1998**, *273*, 16962–16967.
(83) Zhang, Z.; Ren, J. S.; Harlos, K.; McKinnon, C. H.; Clifton, I. J.; Schofield, C. J. *FEBS Lett.* **2002**, *517*, 7–12.
(84) Lehmann, T. E.; Ming, L. J.; Rosen, M. E.; Que, L. *Biochemistry* **1997**, *36*, 2807–2816.
(85) Takahashi, S.; Sam, J. W.; Peisach, J.; Rousseau, D. L. *J. Am. Chem. Soc.* **1994**, *116*, 4408–4413.
(86) Dumas, P.; Bergdoll, M.; Cagnon, C.; Masson, J. M. *EMBO J.* **1994**, *13*, 2483–2492.
(87) Kovaleva, E. G.; Lipscomb, J. D. *Nat. Chem. Biol.* **2008**, *4*, 186–193.
(88) Ryle, M. J.; Hausinger, R. P. *Curr. Opin. Chem. Biol.* **2002**, *6*, 193–201.
(89) Solomon, E. I.; Brunold, T. C.; Davis, M. I.; Kemsley, J. N.; Lee, S. K.; Lehnert, N.; Neese, F.; Skulan, a J.; Yang, Y. S.; Zhou, J. *Chem. Rev.* **2000**, *100*, 235–350.

(90) Miller, A.-F. *FEBS Lett.* **2012**, *586*, 585–595.
(91) Wuerges, J.; Lee, J.-W.; Yim, Y.-I.; Yim, H.-S.; Kang, S.-O.; Djinovic Carugo, K. *Proc. Natl. Acad. Sci. U. S. A.* **2004**, *101*, 8569–8574.
(92) Zhang, N.-N.; He, Y.-X.; Li, W.-F.; Teng, Y.-B.; Yu, J.; Chen, Y.; Zhou, C.-Z. *Proteins Struct. Funct. Genet.* **2010**, *78*, 1999–2004.
(93) Stallings, W. C.; Pattridge, K. a; Strong, R. K.; Ludwig, M. L. *J. Biol. Chem.* **1984**, *259*, 10695–10699.
(94) Stallings, W. C.; Powers, T. B.; Pattridge, K. A.; Fee, J. A.; Ludwig, M. L. *Proc. Natl. Acad. Sci. U. S. A.* **1983**, *80*, 3884–3888.
(95) Yamakura, F.; Suzuki, K. *J. Biochem.* **1980**, *88*, 191–196.
(96) Brock, C. J.; Harris, J. I. *Biochem. Soc. Trans.* **1977**, *5*, 1537–1539.
(97) Ose, D. E.; Fridovich, I. *Arch. Biochem. Biophys.* **1979**, *194*, 360–364.
(98) Vance, C. K.; Miller, A.-F. *J. Am. Chem. Soc.* **1998**, *120*, 461–467.
(99) Miller, A.-F. *Acc. Chem. Res.* **2008**, *41*, 501–510.
(100) Stallings, W. C.; Metzger, A. L.; Pattridge, K. A.; Fee, J. A.; Ludwig, M. L. *Free Radic. Res. Commun.* **1991**, *12-13 Pt 1*, 259–268.
(101) Pinto, A. L.; Hellinga, H. W.; Caradonna, J. P. *Proc. Natl. Acad. Sci. U. S. A.* **1997**, *94*, 5562–5567.
(102) Richardson, D. J.; Watmough, N. J. *Curr. Opin. Chem. Biol.* **1999**, *3*, 207–219.
(103) Watmough, N. J.; Butland, G.; Cheesman, M. R.; Moir, J. W.; Richardson, D. J.; Spiro, S. *Biochim. Biophys. Acta* **1999**, *1411*, 456–474.
(104) Sigman, J. A.; Kwok, B. C.; Lu, Y. *J. Am. Chem. Soc.* **2000**, *122*, 8192–8196.
(105) Yeung, N.; Lin, Y.-W.; Gao, Y.-G.; Zhao, X.; Russell, B. S.; Lei, L.; Miner, K. D.; Robinson, H.; Lu, Y. *Nature* **2009**, *462*, 1079–1082.
(106) Lin, Y.-W.; Yeung, N.; Gao, Y.-G.; Miner, K. D.; Tian, S.; Robinson, H.; Lu, Y. *Proc. Natl. Acad. Sci. U. S. A.* **2010**, *107*, 8581–8586.
(107) Flock, U.; Lachmann, P.; Reimann, J.; Watmough, N. J.; Adelroth, P. *J. Inorg. Biochem.* **2009**, *103*, 845–850.
(108) Butland, G.; Spiro, S.; Watmough, N. J.; Richardson, D. J. *J. Bacteriol.* **2001**, *183*, 189–199.
(109) Stenkamp, R. E. *Chem. Rev.* **1994**, *94*, 715–726.
(110) Rosenzweig, A. C.; Frederick, C. A.; Lippard, S. J.; Nordlund, P. *Nature* **1993**, *366*, 537–543.
(111) deMaré, F.; Nordlund, P.; Gupta, N.; Shenvi, N. V.; Cui, X.; Kurtz, D. M. *Inorganica Chim. Acta* **1997**, *263*, 255–262.
(112) Ormö, M.; DeMaré, F.; Regnström, K.; Aberg, A.; Sahlin, M.; Ling, J.; Loehr, T. M.; Sanders-Loehr, J.; Sjöberg, B. M. *J. Biol. Chem.* **1992**, *267*, 8711–8714.
(113) Larsson, A.; Sjöberg, B. M. *EMBO J.* **1986**, *5*, 2037–2040.
(114) Nordlund, P.; Sjöberg, B. M.; Eklund, H. *Nature* **1990**, *345*, 593–598.
(115) Maglio, O.; Nastri, F.; Martin de Rosales, R. T.; Faiella, M.; Pavone, V.; DeGrado, W. F.; Lombardi, A. *Comptes Rendus Chim.* **2007**, *10*, 703–720.
(116) Calhoun, J. R.; Nastri, F.; Maglio, O.; Pavone, V.; Lombardi, A.; DeGrado, W. F. *Biopolymers* **2005**, *80*, 264–278.
(117) Lombardi, A.; Summa, C. M.; Geremia, S.; Randaccio, L.; Pavone, V.; DeGrado, W. F. *Proc. Natl. Acad. Sci. U. S. A.* **2000**, *97*, 6298–6305.

(118) Di Costanzo, L.; Wade, H.; Geremia, S.; Randaccio, L.; Pavone, V.; DeGrado, W. F.; Lombardi, A. *J. Am. Chem. Soc.* **2001**, *123*, 12749–12757.
(119) Torres Martin de Rosales, R.; Faiella, M.; Farquhar, E.; Que, L.; Andreozzi, C.; Pavone, V.; Maglio, O.; Nastri, F.; Lombardi, A. *J. Biol. Inorg. Chem.* **2010**, *15*, 717–728.
(120) Pasternak, A.; Kaplan, J.; Lear, J. D.; Degrado, W. F. *Protein Sci.* **2001**, *10*, 958–969.
(121) Maglio, O.; Nastri, F.; Pavone, V.; Lombardi, A.; DeGrado, W. F. *Proc. Natl. Acad. Sci. U. S. A.* **2003**, *100*, 3772–3777.
(122) Khare, S. D.; Kipnis, Y.; Greisen, P.; Takeuchi, R.; Ashani, Y.; Goldsmith, M.; Song, Y.; Gallaher, J. L.; Silman, I.; Leader, H.; Sussman, J. L.; Stoddard, B. L.; Tawfik, D. S.; Baker, D. *Nat. Chem. Biol.* **2012**, *8*, 294–300.
(123) Der, B. S.; Edwards, D. R.; Kuhlman, B. *Biochemistry* **2012**, *51*, 3933–3940.
(124) Zastrow, M. L.; Pecoraro, V. L. *J. Am. Chem. Soc.* **2013**, *135*, 5895–5903.
(125) Zastrow, M. L.; Peacock, A. F. A.; Stuckey, J. A.; Pecoraro, V. L. *Nat. Chem.* **2012**, *4*, 118–123.
(126) Tegoni, M.; Yu, F.; Bersellini, M.; Penner-Hahn, J. E.; Pecoraro, V. L. *Proc. Natl. Acad. Sci. U. S. A.* **2012**, *109*, 21234–21239.
(127) Faiella, M.; Andreozzi, C.; de Rosales, R. T. M.; Pavone, V.; Maglio, O.; Nastri, F.; DeGrado, W. F.; Lombardi, A. *Nat. Chem. Biol.* **2009**, *5*, 882–884.
(128) Kaplan, J.; DeGrado, W. F. *Proc. Natl. Acad. Sci. U. S. A.* **2004**, *101*, 11566–11570.
(129) Geremia, S.; Di Costanzo, L.; Randaccio, L.; Engel, D. E.; Lombardi, A.; Nastri, F.; DeGrado, W. F. *J. Am. Chem. Soc.* **2005**, *127*, 17266–17276.
(130) DeGrado, W. F.; Di Costanzo, L.; Geremia, S.; Lombardi, A.; Pavone, V.; Randaccio, L. *Angew. Chem. Int. Ed. Engl.* **2003**, *42*, 417–420.
(131) Lahr, S. J.; Engel, D. E.; Stayrook, S. E.; Maglio, O.; North, B.; Geremia, S.; Lombardi, A.; DeGrado, W. F. *J. Mol. Biol.* **2005**, *346*, 1441–1454.
(132) Summa, C. M.; Rosenblatt, M. M.; Hong, J.-K.; Lear, J. D.; DeGrado, W. F. *J. Mol. Biol.* **2002**, *321*, 923–938.
(133) Marsh, E. N. G.; DeGrado, W. F. *Proc. Natl. Acad. Sci. U. S. A.* **2002**, *99*, 5150–5154.
(134) Calhoun, J. R.; Kono, H.; Lahr, S.; Wang, W.; DeGrado, W. F.; Saven, J. G. *J. Mol. Biol.* **2003**, *334*, 1101–1115.
(135) Calhoun, J. R.; Liu, W.; Spiegel, K.; Dal Peraro, M.; Klein, M. L.; Valentine, K. G.; Wand, A. J.; DeGrado, W. F. *Structure* **2008**, *16*, 210–215.
(136) Calhoun, J. R.; Bell, C. B.; Smith, T. J.; Thamann, T. J.; DeGrado, W. F.; Solomon, E. I. *J. Am. Chem. Soc.* **2008**, *130*, 9188–9189.
(137) Bell, C. B.; Calhoun, J. R.; Bobyr, E.; Wei, P.-P.; Hedman, B.; Hodgson, K. O.; Degrado, W. F.; Solomon, E. I. *Biochemistry* **2009**, *48*, 59–73.
(138) Reig, A. J.; Pires, M. M.; Snyder, R. A.; Wu, Y.; Jo, H.; Kulp, D. W.; Butch, S. E.; Calhoun, J. R.; Szyperski, T.; Szyperski, T. G.; Solomon, E. I.; DeGrado, W. F. *Nat. Chem.* **2012**, *4*, 900–906.
(139) McCall, K. A.; Huang, C.; Fierke, C. A. *J. Nutr.* **2000**, *130*, 1437S–46S.
(140) Vallee, B. L.; Auld, D. S. *Proc. Natl. Acad. Sci. U. S. A.* **1990**, *87*, 220–224.
(141) Matthews, J.; Sunde, M. *IUBMB Life* **2002**, *54*, 351–355.

(142) Kaptein, R. *Curr. Opin. Struct. Biol.* **1991**, *1*, 63–70.
(143) Yamamoto, K. R. *Annu. Rev. Genet.* **1985**, *19*, 209–252.
(144) Payvar, F.; DeFranco, D.; Firestone, G. L.; Edgar, B.; Wrange, O.; Okret, S.; Gustafsson, J. A.; Yamamoto, K. R. *Cell* **1983**, *35*, 381–392.
(145) Scheidereit, C.; Geisse, S.; Westphal, H.; Beato, M. *Nature* **1983**, *304*, 749–752.
(146) Chandler, V. L.; Maler, B. A.; Yamamoto, K. R. *Cell* **1983**, *33*, 489–499.
(147) Sakai, D. D.; Helms, S.; Carlstedt-Duke, J.; Gustafsson, J. a; Rottman, F. M.; Yamamoto, K. R. *Genes Dev.* **1988**, *2*, 1144–1154.
(148) Evans, R. *Science* **1988**, *240*, 889–895.
(149) Hard, T.; Kellenbach, E.; Boelens, R.; Maler, B.; Dahlman, K.; Freedman, L.; Carlstedt-Duke, J.; Yamamoto, K.; Gustafsson, J.; Kaptein, R. *Science* **1990**, *249*, 157–160.
(150) Schwabe, J. W.; Chapman, L.; Finch, J. T.; Rhodes, D. *Cell* **1993**, *75*, 567–578.
(151) Schwabe, J.; Neuhaus, D.; Rhodes, D. *Nature* **1990**, *348*, 458–461.
(152) Luisi, B.; Xu, W.; Otwinowski, Z.; Freedman, L. P.; Yamamoto, K. R.; Sigler, P. B. *Nature* **1991**, *352*, 497–505.
(153) O'Connor, T. R.; Graves, R. J.; de Murcia, G.; Castaing, B.; Laval, J. *J. Biol. Chem.* **1993**, *268*, 9063–9070.
(154) Miyamoto, I.; Miura, N.; Niwa, H.; Miyazaki, J.; Tanaka, K. *J. Biol. Chem.* **1992**, *267*, 12182–12187.
(155) Ikegami, T.; Kuraoka, I.; Saijo, M.; Kodo, N.; Kyogoku, Y.; Morikawa, K.; Tanaka, K.; Shirakawa, M. *Nat. Struct. Mol. Biol.* **1988**, *5*, 701–706.
(156) Buchko, G. W.; Ni, S.; Thrall, B. D.; Kennedy, M. a. *Nucleic Acids Res.* **1998**, *26*, 2779–2788.
(157) Hartwig, A.; Asmuss, M.; Blessing, H.; Hoffmann, S.; Jahnke, G.; Khandelwal, S.; Pelzer, A.; Bürkle, A. *Food Chem. Toxicol.* **2002**, *40*, 1179–1184.
(158) Takinowaki, H.; Matsuda, Y.; Yoshida, T.; Kobayashi, Y.; Ohkubo, T. *Protein Sci.* **2006**, *15*, 487–497.
(159) Janda, I.; Devedjiev, Y.; Derewenda, U.; Dauter, Z.; Bielnicki, J.; Cooper, D. R.; Graf, P. C. F.; Joachimiak, A.; Jakob, U.; Derewenda, Z. S. *Structure* **2004**, *12*, 1901–1907.
(160) Penner-Hahn, J. *Curr. Opin. Chem. Biol.* **2007**, *11*, 166–171.
(161) Collet, J.-F.; D'Souza, J. C.; Jakob, U.; Bardwell, J. C. A. *J. Biol. Chem.* **2003**, *278*, 45325–45332.
(162) Carballo, E.; Lai, W.; Blackshear, P. *Science* **1998**, *281*, 1001–1005.
(163) Michalek, J. L.; Besold, A. N.; Michel, S. L. J. *Dalton Trans.* **2011**, *40*, 12619–12632.
(164) Cho, Y.; Gorina, S.; Jeffrey, P.; Pavletich, N. *Science* **1994**, *265*, 346–355.
(165) Hainaut, P.; Hollstein, M. *Adv. Cancer Res.* **2000**, *77*, 81–137.
(166) Lai, W. S.; Carballo, E.; Thorn, J. M.; Kennington, E. a; Blackshear, P. J. *J. Biol. Chem.* **2000**, *275*, 17827–17837.
(167) Worthington, M. T.; Amann, B. T.; Nathans, D.; Berg, J. M. *Proc. Natl. Acad. Sci. U. S. A.* **1996**, *93*, 13754–13759.
(168) Anzellotti, A. I.; Farrell, N. P. *Chem. Soc. Rev.* **2008**, *37*, 1629–1651.
(169) Lai, W. S.; Blackshear, P. J. *J. Biol. Chem.* **2001**, *276*, 23144–23154.

(170) Lai, W.; Carballo, E.; Strum, J.; Kennington, E.; Phillips, R.; Blackshear, P. *Mol. Cell. Biol.* **1999**, *19*, 4311–4323.
(171) DiTargiani, R.; Lee, S.; Wassink, S.; Michel, S. *Biochemistry* **2006**, *45*, 13641–13649.
(172) Michel, S.; Guerrerio, A.; Berg, J. *Biochemistry* **2003**, *475*, 4626–4630.
(173) Worthington, M. T.; Pelo, J. W.; Sachedina, M. A.; Applegate, J. L.; Arseneau, K. O.; Pizarro, T. T. *J. Biol. Chem.* **2002**, *277*, 48558–48564.
(174) Brewer, B. Y. *J. Biol. Chem.* **2004**, *279*, 27870–27877.
(175) Klug, A. *Q. Rev. Biophys.* **2010**, *43*, 1–21.
(176) Laity, J. H.; Lee, B. M.; Wright, P. E. *Curr. Opin. Struct. Biol.* **2001**, *11*, 39–46.
(177) Berg, J. M.; Godwin, H. A. *Annu. Rev. Biophys. Biomol. Struct.* **1997**, *26*, 357–371.
(178) Beerli, R. R.; Barbas, C. F. *Nat. Biotechnol.* **2002**, *20*, 135–141.
(179) Urnov, F. D.; Rebar, E. J.; Holmes, M. C.; Zhang, H. S.; Gregory, P. D. *Nat. Rev. Genet.* **2010**, *11*, 636–646.
(180) Kröncke, K.; Klotz, L.-O. *Antioxid. Redox Signal.* **2009**, *11*, 1015–1027.
(181) Lee, M.; Gippert, G.; Soman, K.; Case, D.; Wright, P. *Science* **1989**, *245*, 635–637.
(182) Klevit, R. E.; Herriott, J. R.; Horvath, S. J. *Proteins Struct. Funct. Genet.* **1990**, *7*, 215–226.
(183) Omichinski, J. G.; Clore, G. M.; Appella, E.; Sakaguchi, K.; Gronenborn, a M. *Biochemistry* **1990**, *29*, 9324–9334.
(184) Negi, S.; Imanishi, M.; Matsumoto, M.; Sugiura, Y. *Chem. --Eur. J.* **2008**, *14*, 3236–3249.
(185) Nomura, A.; Sugiura, Y. *Inorg. Chem.* **2004**, *43*, 1708–1713.
(186) Yokono, M.; Saegusa, N.; Matsushita, K.; Sugiura, Y. *Biochemistry* **1998**, *37*, 6824–6832.
(187) Nomura, A.; Sugiura, Y. *J. Am. Chem. Soc.* **2004**, *126*, 15374–15375.
(188) Negi, S.; Umeda, Y.; Masuyama, S.; Kano, K.; Sugiura, Y. *Bioorg. Med. Chem. Lett.* **2009**, *19*, 2789–2791.
(189) Porteus, M. H.; Baltimore, D. *Science* **2003**, *300*, 763.
(190) Nakatsukasa, T.; Shiraishi, Y.; Negi, S.; Imanishi, M.; Futaki, S.; Sugiura, Y. *Biochem. Biophys. Res. Commun.* **2005**, *330*, 247–252.
(191) Zanghellini, A.; Jiang, L.; Wollacott, A. M.; Cheng, G.; Meiler, J.; Althoff, E. A.; Röthlisberger, D.; Baker, D. *Protein Sci.* **2006**, *15*, 2785–2794.
(192) Jiang, L.; Althoff, E. A.; Clemente, F. R.; Doyle, L.; Röthlisberger, D.; Zanghellini, A.; Gallaher, J. L.; Betker, J. L.; Tanaka, F.; Barbas, C. F.; Hilvert, D.; Houk, K. N.; Stoddard, B. L.; Baker, D. *Science* **2008**, *319*, 1387–1391.
(193) Röthlisberger, D.; Khersonsky, O.; Wollacott, A. M.; Jiang, L.; DeChancie, J.; Betker, J.; Gallaher, J. L.; Althoff, E. A.; Zanghellini, A.; Dym, O.; Albeck, S.; Houk, K. N.; Tawfik, D. S.; Baker, D. *Nature* **2008**, *453*, 190–195.
(194) Höst, G.; Mårtensson, L.-G.; Jonsson, B.-H. *Biochim. Biophys. Acta* **2006**, *1764*, 1601–1606.
(195) Höst, G. E.; Jonsson, B.-H. *Biochim. Biophys. Acta* **2008**, *1784*, 811–815.
(196) Park, H.-S.; Nam, S.; Lee, J. K.; Yoon, C. N.; Mannervik, B.; Benkovic, S. J.; Kim, H.-S. *Science* **2006**, *311*, 535–538.

(197) Otten, L. G.; Quax, W. J. *Biomol. Eng.* **2005**, *22*, 1–9.
(198) Mills, J. H.; Khare, S. D.; Bolduc, J. M.; Forouhar, F.; Mulligan, V. K.; Lew, S.; Seetharaman, J.; Tong, L.; Stoddard, B. L.; Baker, D. *J. Am. Chem. Soc.* **2013**, *135*, 13393–13399.
(199) Weston, J. *Chem. Rev.* **2005**, *105*, 2151–2174.
(200) Wilcox, D. E. *Chem. Rev.* **1996**, *96*, 2435–2458.
(201) Jedrzejas, M. J.; Setlow, P. *Chem. Rev.* **2001**, *101*, 607–618.
(202) Lowther, W. T.; Matthews, B. W. *Chem. Rev.* **2002**, *102*, 4581–4608.
(203) Dupureur, C. M. *Curr. Opin. Chem. Biol.* **2008**, *12*, 250–255.
(204) Dupureur, C. M. *Metallomics* **2010**, *2*, 609.
(205) Brown, R. S.; Lu, Z.-L.; Liu, C. T.; Tsang, W. Y.; Edwards, D. R.; Neverov, A. A. *J. Phys. Org. Chem.* **2010**, *23*, 1–15.
(206) Lönnberg, H. *Org. Biomol. Chem.* **2011**, *9*, 1687–1703.
(207) Liu, C.; Wang, L. *Dalton Trans.* **2009**, 227.
(208) Morrow, J. R.; Amyes, T. L.; Richard, J. P. *Acc. Chem. Res.* **2008**, *41*, 539–548.
(209) Mancin, F.; Scrimin, P.; Tecilla, P.; Tonellato, U. *Chem. Commun. (Camb).* **2005**, 2540–2548.
(210) Yatsimirsky, a. *Coord. Chem. Rev.* **2005**, *249*, 1997–2011.
(211) Liu, C.; Wang, M.; Zhang, T.; Sun, H. *Coord. Chem. Rev.* **2004**, *248*, 147–168.
(212) Krämer, R. *Coord. Chem. Rev.* **1999**, *182*, 243–261.
(213) Chin, J. *Acc. Chem. Res.* **1991**, *24*, 145–152.
(214) Vichard, C.; Kaden, T. A. *Inorganica Chim. Acta* **2002**, *337*, 173–180.
(215) Rossi, P.; Felluga, F.; Tecilla, P.; Formaggio, F.; Crisma, M.; Toniolo, C.; Scrimin, P. *J. Am. Chem. Soc.* **1999**, *121*, 6948–6949.
(216) Rossi, P.; Felluga, F.; Tecilla, P.; Formaggio, F.; Crisma, M.; Toniolo, C.; Scrimin, P. *Biopolymers* **2000**, *55*, 496–501.
(217) Sissi, C.; Rossi, P.; Felluga, F.; Gormaggio, F.; Palumbo, M.; Tecilla, P.; Toniolo, C.; Scrimin, P. *J. Am. Chem. Soc.* **2001**, *123*, 3169–3170.
(218) Scarso, A.; Scheffer, U.; Göbel, M.; Broxterman, Q. B.; Kaptein, B.; Formaggio, F.; Toniolo, C.; Scrimin, P. *Proc. Natl. Acad. Sci. U. S. A.* **2002**, *99*, 5144–5149.
(219) Rossi, P.; Tecilla, P.; Baltzer, L.; Scrimin, P. *Chem. --Eur. J.* **2004**, *10*, 4163–4170.
(220) Olofsson, S.; Johansson, G.; Baltzer, L. *J. Chem. Soc. Perkin Trans. 2* **1995**, 2047.
(221) Olofsson, S.; Baltzer, L. *Fold. Des.* **1996**, *1*, 347–356.
(222) Broo, K. S.; Brive, L.; Ahlberg, P.; Baltzer, L. *J. Am. Chem. Soc.* **1997**, *7863*, 11362–11372.
(223) Coleman, J. E. *Annu. Rev. Biochem.* **1992**, *61*, 897–946.
(224) Tripp, B. C.; Smith, K.; Ferry, J. G. *J. Biol. Chem.* **2001**, *276*, 48615–48618.
(225) Smith, K. S.; Ferry, J. G. *FEMS Microbiol. Rev.* **2000**, *24*, 335–366.
(226) Avvaru, B. S.; Kim, C. U.; Sippel, K. H.; Gruner, S. M.; Agbandje-McKenna, M.; Silverman, D. N.; McKenna, R. *Biochemistry* **2010**, *49*, 249–251.
(227) Liljas, A.; Kannan, K. K.; Bergstén, P. C.; Waara, I.; Fridborg, K.; Strandberg, B.; Carlbom, U.; Järup, L.; Lövgren, S.; Petef, M. *Nat. New Biol.* **1972**, *235*, 131–137.
(228) Kannan, K. K.; Notstrand, B.; Fridborg, K.; Lövgren, S.; Ohlsson, A.; Petef, M. *Proc. Natl. Acad. Sci. U. S. A.* **1975**, *72*, 51–55.
(229) Alberts, I. L.; Nadassy, K.; Wodak, S. J. *Protein Sci.* **1998**, *7*, 1700–1716.

(230) Håkansson, K.; Carlsson, M.; Svensson, L. A.; Liljas, A. *J. Mol. Biol.* **1992**, *227*, 1192–1204.
(231) Christianson, D. W.; Fierke, C. A. *Acc. Chem. Res.* **1996**, *29*, 331–339.
(232) Kiefer, L. L.; Ippolito, J. A.; Fierke, C. A.; Christianson, D. W. *J. Am. Chem. Soc.* **1993**, *115*, 12581–12582.
(233) Alexander, R. S.; Kiefer, L. L.; Fierke, C. A.; Christianson, D. W. *Biochemistry* **1993**, *32*, 1510–1518.
(234) Lesburg, C. A.; Huang, C.; Christianson, D. W.; Fierke, C. A. *Biochemistry* **1997**, *36*, 15780–15791.
(235) Kiefer, L. L.; Paterno, S. A.; Fierke, C. A. *J. Am. Chem. Soc.* **1995**, *117*, 6831–6837.
(236) Lesburg, C. A.; Christianson, D. W. *J. Am. Chem. Soc.* **1995**, *117*, 6838–6844.
(237) Ippolito, J. A.; Baird, T. T.; McGee, S. A.; Christianson, D. W.; Fierke, C. A. *Proc. Natl. Acad. Sci. U. S. A.* **1995**, *92*, 5017–5021.
(238) Kiefer, L. L.; Fierke, C. A. *Biochemistry* **1994**, *33*, 15233–15240.
(239) Fierke, C. A.; Calderone, T. L.; Krebs, J. F. *Biochemistry* **1991**, *30*, 11054–11063.
(240) Kiefer, L. L.; Krebs, J. F.; Paterno, S. A.; Fierke, C. A. *Biochemistry* **1993**, *32*, 9896–9900.
(241) Krebs, J. F.; Fierke, C. A.; Alexander, R. S.; Christianson, D. W. *Biochemistry* **1991**, *30*, 9153–9160.
(242) Ippolito, J. A.; Christianson, D. W. *Biochemistry* **1993**, *32*, 9901–9905.
(243) Carter, N. D.; Dodgson, S. J.; Gros, G.; Tashian, R. E. *The Carbonic Anhydrases: Cellular Physiology and Molecular Genetics*; Springer, 1991; p. 379.
(244) Elleby, B.; Sjoblom, B.; Lindskog, S. *Eur. J. Biochem.* **1999**, *262*, 516–521.
(245) Gould, S. M.; Tawfik, D. S. *Biochemistry* **2005**, *44*, 5444–5452.
(246) Molecular Simulations, Inc., 2000.
(247) Dill, K. A.; Bromberg, S.; Kaizhi, Y.; Fiebig, K. M.; Yee, D. P.; Thomas, P. D.; Chan, H. S.; Yue, K. *Protein Sci.* **1995**, *4*, 561–602.
(248) Berne, B. J.; Weeks, J. D.; Zhou, R. *Annu. Rev. Phys. Chem.* **2009**, *60*, 85–103.
(249) Agashe, V. R.; Shastry, M. C.; Udgaonkar, J. B. *Nature* **1995**, *377*, 754–757.
(250) Gutin, a M.; Abkevich, V. I.; Shakhnovich, E. I. *Biochemistry* **1995**, *34*, 3066–3076.
(251) Ghosh, D.; Pecoraro, V. L. *Inorg. Chem.* **2004**, *43*, 7902–7915.
(252) Peacock, A. F. A.; Iranzo, O.; Pecoraro, V. L. *Dalton Trans.* **2009**, *9226*, 2271–2280.
(253) Su, J. Y.; Hodges, R. S.; Kay, C. M. *Biochemistry* **1994**, *33*, 15501–15510.
(254) Ghosh, D.; Lee, K.-H.; Demeler, B.; Pecoraro, V. L. *Biochemistry* **2005**, *44*, 10732–10740.
(255) Ptitsyn, O. B.; Pain, R. H.; Semisotnov, G. V; Zerovnik, E.; Razgulyaev, O. I. *FEBS Lett.* **1990**, *262*, 20–24.
(256) Ptitsyn, O. B. In *Protein folding*; W. H. Freeman and Co., 1992; pp. 243 – 300.
(257) Ptitsyn, O. B. *Adv. Protein Chem.* **1995**, *47*, 83–229.
(258) Ghadiri, M. R.; Case, M. A. *Angew. Chem. Int. Ed. Engl.* **1993**, *32*, 1594–1597.
(259) Pecoraro, V. L.; Peacock, A. F. A.; Iranzo, O.; Luczkowski, M. In *ACS Symposium Series*; American Chemical Society, **2009**; pp. 183–197.

(260) Wright, J. G.; Tsang, H. T.; Penner-Hahn, J. E.; O'Halloran, T. V. *J. Am. Chem. Soc.* **1990**, *112*, 2434–2435.
(261) Holm, R. H.; Kennepohl, P.; Solomon, E. I. *Chem. Rev.* **1996**, *96*, 2239–2314.
(262) Brown, N. L.; Stoyanov, J. V; Kidd, S. P.; Hobman, J. L. *FEMS Microbiol. Rev.* **2003**, *27*, 145–163.
(263) Utschig, L. M.; Bryson, J. W.; O'Halloran, T. V. *Science* **1995**, *268*, 380–385.
(264) Summers, A. O. *J. Bacteriol.* **1992**, *174*, 3097–3101.
(265) Kimura, E.; Shiota, T.; Koike, T.; Shiro, M.; Kodama, M. *J. Am. Chem. Soc.* **1990**, *112*, 5805–5811.
(266) Koerner, T. B.; Brown, R. S. *Can. J. Chem.* **2002**, *80*, 183–191.
(267) Bazzicalupi, C.; Bencini, A.; Bianchi, A.; Fusi, V.; Giorgi, C.; Paoletti, P.; Valtancoli, B.; Zanchi, D. *Inorg. Chem.* **1997**, *36*, 2784–2790.
(268) Verpoorte, J. A.; Mehta, S.; Edsall, J. T. *J. Biol. Chem.* **1967**, *242*, 4221–4229.
(269) Innocenti, A.; Scozzafava, A.; Parkkila, S.; Puccetti, L.; De Simone, G.; Supuran, C. T. *Bioorg. Med. Chem. Lett.* **2008**, *18*, 2267–2271.
(270) Liang, Z.; Xue, Y.; Behravan, G.; Jonsson, B. H.; Lindskog, S. *Eur. J. Biochem.* **1993**, *211*, 821–827.
(271) Krebs, J. F.; Ippolito, J. A.; Christianson, D. W.; Fierke, C. A. *J. Biol. Chem.* **1993**, *268*, 27458–27466.
(272) Woolley, P. *Nature* **1975**, *258*, 677–682.
(273) Huguet, J.; Brown, R. S. *J. Am. Chem. Soc.* **1980**, *102*, 7571–7572.
(274) Brown, R. S.; Curtis, N. J.; Huguet, J. *J. Am. Chem. Soc.* **1981**, *103*, 6953–6959.
(275) Brown, R. S.; Salmon, D.; Curtis, N. J.; Kusuma, S. *J. Am. Chem. Soc.* **1982**, *104*, 3188–3194.
(276) Slebocka-Tilk, H.; Cocho, J. L.; Frackman, Z.; Brown, R. S. *J. Am. Chem. Soc.* **1984**, *106*, 2421–2431.
(277) Zhang, X.; van Eldik, R.; Koike, T.; Kimura, E. *Inorg. Chem.* **1993**, *32*, 5749–5755.
(278) Zhang, X.; van Eldik, R. *Inorg. Chem.* **1995**, *34*, 5606–5614.
(279) Nakata, K.; Shimomura, N.; Shiina, N.; Izumi, M.; Ichikawa, K.; Shiro, M. *J. Inorg. Biochem.* **2002**, *89*, 255–266.
(280) Pessi, A.; Bianchi, E.; Crameri, A.; Venturini, S.; Tramontano, A.; Sollazzo, M. *Nature* **1993**, *362*, 367–369.
(281) Müller, H. N.; Skerra, A. *Biochemistry* **1994**, *33*, 14126–14135.
(282) Vita, C.; Roumestand, C.; Toma, F.; Ménez, A. *Proc. Natl. Acad. Sci. U. S. A.* **1995**, *92*, 6404–6408.
(283) Stewart, J. D.; Roberts, V. A.; Crowder, M. W.; Getzoff, E. D.; Benkovic, S. J. *J. Am. Chem. Soc.* **1994**, *116*, 415–416.
(284) Wade, W. S.; Koh, J. S.; Han, N.; Hoekstra, D. M.; Lerner, R. A. *J. Am. Chem. Soc.* **1993**, *115*, 4449–4456.
(285) Handel, T.; Williams, S. A.; DeGrado, W. F. *Science* **1993**, *261*, 879–885.
(286) Hitomi, Y.; Outten, C. E.; O'Halloran, T. V. *J. Am. Chem. Soc.* **2001**, *123*, 8614–8615.
(287) Fierke, C. A.; Thompson, R. B. *Biometals* **2001**, *14*, 205–222.
(288) Song, H.; Wilson, D. L.; Farquhar, E. R.; Lewis, E. a; Emerson, J. P. *Inorg. Chem.* **2012**, *51*, 11098–11105.

(289) Der, B. S.; Machius, M.; Miley, M. J.; Mills, J. L.; Szyperski, T.; Kuhlman, B. *J. Am. Chem. Soc.* **2012**, *134*, 375–385.
(290) Gomez-Tagle, P.; Vargas-Zúñiga, I.; Taran, O.; Yatsimirsky, A. K. *J. Org. Chem.* **2006**, *71*, 9713–9722.
(291) Lu, Y. *Compr. Coord. Chem. II* **2003**, *8*, 91–122.
(292) Messerschmidt, A.; Huber, R.; Poulos, T.; Wieghardt, K. *Handbook of Metalloproteins: Cupredoxins (Type-1 Copper Proteins)*; 2001; pp. 1153–1241.
(293) Hart, P.; Nersissian, A.; George, S. Copper Proteins with Type 1 Sites. *Encyclopedia of Inorganic and Bioinorganic Chemistry*, **2011**.
(294) Malmström, B. G. *Chem. Rev.* **1990**, *90*, 1247–1260.
(295) Tavares, P.; Pereira, a S.; Moura, J. J. G.; Moura, I. *J. Inorg. Biochem.* **2006**, *100*, 2087–2100.
(296) Gray, H. B.; Malmström, B. G.; Williams, R. J. P. *J. Biol. Inorg. Chem.* **2000**, *5*, 551–559.
(297) Solomon, E.; Gorelsky, S.; Dey, A. *Wiley Intersci.* **2006**, *405*, 1415–1428.
(298) Lowery, M.; Solomon, E. *Inorganica Chim. Acta* **1992**, *200*, 233–243.
(299) Solomon, E. I.; Hare, J. W.; Gray, H. B. *Proc. Natl. Acad. Sci. U. S. A.* **1976**, *73*, 1389–1393.
(300) Canters, G. W.; Gilardi, G. *FEBS Lett.* **1993**, *325*, 39–48.
(301) Solomon, E. I.; Baldwin, M. J.; Lowery, M. D. *Chem. Rev.* **1992**, *92*, 521–542.
(302) Solomon, E.; Lowery, M.; Lacroix, L.; Root, D. *Methods Enzymol.* **1993**, *226*, 1–33.
(303) Solomon, E.; Lowery, M. *Science* **1993**, *259*, 1575–1581.
(304) Guckert, J. A.; Lowery, M. D.; Solomon, E. I. *J. Am. Chem. Soc.* **1995**, *117*, 2817–2844.
(305) Solomon, E. I.; Penfield, K. W.; Gewirth, A. A. *Inorganica Chim. Acta* **1996**, *243*, 67–78.
(306) Lacroix, L. B.; Shadle, S. E.; Wang, Y.; Averill, B. A.; Hedman, B.; Hodgson, K. O.; Solomon, E. I. *J. Am. Chem. Soc.* **1996**, 7755–7768.
(307) LaCroix, L.; Randall, D. *J. Am. Chem. Soc.* **1998**, 9621–9631.
(308) Solomon, E. I.; Randall, D. W.; Glaser, T. *Coord. Chem. Rev.* **2000**, *200-202*, 595–632.
(309) Hannan, J. P.; Busch, J. L. H.; Breton, J.; James, R.; Thomson, A. J.; Moore, G. R.; Davy, S. L. *J. Biol. Inorg. Chem.* **2000**, *5*, 432–447.
(310) Solomon, E. I.; Szilagyi, R. K.; DeBeer George, S.; Basumallick, L. *Chem. Rev.* **2004**, *104*, 419–458.
(311) Solomon, E. I. *Inorg. Chem.* **2006**, *45*, 8012–8025.
(312) Solomon, E. I.; Hadt, R. G. *Coord. Chem. Rev.* **2011**, *255*, 774–789.
(313) Blackburn, N. J.; Barr, M. E.; Woodruff, W. H.; van der Ooost, J.; de Vries, S. *Biochemistry* **1994**, *33*, 10401–10407.
(314) Blackburn, N. J.; de Vries, S.; Barr, M. E.; Houser, R. P.; Tolman, W. B.; Sanders, D.; Fee, J. A. *J. Am. Chem. Soc.* **1997**, *119*, 6135–6143.
(315) Solomon, E. I.; Xie, X.; Dey, A. *Chem. Soc. Rev.* **2008**, *37*, 623–638.
(316) Hay, M.; Ang, M.; Gamelin, D.; Solomon, E.; Antholine, W. E.; Ralle, M.; Blackburn, N. J.; Massey, P. D.; Wang, X.; Kwon, A. H.; Lu, Y. *Inorg. Chem.* **1998**, 191–198.

(317) Gamelin, D. R.; Randall, D. W.; Hay, M. T.; Houser, R. P.; Mulder, T. C.; Canters, G. W.; Vries, S. De; Tolman, W. B.; Lu, Y.; Solomon, E. I. *J. Am. Chem. Soc.* **1998**, 5246–5263.
(318) Szilagyi, R. K.; Solomon, E. I. *Curr. Opin. Chem. Biol.* **2002**, *6*, 250–258.
(319) Brown, K.; Tegoni, M.; Prudêncio, M.; Pereira, A. S.; Besson, S.; Moura, J. J.; Moura, I.; Cambillau, C. *Nat. Struct. Biol.* **2000**, *7*, 191–195.
(320) Korszun, Z. R. *J. Mol. Biol.* **1987**, *196*, 413–419.
(321) Adman, E. T.; Stenkamp, R. E.; Sieker, L. C.; Jensen, L. H. *J. Mol. Biol.* **1978**, *123*, 35–47.
(322) Baker, E. N. *J. Mol. Biol.* **1988**, *203*, 1071–1095.
(323) Nar, H.; Messerschmidt, A.; Huber, R.; van de Kamp, M.; Canters, G. W. *J. Mol. Biol.* **1991**, *221*, 765–772.
(324) Vijgenboom, E.; Busch, J. E.; Canters, G. W. *Microbiology* **1997**, *143*, 2853–2863.
(325) Pascher, T.; Karlsson, B. G.; Nordling, M.; Malmström, B. G.; Vänngård, T. *Eur. J. Biochem.* **1993**, *212*, 289–296.
(326) Piccioli, M.; Luchinat, C.; Mizoguchi, T. J.; Ramirez, B. E.; Gray, H. B.; Richards, J. H. *Inorg. Chem.* **1995**, *34*, 737–742.
(327) Faham, S.; Mizoguchi, T. J.; Adman, E. T.; Gray, H. B.; Richards, J. H.; Rees, D. C. *J. Biol. Inorg. Chem.* **1997**, *2*, 464–469.
(328) DeBeer, S.; Kiser, C. N.; Mines, G. A.; Richards, J. H.; Gray, H. B.; Solomon, E. I.; Hedman, B.; Hodgson, K. O. *Inorg. Chem.* **1999**, *38*, 433–438.
(329) Lancaster, K. M.; DeBeer George, S.; Yokoyama, K.; Richards, J. H.; Gray, H. B. *Nat. Chem.* **2009**, *1*, 711–715.
(330) Lancaster, K. M.; Sproules, S.; Palmer, J. H.; Richards, J. H.; Gray, H. B. *J. Am. Chem. Soc.* **2010**, *132*, 14590–14595.
(331) Lancaster, K. M.; Farver, O.; Wherland, S.; Crane, E. J.; Richards, J. H.; Pecht, I.; Gray, H. B. *J. Am. Chem. Soc.* **2011**, *133*, 4865–4873.
(332) Karlsson, B. G.; Aasa, R.; Malmström, B. G.; Lundberg, L. G. *FEBS Lett.* **1989**, *253*, 99–102.
(333) Karlsson, B. G.; Nordling, M.; Pascher, T.; Tsai, L.; Sjölin, L.; Lundberg, L. G. *Protein Eng.* **1991**, *4*, 343–349.
(334) Tsai, L. C.; Bonander, N.; Harata, K.; Karlsson, G.; Vänngård, T.; Langer, V.; Sjölin, L. *Acta Crystallogr. D. Biol. Crystallogr.* **1996**, *52*, 950–958.
(335) Kroes, S. J.; Hoitink, C. W. G.; Andrew, C. R.; Ai, J.; Sanders-Loehr, J.; Messerschmidt, A.; Hagen, W. R.; Canters, G. W. *Eur. J. Biochem.* **1996**, *240*, 342–351.
(336) Bonander, N.; Karlsson, B. G.; Vänngård, T. *Biochemistry* **1996**, *35*, 2429–2436.
(337) Salgado, J.; Kroes, S. J.; Berg, A.; Moratal, J. M.; Canters, G. W. *J. Biol. Chem.* **1998**, *273*, 177–185.
(338) Messerschmidt, A.; Prade, L.; Kroes, S. J.; Sanders-Loehr, J.; Huber, R.; Canters, G. W. *Proc. Natl. Acad. Sci. U. S. A.* **1998**, *95*, 3443–3448.
(339) Mizoguchi, T. T. J.; Di Bilio, A. J.; Gray, H. B.; Richards, J. H.; Bilio, A. Di. *J. Am. Chem. Soc.* **1992**, *114*, 10076–10078.
(340) Berry, S. M.; Gieselman, M. D.; Nilges, M. J.; van der Donk, W. A.; Lu, Y. *J. Am. Chem. Soc.* **2002**, *124*, 2084–2085.

(341) Ralle, M.; Berry, S. M.; Nilges, M. J.; Gieselman, M. D.; van der Donk, W. a; Lu, Y.; Blackburn, N. J. *J. Am. Chem. Soc.* **2004**, *126*, 7244–7256.
(342) Garner, D. K.; Vaughan, M. D.; Hwang, H. J.; Savelieff, M. G.; Berry, S. M.; Honek, J. F.; Lu, Y. *J. Am. Chem. Soc.* **2006**, *128*, 15608–15617.
(343) Clark, K. M.; Yu, Y.; Marshall, N. M.; Sieracki, N. A.; Nilges, M. J.; Blackburn, N. J.; van der Donk, W. a; Lu, Y. *J. Am. Chem. Soc.* **2010**, *132*, 10093–10101.
(344) Berry, S. M.; Ralle, M.; Low, D. W.; Blackburn, N. J.; Lu, Y. *J. Am. Chem. Soc.* **2003**, *125*, 8760–8768.
(345) Marshall, N. M.; Garner, D. K.; Wilson, T. D.; Gao, Y.-G.; Robinson, H.; Nilges, M. J.; Lu, Y. *Nature* **2009**, *462*, 113–116.
(346) Muir, T. W.; Sondhi, D.; Cole, P. A. *Proc. Natl. Acad. Sci. U. S. A.* **1998**, *95*, 6705–6710.
(347) Farver, O.; Marshall, N. M.; Wherland, S.; Lu, Y.; Pecht, I. *Proc. Natl. Acad. Sci. U. S. A.* **2013**, *110*, 10536–10540.
(348) Van der Oost, J.; Lappalainen, P.; Musacchio, A.; Warne, A.; Lemieux, L.; Rumbley, J.; Gennis, R. B.; Aasa, R.; Pascher, T.; Malmström, B. G. *EMBO J.* **1992**, *11*, 3209–3217.
(349) Kelly, M.; Lappalainen, P.; Talbo, G.; Haltia, T.; van der Oost, J.; Saraste, M. *J. Biol. Chem.* **1993**, *268*, 16781–16787.
(350) Hay, M.; Richards, J. H.; Lu, Y. *Proc. Natl. Acad. Sci. U. S. A.* **1996**, *93*, 461–464.
(351) Hwang, H. J.; Lu, Y. *Proc. Natl. Acad. Sci. U. S. A.* **2004**, *101*, 12842–12847.
(352) Hwang, H. J.; Berry, S. M.; Nilges, M. J.; Lu, Y. *J. Am. Chem. Soc.* **2005**, *127*, 7274–7275.
(353) Farver, O.; Lu, Y.; Ang, M. C.; Pecht, I. *Proc. Natl. Acad. Sci. U. S. A.* **1999**, *96*, 899–902.
(354) New, S. Y.; Marshall, N. M.; Hor, T. S. A.; Xue, F.; Lu, Y. *Chem. Commun. (Camb).* **2012**, *48*, 4217–4219.
(355) Hay, M. T.; Milberg, R. M.; Lu, Y. *J. Am. Chem. Soc.* **1996**, *118*, 11976–11977.
(356) Wang, X.; Ang, M. C.; Lu, Y. *J. Am. Chem. Soc.* **1999**, *121*, 2947–2948.
(357) Wilson, T. D.; Savelieff, M. G.; Nilges, M. J.; Marshall, N. M.; Lu, Y. *J. Am. Chem. Soc.* **2011**, *133*, 20778–20792.
(358) Berry, S. M.; Wang, X.; Lu, Y. *J. Inorg. Biochem.* **2000**, *78*, 89–95.
(359) Hwang, H. J.; Nagraj, N.; Lu, Y. *Inorg. Chem.* **2006**, *45*, 102–107.
(360) Dennison, C.; Vijgenboom, E.; de Vries, S.; van der Oost, J.; Canters, G. W. *FEBS Lett.* **1995**, *365*, 92–94.
(361) Jones, L. H.; Liu, A.; Davidson, V. L. *J. Biol. Chem.* **2003**, *278*, 47269–47274.
(362) Schnepf, R.; Hörth, P.; Bill, E.; Wieghardt, K.; Hildebrandt, P.; Haehnel, W. *J. Am. Chem. Soc.* **2001**, *123*, 2186–2195.
(363) Schnepf, R.; Haehnel, W.; Wieghardt, K.; Hildebrandt, P. *J. Am. Chem. Soc.* **2004**, *126*, 14389–14399.
(364) Rau, H. K.; Haehnel, W. *J. Am. Chem. Soc.* **1998**, *120*, 468–476.
(365) Rau, H.; DeJonge, N.; Haehnel, W. *Angew. Chem. Int. Ed. Engl.* **2000**, *39*, 250–253.
(366) Mutter, M.; Altmann, E.; Altmann, K.-H.; Hersperger, R.; Koziej, P.; Nebel, K.; Tuchsecherer, G.; Vuilleumier, S.; Gremlich, H.-U.; Muller, K. *Helv. Chim. Acta* **1988**, *71*, 835–847.

(367) Mutter, M.; Tuchscherer, G. G.; Miller, C.; Altmann, K. H.; Carey, R. I.; Wyss, D. F.; Labhardt, A. M.; Rivier, J. E. *J. Am. Chem. Soc.* **1992**, *114*, 1463–1470.
(368) Mutter, M.; Tuchscherer, G. *Cell. Mol. Life Sci.* **1997**, *53*, 851.
(369) Shiga, D.; Nakane, D.; Inomata, T.; Funahashi, Y.; Masuda, H.; Kikuchi, A.; Oda, M.; Noda, M.; Uchiyama, S.; Fukui, K.; Kanaori, K.; Tajima, K.; Takano, Y.; Nakamura, H.; Tanaka, T. *J. Am. Chem. Soc.* **2010**, *132*, 18191–18198.
(370) Shiga, D.; Hamano, Y.; Kamei, M.; Funahashi, Y.; Masuda, H.; Sakaguchi, M.; Ogura, T.; Tanaka, T. *J. Biol. Inorg. Chem.* **2012**, *17*, 1025–1031.
(371) Shiga, D.; Funahashi, Y.; Masuda, H.; Kikuchi, A.; Noda, M.; Uchiyama, S.; Fukui, K.; Kanaori, K.; Tajima, K.; Takano, Y.; Nakamura, H.; Kamei, M.; Tanaka, T. *Biochemistry* **2012**, *51*, 7901–7907.
(372) Robinson, H.; Ang, M. M. C.; Gao, Y. G.; Hay, M. M. T.; Lu, Y.; Wang, A. H. *Biochemistry* **1999**, *38*, 5677–5683.
(373) Babcock, G.; Wikström, M. *Nature* **1992**, *356*, 302–309.
(374) Ferguson-Miller, S.; Babcock, G. T. *Chem. Rev.* **1996**, *96*, 2889–2908.
(375) García-Horsman, J. A.; Barquera, B.; Rumbley, J.; Ma, J.; Gennis, R. B. *J. Bacteriol.* **1994**, *176*, 5587–5600.
(376) Michel, H.; Behr, J.; Harrenga, A.; Kannt, A. *Annu. Rev. Biophys. Biomol. Struct.* **1998**, *27*, 329–356.
(377) Poulos, T. L.; Li, H.; Raman, C. *Curr. Opin. Chem. Biol.* **1999**, *3*, 131–137.
(378) Namslauer, A.; Brzezinski, P. *FEBS Lett.* **2004**, *567*, 103–110.
(379) Svensson-Ek, M.; Abramson, J.; Larsson, G.; Törnroth, S.; Brzezinski, P.; Iwata, S. *J. Mol. Biol.* **2002**, *321*, 329–339.
(380) Sigman, J. A.; Kim, H. K.; Zhao, X.; Carey, J. R.; Lu, Y. *Proc. Natl. Acad. Sci. U. S. A.* **2003**, *100*, 3629–3634.
(381) Zhao, X.; Yeung, N.; Wang, Z.; Guo, Z.; Lu, Y. *Biochemistry* **2005**, *44*, 1210–1214.
(382) Yoshikawa, S.; Shinzawa-Itoh, K.; Nakashima, R.; Yaono, R.; Yamashita, E.; Inoue, N.; Yao, M.; Fei, M. J.; Libeu, C. P.; Mizushima, T.; Yamaguchi, H.; Tomizaki, T.; Tsukihara, T. *Science* **1998**, *280*, 1723–1729.
(383) Buse, G.; Soulimane, T.; Dewor, M.; Meyer, H. E.; Blüggel, M. *Protein Sci.* **1999**, *8*, 985–990.
(384) Bu, Y.; Cukier, R. I. *J. Phys. Chem. B* **2005**, *109*, 22013–22026.
(385) Kaila, V. R. I.; Johansson, M. P.; Sundholm, D.; Laakkonen, L.; Wikström, M. *Biochim. Biophys. Acta* **2009**, *1787*, 221–233.
(386) Miner, K. D.; Mukherjee, A.; Gao, Y.-G.; Null, E. L.; Petrik, I. D.; Zhao, X.; Yeung, N.; Robinson, H.; Lu, Y. *Angew. Chem. Int. Ed. Engl.* **2012**, *51*, 5589–5592.
(387) Buschmann, S.; Warkentin, E.; Xie, H.; Langer, J. D.; Ermler, U.; Michel, H. *Science* **2010**, *329*, 327–330.
(388) Liu, X.; Yu, Y.; Hu, C.; Zhang, W.; Lu, Y.; Wang, J. *Angew. Chem. Int. Ed. Engl.* **2012**, *51*, 4312–4316.
(389) Otto, S.; Engberts, J. B. F. N. *J. Am. Chem. Soc.* **1999**, *121*, 6798–6806.
(390) Otto, S.; Boccaletti, G.; Engberts, J. B. F. N. *J. Am. Chem. Soc.* **1998**, *120*, 4238–4239.

(391) Boersma, A. J.; Megens, R. P.; Feringa, B. L.; Roelfes, G. *Chem. Soc. Rev.* **2010**, *39*, 2083–2092.
(392) García-Fernández, A.; Roelfes, G. *Met. Ions Life Sci.* **2012**, *10*, 249–268.
(393) Boersma, A. J.; de Bruin, B.; Feringa, B. L.; Roelfes, G. *Chem. Commun. (Camb).* **2012**, *48*, 2394–2396.
(394) Reetz, M. T.; Jiao, N. *Angew. Chem. Int. Ed. Engl.* **2006**, *118*, 2476–2479.
(395) Beismann-Driemeyer, S.; Sterner, R. *J. Biol. Chem.* **2001**, *276*, 20387–20396.
(396) Podtetenieff, J.; Taglieber, A.; Bill, E.; Reijerse, E. J.; Reetz, M. T. *Angew. Chem. Int. Ed. Engl.* **2010**, *49*, 5151–5155.
(397) Roelfes, G.; Feringa, B. L. *Angew. Chem. Int. Ed. Engl.* **2005**, *44*, 3230–3232.
(398) Lang, D.; Thoma, R.; Henn-Sax, M.; Sterner, R.; Wilmanns, M. *Science* **2000**, *289*, 1546–1550.
(399) Lerch, M.; Gafner, V.; Bader, R.; Christen, B.; Folkers, G.; Zerbe, O. *J. Mol. Biol.* **2002**, *322*, 1117–1133.
(400) Bettio, A.; Beck-Sickinger, A. G. *Biopolymers* **2001**, *60*, 420–437.
(401) Li, X. A.; Sutcliffe, M. J.; Schwartz, T. W.; Dobson, C. M. *Biochemistry* **1992**, *31*, 1245–1253.
(402) Coquière, D.; Bos, J.; Beld, J.; Roelfes, G. *Angew. Chem. Int. Ed. Engl.* **2009**, *48*, 5159–5162.
(403) Bos, J.; Fusetti, F.; Driessen, A. J. M.; Roelfes, G. *Angew. Chem. Int. Ed. Engl.* **2012**, *51*, 7472–7475.
(404) Madoori, P. K.; Agustiandari, H.; Driessen, A. J. M.; Thunnissen, A.-M. W. H. *EMBO J.* **2009**, *28*, 156–166.
(405) Agustiandari, H.; Lubelski, J.; van den Berg van Saparoea, H. B.; Kuipers, O. P.; Driessen, A. J. M. *J. Bacteriol.* **2008**, *190*, 759–763.
(406) Greenwood, N. N.; Earnshaw, A. *Chemistry of the Elements*; Elsevier Ltd.: Oxford, Burlington, 1997.
(407) Rubino, J. T.; Franz, K. J. *J. Inorg. Biochem.* **2012**, *107*, 129–143.
(408) Godden, J.; Turley, S.; Teller, D.; Adman, E.; Liu, M.; Payne, W.; LeGall, J. *Science (80-.).* **1991**, *253*, 438–442.
(409) Evans, J. P.; Blackburn, N. J.; Klinman, J. P. *Biochemistry* **2006**, *45*, 15419–15429.
(410) Pettingill, T. M.; Strange, R. W.; Blackburn, N. J. *J. Biol. Inorg. Chem.* **1991**, *266*, 16996–17003.
(411) Chufán, E. E.; Prigge, S. T.; Siebert, X.; Eipper, B. A.; Mains, R. E.; Amzel, L. M. *J. Am. Chem. Soc.* **2010**, *132*, 15565–15572.
(412) Kapoor, A.; Shandilya, M.; Kundu, S. *PLoS One* **2011**, *6*, e26509.
(413) *Copper Amine Oxidases: Structures, Catalytic Mechanisms, and Role in Pathophysiology*; Floris, G.; Mondovi, B., Eds.; CRC Press, **2009**.
(414) Bannister, J. V; Bannister, W. H.; Rotilio, G. *CRC Crit. Rev. Biochem.* **1987**, *22*, 111–180.
(415) Suzuki, S.; Kataoka, K.; Tamaguchi, K. *Acc. Chem. Res.* **2000**, *33*, 728–735.
(416) Averill, B. A. *Chem. Rev.* **1996**, *96*, 2951–2964.
(417) Prigge, S. T.; Eipper, B. A.; Mains, R. E.; Amzel, L. M. *Science* **2004**, *304*, 864–867.

(418) Rudzka, K.; Moreno, D. M.; Eipper, B.; Mains, R.; Estrin, D. A.; Amzel, L. M. *J. Biol. Inorg. Chem.* **2013**, *18*, 223–232.
(419) Ghadiri, M. R.; Fernholz, A. K. *J. Am. Chem. Soc.* **1990**, *112*, 9633–9635.
(420) Ghadiri, M. R.; Soares, C.; Choi, C. *J. Am. Chem. Soc.* **1992**, *114*, 4000–4002.
(421) Suzuki, K.; Hiroaki, H.; Kohda, D.; Tanaka, T. *Protein Eng. Des. Sel.* **1998**, *11*, 1051–1055.
(422) Suzuki, K.; Hiroaki, H.; Kohda, D.; Nakamura, H.; Tanaka, T. *J. Am. Chem. Soc.* **1998**, *120*, 13008–13015.
(423) Strange, R. W.; Dodd, F. E.; Abraham, Z. H. L.; Grossmann, J. G.; Brüser, T.; Eady, R. R.; Smith, B. E.; Hasnain, S. S. *Nat. Struct. Biol.* **1995**, *2*, 287–292.

Chapter II . Cu(II)/(I)(TRIW-H)$_3^{2+/+}$, a structural and functional model for copper nitrite reductase

Introduction

Many of the recent efforts in *de novo* protein design to achieve models of metalloenzymes have been reviewed in the previous chapter. It is important to realize that the design of redox-active centers is still a challenging topic and was particularly true in 2010 when this thesis research was begun. The difficulty arises because one needs to consider the structure and stability of the metal-peptide complexes in both oxidation levels involved in the redox process. The importance of metal ion cofactors in redox catalysis is underscored by the fact that many of the most employed transition metal ions in biological systems are redox active (*e.g.*, iron and copper). The fine-tuning of the first and second coordination spheres of copper centers provides a broad range of redox potentials for many important biological processes, such as electron transfer, activation and transport of dioxygen and oxidative conversion of other small molecules (Figure II-1).[1–11] The fields seeking to understand copper proteins include biochemistry, molecular biology, and medicine; meanwhile, synthesis and spectroscopic characterization of low-molecular-weight copper complexes are undertaken. Designing copper-peptides *de novo* stands at a unique position where it allows the incorporation of native amino acid ligands with well-controlled metal nucleation states in aqueous conditions.

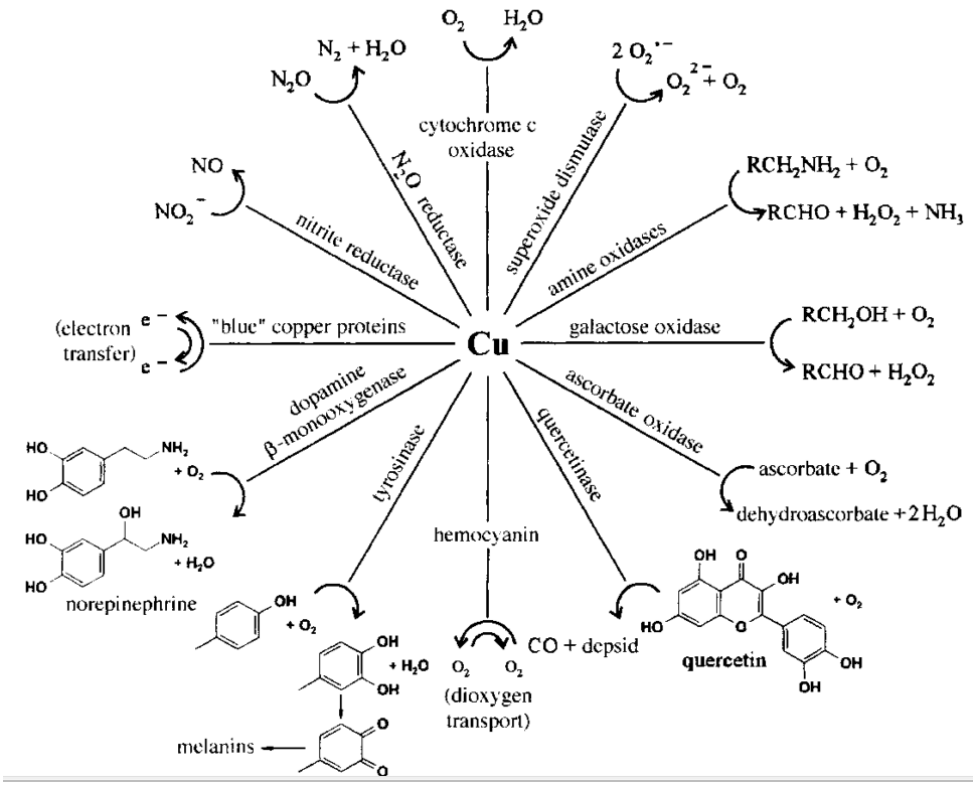

Figure II-1. The "biocopper dial" delineating the essential metabolic functions of copper proteins. Figure reproduced from Ref.[12] with permission.

Of particular interest to us is a type 2 copper (T2Cu) center where copper is bound to three histidines. This mononuclear $Cu(His)_3$ center serves various functions in native proteins. For example, peptidylglycine α-hydroxylating monooxygenase (PHM), which catalyzes the hydroxylation of glycine-extended peptide hormones, contains two types of copper centers (Figure II-2A), a Cu_H center where copper is coordinated to three histidines and a Cu_M center where copper is bound to two histidines and a methionine.[13] The role of the Cu_H center, in this case, is to shuttle an electron to the catalytic Cu_M site, which is involved in oxygen activation.[14–16] Copper nitrite reductase (CuNiR), which carries out the dissimilatory reduction of nitrite to nitric oxide, contains both a T1Cu and a T2Cu center (Figure II-2B). The T2Cu center $Cu(His)_3(OH_2)$ is the catalytic site while the type 1 copper center is the electron transfer site.[2,17–21] In addition, a $Cu(His)_3$ site is a dioxygen activation center in copper amine oxidase (CuAO) and quercetin 2, 3-dioxygenase (2, 3-QD) along with other cofactors.[6,22–29] (Figure II-2C and D)

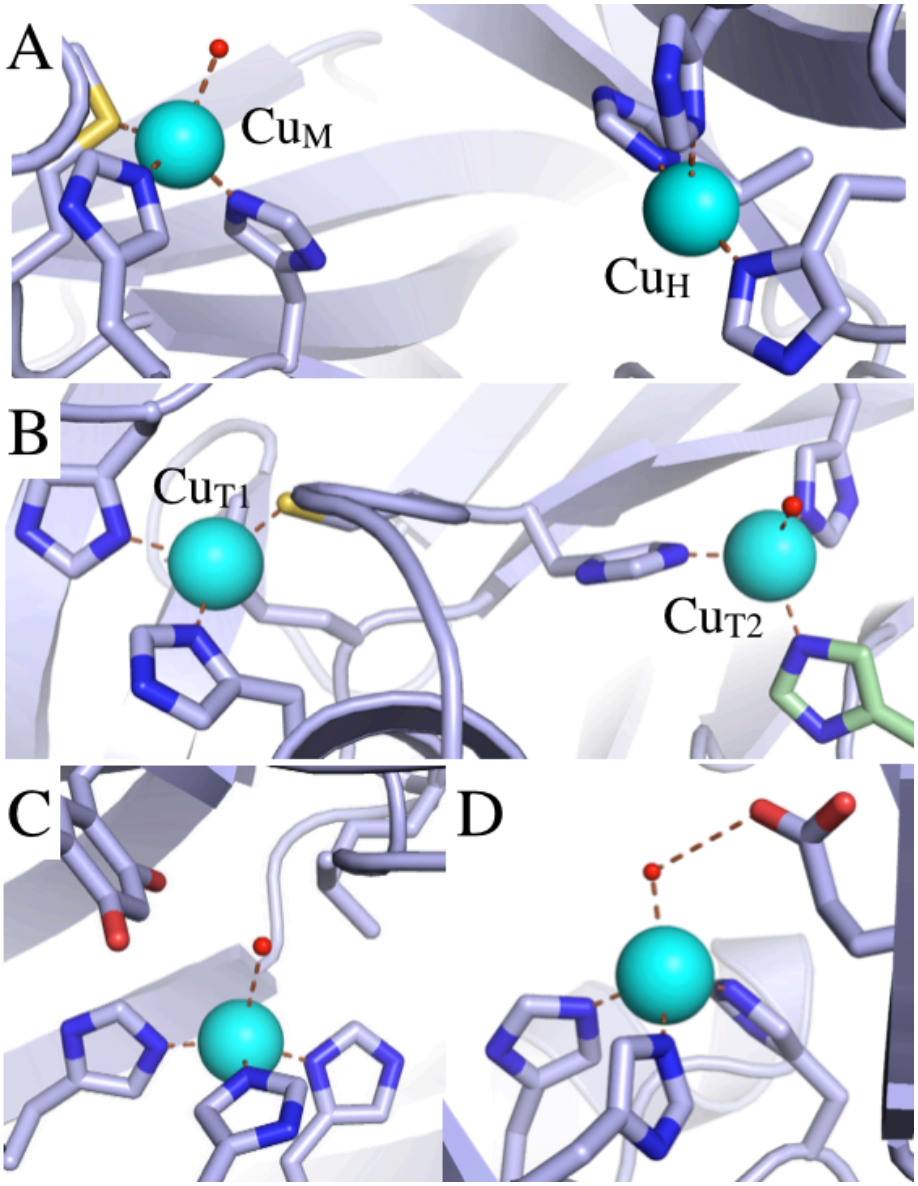

Figure II-2. Crystal structures of copper enzymes. (A) PHM (PDB code: 1PHM); (B) CuNiR (PDB code: 2DY2); (C) CuAO (PDB code: 2OOV); (D) 2, 3-QD (PDB code: 1JUH).

One of the fundamental questions in these systems is how the protein environment differentially selects one function over another, which relates to the importance of understanding the protein structure-function relationship. One approach to understanding this specific T2Cu center is to isolate it into a peptidic environment and investigate its properties. The first *de novo* designed three-stranded coiled coils with a T2Cu center $Cu(His)_3$ was reported in 1993 (see Chapter I).[30] This work represents the first example of

a stable T2Cu center in a *de novo* designed α-helical coiled coil scaffold, laying a solid foundation for the development of catalytic T2Cu centers. Tanaka and coworkers reported a series of IZ-derived α-helical coiled coil peptides that bind to copper, forming a Cu(II)$(His)_3(OH_2)$ center (see Chapter I).[31,32] These systems, however, are not fully characterized in either oxidation level nor have electron transfer or catalysis been explored.

We reported an X-ray crystal structure of Zn(II) bound to three-histidines in a related peptide $Hg_SZn_N(CSL9PenL23H)_3^+$ (Figure II-3).[33] Based on the similarities between Cu(I) and Zn(II), I thought that the TRIW-H system (Table II-1) was a good starting scaffold for copper binding. In this chapter, I will describe 1) the characterization of this system, including the Cu(II)/(I) coordination environment, binding stoichiometry, affinities, and protonation equilibria; 2) studies on small molecule binding by various spectroscopic techniques; 3) nitrite reductase activity studies of $Cu(II)/(I)(TRIW\text{-}H)_3^{2+/+}$. The majority of the work described in this chapter has been published in reference [34].

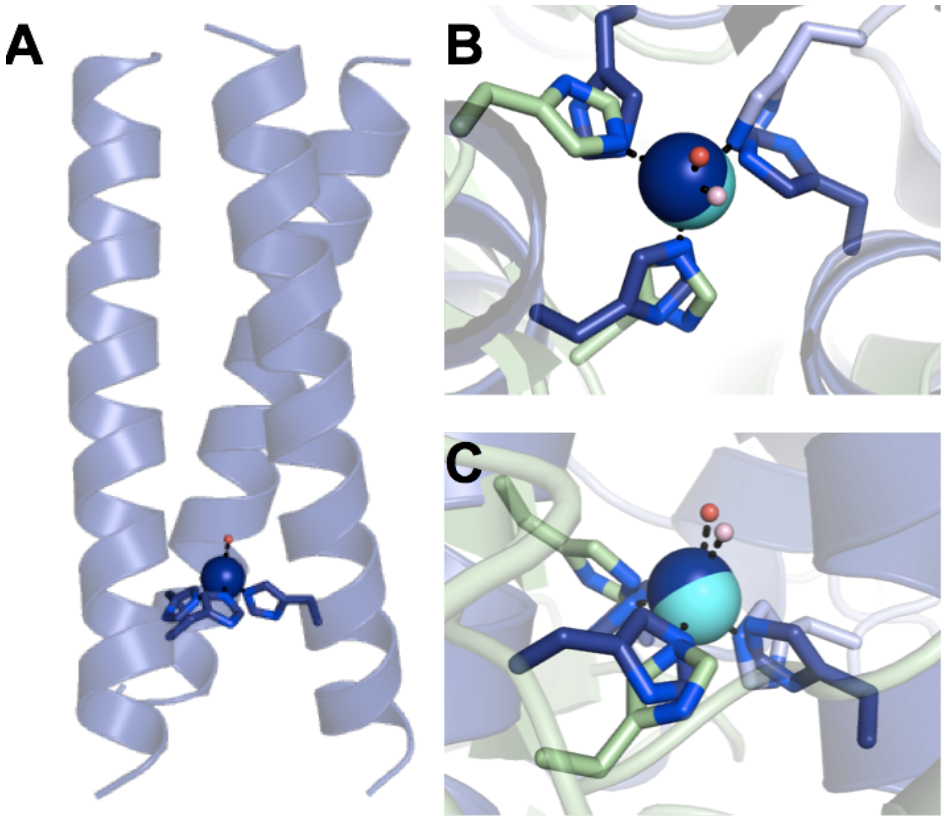

Figure II-3 (A) A model of $Cu(TRIW\text{-}H)_3^{+/2+}$ based on the crystal structure of $Hg(II)_SZn(II)_N(CSL9PenL23H)_3^+$ (PDB code: 3PBJ[33]); Overlay of the $Zn(II)(His)_3(OH_2)$

site in $Hg(II)_S Zn(II)_N(CSL9PenL23H)_3^+$ (protein ligands: dark blue; zinc: dark blue sphere; zinc-bound water: red) and the T2Cu center in copper NiR from *R. sphaeroides* (PDB code: 2DY2[21], protein ligands: light green and teal; copper: cyan sphere; copper-bound water: light pink). (B) Top view; (C) Side view. Figure adapted from Ref [34].

Table II-1. Peptide sequences used in Chapter II

Peptide[a]		*a b c d e f g*	*a b c d e f g*	*a b c d e f g*	*a b c d e f g*	
TRI	Ac-G	LKALEEK	LKALEEK	LKALEEK	LKALEEK	G-NH_2
TRIL2W	Ac-G	WKALEEK	LKALEEK	LKALEEK	LKALEEK	G-NH_2
TRIW-H	Ac-G	WKALEEK	LKALEEK	LKALEEK	HKALEEK	G-NH_2
TRI-H	Ac-G	LKALEEK	LKALEEK	LKALEEK	HKALEEK	G-NH_2
CSL9PenL23H	Ac-E	WEALEKK	P_n[b]AALESK	LQALEKK	HEALEHG	-NH_2

a. N- and C-termini are acetylated and amidated, respectively

b. P_n = Pen, penicillamine

Materials and Methods

General procedures

All samples containing Cu(I) were handled in an inert atmosphere box using oxygen-free buffer solution or water. A stock solution of $[Cu(CH_3CN)_4]BF_4$ was prepared in degassed acetonitrile (*ca.* 0.13 M). $[Cu(CH_3CN)_4]BF_4$ was purchased by Sigma Aldrich and dissolved in degassed acetonitrile to obtain a stock solution (the concentration of which was determined by spectrophotometric titrations using 2,9-dimethyl-1,10-phenantroline).[35] A $CuCl_2/(NO_3)_2$ solution was prepared by dissolving the corresponding Cu(II) salt in water (degassed water for activity studies) and the concentration was determined by inductively coupled plasma (ICP) optical emission spectroscopy located in room 2314 in the chemistry building.

Unless otherwise stated, all $Cu(I)(TRIW\text{-}H)_3^+$ and $Cu(II)(TRIW\text{-}H)_3^{2+}$ solutions were prepared by reacting apo-$(TRIW\text{-}H)_3$ in aqueous solution with stoichiometric amounts of $[Cu(CH_3CN)_4]BF_4$ acetonitrile solution or $CuCl_2$ aqueous solution. The pH values were registered using Hamilton glass microelectrodes. IR spectra were collected on a Perkin Elmer Spectrum BX FTIR spectrometer, using a NaCl window gas IR cell.

UV-visible spectra were collected on a Varian Cary 100 UV-Vis spectrophotometer with a thermostat, using matched quartz cells of 1 and 0.1 cm path length. EPR spectra were recorded on a Bruker EMX X-band EPR spectrometer with a liquid nitrogen cryostat. Fluorescence spectra were collected on a Fluoromax-2 fluorimeter.

Peptide Synthesis and Purification.

All peptides in this study (Table II-1) were synthesized on an Applied Biosystems 433A peptide synthesizer using standard protocols[36] and purified by reverse-phase HPLC on a C18 column at a flow rate of 10 mL/min or 20 mL/min using a linear gradient varying from 0.1% trifluoroacetic acid (TFA) in water to 0.1% TFA in 9:1 CH_3CN: H_2O as previously reported.[37] Peptides were collected over 27-29 min. Pure peptides were characterized by electrospray mass spectrometry located in room 3411. Concentrations of TRIW-H and TRIL2W were determined based on the tryptophan absorbance at 280 nm (ε = 5500 $M^{-1}cm^{-1}$).[38]

Circular Dichroism (CD) Spectroscopy.

CD spectra were collected on an AVIV 62DS spectrometer at 25 ºC using 1 cm quartz cuvettes. Guanidine hydrochloride (GuaHCl) titrations were carried out using an automated titrator with a Microlab 500 series syringe pump based on previously reported procedures.[39]

NMR spectroscopy.

^{1}H NMR spectra were collected on a Varian MR400 spectrometer using gastight tubes where appropriate. Samples of apo-(TRI-H)$_3$ and Cu(I)(TRI-H)$_3^+$ (2.4-5.7 mM) were prepared in deoxygenated 50 mM buffered D_2O (MES or HEPES at pH 6.0 or 7.4, respectively). The ^{1}H-NMR titration of Cu(I)(TRI-H)$_3^+$ (1.6 mM in 25 mM MES buffer in D_2O) was performed in the pH range 7.3-2.3. A 0.1 M NaOD solution in D_2O was used as the titrant. The pH values in D_2O were corrected using the formula reported in the literature.[40]

X-ray absorption spectroscopy.

A 1.0 mM Cu(I)(TRIW-H)$_3^+$ solution was made in the glovebox with 50 mM degassed MES buffer. 1 mM excess apo-3SCC was added to ensure the free Cu(I) concentration was minimum (< 0.01 %). The samples were mixed with 50 % glycerol as a glassing agent and loaded into a sample cell and frozen in liquid nitrogen.

Measurements were carried out at Stanford Synchrotron Radiation Lightsource (SSRL) beamline 7-3 with a Si(220) double-crystal monochromator and a flat Rh-coated harmonic rejection mirror. Samples were maintained below 10K with an Oxford Instruments liquid helium cryostat. Data were measured as fluorescence excitation spectra using a 30-element Ge detector array normalized to incident intensity measured with a N_2 filled ion chamber. Data were measured with steps of 0.25 eV in the XANES region (1 sec. integration time) and 0.05 Å^{-1} in the EXAFS region to k = 13.5 Å^{-1} (1-20 sec. integration, k^3 weighted). Energies were calibrated by assigning the lowest energy inflection point of a copper metal foil as 8980.3 eV. An initial E_0 value of 9000 eV was used to convert data to k-space, and the background was removed using a 3-region cubic spline. EXAFS data analyzed using EXAFSPAK[41] and FEFF 9.0.[42] A more detailed description of the application of XAS on metalloproteins is in Chapter V.

EXAFS data fitting procedure.

Single- and multiple scattering fitting of EXAFS data were performed using EXAFSPAK[41] with *ab initio* amplitude and phase parameters calculated using FEFF 9.0.[42] XANES data were normalized using EXAFSPAK. An initial model of Cu(I)-imidazole coordination was built based on the averaged bond distances reported for the crystal structures of synthetic molecules containing Cu(I)-imidazole constituent.

Cu(II)(TRIW-H)$_3^{2+}$ deprotonation equilibria.

The visible spectra of Cu(II)(TRIW-H)$_3^{2+}$ (0.26 mM) at different pH conditions were collected with an un-buffered aqueous solution by adjusting the pH using small aliquots of concentrated KOH.

Specifically, an n-proton protonation equilibrium can be written as:

$$EH_n \rightleftharpoons^{K_a^n} nH^+ + E^{n-}$$

$$K_a^{\,n} = \frac{[H^+]^n[E^{n-}]}{[EH_n]},$$

which leads to the ratio of concentration $\frac{[EH_n]}{[E^{n-}]} = 10^{n(pK_{a1}-pH)}$.

The total absorbance at a particular wavelength can be written as

$$A_{total} = \varepsilon_{total} \bullet ([E^{n-}] + [EH_n]) = \varepsilon_{E^{n-}} \bullet [E^{n-}] + \varepsilon_{EH_n} \bullet [EH_n]$$

so $$\varepsilon_{total} = \frac{\varepsilon_{E^{n-}} \bullet [E^{n-}] + \varepsilon_{EH_n} \bullet [EH_n]}{[E^{n-}] + [EH_n]} = \frac{\varepsilon_{E^{n-}} + \varepsilon_{EH_n} \bullet 10^{n(pK_{a1}-pH)}}{1 + 10^{n(pK_{a1}-pH)}}$$

Equation II-1

where $\varepsilon_{E^{n-}}$ and ε_{EH_n} stand for the extinction coefficients of the individual species in different protonation states.

Binding constants determination.

The affinity of the $(His)_3$ site in the 3SCC for Cu(I) was determined using a competitive chelation assay. We chose the well-defined Cu(I) chelator bathocuproine disulfonate (BCS^{2-}), which binds Cu(I) into a colored species $[Cu(BCS)_2]^{3-}$ (λ_{max} = 483 nm; $\varepsilon^{483\,nm}$ = 13300 M^{-1} cm^{-1}; log β_2 = 19.8).[43] The concentration of peptide stock solution was determined from Trp absorbance at 280 nm.[44] A solution of 40 μM Cu(I) and 80 μM $(TRIW\text{-}H)_3$ was prepared in an inert atmosphere box in an aqueous 50 mM buffer solution (MES pH 5.9, HEPES pH 7.4) and titrated with a 5.00 mM bathocuproine disulfonate solution. The formation of $[Cu(BCS)_2]^{3-}$ was monitored by the increase of absorbance at 483 nm with UV-visible spectroscopy. All titrant additions were carried out in the glovebox. Specfit32 was used to fit the spectrophotometric data taking into account the protonation equilibrium of BCS^{2-} at pH 5.9.[45]

A 500 – 800 nM solution of $(TRIW\text{-}H)_3$ in 50 mM buffer (MES pH 5.9, HEPES pH 7.4) was titrated with a 486 μM $CuCl_2$ solution, which was diluted from a 0.0486 M $CuCl_2$ solution. The concentration of the $CuCl_2$ stock solution was determined by ICP.

Upon each addition, the solution was stirred for 10 min to reach equilibrium and fluorescence spectra were recorded. The apo-(TRIW-H)$_3$ was titrated with $CuCl_2$ solution. The dissociation constants were obtained by treating the fluorescence spectra with Specfit32,[45] taking into account the formation of the Cu(II)/HEPES 1:1 complex (log β = 3.22).[46]

Reduction potentials.

While reduction potentials for metalloproteins and small molecules are often determined by direct electrochemical methods, one may extract the same information by determining the binding affinities of the metals in both oxidation states to the proteins and applying the Nernst Equation. This approach has the added benefit that it allows one to track directly the behavior of interest (*e.g.*, reaction rates) not only against the reduction potential, but also to see if correlations exist associated with a specific oxidation level. The reduction potentials of Cu(II)/(I)(TRIW-H)$_3^{2+/+}$ were calculated using the methodology shown in Scheme II-1 and Equation II-2, where $E^o_{(Cu,\,aq)}$ = 0.159 V *vs.* NHE was utilized.[34,47]

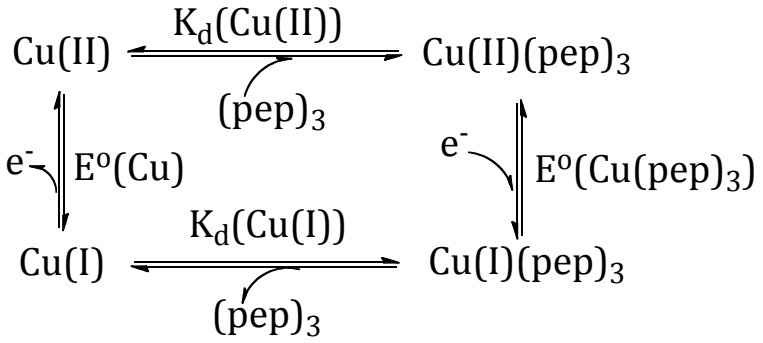

Scheme II-1

$$E^{o}_{(Cu(pep)_3)} = E^{o}_{(Cu,aq)} - \frac{2.303RT}{nF}\log\frac{K_{d(Cu(I)(pep)_3)}}{K_{d(Cu(II)(pep)_3)}}$$

Equation II-2

EPR spectroscopy.

Three sets of EPR spectra were collected to investigate 1) the Cu(II) coordination environment at various pH conditions; 2) how nitrite binding affects the Cu(II) center; 3) how azide binding affects the Cu(II) center. All EPR samples contain 1 mM Cu(II)(TRIW-H)$_3^{2+}$ and 1mM apo-(TRIW-H)$_3$ to ensure that 99% Cu(II) is coordinated to the peptide. 30-50% glycerol was added to the aqueous solution as a glassing agent. The EPR spectra were collected at 77 K. For experiment 1), the pH condition was adjusted by adding small aliquots of concentrated KOH. For experiment 2), small aliquots of 0.1 M $NaNO_2$ was added to a buffered solution of 1mM Cu(II)(TRIW-H)$_3^{2+}$ and 0.5 mM apo-(TRIW-H)$_3$ at pH 5.8 (50 mM MES). The EPR spectra were recorded and the binding of NO_2^- to Cu(II) was tracked by the change of A_{II}. A similar titration was carried out for azide.

Preparation of Cu(I)(CO)(TRIW-H)$_3^+$ IR sample.

A solution of 1 mM Cu(I), 1.5 mM (TRIW-H)$_3$ in 50 mM buffer (HEPES or MES) was made in an inert atmosphere box in 100% D_2O. Carbon monoxide (>99%) was bubbled through the solution for 20 min. *Caution: CO is highly poisonous. Make sure that a functional CO detector is installed close to the hood in which the CO purging is carried out*. The solution was then moved to the glovebox and transferred into an IR cell.

NiR activity.

Reduction of Cu(II)(TRI-H)$_3^{2+}$ by ascorbate. The *in situ* reduction of Cu(II)(TRI-H)$_3^{2+}$ into Cu(I)(TRI-H)$_3^+$ was monitored by addition of sodium ascorbate (0.565 μmol, 1 eq.) to a 0.34 mM Cu(II)(TRI-H)$_3^{2+}$ solution in deoxygenated 200 mM MES buffer (pH 6.0) obtained in 3 mL in a rubber sealed quartz cuvette. The spectra were collected prior and after ascorbate addition.

NO production. $NaNO_2$ stock solutions (~0.5 mM) were prepared in 200 mM aqueous MES pH 6.0, and added to the copper/peptide solution using a gas tight syringe. A 0.01 M $[Fe(EDTA)]^{2-}$ solution was prepared from $FeSO_4 \cdot 7H_2O$ and H_2EDTA in deoxygenated 1 M citrate aqueous buffer at pH 5.0. The latter solution (3 mL) was put in

a rubber sealed quartz cuvette, the spectrum registered, and then the cuvette connected to the reaction vial through a steel canula and kept in an ice bath at 0 °C throughout the entire experiment. The reaction in the first solution was initiated by the addition of 1.13×10^{-3} mmol of $NaNO_2$ (1 eq.) to the copper/peptide solution, using a gas tight syringe. The NO produced was quantified from the difference spectrum ($\varepsilon_{432\ nm}$ = 780 M^{-1} cm^{-1} for $[Fe(NO)(EDTA)]^{2-}$) [48]

The control reaction was performed using an aqueous solution of $[Cu(CH_3CN)_4]BF_4$ under the same conditions described above. The production of NO starting from Cu(II)(TRI-H)$_3^{2+}$ reduced *in situ* with ascorbate was performed using the same condition described above (200 mM MES pH 6.0). $CuCl_2 \cdot 2H_2O$ (1.13 mmol, *ca.* 0.07 M in water) was added to the peptide, followed by sodium ascorbate (0.565 mmol). All solutions were prepared in an inert atmosphere box.

Ascorbate oxidation in the presence of nitrite. The turnover number (expressed as equivalents of electrons *per* equivalent of copper ions) for the oxidation reaction of ascorbate by nitrite in presence of Cu(II)(TRI-H)$_3^{2+}$ as the catalyst was determined by UV spectroscopy. In this assay, the oxidation of ascorbate as sacrificial reductant was monitored spectrophotometrically by observing the decrease of its absorption band at 251 nm (ε = 8250 M cm^{-1}).[49] Since we carried out experiments at different pH conditions, we chose 251 nm, the isosbestic point of protonated and deprotonated forms, to calculate the consumption of ascorbate. A 2.4 mL solution containing (TRI-H)$_3$ (0.30 mM) and sodium nitrite (31.6 mM) was prepared in the glove box using a degassed 200 mM MES solution in water. The pH was corrected to the desired value (5.8 or 5.9) by addition of small aliquots of a concentrated KOH solution in degassed water. Aliquots (ca. 380 μL) of this solution were mixed with 20 μL $CuCl_2$ solution (*ca.* 3.8 mM) to obtain samples containing Cu(II) (0.180 mM), (TRI-H)$_3$ (0.270 mM) and sodium nitrite (30 mM). The reaction of oxidation of ascorbate was triggered in the glove box by injecting 20 μL freshly prepared sodium ascorbate solution in degassed water (21 mM) to obtain a final ascorbate concentration of *ca.* 1.15 mM (corresponding to a 6.4 fold excess with respect to Cu(II)). The solution was transferred into a sealed 0.1 cm path length cuvette, and the UV spectra (240-290 nm) were collected every 5 min for 3-5 h total reaction time. The control samples containing apo-peptide (90 μM) in place of the Cu(II)-peptide complex

were prepared as reported above. This concentration corresponds to the excess apo-peptide in the samples containing Cu(II)(TRI-H)$_3^{2+}$. The oxidation reaction in the presence/absence of copper(II) was monitored in triplicates. The turnover number (equivalents of electrons *per* mole of copper) was calculated as two times the average moles of ascorbate consumed in the sample containing Cu(II)(TRI-H)$_3^{2+}$ subtracted by the moles of ascorbate consumed in the sample containing apo-(TRI-H)$_3$, divided by the moles of copper(II). Additional control samples containing sodium nitrite (30 mM) in the presence/absence of copper chloride (0.21 μM) were prepared in a similar way as described above, and their spectra (240-290 nm) were collected in triplicate every 5 min for 60 min. A 0.21 μM concentration of Cu(II) is *ca*. 1.5 times the calculated amount of free Cu(II) at pH 5.9 in a sample containing the fully oxidized form of the peptide and a 50% excess of apo-peptide, based on the determined stability constants. The control of the stability of ascorbate in the absence of nitrite was carried out by preparing samples containing Cu(II) (0.180 mM), (TRI-H)$_3$ (0.270 mM) and sodium ascorbate (1.15 mM).

The dependence of the reaction rate on the concentration of Cu(II)(TRI-H)$_3^{2+}$ was examined in the 0.171 – 0.513 mM metallopeptide concentration range. All samples contain a 0.5 eq. excess of apo-peptide. Both samples and controls were prepared as described above, all containing 30 mM nitrite and *ca*. 1.15 mM ascorbate. The control samples contain 0.085 – 0.257 mM apo-peptide corresponding to the excess apo-peptide in the corresponding metallopeptide samples. The spectra in the 240-290 nm range were collected every 3 min in triplicates. The pH dependence of the rate of oxidation of ascorbate in the presence of Cu(II)(TRI-H)$_3^{2+}$ was investigated in from pH 5.3 to 6.5. The samples were prepared as described above, containing 0.180 mM $CuCl_2$ and 0.270 mM (TRI-H)$_3$ (corresponding to a 0.180 mM Cu(II)(TRI-H)$_3^{2+}$ and a 0.090 mM excess apo-peptide), 30 mM sodium nitrite and *ca*. 1.15 mM sodium ascorbate. All samples were prepared in 200 mM MES buffer solution in water and the pH was checked before the addition of the freshly prepared sodium ascorbate solution to initiate the reaction. The control samples all contain 0.090 mM apo-peptide, 30 mM nitrite and *ca*. 1.15 mM ascorbate.

Detection of N_2O. A reaction mixture of 0.33 mM Cu(II)(TRIW-H)$_3$ with 0.17 mM *apo*-(TRIW-H)$_3$ and 0.1 M $NaNO_2$ was prepared in the glovebox with 50 mM

phosphate buffer at pH 5.8 in a schlenk flask. The reaction was initiated by injecting a stock solution of sodium ascorbate, pre-adjusted to pH 5.8. The final concentration of sodium ascorbate in the solution was 0.017 M. The control reaction was set up with 0.17 mM apo-$(TRIW\text{-}H)_3$ and all the other conditions were kept the same. The gas IR cell (10 cm, NaCl window) was evacuated using vacuum before connecting to the reaction flask with a setup shown as Figure II-4. The IR spectra were collected on a Perkin-Elmer FT-IR Spectrum BX instrument. Henry's Law was used to calculate the distribution of the putative production of N_2O in aqueous and gaseous phase. Henry's constant for N_2O/water at room temperature was calculated based on literature values[50]. A calibration curve was made by diluting a series of N_2O saturated 50 mM phosphate buffer solution into the same reaction setup with the same headspace volume. The system was equilibrated for 1 h before connecting to the gas IR cell and FTIR data were collected. The absorption peaks at 2234.8 and 2212.9 cm^{-1} were integrated to calculate the N_2O production.

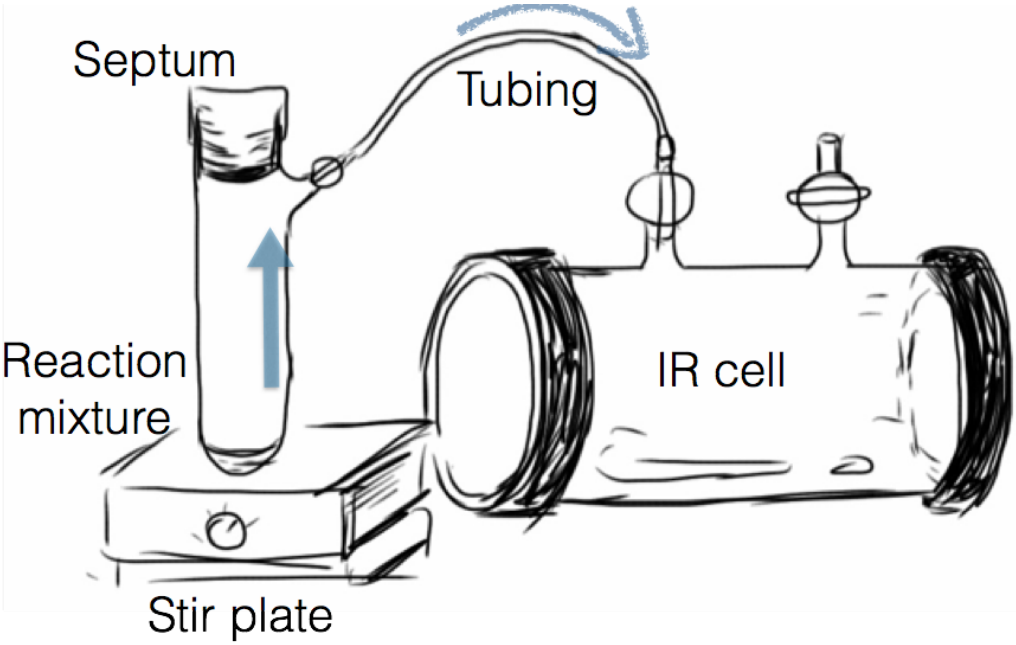

Figure II-4. Experimental setup for N_2O detection using FTIR spectroscopy.

Results

Characterization of apo-peptide

Guanidinium chloride denaturation titrations monitored by Circular Dichroism spectroscopy

A CD spectrum was collected for a solution containing 20 μM TRIW-H monomer, 10 mM potassium phosphate at pH 7.0 (Figure II-5). The double well at 208 and 222 nm signifies α-helical coiled coils. The molar ellipticity of TRIW-H at 222 nm is ~-30,000 deg•cm^2/dmol. Guanidinium chloride (GuaHCl) denaturation titration was carried out to evaluate the influence of chemical denaturant on the α-helical character of the peptide. This data cannot be quantitatively fit to a two-state model because the titration curve did not level off at zero concentration of denaturant.

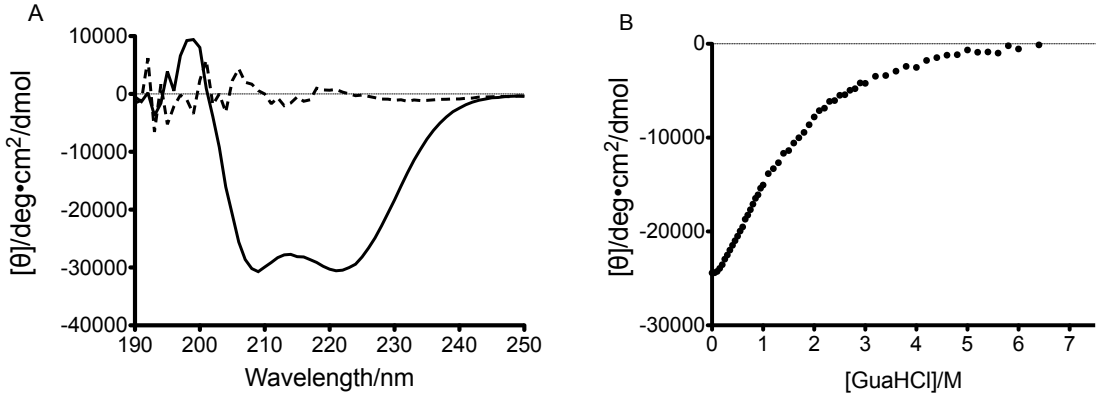

Figure II-5 (A) CD spectra of apo-TRIW-H in phosphate buffer (10 mM) at pH 7.0 (solid line) and apo-TRIW-H after 6.5 M GuaHCl was added (dashed line). (B) GuaHCl denaturation of apo-TRIW-H monitored by the molar ellipticity at 222 nm.

Monitoring the transition of 2SCC to 3SCC by ^{1}H NMR (completed by Dr. Matteo Tegoni)

^{1}H NMR was used to monitor the transition of 2SCC to 3SCC for TRI-H. Specifically, we tracked the chemical shift of the unexchangeable protons on the imidazoles (Figure II-6). As the pH was increased from 3.52 to 9.71, we observed the transition of two major resonances from (7.37, 8.74 ppm) to (6.75, 7.48 ppm). The two resonances at up and down field correspond to H_δ and H_ε, respectively. This transition can be visualized better if we plot the pH against the H_δ and H_ε resonances (Figure II-7). In addition, by integrating the signals representing 2SCC and 3SCC and taking the ratios

of the two types of signals, we were able to extract a pK_a of 6.0(3), which corresponds to a 1.38(5) deprotonation process. This pK_a, however, could be a combination of two deprotonation processes: the deprotonation of glutamic acid into glutamate (pK_a ~ 3.9), and the deprotonation of imidazolium into imidazole (pK_a ~ 6). Both processes will lead to the change of the chemical environment of H_δ and H_ε. It is worth noting that when the apo-peptide forms 100% 3SCC, there are only two resonances, indicating that the imidazoles are three-fold symmetric.

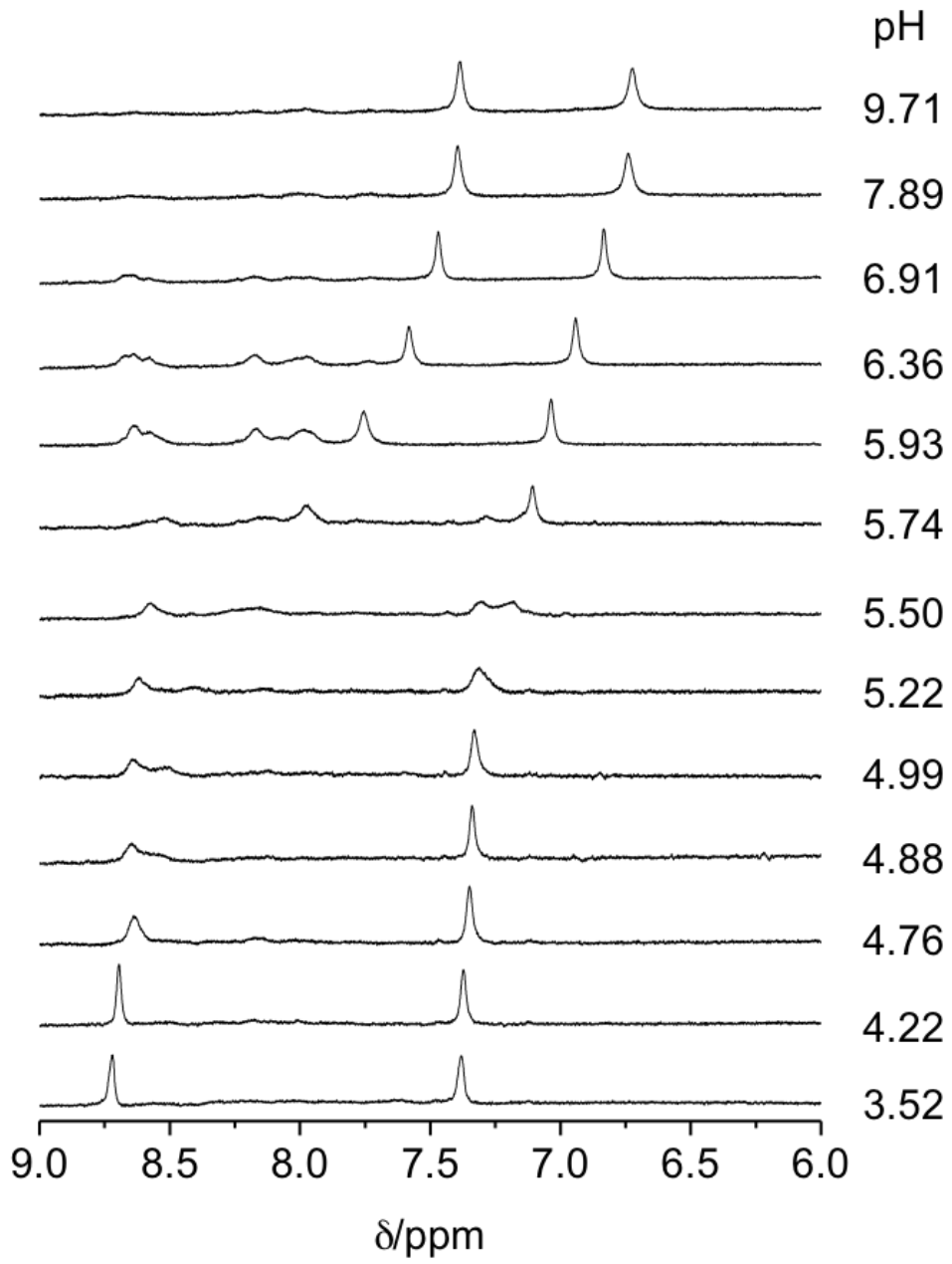

Figure II-6. ^{1}H NMR of apo-$(TRI\text{-}H)_3$ under different pH conditions.

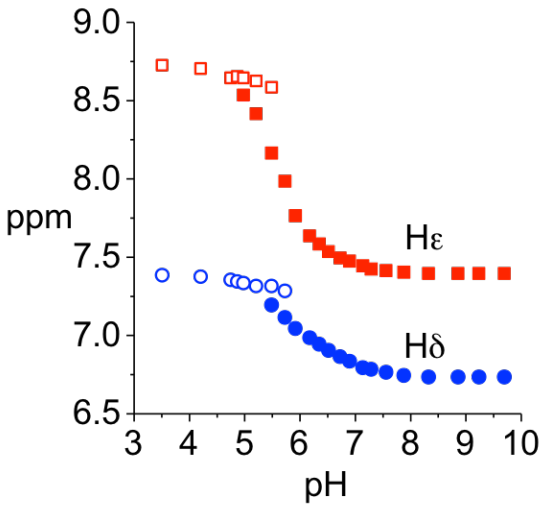

Figure II-7. Transition from 2SCC to 3SCC monitored by the chemical shift of H_ε and H_δ.

Characterization of Cu(I)(TRIW-H)$_3^+$ and Cu(I)(TRI-H)$_3^+$

Coordination environment

The coordination of Cu(I) in Cu(I)(TRIW-H)$_3^+$ complex was investigated by XAS. The X-ray absorption spectroscopy edge region of Cu(I) complexes frequently shows a resolved transition at ~8,984 eV attributed to a 1s→4p transition; this is very intense for two- coordinate Cu(I), moderately intense for three-coordinate Cu(I), and almost undetectable for four-coordinate Cu(I).[51] The X-ray absorption near-edge structure (XANES) data for Cu(I)(TRIW-H)$_3^+$ (Figure II-8A) show a resolved 1s→4p transition at ~8,984 eV, characteristic of three-coordinate complexes.[51] The spectra for Cu(I)(TRIW-H)$_3^+$ at pH 5.9 and 7.4 are indistinguishable, demonstrating that the Cu(I) structure is independent of the pH condition over this range. The extended X-ray absorption fine structure (EXAFS) spectra for Cu(I)(TRIW-H)$_3^+$ (Figure II-8B and C) show peaks for both nearest-neighbor scattering and outer-shell scattering characteristic of imidazole ligation. The nearest-neighbor scattering has an amplitude consistent with three low atomic weight ligands, with an apparent Cu-(N/O) distance of 1.93 Å, as expected for a three-coordinate Cu(I) site. The nearest neighbor and outer-shell scatterings are well modeled by using three imidazoles modeled as rigid groups with only a variable Cu-N distance and Debye-Waller factors proportional to those calculated *ab initio*.[52] Inclusion

of an additional shell to model a putative water ligand did not improve the fit. This, together with the XANES evidence for a three-coordinate Cu(I) and the relatively short Cu-N distance, all point to a Cu(I) that is ligated only to the three histidine ligands. The fitted Debye-Waller factor for the Cu-N shell is large (~9 × 10^{-3} $Å^2$), suggesting that the site is distorted, as is often seen for three-coordinate Cu(I) sites. Assuming that the dynamic Debye-Waller factor is ~4 × 10^{-3} $Å^2$, as seen in model compounds, the observed value implies a spread in distances of ~0.1–0.15 Å (Table II-2).

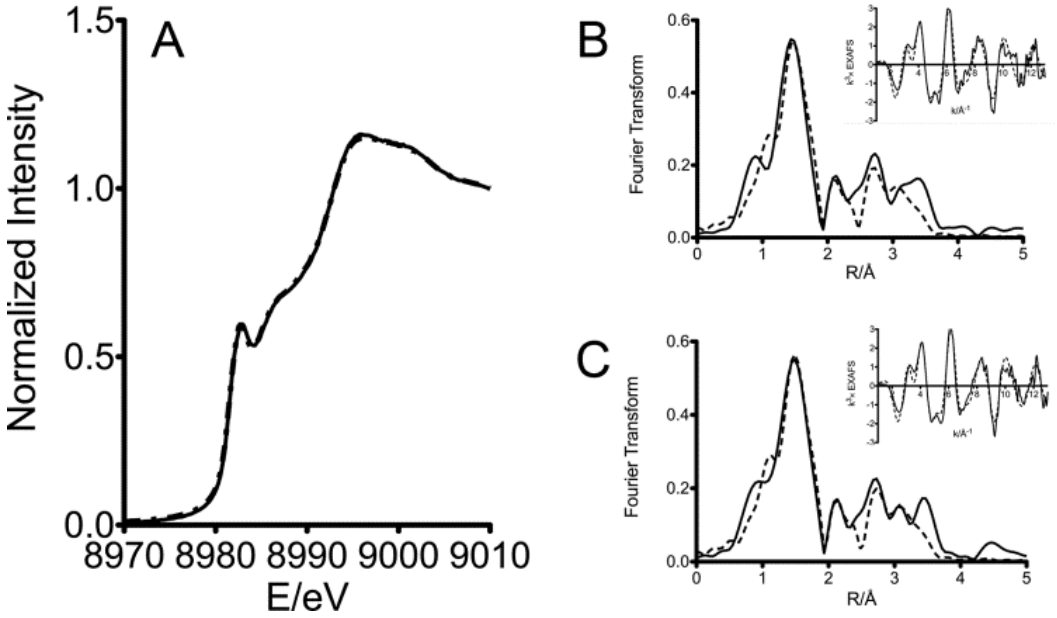

Figure II-8 (A) XANES of Cu(I)(TRIW-H)$_3^+$ at pH 5.9 (dashed line) and pH 7.4 (solid line). (B) Fourier transform of EXAFS of Cu(I)(TRIW-H)$_3^+$ at pH 5.9. Insert: EXAFS (solid line) and simulation (dashed line). (C) Fourier transform of EXAFS of Cu(I)(TRIW-H)$_3^+$ at pH 7.4. Insert: EXAFS (solid line) and simulation (dashed line).

Table II-2. EXAFS fitting parameters

First shell			Outer shells		
Shell (X)	R(Å)	σ^2(Å^2)	Shell (Y)	R(Å)	σ^2(Å^2)
$Cu(I)(TRIW\text{-}H)_3^+$ pH 5.9	$F = 0.408 \times 10^2$	$E_0 = -10.88$			
3 imid	1.93	0.009	$3Cu\text{-}C^{(1)}$(imid)	2.92	0.013
			$3Cu\text{-}C^{(2)}$(imid)	2.95	0.013
			$3Cu\text{-}N^{(2)}$(imid)	4.06	0.018
			$3Cu\text{-}C^{(3)}$(imid)	4.07	0.018
$Cu(I)(TRIW\text{-}H)_3^+$ pH 5.9	$F = 0.408 \times 10^2$	$E_0 = -12.20$			
3 imid	1.93	0.009	$3Cu\text{-}C^{(1)}$(imid)	2.91	0.014
1 water	1.81	0.037	$3Cu\text{-}C^{(2)}$(imid)	2.94	0.014
			$3Cu\text{-}N^{(2)}$(imid)	4.05	0.019
			$3Cu\text{-}C^{(3)}$(imid)	4.06	0.019
$Cu(I)(TRIW\text{-}H)_3^+$ pH 7.4	$F = 0.349 \times 10^2$	$E_0 = -10.62$			
3 imid	1.93	0.009	$3Cu\text{-}C^{(1)}$(imid)	2.92	0.014
			$3Cu\text{-}C^{(2)}$(imid)	2.96	0.014
			$3Cu\text{-}N^{(2)}$(imid)	4.07	0.019
			$3Cu\text{-}C^{(3)}$(imid)	4.08	0.019

Cu(I) affinities to (TRIW-H)$_3$

The affinity of Cu(I) to (TRIW-H)$_3$ was determined by competitive chelation assay using BCS^{2-} as a chelator (Figure II-9). Titrations were carried out in triplicate. Cu(I) has a high affinity to (TRIW-H)$_3$ at both pH 5.9 (K_d = 3.1(7) pM) and 7.4 (K_d = 0.20(6) pM).

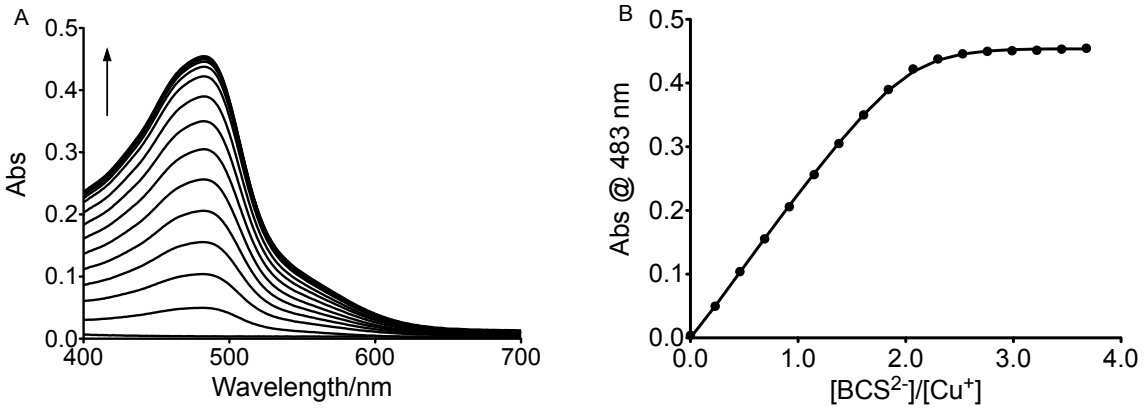

Figure II-9 (A) Cu(I)(TRIW-H)$_3^+$ solution titrated with a 5.00 mM BCS^{2-} solution. The increased absorbance indicates the formation of Cu(BCS)$_2^{3-}$ complex. (B) Observed absorbance values at 483 nm (dots) and the calculated titration curve (solid line).

Carbon monoxide binding

Since I aimed to design a model for CuNiR, it is necessary to evaluate whether the copper center is capable of small molecule binding. The stretching frequency ν_{CO} is 2064 cm^{-1} ($\omega_{1/2}$ = 14 cm^{-1}) when CO is bound to Cu(I)(TRIW-H)$_3^+$ at pH 7.4 (experiment completed by Dr. Matteo Tegoni). While this stretching frequency provides definitive information of the presence of a four-coordinate Cu(I)(CO)(His)$_3$ center, it does not necessarily prove that in the absence of CO, Cu(I) is three-coordinate (See Chapter IV).

XANES of the Cu(I)(CO)(TRIW-H)$_3^+$ corroborated the observation from FTIR. The pre-edge feature of Cu(I) decreased, suggesting the formation of a four-coordinate Cu(I) species (Figure II-10). Since it is relatively challenging to quantify the percentage of Cu(I) that is bound to CO, the red spectrum from Figure II-10 might contain mixed species of three-coordinate Cu(I)(TRIW-H)$_3^+$ and four-coordinate Cu(I)(CO)(TRIW-H)$_3^+$. Nonetheless, the decrease of the pre-edge peak indicates the formation of a higher coordination number Cu(I) species in the sample, pointing to a CO-bound Cu(I)(His)$_3$ site.

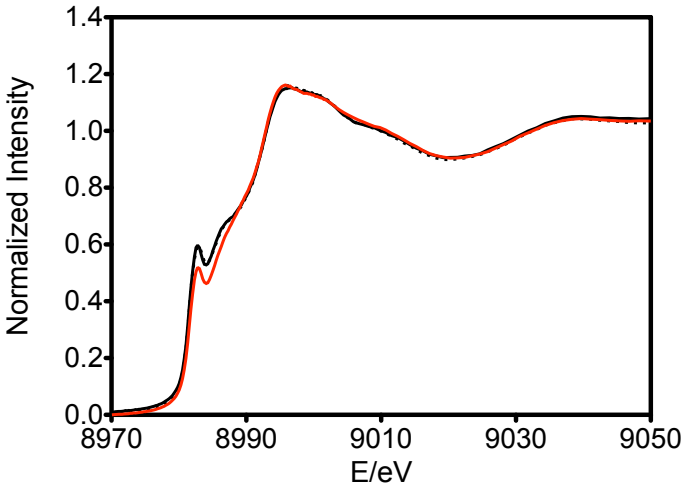

Figure II-10. XANES of Cu(I)(TRIW-H)$_3^+$ at pH 7.4 (solid black line) and pH 5.8 (dashed black line), compared to Cu(I)(CO)(TRIW-H)$_3^+$ at pH 7.4 (solid red line).

Characterization of Cu(II)(TRIW-H)$_3^{2+}$ and Cu(II)(TRI-H)$_3^{2+}$

Binding stoichiometry

Cu(II) binding to (TRIW-H)$_3$ was examined by UV-vis spectroscopy. Small aliquots of 0.05 M $CuCl_2$ (2 μL/aliquot) were added into a buffered solution of (TRIW-H)$_3$ (pH 7.4 HEPES) and observed the increase of Cu(II) d-d band absorbance (Figure II-11A). The Cu(II)(TRIW-H)$_3^{2+}$ complex exhibits a broad band centered at 643 nm. The change of slopes below and above 1 eq. of Cu(II) indicates the 1:1 binding of Cu(II) to (TRIW-H)$_3$ (Figure II-11B). The molar extinction coefficients of Cu(II)(TRI-H)$_3^{2+}$ and Cu(II)(TRIW-H)$_3^{2+}$ are both 135(3) M^{-1} cm^{-1} in the pH range of 5.7–7.5.

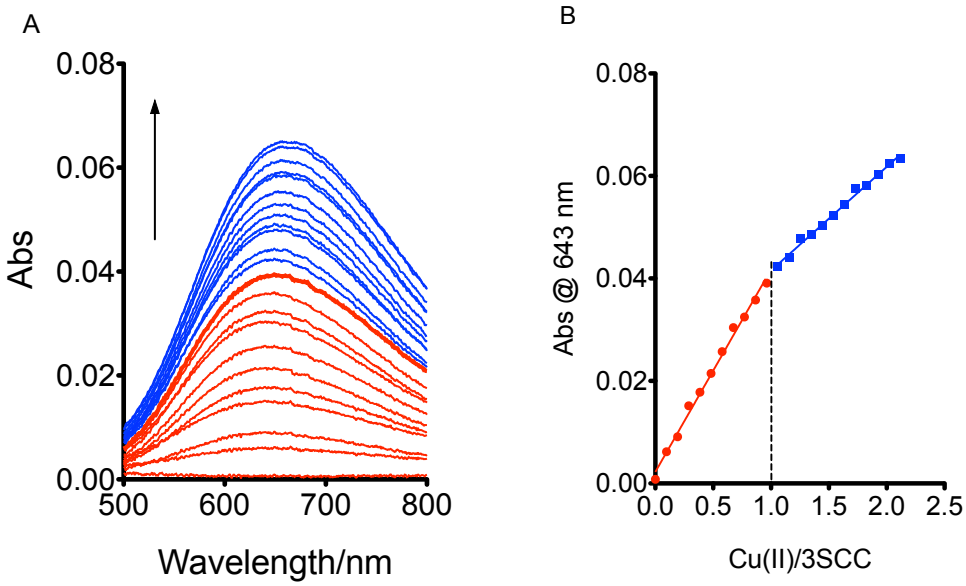

Figure II-11. (A) Titration spectra of Cu(II) into a solution of $(TRIW\text{-}H)_3$ at pH 7.4. (B) A titration curve showing the binding stoichiometry of Cu(II) to 3SCC. Red spectra and dots represent Cu(II) below 1 eq. (with respect to 3SCC); blue spectra and dots represent Cu(II) above 1 eq.

Coordination environment

The *d-d* band absorption maxima are consistent, for both $Cu(II)(TRI\text{-}H)_3^{2+}$ and $Cu(II)(TRIW\text{-}H)_3^{2+}$, with a $Cu(II)(His)_3$ site that might contain either one or two exogenous water ligands (predicted λ_{max} of 634 ± 11 nm).[53] Since a λ_{max} of ~690 nm is expected for a $Cu(II)(His)_2(OH_2)_2$ site,[53] these observations support the existence of a $Cu(II)(His)_3(OH_2)_{1-2}$ site in pH 5.8–7.4.

The EPR spectra of both $Cu(II)(TRI\text{-}H)_3^{2+}$ and $Cu(II)(TRIW\text{-}H)_3^{2+}$ have features typical of T2Cu centers, and for the latter, the spectra do not change significantly in the pH range 5.19–7.80 (Figure II-12, Figure II-13), which is consistent with the invariance of the λ_{max} and ε from the visible spectra. The observed g values (g_{II} = 2.27) and hyperfine coupling constants (A_{II} = 186 G and 188 G for the two peptides, respectively) are somewhat larger than those observed for NiR in which a $Cu(His)_3(OH_2)$ site is present.[54,55] These parameters are more consistent with a five-coordinate structure $Cu(His)_3(OH_2)_2$,[56–58] with a distorted square pyramidal geometry containing three quasi-in-plane imidazoles, as consistent with the observed d–d transition at 643 nm.

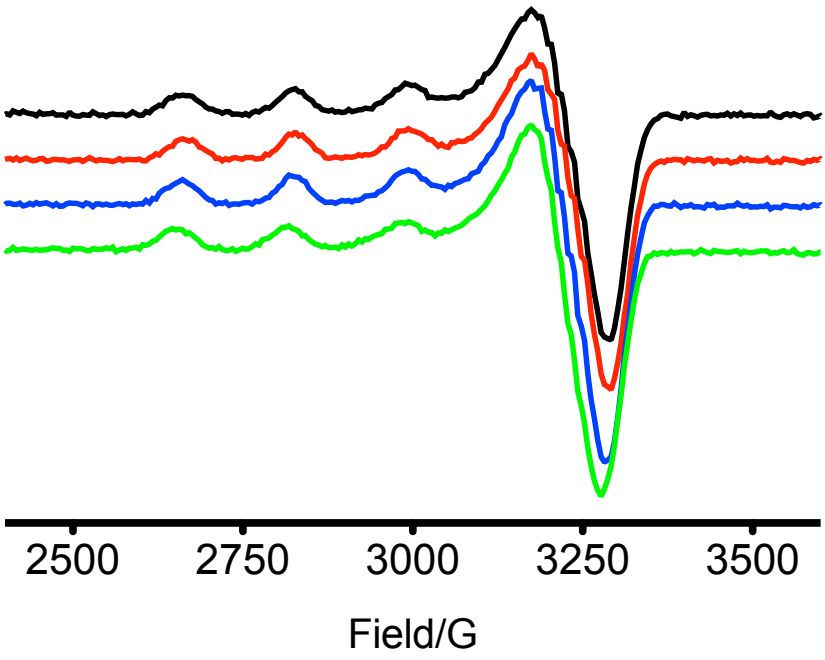

Figure II-12. EPR spectra of Cu(II)(TRIW-H)$_3^{2+}$ at pH 5.19 (green), 5.87 (blue), 6.75 (red), and 7.80 (black).

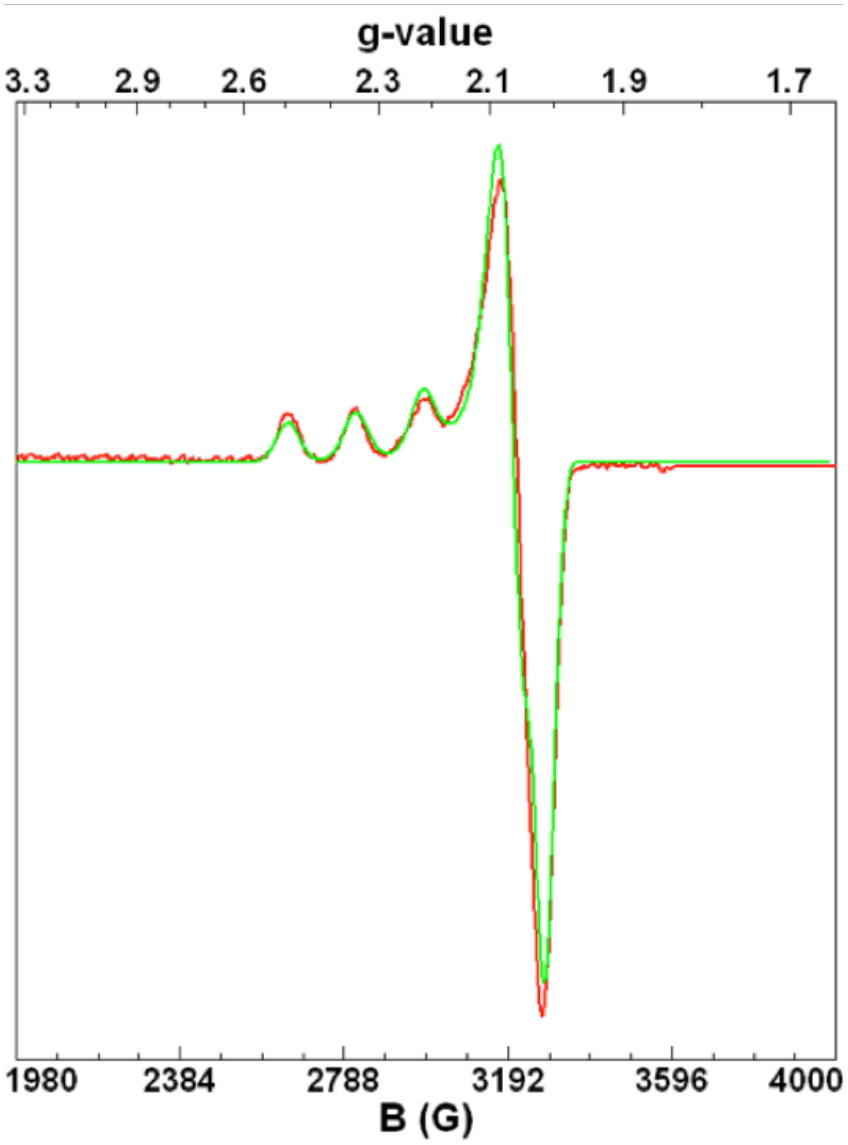

Figure II-13. The EPR spectrum of Cu(II)(TRIW-H)$_3^{2+}$ at pH 5.19. Red spectrum: data; green spectrum: simulation.

Cu(II) affinities to (TRIW-H)$_3$

The binding affinity of Cu(II) to (TRIW-H)$_3$ was examined by tracking the Trp fluorescence quenching upon Cu(II) binding (Figure II-14). The dissociation constants were determined at both pH 5.9 (K_d = 40(8) nM) and pH 7.4 (K_d = 8.7(11) nM). To ensure that the quenching of Trp is not due to non-specific binding of Cu(II) to (TRIW-H)$_3$, I carried out a titration of Cu(II) into a solution of TRIL2W, which does not have the His residue for Cu(II) binding. No significant change of Trp emission upon the addition

of Cu(II) was observed, indicating that the decrease of Trp fluorescence intensity in the case of $(TRIW\text{-}H)_3$ is due to Cu(II) binding to the $(His)_3$ site (Figure II-15). Based on the affinities of Cu(II) and Cu(I) to $(TRIW\text{-}H)_3$, the reduction potentials were calculated using the Nernst Equation (Scheme II-1 and Equation II-2). The calculated reduction potential at pH 5.9 is 400 (30) mV using Cl^- as an anion. At pH 7.4, the potential is 430 (30) mV.

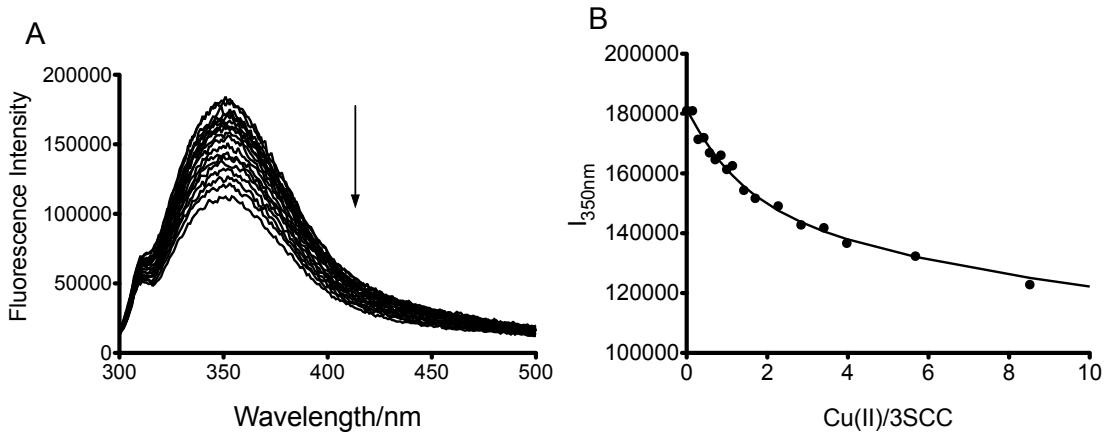

Figure II-14. Cu(II) titration into $(TRIW\text{-}H)_3$ at pH 7.4 (50 mM HEPES). (A) Titration spectra showing the decrease of Trp fluorescence emission upon Cu(II) addition; (B) Observed I_{350nm} values (dots) and calculated titration curve (solid line)

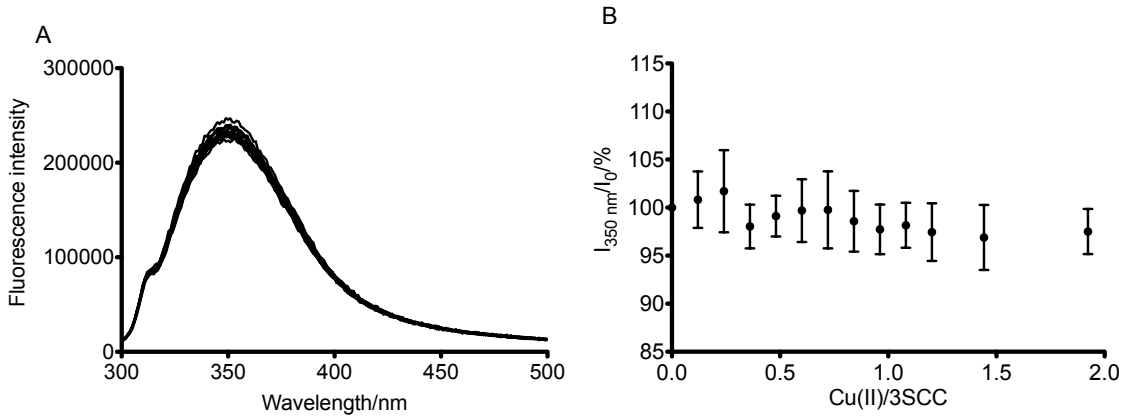

Figure II-15. Cu(II) titration into $(TRIL2W)_3$ at pH 7.4. (A) Titration spectra; (B) Cu(II) equivalents added plotted against the quenching percentage of Trp emission at 350 nm.

Nitrite binding to Cu(II)(TRIW-H)$_3^{2+}$

Upon the addition of small aliquots of sodium nitrite into a solution of Cu(II)(TRIW-H)$_3^{2+}$, a decrease of A_{II} was observed (Figure II-16). Based on the amount of NO_2^- added in relation to simulated A_{II}, a NO_2^- dissociation constant range of 1.5 ~ 2.1 mM can be extracted.

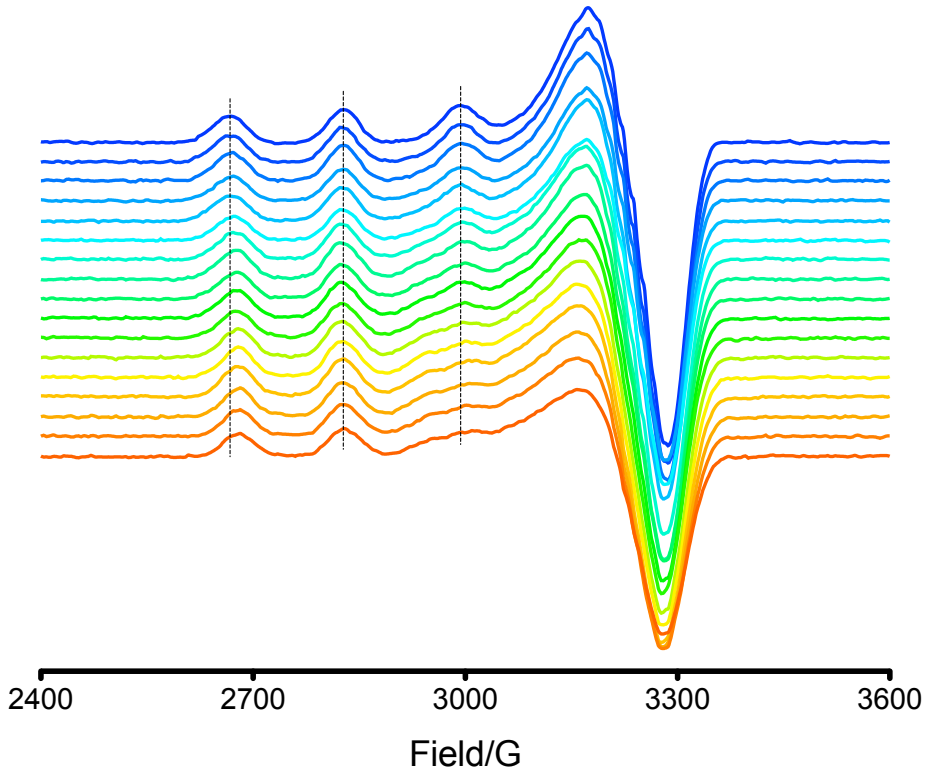

Figure II-16. NO_2^- titration into 1 mM Cu(II)(TRIW-H)$_3^{2+}$ at pH 5.8 monitored by EPR. Blue spectrum: Cu(II)(TRIW-H)$_3^{2+}$; red spectrum: Cu(II)(TRIW-H)$_3^{2+}$ in the presence of 50 equiv. NO_2^- (with respect to Cu(II)). The equivalents of NO_2^- added from the top spectrum to the bottom spectrum: 0, 0.25, 0.5, 0.75, 1, 1.5, 2, 2.5, 3, 4, 5, 7, 10, 15, 20, 30, 50.

Azide binding to Cu(II)(TRIW-H)$_3^{2+}$

Azide is used as a general probe of the interaction between dioxygen species and T2Cu centers. The purpose of doing the following experiments is to evaluate whether a triatomic anion can bind to Cu(II) center. The azide-bound form of Cu(II)(TRIW-H)$_3^{2+}$ will be utilized as a calibration point for the water-counting studies using ESEEM (In collaboration with Prof. David Britt). In addition, the copper-azide complex can serve as

a model for copper-dioxgyen active species, which lays a foundation for future studies on the oxygen-related activities of this system.

Titration of a solution of azide into a solution of Cu(II)(TRIW-H)$_3^{2+}$ at pH 5.8 (MES) and pH 7.4 (HEPES) was carried out monitored by UV-vis spectroscopy (Figure II-17). Under both pH conditions, a peak at 388 nm grows in as azide is added into Cu(II)(TRIW-H)$_3^{2+}$, which was assigned as LMCT from azide to Cu(II) based on the absorption spectra for copper-azide adducts in the literature.[59–61] The dissociation constants of azide to Cu(II)(TRIW-H)$_3^{2+}$ were extracted using Equation II-3. The dissociation constants are 10.2 mM at pH 5.8 and 40 mM at pH 7.4. The binding of azide to Cu(II)(TRIW-H)$_3^{2+}$ is further confirmed by EPR spectroscopy. The addition of azide leads to a compressed hyperfine region (Figure II-18).

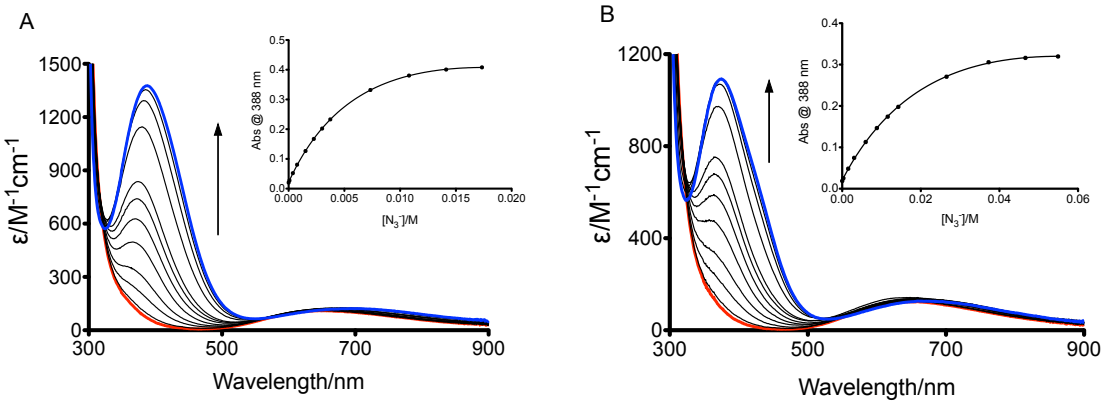

Figure II-17. Azide titration into a solution of Cu(II)(TRIW-H)$_3^{2+}$ monitored by UV-vis spectroscopy. (A) pH 5.8 (50 mM MES). Insert: titration curve (dots: data points; solid line: fitting). (B) pH 7.4 (50 mM HEPES). Insert: titration curve (dots: data points; solid line: fitting).

$$Y = B_{max} \bullet X/(K_d + X) + NS \bullet X + Y_0$$

Equation II-3

(B_{max}: maximum binding as a constant; K_d: dissociation constant; NS: slope of the non-specific binding; Y_0: background. Y: absorbance at 388 nm; X: concentration of N_3^-)

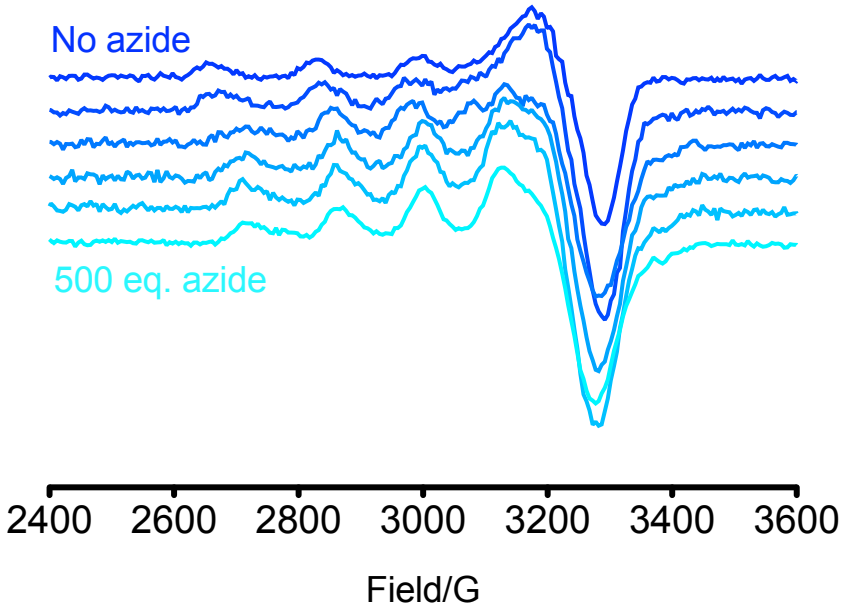

Figure II-18. Azide titration into 1 mM Cu(II)(TRIW-H)$_3^{2+}$ at pH 7.4 (50 mM HEPES). Royal blue spectrum: Cu(II)(TRIW-H)$_3^{2+}$; from the second spectrum to the bottom one, titrated in 1, 10, 100, 200, and 500 eq. of sodium azide (with respect to Cu(II)).

pK_a of Cu(II)(TRIW-H)$_3^{2+}$

The pH-dependent *d-d* band spectral transformation of Cu(II)(TRIW-H)$_3^{2+}$ was examined by adding small aliquots of concentrated KOH in to a un-buffered solution of Cu(II)(TRIW-H)$_3^{2+}$.

The appearance of a broad band with a maximum absorbance at 643 nm is observed as the pH of a Cu(II)(TRIW-H)$_3^{2+}$ solution increases from 2.92 to 5.52 (Figure II-19A). This spectrum corresponds to Cu(II)(His)$_3$(OH$_2$)$_{1-2}$.[34] When the pH is raised above 7.6, a new set of spectra containing an isosbestic point at 571 nm is observed (Figure II-19B). The absorbance at 643 nm decreases while a new band at 514 nm grows in intensity. From a fit of the absorbance at 643 nm to Equation II-1, a pK_a^w value of 8.53(2) corresponding to the changes in the absorption spectra described above can be extracted; this value corresponds to a one-proton deprotonation process (n = 1.11(8)).

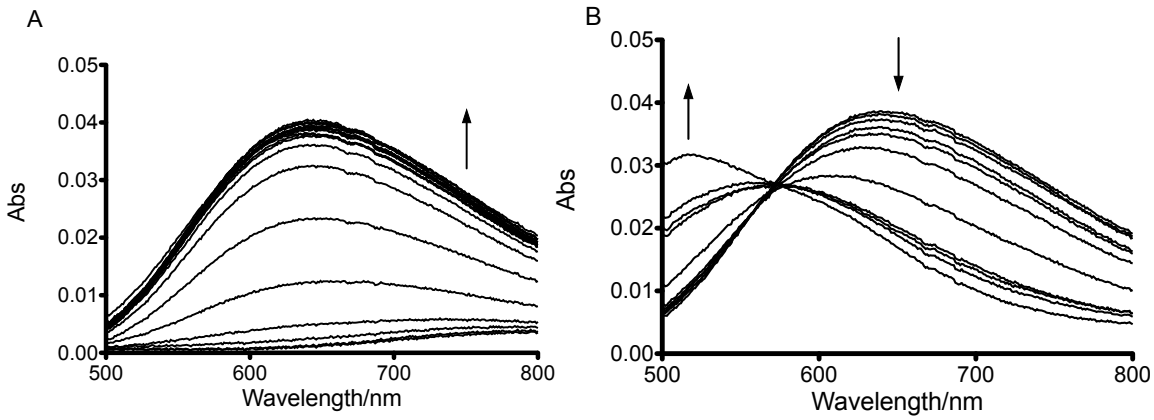

Figure II-19. pH titration spectra of Cu(II)(TRIW-H)$_3^{2+}$ at (A) lower pH (2.92–7.45) and (B) higher pH (7.60–10.80).

A set of pH titration monitored by EPR spectroscopy supports the existence of this deprotonation equilibrium. EPR spectra of Cu(II)(TRIW-H)$_3^{2+}$ were collected from pH 7.80 to pH 9.14, and they show decreased A_{II} values and increased g_{II} values (Figure II-20, Table II-3).

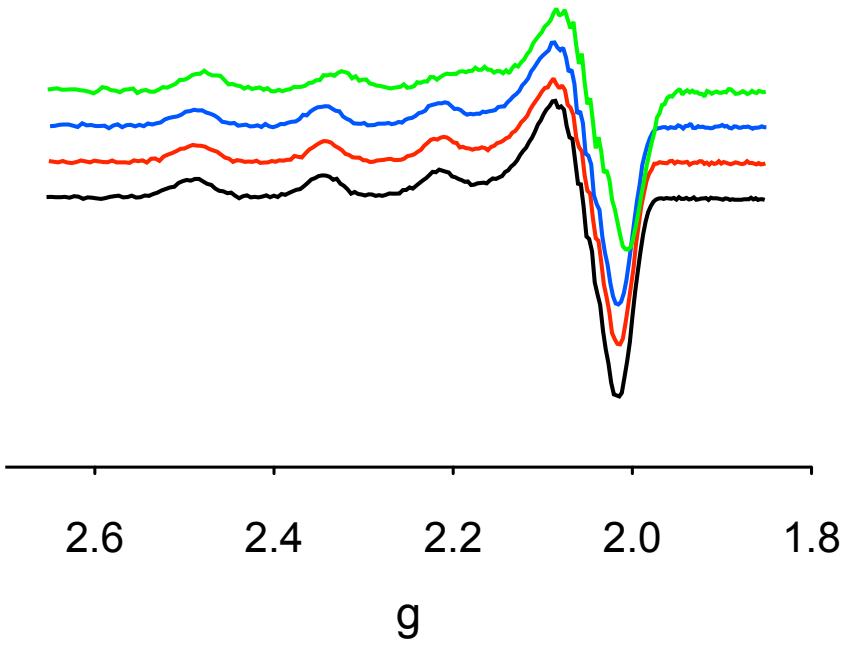

Figure II-20. EPR spectra of 1 mM Cu(II)(TRIW-H)$_3^{2+}$ at different pH conditions. Black spectrum: pH 5.87; red spectrum: pH 6.75; blue spectrum: pH 7.80; green spectrum: pH 9.14.

Table II-3. EPR simulation parameters of Cu(II)(TRIW-H)$_3^{2+}$.

pH	$g_\perp$	g_{II}	$A_\perp$	A_{II}/mT	A_{iso}/mT
5.87	2.05	2.27	0.64	18.58	6.62
6.75	2.05	2.27	0.64	18.58	6.62
7.80	2.05	2.27	0.64	18.58	6.62
9.14	2.05	2.26	0.64	19.29	6.86

NiR activity

Reduction of Cu(II)(TRI-H)$_3^{2+}$ and oxidation of Cu(I)(TRI-H)$_3^{2+}$

The reduction of Cu(II)(TRI-H)$_3^{2+}$ by the addition of a stoichiometric amount of ascorbate can be achieved within the mixing time (Figure II-21A). Although samples of Cu(II)(TRI-H)$_3^{2+}$ reduced with sodium ascorbate did not undergo reoxidation for 24 h when stored in a sealed cuvette, the visible band at 640 nm reappeared after the solutions were exposed to air.

The capability of nitrite to oxidize Cu(I)(TRI-H)$_3^{2+}$ generated *in situ* using ascorbate was assessed. The 640 nm absorbance of Cu(II)(TRI-H)$_3^{2+}$ increases over time in samples containing a 100-fold excess of nitrite (Figure II-21B and C). At pH 5.8, the recovery of 77% of the initial absorbance is obtained in 70 min. Although the recovery of 100% of the initial absorbance was not achieved, successive additions of ascorbate to the same sample allowed reduction–reoxidation cycles of the Cu(II)(TRI-H)$_3^{2+}$ sample for another three additions of reductant, with absorbance recoveries of over 65% of the initial absorbance (Figure II-22).

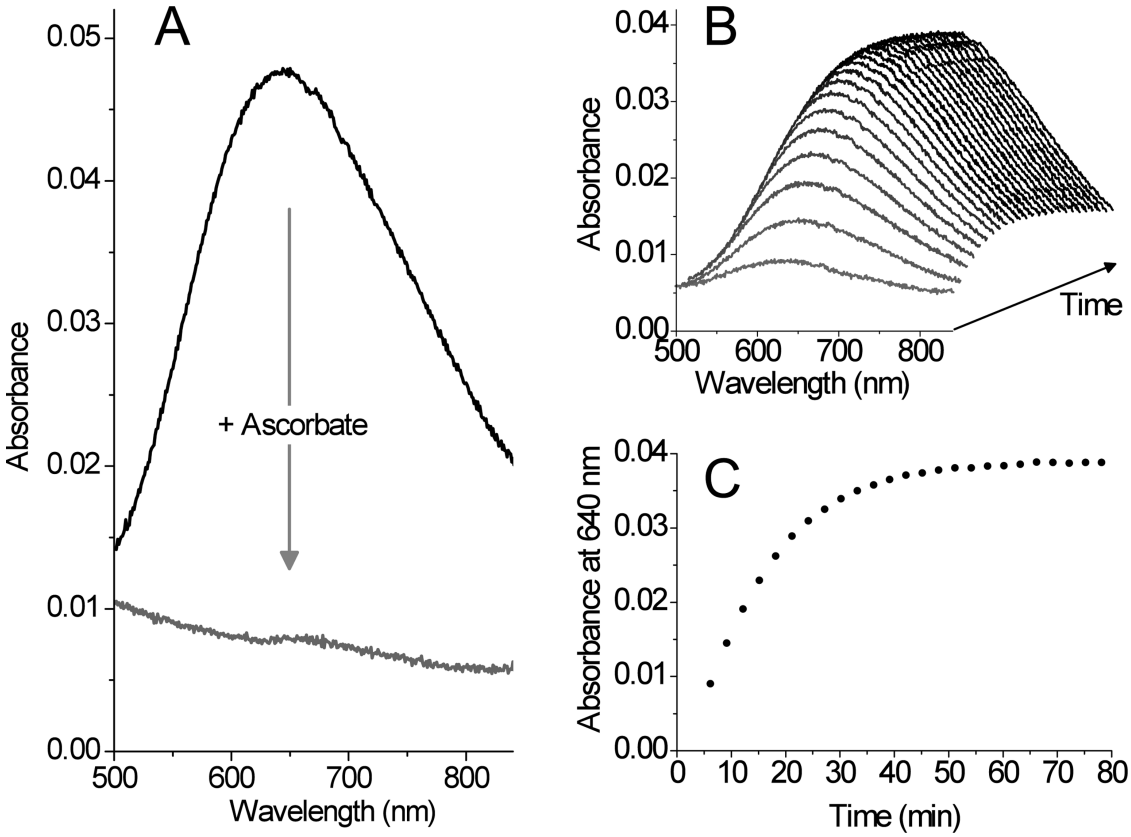

Figure II-21. Visible spectra of Cu(II)(TRI-H)$_3^{2+}$ under various conditions. (A) Spectrum of a 0.34 mM solution of Cu(II)(TRI-H)$_3^{2+}$ in presence of 30 mM sodium nitrite in deoxygenated H_2O before (black line) and after (gray line) the addition of 1 equiv. of sodium ascorbate (200 mM buffer MES, pH 5.8). (B) Recovery of Cu(II)(TRI-H)$_3^{2+}$ absorbance. The spectra were collected every 3 min after ascorbate addition. (C) Absorbance values at 640 nm vs. time.

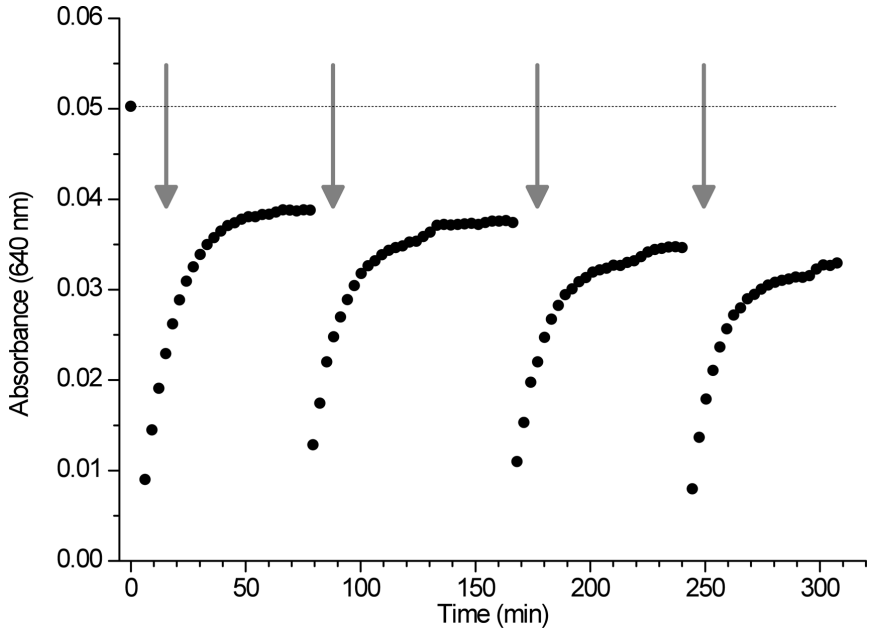

Figure II-22. Absorbance values at 640 nm as a function of time for a 0.38 mM solution of Cu(II)(TRI-H)$_3^{2+}$ in the presence of 30 mM sodium nitrite in deoxygenated 200 mM aqueous MES buffer at pH 5.8. 1 eq. of sodium ascorbate was added into the solution. The arrows indicate further additions of ascorbate (1 eq. each). Dashed line: absorbance of the initial Cu(II)(TRI-H)$_3^{2+}$ solution.

Nitric oxide production

The production of NO by reacting Cu(I)(TRI-H)$_3^+$ with 1 eq of nitrite at pH 5.8 was demonstrated by visible spectroscopy by trapping the evolved gas as the colored [Fe(NO)(EDTA)]$_2^-$ complex (Figure II-23).[48] More importantly, the production of NO was observed at pH 5.8 using both Cu(I)(TRI-H)$_3^+$ and ascorbate-reduced Cu(II)(TRI-H)$_3^{2+}$. For these two samples, the amounts of trapped NO are 71% and 48% after 1 h of that of a control sample containing [Cu(I)(CH$_3$CN)$_4$]$^+$, respectively.

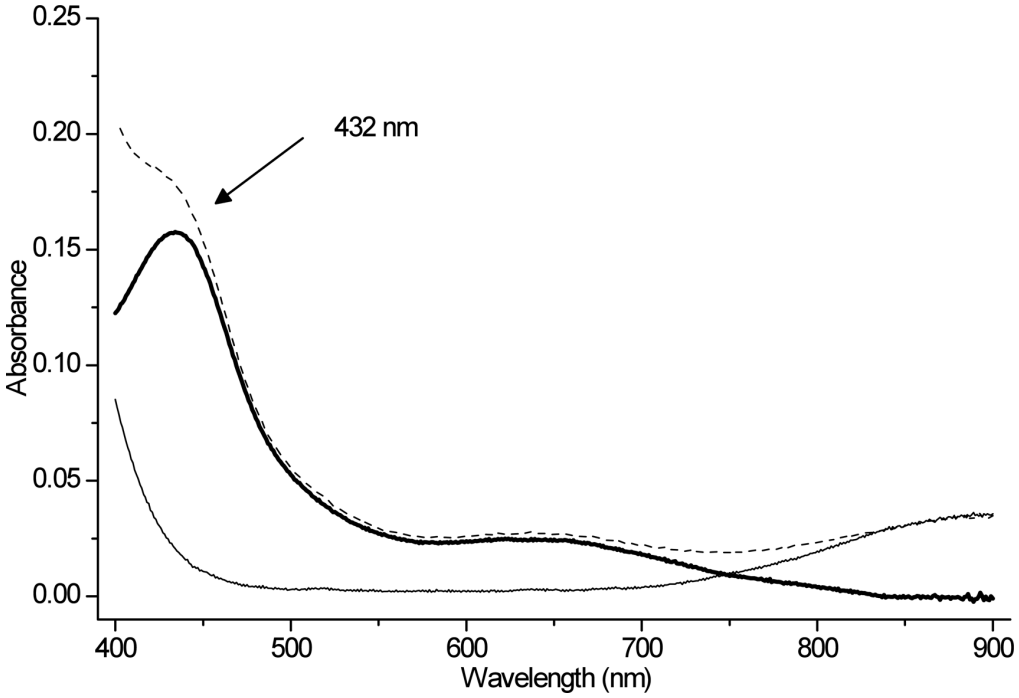

Figure II-23. Spectra of a solution of $[Fe(EDTA)]^{2-}$ in aqueous 1 M citrate buffer at pH 5 before (thin line) and after (dashed line) being sparged with a nitrogen stream previously fluxed into a reaction vessel containing $Cu(I)(TRI\text{-}H)_3^{+}$ and sodium nitrite (both 2.26 mM) in deoxygenated aqueous 200 mM MES buffer at pH 5.8. The thick line is the difference between the two spectra described above.

Detection of nitrous oxide

Based on Henry's Law, the concentrations of a series of standard samples of nitrous oxide aqueous solutions (total N_2O range: 8.18×10^{-6}~6.95×10^{-5} mol) were calculated. The concentrations were then correlated with the integration of IR absorbance of the doubled peaks at 2234.8 and 2212.9 cm^{-1} (Figure II-24A and B).[62,63] The headspace gas collected at different time points (3.5, 23, 28, 30, 41, 45 h) for the reaction mixture of nitrite reduction was examined for its N_2O percentage (Figure II-24A). The amount of N_2O produced has a yield lower than 0.09%, which is within the error of this experiment. A control experiment was carried out with apo-peptide for which the N_2O level was below the detection limit. Therefore, nitrite reduction catalyzed by $Cu(II)(TRIW\text{-}H)_3^{2+}$ does not produce N_2O.

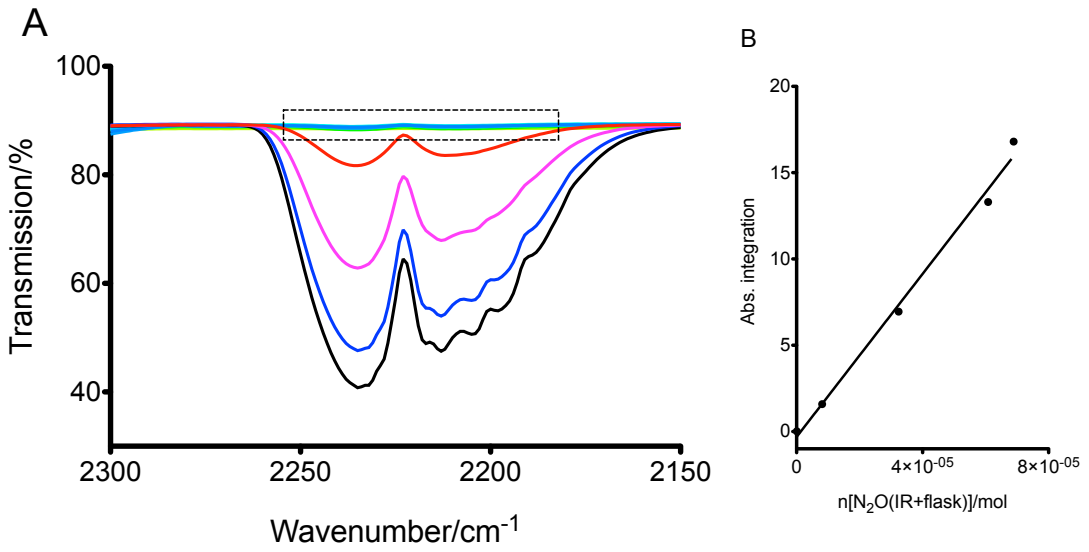

Figure II-24. (A) FTIR spectra of a series of known concentrations of N_2O (black, blue, purple, red, and cyan spectra) and the gas collected from the headspace of nitrite reduction catalyzed by Cu(II)(TRIW-H)$_3^{2+}$ at pH 5.8 (rectangular box). (B) Calibration curve resulting in $y = 2.4 \times 10^6 x$ ($R^2 = 0.9928$).

NiR activity under catalytic conditions

The NiR activity under catalytic conditions ([Asc$^-$]= 1.15 mM, [NO_2^-] = 30 mM, [Cu(II)(TRIW-H)$_3^{2+}$] or [Cu(II)(TRI-H)$_3^{2+}$] = 0.180 mM) were examined. The quantity of ascorbate oxidized in 175 min at pH 5.9, correcting for the background reaction, corresponds to 1.5(2) times the amount of Cu(II)(TRI-H)$_3^{2+}$, which results in a turnover number of 3.0 expressed as moles of electrons per mole of Cu(II)(TRI-H)$_3^{2+}$. Moreover, five turnovers were achieved at pH 5.8 in 220 min (Figure II-25B). The rate of the background reaction of ascorbate with nitrite is not influenced by the presence of either traces of Cu(II) ion (0.21 μM) or apo-(TRI-H)$_3$ (0.90 mM, Figure II-26A), and ascorbate is stable in the absence of nitrite (Figure II-26A). The oxidation rate of the ascorbate also linearly depends on the concentration of Cu(II)(TRI-H)$_3^{2+}$ (0.171–0.513 mM, Figure II-26B and C). These observations suggest that ascorbate acts as a sacrificial reductant for Cu(II)(TRI-H)$_3^{2+}$, and that the Cu(I)(TRI-H)$_3^+$ species is catalytically active in reducing nitrite to NO. Both the kinetics of oxidation of Cu(I)(TRI-H)$_3^+$ (through the recovery of absorbance at 640 nm) and of ascorbate (through the decrease of absorbance at 265 nm) were studied as a function of pH. The initial rate of reoxidation of Cu(I)(TRI-H)$_3^+$ ($v_{Cu,ox}$)

was examined between pH 5.8 and 7.4. The initial rate decreases as pH increases from 5.8 to 7.4 (Figure II-27A). The pseudo-first order rate constants $k_{first,Cu}$ ($v_{Cu,ox}$ = $k_{first,Cu}$·[Cu(II)(TRI-H)$_3^{2+}$]) determined from the initial rates (12 min) as a function of pH are reported in Table II-4 and in Figure II-27. The rate of oxidation of ascorbate in the presence of Cu(I)(TRI-H)$_3^+$ and nitrite ($v_{Asc,ox}$) was studied in the pH range 5.3–6.5. The initial rate of the reaction depicted in Scheme II-2 decreases with increasing pH, as shown in Figure II-27C and D (dH-Asc = dehydroascorbate).

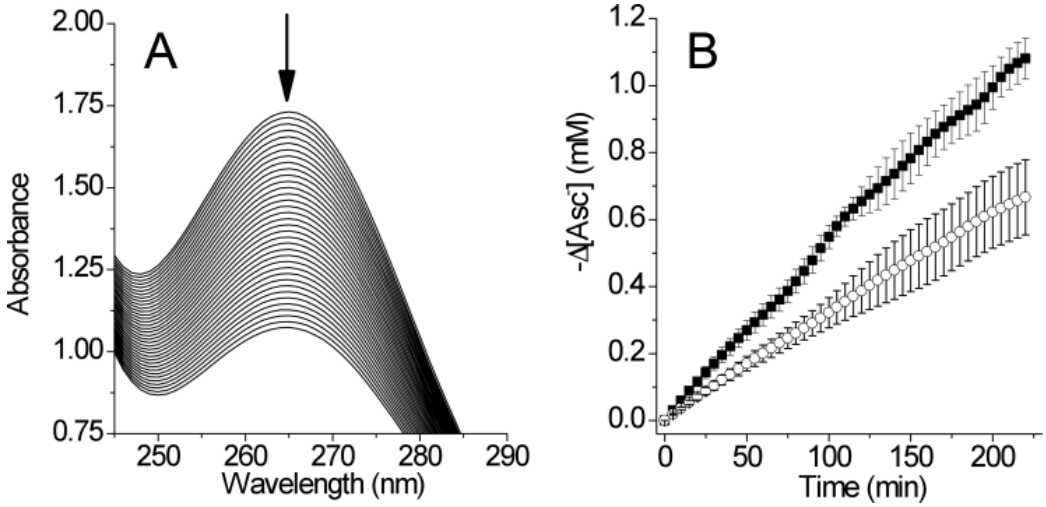

Figure II-25. (A) UV spectra of a solution of sodium ascorbate and sodium nitrite (pH 5.9) collected every 5 min, containing Cu(II)(TRI-H)$_3^{2+}$ (0.180 mM) and apo-(TRI-H)$_3$ (0.090 mM). (B) ■, decrease of [Asc$^-$] vs. time in samples, as in A; ○, samples containing only apo-(TRI-H)$_3$ (0.090 mM), pH 5.8.

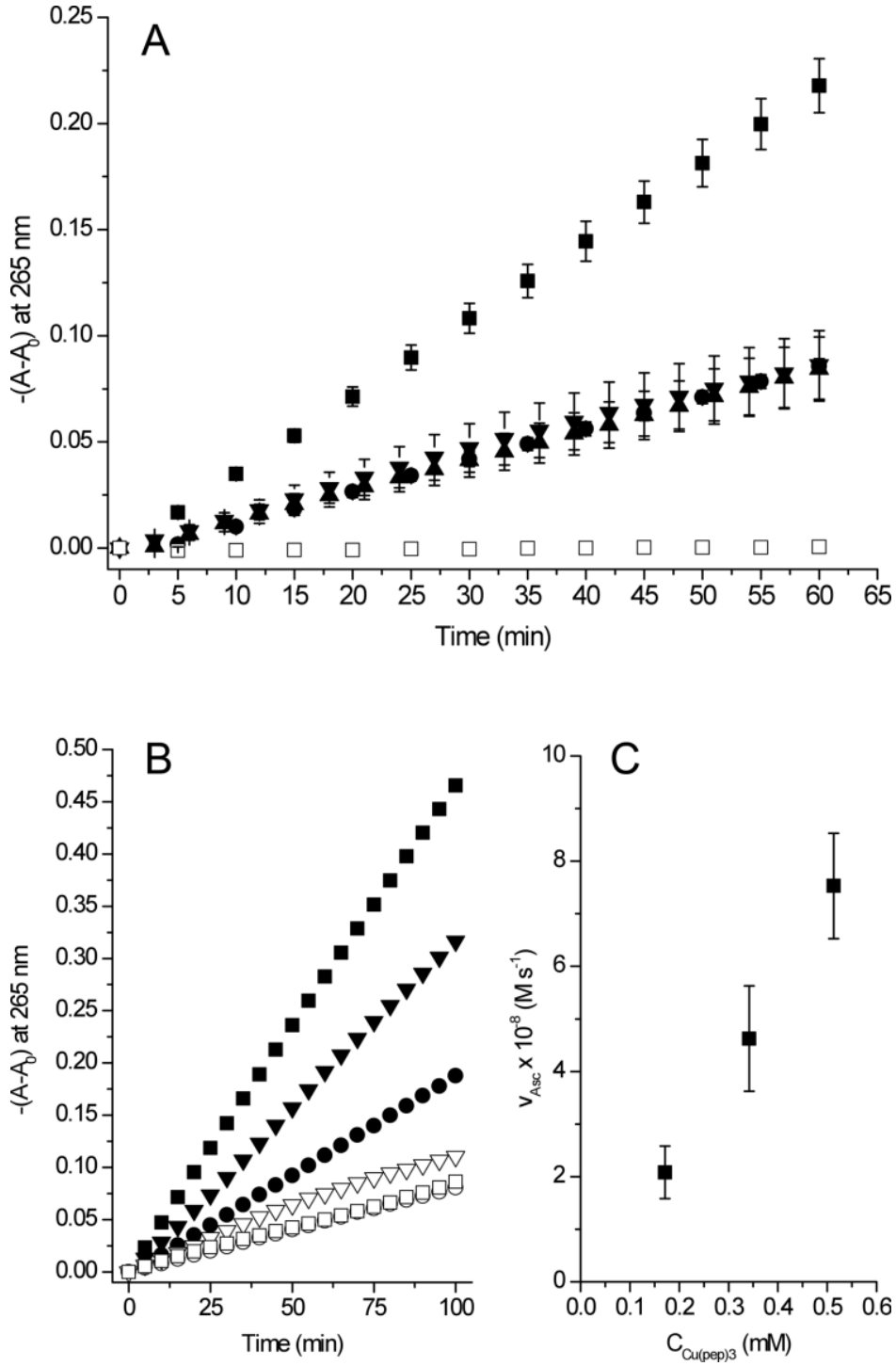

Figure II-26. (A) Values of $-(A-A_0)$ at 265 nm *vs*. time for solutions of sodium ascorbate (1.15 mM) and sodium nitrite (30 mM) in deoxygenated aqueous 200 mM MES buffer at pH 5.9, containing: $Cu(II)(TRI\text{-}H)_3^{2+}$ (0.180 mM) (squares), apo-$(TRI\text{-}H)_3$ (90 μM) (circles), Cu(II) chloride (0.21 μM) (up triangle), or only ascorbate and nitrite (down triangle). Open squares: sodium ascorbate (1.15 mM) in deoxygenated 200 mM MES buffer at pH 5.9. (B) Values of $-(A-A_0)$ at 265 nm as a function of time for solutions of

sodium ascorbate (1.15 mM) and sodium nitrite (30 mM) in deoxygenated aqueous 200 mM MES buffer at pH 5.9 for increasing concentrations of Cu(II)(TRI-H)$_3^{2+}$ (Cu(pep)$_3$; filled squares: 0.171 mM, filled triangles: 0.342 mM, filled circles: 0.513 mM) or apo-(TRI-H)$_3$ (open squares: 86 μM, open triangles: 171 μM, open circles: 257 μM). (C) Rate constants for the Cu(II)(TRI-H)$_3^{2+}$ - catalyzed reaction as a function of the concentration of the metallopeptide.

Table II-4. Pseudo-first order rate constants for the oxidation of Cu(I)(TRI-H)$_3^+$ ($k_{1st,Cu}$) and of oxidation of ascorbate ($k_{1st,Asc}$) as a function of the pH.

pH	$k_{1st,Cu}$ /10^{-4} (s^{-1})	$k_{1st,Asc}$ /10^{-4} (s^{-1})
5.3	-	12(3)
5.5	-	9(1)
5.8	5.2(3)	4.6(3)
5.9	-	4.40(16)
6.0	2.8(3)	2.4(2)
6.5	0.65(3)	0.68(3)
7.0	0.22(8)	-

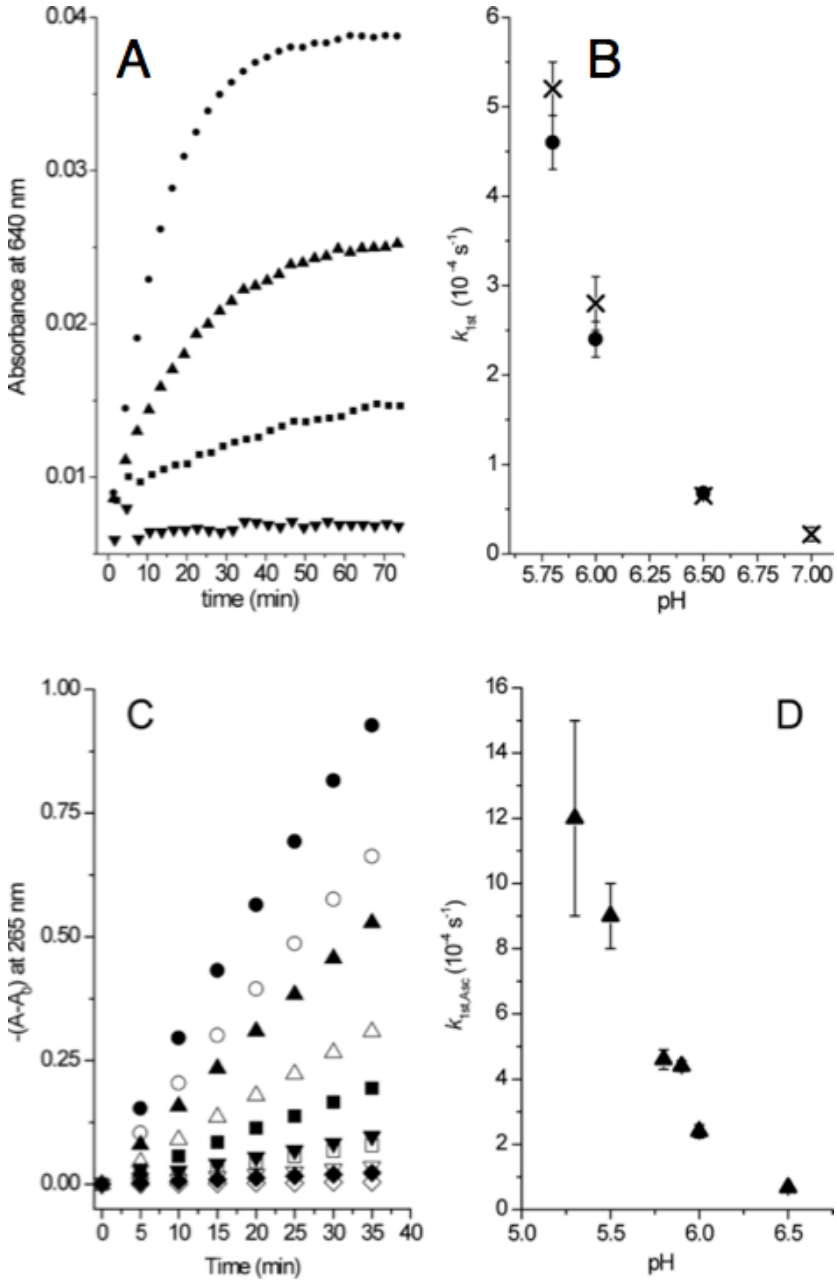

Figure II-27. (A) Absorbance at 640 nm *vs*. time for Cu(II)(TRI-H)$_3^{2+}$ solutions (0.30-0.34 mM, 30 mM sodium nitrite) in deoxygenated H_2O, added with 1 eq. of sodium ascorbate. Circles: pH 5.8; up triangles: pH 6.0; squares: pH 6.5; down triangles: pH 7.0. (*B*) Values of $k_{1st,Cu}$ (crosses) and $k_{1st,Asc}$ (filled circles) as a function of the pH. (*C*) Values of –(A-A_0) at 265 nm *vs*. time for solutions of sodium ascorbate (1.15 mM) and sodium nitrite (30 mM) in deoxygenated aqueous 200 mM MES buffer at pH 5.9 containing either Cu(II)(TRI-H)$_3^{2+}$ (0.180 mM) (filled symbols) or apo-(TRI-H)$_3$ (90 μM) (open symbols). Circles: pH 5.3; up triangles: pH 5.5; squares: pH 5.8; down triangles: pH 6.0; diamonds: pH 6.5. A_0 is the absorbance before the addition of ascorbate. (*D*) Pseudo-first order rate constants ($k_{1st,Asc}$) values as a function of the pH.

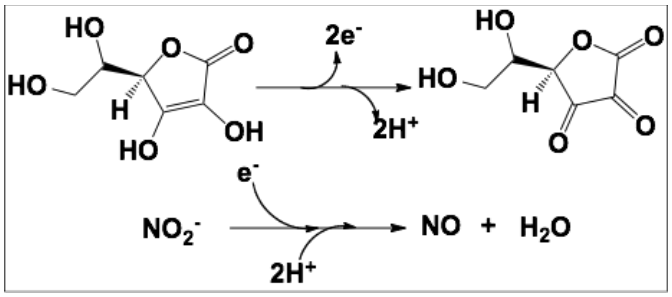

Scheme II-2

Discussion

In a recent study, we showed that a *de novo* design strategy is highly effective for providing mimics of carbonic anhydrase using a mononuclear Zn(II)-based hydrolytic system.[33,64] In this work, I explore the more challenging objective of obtaining a *de novo* designed redox-based assembly that carries out NiR reaction, which occurs at the T2Cu site in native CuNiR. Because both Zn(II) and Cu(I) are d^{10} metals, the latter ion may bind to the $(His)_3$ site in a same fashion as Zn(II) in $Hg_SZn_N(CSL9PenL23H)_3^+$.[33] A comparison of this Zn(II) site to that of the T2Cu in CuNiR [*R. sphaeroides* NiR, Protein Data Bank (PDB) ID code 2DY2] is shown in Figure II-3. The metal ions and the atoms on the first coordination sphere are well matched in both structures, which serves as a starting point for copper-binding studies. To establish fully a structural model for CuNiR, I characterized the copper-peptides in both oxidation states.

Characterization of Cu(I)(TRIW-H)$_3^+$

Cu(I) binds to $(TRI\text{-}H)_3$ stoichiometrically with 1:1 [Cu(I):3SCC] ratio.[34] Unlike apo-$(TRI\text{-}H)_3$, which has two resonances in the aromatic region in its ^1H NMR spectrum, at the same pH, Cu(I)$(TRI\text{-}H)_3^+$ complex has more resonance peaks.[34] This suggests that the $^{\delta}H$ and $^{\varepsilon}H$ on three imidazoles are not chemically equivalent, which could be the result of the following scenarios based on different coordination numbers of Cu(I): 1) Cu(I) only binds to two of the imidazoles, the third imidazole stays unbound; 2) Cu(I) binds to three imidazoles and at least one other ligand (likely a water molecule) in a pseudo-tetrahedral geometry; 3) Cu(I) binds to three imidazoles in a distorted trigonal

planar geometry. In addition to these possible cases of different Cu(I) coordination numbers, the imidazoles might bind Cu(I) with either $^{\delta}$N or $^{\varepsilon}$N. In order to narrow down the available structural possibilities, additional spectroscopic characterization was required.

Based on the XANES of Cu(I)(TRIW-H)$_3^+$ at both pH 5.9 and 7.4, Cu(I) is three-coordinate. EXAFS fitting shows typical three-coordinate Cu(I)-N bond distances (1.93 Å, Table II-5), similar to the reported values of three-coordinate Cu(I)-N centers in native proteins[16,65] and synthetic copper complexes.[66–69] In addition, the Debye-Waller factors are relatively large in the EXAFS simulations, indicating that the Cu(I) environment is somewhat more distorted than that in psAO or in the synthetic Cu(I) complex.[65,66] The best depiction of the Cu(I) coordination environment in Cu(I)(TRIW-H)$_3^+$ based on NMR and XAS data is shown in Figure II-28, which describes a three-coordinate Cu(I)N(imid)$_3$ center in a distorted trigonal plane, possibly with different coordinating nitrogens from the imidazoles. These experiments, however, do not provide information of the orientation of the imidazole, the imidazole plane could be perpendicular or parallel to the helical axis, nor the coordinating imidazole $^{\delta}$N or $^{\varepsilon}$N atoms, both of which could potentially influence the electronic properties of the Cu(I) center. The ascorbate-reduced T2Cu in native NiR is also a three-coordinate center, revealed by X-ray crystallography and EXAFS, which is the inactive form because it does not bind to exogenous ligands.[70–74]

Dr. Matteo Tegoni carried out carbon monoxide binding experiments to test whether Cu(I)(TRI-H)$_3^+$ can coordinate a small molecule inside the helical coiled coils. Carbon monoxide is a commonly used small molecule to probe the coordination environment of Cu(I) in synthetic small molecules as well as copper proteins,[22,75–79] although my later study on TRI-HL19A peptide shows that CO can induce the binding of a third imidazole to a Cu(I)(imid)$_2$ center, forming a Cu(I)(CO)(imid)$_3$ center (See Chapter IV). The CO-bound Cu(I)(TRIW-H)$_3^+$ shows a typical CO stretching frequency when it is terminally bound to a Cu(I)N$_3$ center, which is similar to the reported Cu(His)$_3$ centers in cuproproteins but different from the situation where CO is bound to a linear Cu(I)N$_2$ center (Table II-6). This piece of evidence points to a tetrahedral Cu(I)(CO)(imid)$_3$ center. Further 2DIR studies on the vibrational anharmonicity of the C–

O bond in collaboration with Prof. Kevin Kubarych from the University of Michigan support that CO is buried in the hydrophobic interior of the coiled coils.

Table II-5. Bond lengths of Cu(I)(TRIW-H)$_3^+$ in comparison to relevant Cu(I) centers

	Shell	R/Å	σ^2/Å^2	E^o/eV	Ref
Cu(I)(TRIW-H)$_3^+$, pH 5.9	3 N_{imid}	1.93	0.009	-10.88	This
Cu(I)(TRIW-H)$_3^+$, pH 7.4	3 N_{imid}	1.93	0.009	-10.62	work
Reduced psAO	3 N_{imid}	1.94	0.006	-13.32	[65]
Reduced PHM*cc*	2.5 N_{imid}	1.92	0.017	-10.34	[16]
(pH 7.5)	0.5 S_{Met}	2.24	0.012		
$(Met_2Im)_3Cu(I)^a$	2 N_{imid}	1.89	0.010	-	[66]
	1 N	2.08	0.003		

[a]Tris(1,2-dimethylimidazole)copper(I)

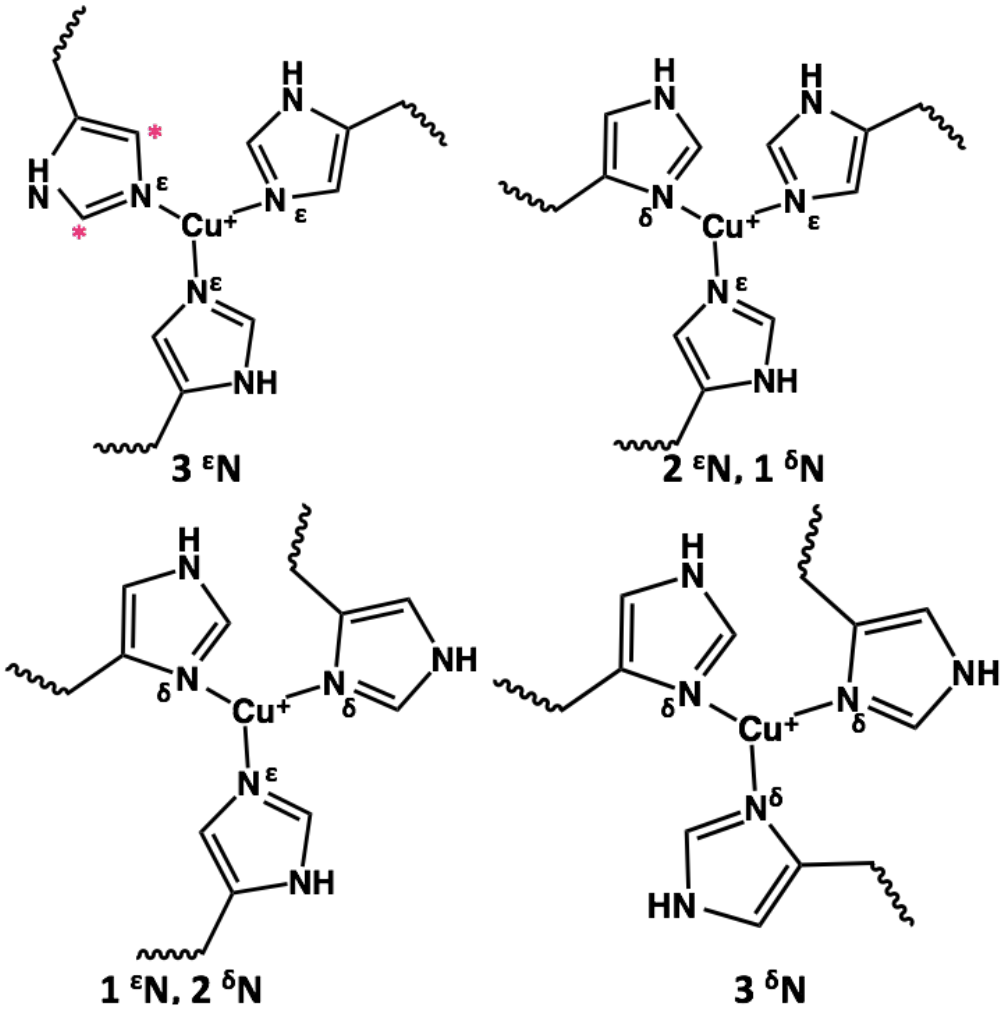

Figure II-28. Possible coordination modes of imidazoles with either N^{δ} or N^{ε} to Cu(I)

Table II-6. CO stretching frequency of Cu(I)(CO)(TRIW-H)$_3^+$ in comparison to selected copper proteins and compounds

	ν(C-O)/cm^{-1}	$\omega_{1/2}$/cm^{-1}	Ref
Cu(I)(CO)(TRIW-H)$_3^+$	2063	14	This work
*Af*NiR	2050 (T2Cu)	11-15	[77]
CuAO	2064/2085		[22]
PHM	2062 (Cu_H) 2092 (Cu_M)		[78]
$[Cu_2(Me3p)(CO)_2]^{2+a}$	2060		[80]
$[Cu(I)L_{5.1}(CO)]^{+b}$	2073		[81]

$[Cu(I)(iPr_3TACH)(CO)]^{+c}$	2068		[75]
$[L_\delta Cu(I)(CO)]^{d}$	2110	5	[79]

[a, b, ,c]The chemdraw schemes of these compounds are shown in Scheme II-3

[d]The chemdraw scheme of this compound without CO bound is shown in Scheme II-4.

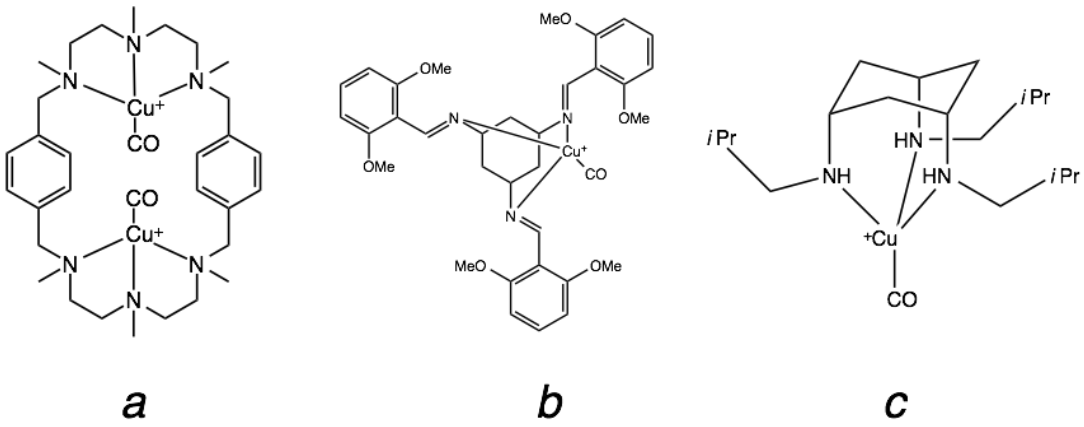

Scheme II-3

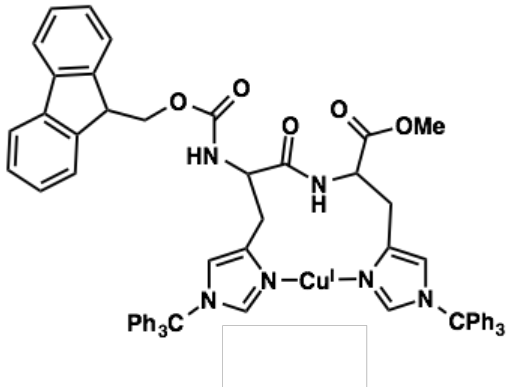

Scheme II-4

Characterization of Cu(II)(TRIW-H)$_3^{2+}$

With the coordination environment of the Cu(I)-peptide well defined, spectroscopic studies on Cu(II)(TRIW-H)$_3^{2+}$ were next undertaken. The absorption spectra of Cu(II)(TRIW-H)$_3^{2+}$ show characteristic features of a T2Cu center, with a weak visible *d-d* transition at 643 nm in pH range 5.7–7.5. Based on a spectrum-structure

correlation for Cu(II) complexes in aqueous solutions reported by Prenesti *et al.* (Equation II-4, Table II-7),[53] for a hypothetic model of a four equatorially coordinated Cu(II) center with three imidazoles and one water molecule, the *d-d* transition is predicted to be centered at 634 nm, close to what is observed for Cu(II)(TRIW-H)$_3^{2+}$. For a Cu(II)(imid)$_2$(OH$_2$)$_2$ center, however, the *d-d* transition is expected to be at 692 nm. Granted that the symmetry of my system might be different from the model, the visible spectra support the assignment that all three imidazoles are coordinated to Cu(II), however, this analysis does not provide definitive information of the coordination number of Cu(II).

Cu(II)(TRIW-H)$_3^{2+}$ has EPR parameters for a typical T2Cu center, with *g* tensors showing a typical $d_{x^2-y^2}$ ground state ($g_{\parallel} > g_{\perp}$) and $A_{\parallel}$ larger than 14 mT (Table II-8).[4,7] In NiR, three histidine residues and a water molecule bind Cu(II) in a four-coordinate, tetrahedral geometry, whereas the EPR spectra of Cu(II)(TRIW-H)$_3^{2+}$ indicate that the center likely is five-coordinate, especially when compared to Cu(II)N$_3$O$_2$ centers in synthetic model compounds for both EPR and UV-Vis parameters (Table II-8). Spectroscopies suggest that Cu(II) is bound to three imidazoles from histidine residues on a quasi-equatorial plane and one or two water molecules.

$$\lambda_{\max} = 10^3 / \sum_{i=1}^{4} n_i \bar{\nu}_i$$

Equation II-4

Table II-7. Selected coefficient values ($\bar{\nu}_i$) for the estimation of the $\lambda_{\max}$ values of equatorially-coordinated Cu(II) complexes in aqueous solution.[53]

Donor group	Coefficient ($\bar{\nu}_i$)
Imidazole nitrogen	0.427 ± 0.009
Water oxygen	0.296 ± 0.006
Hydroxide oxygen	0.39 ± 0.03

Table II-8. Spectroscopic parameters of Cu(II)(TRIW-H)$_3^{2+}$ compared to similar systems.

	pH, solvent	$g_\perp$	g_{II}	A_{II}/mT	λ_{max} (ε/M cm^{-1})/nm	Ref
Cu(II)(TRIW-H)$_3^{2+}$	6.75, aq.	2.06	2.27	18.58	643 (135)	34
NiR (T2Cu)	Aq.	2.05	2.3	14		82
PHM	pH~6.0, aq.	2.05	2.29	16.81		83
AO	Aq.	2.04	2.25	15.52		84
[Cu(acac)$_2$trien]NaY[a]	Solid state	2.03	2.21	17.64	800, 760, 650	56
{Cu[26]py$_2$N$_4$}$^{2+}$[b]	H$_2$O:DMSO 1:1	2.06	2.24	17.27	660	57
[Cu$_2$(tqbd)(H$_2$O)$_4$][S$_2$O$_6$]$_2$[c]	Methanol-DMF	2.06	2.25	17.6		58
[Cu(bpba)(MeOH)](ClO$_4$)$_2$[d]	Acetone	2.07	2.25	15.0	640(125)	85
[Cu(*tpy*)(H$_2$O)(ClO$_4$)]ClO$_4$[e]	Methanol-water	2.067	2.277	16.8	693(65)	86
Mer-[CuL$_3$](NO$_3$)$_2$(H$_2$O)(*i*-PrOH)[f]	Solid state	2.062	2.255	18.1	715(61)	87

The chemdraw schemes of compounds *a, b, c, d, e, f* are shown in Scheme II-5.

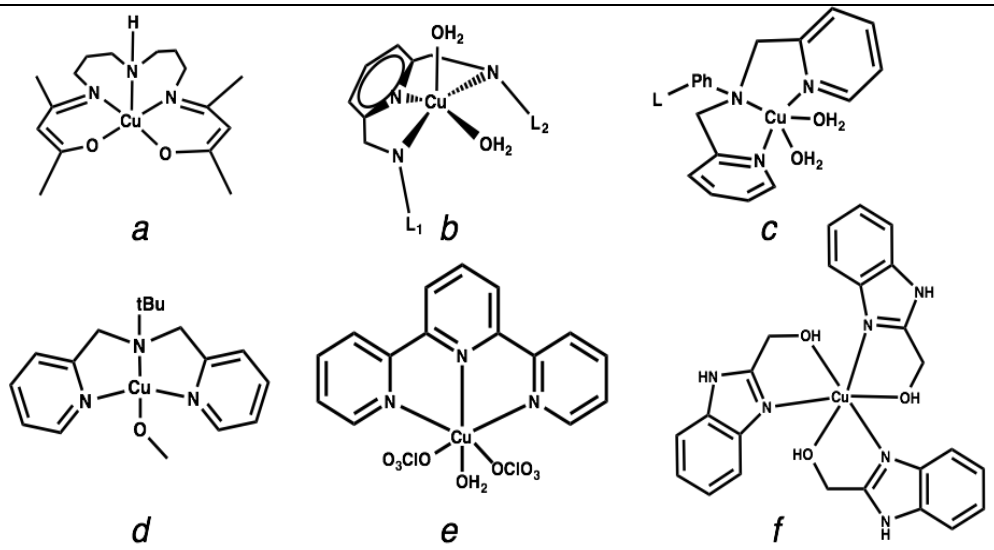

Scheme II-5

The coordination of at least one water molecule to the Cu(II) center is further substantiated by a set of pH titration, which partially aims to examine the Cu(II)-bound water deprotonation equilibrium reflected by the transformation of Cu(II) *d-d* band. A sharp rise in the *d-d* band moving from pH 3 until the spectra level out by pH ~5 is observed for Cu(II)(TRIW-H)$_3^{2+}$. Two major processes occur over this pH range. The first is the conversion of the 2SCCs to 3SCCs through the deprotonation of glutamic acids located at the *e* positions of the heptads. This conversion for the apo-peptide is not reflected in these spectroscopic changes. The second process is the binding of Cu(II) to the 3SCCs, which is directly reflected by these spectra, as they arise from the *d–d* transition of Cu(II). The UV–vis spectra of all these peptides are consistent with a four- or five-coordinate Cu(II) until at least pH 6.0.

As shown in Figure II-19B, Cu(II)(TRIW-H)$_3^{2+}$ exhibits a second significant absorption change at a higher pH with a pK_a^W of 8.53. This is thought to be associated with the deprotonation of the Cu(II)-bound water into a Cu(II)-bound hydroxide because the blue shift upon this deprotonation is in accordance with the prediction of the same process in an equatorially coordinated Cu(II) complex (Equation II-4, Table II-7).[53] Spectral perturbations over this range are also observed in the EPR spectra of Cu(II)(TRIW-H)$_3^{2+}$. As the pH increased from 7.80 to 9.14, g_{II} decreased from 2.27 to 2.26 while A_{II} increased from 18.58 to 19.29 mT (Table II-3). This observed trend is consistent with the reported case of copper-bound water deprotonation at the T2Cu center in the mercury derivative of laccase.[88] This piece of evidence, combined with the transformation of the UV–vis spectra in this pH region, supports that the pK_a^w at 8.53 for Cu(II)(TRIW-H)$_3^{2+}$ corresponds to a Cu(II)-bound water deprotonation, producing a [Cu(II)(His)$_3$(OH)(OH$_2$)$_{0-1}$]$^+$ species.

At this point, although a crystal structure of either oxidation state of this copper-peptide complex is not available, the spectroscopic data can help me draw a picture of the coordination environment of the copper center in this construct (Figure II-29). Going from the cuprous form to the cupric form, the copper center experiences a change in coordination number from three to four (or five), which would require the copper ion to move from the N_3 plane to a location above the plane for water coordination. This change of copper coordination number also involves the alteration of the orientation of the

imidazoles inside the helical coiled coils, if the imidazole planes are perpendicular to the helical axis in the cuprous state. In native CuNiR, however, both oxidation levels of copper maintain four- or five-coordination during the catalytic cycle.[23,4] As a result, there is no significant energy barrier due to the change of coordination number, especially the in- and out-of-the-plane motion of the copper ion, associated with the catalytic cycle. One can expect that the difference between this construct and the T2Cu in native CuNiR in the coordination environment of both Cu(I) and Cu(II) might lead to differences in their redox properties and reactivity.

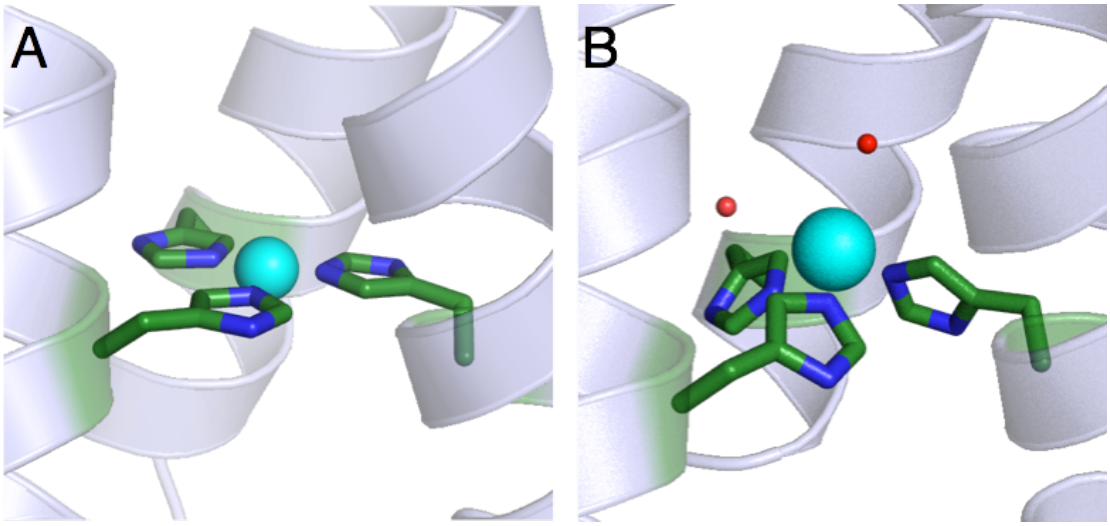

Figure II-29. PyMol models of (A) Cu(I)(TRIW-H)$_3^+$ and (B) Cu(II)(TRIW-H)$_3^{2+}$. Models are made based on the crystal structure of Hg(II)$_S$Zn(II)$_N$(CSL9PenL23H)$_3^+$ (PDB code: 3PBJ[33]).

Binding Affinities and Reduction Potentials for Cu(TRI-H)$_3^{n+}$

After demonstrating that copper binds to 3SCC stoichiometrically, the next step was to determine the affinity in both oxidation states. The purpose of these experiments was two-fold: 1) binding affinity is an important basis to set up catalytic reactions to ensure that there is no free copper ions for either oxidation level; 2) the redox potential of the system can be calculated from the affinities based on the Nernst equation (Scheme II-1, Equation II-2), which allows one to assess the relationship between NiR activity and reduction potential.

The dissociation constants of Cu(I) to $(TRIW\text{-}H)_3$ at both pH 5.9 and 7.4 (Table II-9) are remarkably close to that of the N-terminal fragment 1–14 of human copper transporter hCtr1, which contains three histidine residues[90] and much higher than that of Aβ42[91]. Cu(I) affinity to $(TRIW\text{-}H)_3$ maintains on a picomolar/sub-picomolar level, indicating that the Cu(I) coordination environment is very similar at these two pH conditions, consistent with the previous observations. The slight decrease in affinity when pH decreases from 7.4 to 5.9 could be attributed to the subtle changes in the secondary coordination sphere due to the protonation of the glutamates along the helices. Similarly, Cu(II) affinity decreases by approximately one magnitude when pH decreases from 7.4 to 5.9. The nanomolar level dissociation constants fall within the range of Cu(II) dissociation constants in similar systems (Table II-9). The binding affinities of Cu(I) and Cu(II) to $(TRIW\text{-}H)_3$ differ by ~four orders of magnitude at each pH condition, which is possibly due to the stabilization of a trigonal planar Cu(I) or the unfavorable incorporation of a +2 charged ion (Cu^{2+}) as compared to a +1 charged ion (Cu^{+}) into the hydrophobic interior of the helical coiled coils.

Based on the dissociation constants for both Cu(I) and Cu(II), the reduction potentials for $Cu(II)(TRIW\text{-}H)_3^{2+}$ were calculated to be 400(30) mV at pH 5.9 and 430(30) mV at pH 7.4. The 30 mV error originates from the reported E^o of $Cu(II)/(I)_{aq}$ redox couple, not from experiments. If one takes the experimental error and calculates the standard deviation of the reduction potentials, they are less than ±10 mV for both pH conditions. This redox potential value is higher than those measured for T2Cu centers in NiR (218 mV at pH 6.0 and 137 mV at pH 8.4 for *R. sphaeroides*, 220–310 mV at pH 7.0 for *A. cycloclastes* and *A. xylosoxidans*).[21,92] One possible explanation for this relatively high reduction potential for this system is that Cu(I) is strongly stabilized by its distorted trigonal planar structure. The coordination number changes from three to five when $Cu(I)(TRIW\text{-}H)_3^{+}$ is oxidized to $Cu(II)(TRIW\text{-}H)_3^{2+}$, which requires the change of geometry of the site, creating a relatively large energy barrier for oxidation. The T2Cu sites in native cuproproteins are coupled with either a T1Cu site or other cofactors to function. Although the potential of the T1Cu sites in native proteins spans from 350 to 790 mV,[7,93] those of T2Cu centers are lower. For example, the potential of the T2Cu site in laccase (extracted from *Rhus vernicifera*), is one of the highest (390 mV at pH 7.4),

but still lower than that of our construct.[94] The different redox potential between Cu(II)/(I)(TRIW-H)$_3^{2+/+}$ system and the T2Cu center in CuNiR mainly originates from the difference in copper coordination environment. To use the thermodynamic box shown in Scheme II-1, the system has to reach an equilibrium for all the species involved, which requires the association of water molecule(s) and the re-orientation of imidazoles when Cu(I)(TRIW-H)$_3^+$ loses one electron.

Table II-9. Dissociation constants of Cu(n)(TRIW-H)$_3^{n+}$ compared to similar systems

Cu(I) affinity	K_d/M	Conditions	Ref
TRIW-H	$3.09(66) \times 10^{-12}$	pH 5.9	34
	$2.00(61) \times 10^{-13}$	pH 7.4	
Ctr1–14	1.58×10^{-13}	pH 7.4	90
Aβ42	5.3×10^{-8}	pH 7.4	91
Aβ16	1.3×10^{-7}	pH 7.4	91
Cu(II) affinity	**K_d/M**	**Conditions**	**Ref**
TRIW-H	$4.04(83) \times 10^{-8}$	pH 5.9	34
	$8.69(112) \times 10^{-9}$	pH 7.4	
Ctr1–14	1.00×10^{-11}	pH 7.4	90
mPrP(90-114)	1.3×10^{-8}	pH 7.4	95
CopC	10^{-13}	pH 7.0	96
Aβ42	$7(2) \times 10^{-7}$	pH 7.4	97
Aβ16	$1.0(2) \times 10^{-6}$	pH 7.4	97

Kinetics of nitrite reduction catalyzed by Cu(II)(TRIW-H)$_3^{2+}$

Although higher than those of NiRs, these redox potentials suggest that Cu(I)(TRIW-H)$_3^+$ could have NiR activity [formal E^0 of nitrite ~1.3 V at pH 6.0[2]]. Because the redox potential of ascorbate in the pH range 5–7 is ~100 mV, the bleaching of the 643 nm *d–d* band occurs within the mixing time, forming reduced Cu(I)(TRI-H)$_3^+$ *in situ*. The reductive half reaction (the reduction of nitrite to nitric oxide), however, is

much slower than the oxidative half (the oxidation of ascorbate to dehydroascorbate), and is pH-dependent. The plot of the logarithm of the rate of the reaction against the pH shows a linear correlation with a slope of 0.85, indicating that the rate-limiting step of the reaction is a one-proton process. The reasons for this pH dependence do not stand, as found for the native CuNiR, in the deprotonation of a coordinated water molecule at the Cu(II)$(His)_3$ site,[21,98] as both the visible absorption and the EPR spectra do not show significant changes in the pH range 5.2–7.4. Spectroscopic studies suggest that the pK_a of coordinated water is 8.53(2) (Figure II-19B), which is out of the pH range that I carried out the NiR assay. More likely, this pH dependence is the result of either some changes at the Cu(I)$(His)_3$ active site in that pH range [as suggested by changes in the NMR spectra of Cu(I)$(TRI\text{-}H)_3^+$][34] or the involvement of H^+ in the reduction step of nitrite to NO (Scheme II-2).

Under catalytic conditions, Cu(II)$(TRIW\text{-}H)_3^{2+}$ undergoes five turnovers after 220 min, expressed as moles of electrons per mole of Cu(II). No catalyst decomposition is observed as the progress curve for absorbance vs. time remains in the linear regime throughout the 220 min reaction time. Hence, the turnover number is limited by the amount of the electron donor rather than the stability of the catalyst. The rate constants for the oxidation of ascorbate by Cu(II)$(TRI\text{-}H)_3^{2+}$ ($k_{first,Asc}$, Table II-4) under catalytic conditions match the first-order rate constants $k_{first,Cu}$ for the oxidation of Cu(I)$(TRI\text{-}H)_3^+$ by nitrite (both k_{first} values refer to samples containing 30 mM nitrite) reasonably well. This demonstrates that the electron transfer from Cu(I)$(TRI\text{-}H)_3^+$ to nitrite with the formation of Cu(II)$(TRI\text{-}H)_3^{2+}$ is the rate-determining step of the overall catalytic process, and rules out the possibility of ascorbate consumption by the NO formed from the reaction, which should lead to the observed values for $k_{first,Asc}$ significantly larger than those of $k_{first,Cu}$.

One should be cautious that the mechanism of this model may differ from that of the native CuNiR because the oxidation states for copper under turnover conditions are not the same. In CuNiR, nitrite binds to Cu(II) followed by electron transfer, which initiates the reduction of the substrate.[20,73,99] Dr. Matteo Tegoni demonstrated the binding of a diatomic molecule carbon monoxide to Cu(I)$(TRI\text{-}H)_3^+$, which mimics the *product-enzyme intermediate* in the catalytic cycle of native CuNiR. I examined the possibility of

binding NO_2^- to Cu(II)(TRIW-H)$_3^{2+}$ as a model for the *substrate-enzyme complex*. The addition of NO_2^- induces changes in both g_{II} and A_{II} values, which are comparable to those reported for native CuNiRs (Table II-10). Nitrite can bind to a copper center in a few possible modes (Figure II-30). Based on DFT calculations for small molecule models, η^2 – O, O Cu(II)-NO_2^- has the lowest energy, although not much lower than the other two forms.[100] This lowest-energy mode is consistent with the crystal structure for nitrite-bound CuNiR (PDB code: 1AS6).[70] Similar to nitrite binding to native T2Cu in CuNiR, the nitrite-bound form of the Cu(II)(TRIW-H)$_3^{2+}$ still has the commonly observed $d_{x^2-y^2}$ as its ground state, which corresponds to an symmetric η^2 – O, O binding mode. Further interrogation of the binding modes and metric parameters of the substrate-bound form is necessary to understand the mechanistic details of this system.

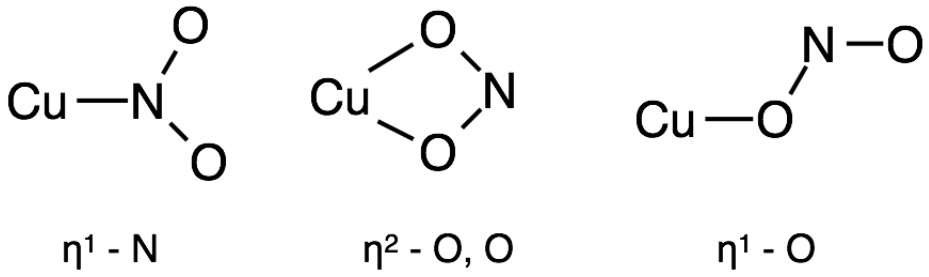

Figure II-30. Possible binding modes of nitrite to copper

Table II-10. EPR parameters of Cu(II)(TRIW-H)$_3^{2+}$ with/without NO_2^- compared to the T2Cu center in NiR

		$g_\perp$	g_{II}	A_{II}/mT	Organism	Ref
Cu(II)(TRIW-H)$_3^{2+}$	Without NO_2^-	2.050	2.270	18.6	-	This work
	With 50 eq. NO_2^-	2.034	2.282	16.4		
NiR (T2Cu)	Without NO_2^-	2.038	2.355	9.0	*Alcaligenes xylosoxidans*	101
	With 2 eq. NO_2^-	2.045	2.290	11.0		
NiR (T2Cu)	Without NO_2^-	-	2.34	12.5	*Rhodobacter sphaeroides*	54
	With 12 eq. NO_2^-	-	2.30	11.2		

Under turnover conditions in this system, however, the rapid reduction of Cu(II) by ascorbate ensures that the resting form of the enzyme is Cu(I). Thus, the interaction of nitrite with the reduced Cu(I) likely initiates catalysis. On the other hand, in the synthetic small molecule studies, nitrite prefers binding Cu(I) via the nitrogen atom, adopting η^1 – N binding mode (Figure II-30).[102–104] If this is true for this *de novo* designed system, the actual chemical conversion may not follow the same pathway as that in the native NiR. Cu(II)(TRI-H)$_3^{2+}$ exhibits a pseudo-first-order rate constant $k_{first,Asc}$ of 4.40×10^{-4} s^{-1} at pH 5.9 (Table II-4) with five turnovers in 3.7 h (pH 5.8), which is not very efficient as compared to native CuNiR (~1500 s^{-1} at pH 5.8 for *Alcaligenes faecalis* NiR with Pseudoazurin as the electron donor).[98] Nonetheless, these alternate reaction schemes suggest that the *de novo* designed Cu(II)/(I)(TRIW-H)$_3^{2+/+}$ may provide a unique approach to evaluate both types of chemistry within the same framework. For example, one may evaluate nitrite reduction from the cuprous form using existing protocols, but probe the chemistry of nitrite reduction from the cupric enzyme by photoinduced electron transfer after the nitrite has bound to Cu(II).

Numerous other mononuclear models that examine NiR reactivity have been explored so far.[102,104–108] These compounds are split into those whose activities have been investigated in nonaqueous solutions[48,107,108] and those that have been examined in aqueous solutions[102,106,109–112]. In the case of nonaqueous systems, the reaction rates are higher than those observed in aqueous solutions, and the ligands in some cases model the tris-His environment of NiR relatively well.[107,108,113] Although the nonaqueous conditions allow the control of the number of coordinating water, the use of these complexes does not account for several features of the NiR reaction, such as the different dielectrics between the exterior and the enzyme pocket and the hydrogen bonding network close to the T2Cu site. There are only a few examples of functional copper complexes that can reduce nitrite in aqueous solutions, and in general these systems have far lower rates that those observed in nonaqueous conditions. In some cases, these complexes produced N_2O rather than NO,[102,112] whereas the systems in which multiple turnovers were observed have been associated mostly with electrocatalytic reactions, particularly heterogeneous systems (i.e., catalyst linked to the electrode surface).[102,106,109,112] For example, a bis(6-methyl-2-pyridylmethyl)amine copper complex ($CuMe_2$bpa) has been reported that is

capable of at least four turnovers in 15 min using photoactivated $[Ru(II)(bpy)_3]^{2+}$ as the electron donor. This complex saw a significant decrease in nitric oxide generation after two turnovers.[110] Once this complex is attached to an electrode surface coated with a collagen film, the nitric oxide production rate goes up at the expense of the stability of the complex.[106] In contrast, our data demonstrate that $Cu(n)(TRIW\text{-}H)_3^{n+}$ is robust and carries out multiple turnovers with no decrease in efficiency. Equally important, the product of our reaction is dominantly NO as opposed to other homogeneous catalysts, which also form N_2O.[102,112] The latter point may reflect the steric constraints and the proper matching of the coordination geometry for Cu(I) and Cu(II) in our system.

I have described in this chapter the first generation of a *de novo* designed CuNiR model based on the TRI family peptide. This is a good, although not exact, structural model for the T2Cu center. It is also functional in catalyzing the reduction of nitrite into nitric oxide with modest rates. I have incorporated some of the most important features of this T2Cu center (protein environment, native histidines as binding residues, coordinated water molecule(s), stable oxidation states, *etc*.). This first generation of design is focused on the first coordination sphere, establishing a "reference point" for the properties of a $Cu(His)_3$ center, although there is still chemical space for improvement. Other key features that contribute to the activity in the native CuNiR include: 1) appropriate local environment (geometry, orientation of the imidazoles, local dielectrics) to achieve a relatively low redox potential of the copper center for nitrite reduction; 2) proper access and positioning of the substrate aided by a few important residues (Asp98, His255, Ile257) close to the copper center (Figure II-31); 3) an extended hydrogen bonding network proposed to be the proton transfer chain (Figure II-32). The effect of the important residues responsible for fixing nitrite can be most clearly seen if one compares the nitrite affinity to $Cu(II)(TRIW\text{-}H)_3^{2+}$ (1.5 ~ 2.1 mM) to that for the T2Cu in CuNiR (52 μM) from *Nitrosococcus oceani*.[114] The following two chapters will focus on a few of these features to tune the reduction potentials and improve the activity.

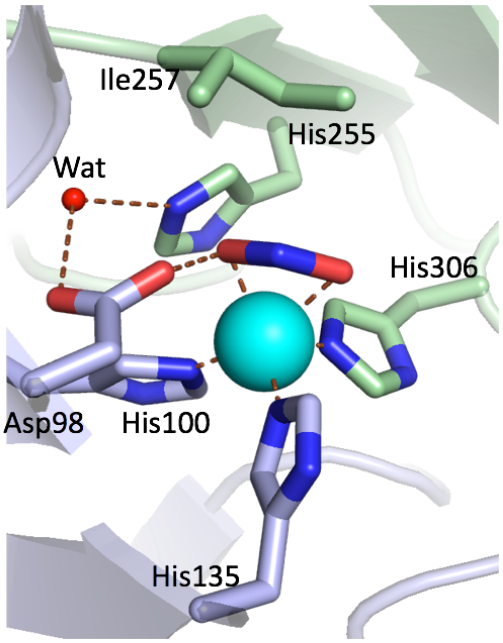

Figure II-31. Important residues involved in positioning nitrite. (PDB code: 1SJM)[99]

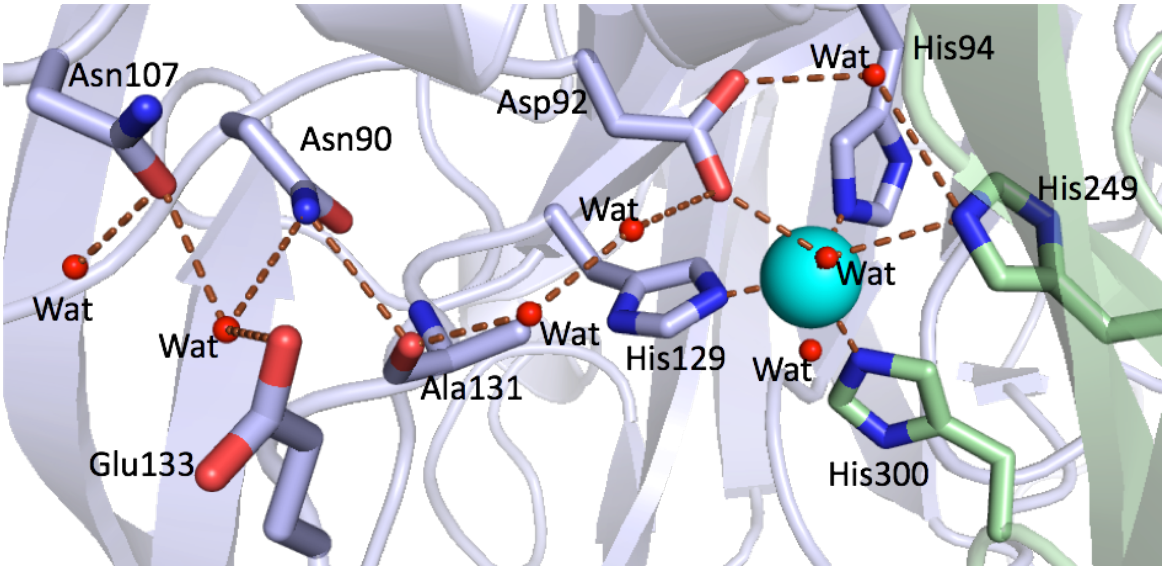

Figure II-32. Proposed proton transfer chain close to the T2Cu in CuNiR. (PDB code: 1HAU)[115]

Conclusion

The work discussed in this chapter demonstrates the first *de novo* designed functional CuNiR model. Utilizing a well understood scaffold TRI, we have previously

shown the design of a hydrolytic center that exhibits CA activity, which is one of the fastest designed models.[33] Designing a redox-active metal center in the helical coiled coils is arguably more challenging because a stable complex on both oxidation levels needs to be achieved. Compared to numerous small molecule mimics, this system represents an advanced stage of model chemistry. The hydrophobic/hydrophilic interface in the 3SCC mimics well the situation in native NiR, where the macromolecule is soluble in aqueous solutions while the interior is not necessarily hydrophilic. In addition, the isolation of the T2Cu center from native CuNiR to a designed protein environment excludes the interference from other chromophores. Not only is our construct stable on both oxidation levels, but its spectroscopic parameters are highly similar to the $Cu(His)_3$ centers in many copper proteins, establishing a foundation for expanding its reactivities. Although the current construct Cu(II)/(I)$(TRIW\text{-}H)_3^{2+/+}$ has a redox potential that is higher than most reported cases of $Cu(His)_3$ centers in a protein matrix, the *in situ* cyclic reduction/oxidation of the system is still achieved by adding sodium ascorbate/nitrite. More importantly, Cu(II)/(I)$(TRIW\text{-}H)_3^{2+/+}$ is a functional mimic for CuNiR, catalyzing the reduction of nitrite exclusively into nitric oxide. Using this first generation model, I can really start to address the question of how much NiR activity a $Cu(His)_3$ center can confer, then build extended structures (H-bonding, altered side-chain packing) upon this model to improve the activity. The highly modular nature of the TRI family peptides allows for designs beyond the first coordination sphere of the metal center. In summary, Cu(II)/(I)$(TRIW\text{-}H)_3^{2+/+}$ is an advanced structural and functional NiR model in aqueous solutions.

References

(1) Klinman, J. P. *Chem. Rev.* **1996**, *96*, 2541–2562.
(2) Averill, B. A. *Chem. Rev.* **1996**, *96*, 2951–2964.
(3) Crichton, R. R.; Pierre, J. L. *Biometals* **2001**, *14*, 99–112.
(4) Solomon, E. I.; Szilagyi, R. K.; DeBeer George, S.; Basumallick, L. *Chem. Rev.* **2004**, *104*, 419–458.
(5) Rosenzweig, A. C.; Sazinsky, M. H. *Curr. Opin. Struct. Biol.* **2006**, *16*, 729–735.
(6) MacPherson, I. S.; Murphy, M. E. P. *Cell. Mol. Life Sci.* **2007**, *64*, 2887–2899.
(7) Solomon, E. I.; Sundaram, U. M.; Machonkin, T. E. *Chem. Rev.* **1996**, *96*, 2563–2606.
(8) Solomon, E. I.; Ginsbach, J. W.; Heppner, D. E.; Kieber-Emmons, M. T.; Kjaergaard, C. H.; Smeets, P. J.; Tian, L.; Woertink, J. S. *Faraday Discuss.* **2011**, *148*, 11.
(9) Solomon, E. I.; Hadt, R. G. *Coord. Chem. Rev.* **2011**, *255*, 774–789.
(10) Solomon, E. I.; Chen, P.; Metz, M.; Lee, S.-K.; Palmer, A. E. *Angew. Chem. Int. Ed. Engl.* **2001**, *40*, 4570–4590.
(11) Hannan, J. P.; Busch, J. L. H.; Breton, J.; James, R.; Thomson, A. J.; Moore, G. R.; Davy, S. L. *J. Biol. Inorg. Chem.* **2000**, *5*, 432–447.
(12) Kaim, W.; Rall, J. *Angew. Chem. Int. Ed. Engl.* **1996**, *35*, 43–60.
(13) Prigge, S. T.; Kolhekar, A. S.; Eipper, B. A.; Mains, R. E.; Amzel, L. M. *Science* **1997**, *278*, 1300–1305.
(14) Chufán, E. E.; Prigge, S. T.; Siebert, X.; Eipper, B. A.; Mains, R. E.; Amzel, L. M. *J. Am. Chem. Soc.* **2010**, *132*, 15565–15572.
(15) Evans, J. P.; Blackburn, N. J.; Klinman, J. P. *Biochemistry* **2006**, *45*, 15419–15429.
(16) Kline, C. D.; Mayfield, M.; Blackburn, N. J. *Biochemistry* **2013**, *52*, 2586–2596.
(17) Libby, E.; Averill, B. A. *Biochem. Biophys. Res. Commun.* **1992**, *187*, 1529–1535.
(18) Moura, I.; Moura, J. J. *Curr. Opin. Chem. Biol.* **2001**, *5*, 168–175.
(19) Pinho, D.; Besson, S.; Brondino, C. D.; de Castro, B.; Moura, I. *Eur. J. Biochem.* **2004**, *271*, 2361–2369.
(20) Tocheva, E. I.; Rosell, F. I.; Mauk, a G.; Murphy, M. E. P. *Science* **2004**, *304*, 867–870.
(21) Jacobson, F.; Pistorius, A.; Farkas, D.; De Grip, W.; Hansson, O.; Sjölin, L.; Neutze, R. *J. Biol. Chem.* **2007**, *282*, 6347–6355.
(22) Hirota, S.; Iwamoto, T.; Tanizawa, K.; Adachi, O.; Yamauchi, O. *Biochemistry* **1999**, *38*, 14256–14263.
(23) *Copper Amine Oxidases: Structures, Catalytic Mechanisms, and Role in Pathophysiology*; Floris, G.; Mondovi, B., Eds.; CRC Press, **2009**.
(24) Johnson, B. J.; Cohen, J.; Welford, R. W.; Pearson, A. R.; Schulten, K.; Klinman, J. P.; Wilmot, C. M. *J. Biol. Chem.* **2007**, *282*, 17767–17776.
(25) Oka, T.; Simpson, F. J. *Biochem. Biophys. Res. Commun.* **1971**, *43*, 1–5.
(26) Steiner, R. A.; Kooter, I. M.; Dijkstra, B. W. *Biochemistry* **2002**, *41*, 7955–7962.
(27) Steiner, R. A.; Meyer-Klaucke, W.; Dijkstra, B. W. *Biochemistry* **2002**, *41*, 7963–7968.

(28) Fusetti, F.; Schro, K. H.; Steiner, R. a; Noort, P. I. Van; Pijning, T.; Rozeboom, J.; Dijkstra, B. W.; Groningen, A. G.; Noortlaan, O. Van; Schröter, K. H.; van Noort, P. I.; Rozeboom, H. J.; Kalk, K. H.; Egmond, M. R. *Structure* **2002**, *10*, 259–268.
(29) Schaab, M. R.; Barney, B. M.; Francisco, W. A. *Biochemistry* **2006**, *45*, 1009–1016.
(30) Ghadiri, M. R.; Case, M. A. *Angew. Chem. Int. Ed. Engl.* **1993**, *32*, 1594–1597.
(31) Tanaka, T.; Mizuno, T.; Fukui, S.; Hiroaki, H.; Oku, J.-I.; Kanaori, K.; Tajima, K.; Shirakawa, M. *J. Am. Chem. Soc.* **2004**, *126*, 14023–14028.
(32) Kiyokawa, T.; Kanaori, K.; Tajima, K.; Koike, M.; Mizuno, T.; Oku, J. J.-I. I.; Tanaka, T. *J. Pept. Res.* **2004**, *63*, 347–353.
(33) Zastrow, M. L.; Peacock, A. F. A.; Stuckey, J. A.; Pecoraro, V. L. *Nat. Chem.* **2012**, *4*, 118–123.
(34) Tegoni, M.; Yu, F.; Bersellini, M.; Penner-Hahn, J. E.; Pecoraro, V. L. *Proc. Natl. Acad. Sci. U. S. A.* **2012**, *109*, 21234–21239.
(35) Meyer, M.; Albrecht-Gary, A.-M.; Dietrich-Buchecker, C. O.; Sauvage, J.-P. *Inorg. Chem.* **1999**, *38*, 2279–2287.
(36) Chang, W. C.; White, P. D. In *Fmoc Solid Phase Peptide Synthesis: A Practical Approach*; Chang, W. C.; White, P. D., Eds.; Oxford University Press: New York, **2000**.
(37) Farrer, B. T.; Harris, N. P.; Valchus, K. E.; Pecoraro, V. L. *Biochemistry* **2001**, *40*, 14696–14705.
(38) *The Protein Protocols Handbook*; Walker, J. M., Ed.; Second Edi.; Humana Press Inc.: Totowa, NJ, **2002**.
(39) Dieckmann, G. R.; McRorie, D. K.; Lear, J. D.; Sharp, K. A.; DeGrado, W. F.; Pecoraro, V. L. *J. Mol. Biol.* **1998**, *280*, 897–912.
(40) Krężel, A.; Bal, W. *J. Inorg. Biochem.* **2004**, *98*, 161–166.
(41) George, G. N. EXAFSPAK. SSRL, Stanford University, USA. Available at http://ssrl. slac. stanford. edu/exafspak/html. *EXAFSPAK*, 2000.
(42) Ankudinov, A.; Rehr, J. *Phys. Rev. B* **1997**, *56*, R1712–R1716.
(43) Xiao, Z.; Loughlin, F.; George, G. N.; Howlett, G. J.; Wedd, A. G. *J. Am. Chem. Soc.* **2004**, *126*, 3081–3090.
(44) Noble, J. E.; Bailey, M. J. A. In *Methods in enzymology*; Elsevier Inc., **2009**; Vol. 463, pp. 73–95.
(45) Binstead, R. A.; Zuberbühler, A. D.; Jung, B. SPECFIT/32, **2004**.
(46) Sokołowska, M.; Bal, W. *J. Inorg. Biochem.* **2005**, *99*, 1653–1660.
(47) Atkins, P.; Overton, T.; Rourke, J.; Weller, M.; Armstrong, F.; Hagerman, M. *Inorganic Chemistry*; Fifth Edit.; Oxford University Press, W. H. Freeman and Company: New York, **2010**.
(48) Monzani, E.; Anthony, G. J.; Koolhaas, a; Spandre, a; Leggieri, E.; Casella, L.; Gullotti, M.; Nardin, G.; Randaccio, L.; Fontani, M.; Zanello, P.; Reedijk, J. *J. Biol. Inorg. Chem.* **2000**, *5*, 251–261.
(49) Karayannis, M. I.; Samios, D. N.; Gousetis, C. H. P. *Anal. Chim. Acta* **1977**, *93*, 275–279.
(50) Yaghi, B.; Houache, O. *J. Eng. Comput. Archit.* **2008**, *2*, 11–21.
(51) Kau, L. S.; Spira-Solomon, D. J.; Penner-Hahn, J. E.; Hodgson, K. O.; Solomon, E. I. *J. Am. Chem. Soc.* **1987**, *109*, 6433–6442.

(52) Dimakis, N.; Bunker, G. *Phys. Rev. B* **2002**, *65*, 201103.
(53) Prenesti, E.; Daniele, P. G.; Prencipe, M.; Ostacoli, G. *Polyhedron* **1999**, *18*, 3233–3241.
(54) Olesen, K.; Veselov, A.; Zhao, Y.; Wang, Y.; Danner, B.; Scholes, C. P. P.; Shapleigh, J. P. P. *Biochemistry* **1998**, *37*, 6086–6094.
(55) Fittipaldi, M.; Wijma, H. J.; Verbeet, M. P.; Canters, G. W.; Huber, M. *Appl. Magn. Reson.* **2006**, *30*, 417–426.
(56) Neves, I.; Freire, C.; Zakhárov, A. N.; de Castro, B.; Figueiredo, J. L. *Colloids Surf. A. Physicochem. Eng. Asp.* **1996**, *115*, 249–256.
(57) Li, F.; Delgado, R.; Costa, J.; Drew, M. G. B.; Felix, V. *Dalton Trans.* **2005**, 82–91.
(58) Buchen, T.; Hazell, A.; Jessen, L.; McKenzie, C. J.; Nielsen, L. P.; Pedersen, J. Z.; Schollmeyer, D. *Dalton Trans.* **1997**, 2697–2704.
(59) Shepard, E. M.; Juda, G. a; Ling, K.-Q.; Sayre, L. M.; Dooley, D. M. *J. Biol. Inorg. Chem.* **2004**, *9*, 256–268.
(60) Deligeer; Kataoka, K.; Suzuki, S. *Bull. Chem. Soc. Jpn.* **2001**, *74*, 183–184.
(61) Casella, L.; Carugo, O.; Gullotti, M.; Doldi, S.; Frassoni, M. *Inorg. Chem.* **1996**, *35*, 1101–1113.
(62) Xu, N.; Campbell, A. L. O.; Powell, D. R.; Khandogin, J.; Richter-Addo, G. B. *J. Am. Chem. Soc.* **2009**, *131*, 2460–2461.
(63) Kagann, R. H. *J. Mol. Spectrosc.* **1982**, *95*, 297–305.
(64) Zastrow, M. L.; Pecoraro, V. L. *J. Am. Chem. Soc.* **2013**, *135*, 5895–5903.
(65) Dooley, D. M.; Scott, R. A.; Knowles, P. F.; Colangelo, C. M.; McGuirl, M. A.; Brown, D. E. *J. Am. Chem. Soc.* **1998**, *120*, 2599–2605.
(66) Sanyal, I.; Karlin, K. D.; Strange, R. W.; Blackburn, N. J. *J. Am. Chem. Soc.* **1993**, *115*, 11259–11270.
(67) Wang, J.-W.; Cui, G.-H.; Qin, L.; Xiao, S.-L. *Zeitschrift für Naturforsch. B* **2013**, *68b*, 250–256.
(68) Flores, J. a; Andino, J. G.; Tsvetkov, N. P.; Pink, M.; Wolfe, R. J.; Head, A. R.; Lichtenberger, D. L.; Massa, J.; Caulton, K. G. *Inorg. Chem.* **2011**, *50*, 8121–8131.
(69) Zhang, J.-P.; Lin, Y.-Y.; Huang, X.-C.; Chen, X.-M. *Dalton Trans.* **2005**, 3681–3685.
(70) Murphy, M. E.; Turley, S.; Adman, E. T. *J. Biol. Chem.* **1997**, *272*, 28455–28460.
(71) Boulanger, M. J.; Murphy, M. E. P. *Biochemistry* **2001**, *40*, 9132–9141.
(72) Boulanger, M. J.; Kukimoto, M.; Nishiyama, M.; Horinouchi, S.; Murphy, M. E. *J. Biol. Chem.* **2000**, *275*, 23957–23964.
(73) Kataoka, K.; Furusawa, H.; Takagi, K.; Yamaguchi, K.; Suzuki, S. *J. Biochem.* **2000**, *127*, 345–350.
(74) Wijma, H. J.; Jeuken, L. J. C.; Verbeet, M. P.; Armstrong, F. a; Canters, G. W. *J. Am. Chem. Soc.* **2007**, *129*, 8557–8565.
(75) Matsumoto, J.; Kajita, Y.; Masuda, H. *Eur. J. Inorg. Chem.* **2012**, *2012*, 4149–4158.
(76) Kou, X.; Wu, J.; Cundari, T. R.; Dias, H. V. R. *Dalton Trans.* **2009**, *5887*, 915–917.

(77) Zhang, H.; Boulanger, M. J.; Mauk, A. G.; Murphy, M. E. P. *J. Phys. Chem. B* **2000**, *104*, 10738–10742.
(78) Jaron, S.; Blackburn, N. J. *Biochemistry* **2001**, *40*, 6867–6875.
(79) Himes, R. A.; Park, G. Y.; Barry, A. N.; Blackburn, N. J.; Karlin, K. D. *J. Am. Chem. Soc.* **2007**, *129*, 5352–5353.
(80) Costas, M.; Xifra, R.; Llobet, A.; Solà, M.; Robles, J.; Parella, T.; Stoeckli-Evans, H.; Neuburger, M. *Inorg. Chem.* **2003**, *42*, 4456–4468.
(81) Ebrahimpour, P.; Cushion, M.; Haddow, M. F.; Hallett, A. J.; Wass, D. F. *Dalton Trans.* **2010**, *39*, 10910–10919.
(82) Ferroni, F. M.; Guerrero, S. a; Rizzi, A. C.; Brondino, C. D. *J. Inorg. Biochem.* **2012**, *114*, 8–14.
(83) Chen, P.; Bell, J.; Eipper, B. a; Solomon, E. I. *Biochemistry* **2004**, *43*, 5735–5747.
(84) Dooley, D. M.; Coté, C. E. *J. Biol. Chem.* **1984**, *259*, 2923–2926.
(85) Fujii, T.; Naito, A.; Yamaguchi, S.; Wada, A.; Funahashi, Y.; Jitsukawa, K.; Nagatomo, S.; Kitagawa, T.; Masuda, H. *Chem. Commun. (Camb).* **2003**, *1*, 2700–2701.
(86) Sant'Ana, a. .; Alves, W. .; Santos, R. H. .; Ferreira, a. M. .; Temperini, M. L. . *Polyhedron* **2003**, *22*, 1673–1682.
(87) Barszcz, B.; Jabłońska-Wawrzycka, A.; Stadnicka, K.; Jezierska, J. *Polyhedron* **2008**, *27*, 3500–3508.
(88) Tamilarasan, R.; McMillin, D. R. *Biochem. J.* **1989**, *263*, 425–429.
(89) Antonyuk, S. V; Strange, R. W.; Sawers, G.; Eady, R. R.; Hasnain, S. S. *Proc. Natl. Acad. Sci. U. S. A.* **2005**, *102*, 12041–12046.
(90) Haas, K. L.; Putterman, A. B.; White, D. R.; Thiele, D. J.; Franz, K. J. *J. Am. Chem. Soc.* **2011**, *133*, 4427–4437.
(91) Alies, B.; Badei, B.; Faller, P.; Hureau, C. *Chem. --Eur. J.* **2012**, *18*, 1161–1167.
(92) Suzuki, S.; Yamaguchi, K.; Kataoka, K.; Kobayashi, K.; Tagawa, S.; Kohzuma, T.; Shidara, S.; Iwasaki, H. *J. Biol. Inorg. Chem.* **1997**, *2*, 265–274.
(93) Ghosh, S.; Xie, X.; Dey, A.; Sun, Y.; Scholes, C. P.; Solomon, E. I. *Proc. Natl. Acad. Sci. U. S. A.* **2009**, *106*, 4969–4974.
(94) Reinhammar, B. R. M.; Vangard, T. I.; Reinhammer, Bengt, R. M.; Vanngbrd, T. I. *Eur. J. Biochem.* **1971**, *18*, 463–468.
(95) Nadal, R. C.; Davies, P.; Brown, D. R.; Viles, J. H. *Biochemistry* **2009**, *48*, 8929–8931.
(96) Zhang, L.; Koay, M.; Maher, M. J.; Xiao, Z.; Wedd, A. G. *J. Am. Chem. Soc.* **2006**, *128*, 5834–5850.
(97) Maiti, N. C.; Jiang, D.; Wain, A. J.; Patel, S.; Dinh, K. L.; Zhou, F. *J. Phys. Chem. B* **2008**, *112*, 8406–8411.
(98) Wijma, H. J.; Jeuken, L. J. C.; Verbeet, M. P.; Armstrong, F. A.; Canters, G. W. *J. Biol. Chem.* **2006**, *281*, 16340–16346.
(99) Tocheva, E. I.; Eltis, L. D.; Murphy, M. E. *Biochemistry* **2008**, *47*, 4452–4460.
(100) Lehnert, N.; Cornelissen, U.; Neese, F.; Ono, T.; Noguchi, Y.; Okamoto, K.-I.; Fujisawa, K. *Inorg. Chem.* **2007**, *46*, 3916–3933.
(101) Howes, B. D.; Abraham, Z. H. L.; Lowe, D. J.; Bruser, T.; Eady, R. R.; Smith, B. E. *Biochemistry* **1994**, *33*, 3171–3177.

(102) Komeda, N.; Nagao, H.; Kushi, Y.; Adachi, G.; Suzuki, M.; Uehara, A.; Tanaka, K. *Bull. Chem. Soc. Jpn.* **1995**, *68*, 581–589.
(103) Fujisawa, K.; Tateda, A.; Miyashita, Y.; Okamoto, K.; Paulat, F.; Praneeth, V. K. K.; Merkle, A.; Lehnert, N. *J. Am. Chem. Soc.* **2008**, *130*, 1205–1213.
(104) Kujime, M.; Izumi, C.; Tomura, M.; Hada, M.; Fujii, H. *J. Am. Chem. Soc.* **2008**, *130*, 6088–6098.
(105) Richards, R. L.; Durrant, M. C. *J. Chem. Res.* **2002**, *2002*, 95–98.
(106) Isoda, N.; Yokoyama, H.; Nojiri, M.; Suzuki, S.; Yamaguchi, K. *Bioelectrochemistry* **2010**, *77*, 82–88.
(107) Kujime, M.; Fujii, H. *Angew. Chem. Int. Ed. Engl.* **2006**, *45*, 1089–1092.
(108) Woollard-Shore, J. G.; Holland, J. P.; Jones, M. W.; Dilworth, J. R. *Dalton Trans.* **2010**, *39*, 1576–1585.
(109) Hiratsu, T.; Suzuki, S.; Yamaguchi, K. *Chem. Commun. (Camb).* **2005**, 4534–4535.
(110) Yamaguchi, K.; Okada, T.; Suzuki, S. *Inorg. Chem. Commun.* **2006**, *9*, 989–991.
(111) Migita, Y.; Yokoyama, H.; Minami, A.; Mori, T.; Nojiri, M.; Suzuki, S.; Yamaguchi, K. *Electroanalysis* **2009**, 2441–2446.
(112) Nagao, H.; Komeda, N.; Mukaida, M.; Suzuki, M.; Tanaka, K. *Inorg. Chem.* **1996**, *35*, 6809–6815.
(113) Wasser, I. M.; de Vries, S.; Moënne-Loccoz, P.; Schröder, I.; Karlin, K. D. *Chem. Rev.* **2002**, *102*, 1201–1234.
(114) Kondo, K.; Yoshimatsu, K.; Fujiwara, T. *Microbes Environ.* **2012**, *27*, 407–412.
(115) Ellis, M. J.; Dodd, F. E.; Strange, R. W.; Prudêncio, M.; Sawers, G.; Eady, R. R.; Hasnain, S. S. *Acta Crystallogr. Sect. D Biol. Crystallogr.* **2001**, *57*, 1110–1118.

Chapter III . Modifications of charged residues at the helical interface to modulate the redox properties and NiR rates

Introduction

Understanding the relationship between structure and function has always been a major goal of biomimetic studies. Redox-active enzymes are critical in many biological processes, with metal cofactors accounting for many of the redox-related reactions.[1–5] For these metalloproteins, the redox-properties of the metal centers are highly sensitive to their protein environment. The influence of the coordinating ligands on the redox properties of the metal centers is evident.[6,7] Besides the first coordination sphere, factors on the outer coordination spheres also play an important role in fine-tuning the redox potentials. For example, the hydrophobicity of the environment could modulate the stability of the relevant oxidation states; the bulkiness of the amino acid residue side chains close to the active site could regulate the solvent/substrate access, changing the coordination number of different oxidation states; polar residues around the metal center can H-bond to metal-bound water molecules or coordinating ligands. All of these effects would influence the redox potential of a particular metal center. In addition, electrostatic interactions around the metal site are recognized to influence the redox properties. Charged amino acid residues, e.g. Glu, Lys, both in the interior and on the surface of the proteins, can participate in fine-tuning the potentials of redox-active metal sites.[8–11] Considerable effort has been devoted to understanding these interactions in native proteins, however, due to the complexity of native systems, it is always challenging to disentangle the contribution of each potentially influential factor.

A *de novo* design strategy provides an opportunity to generate biologically relevant models to understand structure-function relationships using a minimal construct.[12–15] In the previous chapter, I described the first generation of a NiR model based on a *de novo* design strategy, which represents one of the most efficient model

systems for NiR in aqueous solutions.[16] Prior to this work, there were very few cases of $Cu(His)_3$ sites in *de novo* designed peptides with controlled copper coordination.[17–19] $Cu(II)/(I)(TRIW\text{-}H)_3^{2+/+}$ is the first to have relatively well-characterized, stable Cu(I) and Cu(II) oxidation states that exhibits NiR activity in aqueous solutions. This initial design was focused solely on the first coordination sphere of copper, yielding a modest catalyst. To design a model with higher rates, the next logical step was to explore systematically secondary coordination sphere modifications around the copper. Of course, such studies are potentially relevant to understanding how solely electron transfer centers as found in PHM[20–23] are influenced by the same secondary coordination sphere modifications.

With a simplified polypeptide sequence, the local environment of metal centers may be modified rationally in order to investigate the important factors that govern the properties and functions of a specific site. After examining the sequence of TRI peptide, one realizes that the copper-binding His residues are in between two Lys residues, and there are a few Glu residues farther along the sequence. The role of these charged residues is to form salt bridges in a neutral pH range to stabilize the 3SCC. In the context of designing a redox-active center, the electric field framed by these charged residues can influence the redox potential of a metal center embedded in helical coiled coils. This prompted me to design a series of peptides to investigate how the charged residues influence the properties of $Cu(His)_3$ center. The sequences of the peptides involved in this chapter are shown in Table III-1. The work described in this chapter is based on reference [24].

The initial thought behind these designs was to decrease the local positive charge imparted by the Lys residues close to the His site. Since Lys as 22nd position is the closest to the copper-binding site, I replaced it with a Glu residue, leading to the parent peptide of the TRIW-EH series. Modifications are then applied to the other charged residues close to the copper binding site, yielding a series of peptides with 0, -3, -6, -9, and -12 charge differences from the first generation TRIW-H (Table III-1). In addition, TRIW-HK22Q, TRIW-HK24E, and TRIW-E_MH were designed as a comparison to the TRIW-EH series of peptides to examine the effect of Glu22.

Table III-1. Peptide sequences used in Chapter III. The color code used throughout corresponds to a change of charge compared to a single TRIW-H peptide. A difference of -2 charges is given in red, -1 in magenta, +1 in purple and +2 in blue.

Peptide[1]	Sequence	Δ_{charge}[2]
	a b c d e f g a b c d e f g a b c d e f g a b c d e f g	
TRIW-H	Ac-G WKALEEK LKALEEK LKALEEK HKALEEK G-NH_2	---
TRIW-HK22Q	Ac-G WKALEEK LKALEEK LKALEEQ HKALEEK G-NH_2	-3
TRIW-EHE27K	Ac-G WKALEEK LKALEEK LKALEEE HKALKEK G-NH_2	0
TRIW-EHE27Q	Ac-G WKALEEK LKALEEK LKALEEE HKALQEK G-NH_2	-3
TRIW-EH	Ac-G WKALEEK LKALEEK LKALEEE HKALEEK G-NH_2	-6
TRIW-EHK24Q	Ac-G WKALEEK LKALEEK LKALEEE HQALEEK G-NH_2	-9
TRIW-EHK24E	Ac-G WKALEEK LKALEEK LKALEEE HEALEEK G-NH_2	-12
TRIW-HK24E	Ac-G WKALEEK LKALEEK LKALEEK HEALEEK G-NH_2	-6
TRIW-E_MH[3]	Ac-G WKALEEK LKALEEK LKALEEE $_M$HKALEEK G-NH_2	-6

[1]C-terminus is capped by NH_2 group and N-terminus by acetyl (Ac) group.

[2]Δ_{charge} is defined as the difference in total charge of the specified 3SCC versus $(TRIW\text{-}H)_3$ assuming all Glu are fully deprotonated and all Lys are fully protonated. Polyglutamate or polylysine based ligands can exhibit a wide range of pK_a values when multiple side chains of the same type occur in the same peptide. Therefore, one should recognize that non-integrally charged peptides can exist due to incomplete acid-base chemistry.

[3]$_M$H stands for N-methyl-His, which has a methyl group on the $^{\delta}$N of the imidazole.

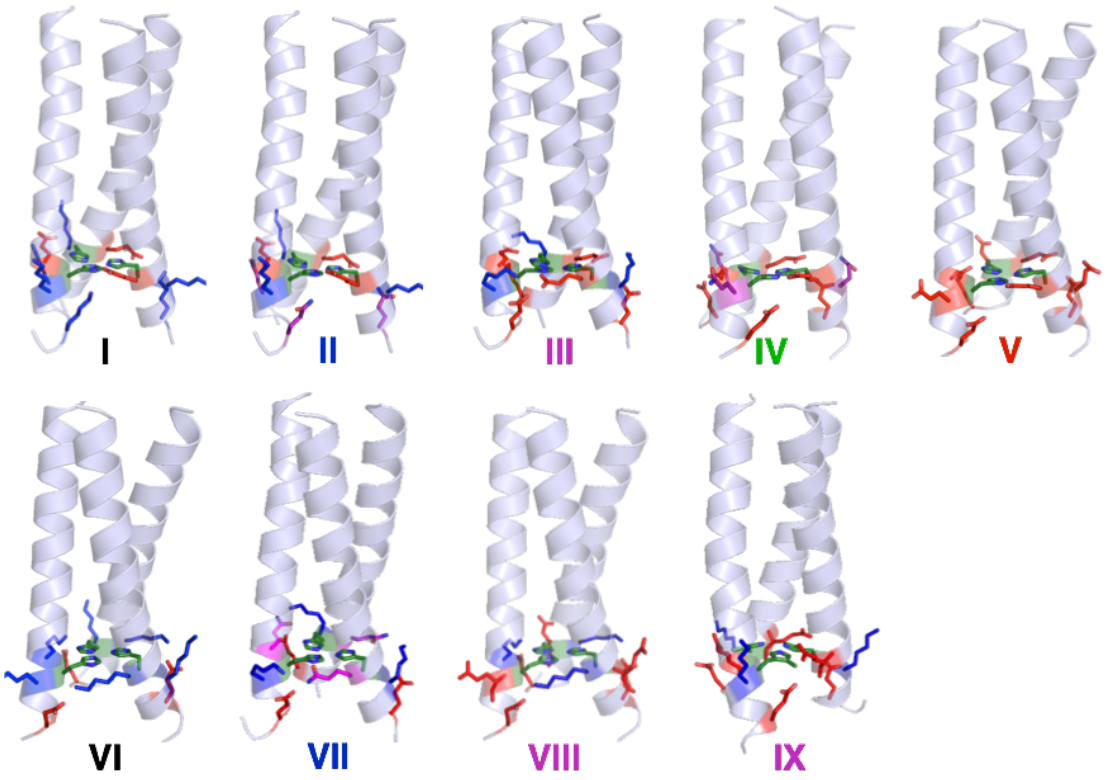

Figure III-1. PyMol models of I. TRIW-EHE27K; II. TRIW-EHE27Q; III. TRIW-EH; IV. TRIW-EHK24Q; V. TRIW-EHK24E; VI. TRIW-H; VII. TRIW-HK22Q; VIII. TRIW-HK24E; IX. TRIW-E_MH. These models are made based on the crystal structure of $Zn(II)_N Hg(II)_S(CSL9PenL23H)_3$ (PDB code: 3PBJ).[25] The same colored texts represent the same Δ_{charge}. Going from the left to the right, Δ_{charge} is 0, –3, –6, –9, and –12 in a neutral pH range.

Materials and methods

The sequences of the peptides used in this work are shown in Table III-1, with each heptad repeat given as *abcdefg*. Variations were made at the *b, e, g* positions of the heptad in addition to the L23H mutation.

General procedures.

The copper-peptide complexes were prepared by adding a solution of Cu(I) tetra(acetonitrile) tetrafluoroborate or Cu(II) chloride into a (buffered) solution of apo-peptide. Since the Cu(I)-peptide complexes undergo slow oxidation under aerobic conditions, all reactions concerning Cu(I) or nitrite reduction were carried out in an inert

atmosphere box. The procedures to determine the concentrations of both Cu(I) and Cu(II) solutions are described in Chapter II.

Peptide synthesis and purification.

All peptides in this work were synthesized on an Applied Biosystem 433A peptide synthesizer using standard protocols[26] and purified and characterized as previously reported.[27] The apo-peptide solution was prepared by dissolving purified dry peptides in doubly distilled water or buffer solutions. The peptide concentration was determined based on the tryptophan (Trp) absorbance at 280 nm (ε = 5500 $M^{-1}cm^{-1}$).[28]

Ultraviolet-Visible (UV-Vis) and fluorescence spectroscopy.

UV-Visible spectra were collected in quartz air-tight cuvettes at 25 ºC on a Cary100 Bio UV-Vis spectrophotometer. Emission spectra were recorded on a Fluomax-2 Fluorimeter at 25 ºC.

Circular Dichroism (CD) Spectroscopy.

CD spectra were collected on an AVIV 62DS spectrometer at 25 ºC using 1 cm quartz cuvettes. Guanidine hydrochloride (GuaHCl) titrations were carried out using an automated titrator with a Microlab 500 series syringe pump based on previously reported procedures.[29]

pK_a determination for Cu(II)-peptides.

The visible spectra of a solution containing 0.27 mM Cu-3SCC and 0.03 mM apo-3SCC (to ensure that > 99 % of Cu(II) is bound to the peptide) at various pH conditions were collected and pK_a fitted to Equation II-3.

Binding constants determination.

The binding constants of Cu(I) and Cu(II) were determined using the same procedure as described in Chapter II.

Redox potentials.

The redox potentials of Cu(II)/(I)-3SCC were calculated as described in Chapter II.

X-ray absorption spectroscopy (XAS).

Samples were made based on the same procedure as described in Chapter II. Data collection parameters follow those described in Chapter II. A detailed data fitting procedure is described in Chapter II.

EPR spectroscopy.

X-band EPR spectra were collected on a Bruker EMX electron spin resonance spectrometer with a Varian liquid nitrogen cryostat at 77 K. A sample of ~1mM Cu(II)$(3SCC)_3$ was prepared in a 50 mM buffer solution, and the pH was adjusted by adding concentrated HCl or KOH solution into the sample. An extra 0.5 mM apo-3SCC was added to ensure that the free Cu(II) is less than 0.1 %. 50% glycerol was used as a glassing agent. The EPR parameters were extracted by fitting the collected spectra to the simulated spectra using the EPR data fitting software SpinCount.

NiR activity.

NiR rates. 30 mM $NaNO_2$ was mixed with 0.18 mM Cu(II)(3SCC) and 0.09 mM apo-3SCC (to ensure that over 99% of Cu(II) is bound to the peptide). The reaction was initiated by adding 6 equivalents of sodium ascorbate (NaAsc) with respect to Cu(II). The consumption of sodium ascorbate (NaAsc) was monitored by UV-Visible spectroscopy. The control was a mixture of 30 mM $NaNO_2$ and 0.09 mM apo-3SCC with the same amount of NaAsc. The rates of the reaction were calculated by two times the different rates of NaAsc consumption (decrease of absorbance at 251 nm) between the sample and the control. The production of nitric oxide was examined using the method previously reported.[16]

Production of nitric oxide. A solution of 0.18 mM Cu(I), 0.27 mM 3SCC and 1.1 mM NaAsc in 50 mM potassium phosphate buffer was prepared in an inert atmosphere in a gas-tight reaction vessel. The pH was adjusted to 5.8 using small aliquots of KOH. The reaction was initiated by injecting a solution of $NaNO_2$ ($[NO_2^-]$ = 30 mM). The reaction mixture was stirred for 2-3 h. A 0.01 M pH 5.0 $[Fe(EDTA)]^{2-}$ solution was prepared by mixing 0.01 M $FeSO_4$ and 0.01 M H_2EDTA solution in a 1:1 ratio in an air-tight cuvette with a septum attached. The gas in the headspace of the reaction vessel was cannula-transferred to the cuvette. The absorption spectra were collected. $[Fe(NO)(EDTA)]^{2-}$ was quantified by the absorbance at 432 nm (ε = 780 $M^{-1}cm^{-1}$).[16,30]

Results

CD spectra of apo-peptides.

The CD spectra were collected for a solution of 20 μM apo-peptide monomer, 10 mM potassium phosphate at pH 7.0 (Figure III-2, Figure III-3). The double-well at 208 and 222 nm for all of the peptides involved in this study indicates the formation of helical coiled coils. Due to the lack of an initial plateau in the denaturation curves, I cannot extract a free energy of folding because the curves cannot be fitted to a two-state model.

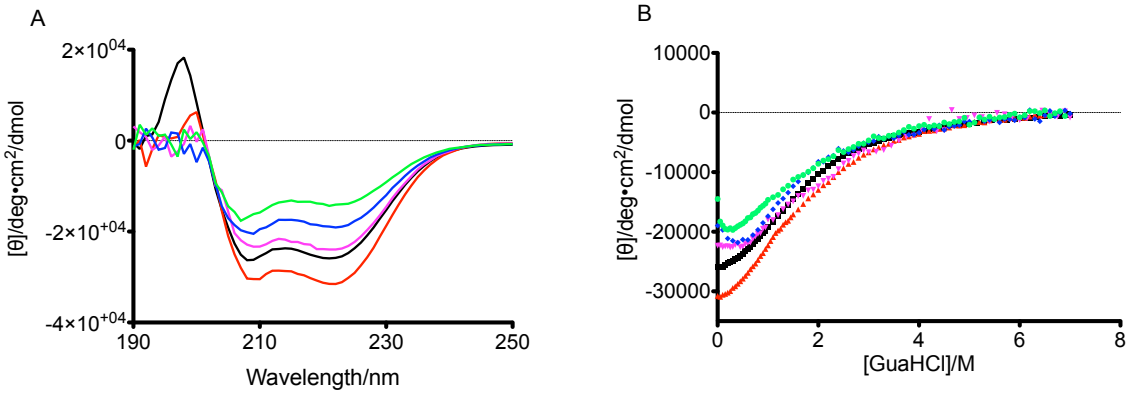

Figure III-2. (A) CD spectra of apo-peptides in the TRIW-EH series at pH 7.0. Black spectrum: TRIW-EHE27K; red spectrum: TRIW-EHE27Q, magenta spectrum: TRIW-EH; blue spectrum: TRIW-EHK24Q; green spectrum: TRIW-EHK24E. (B) GuaHCl denaturation titration for the above-described peptides at pH 7.0. The same color coding applies.

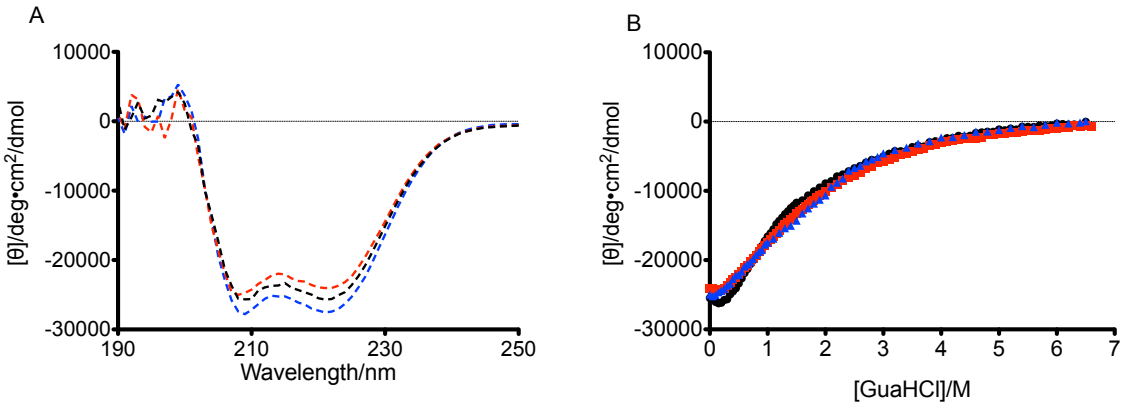

Figure III-3. (A) CD spectra of other peptides involved in this study at pH 7.0. Red dashed line: TRIW-E_MH; black dashed line: TRIW-HK24E; blue dashed line: TRIW-HK22Q. (B) GuaHCl denaturation titration for these peptides. The same color coding applies.

XAS of Cu(I)(TRIW-EH)$_3^+$ and its derivatives.

The XANES spectra of Cu(I)(TRIW-EHK24E)$_3^+$, Cu(I)(TRIW-EH)$_3^+$, and Cu(I)(TRIW-EHE27K)$_3^+$, all show a modest intensity peak at ~8983 eV, similar to that of Cu(I)(TRIW-H)$_3^+$ at pH 5.9 (Figure III-4). This is typical of Cu(I) in an approximately trigonal environment.[16,31] The near identity of these spectra shows that there are only minor structural differences between the copper sites.

The EXAFS data for Cu(I)(TRIW-EH)$_3^+$ and its derivatives support this structural interpretation. The Fourier transform is dominated by a peak at $R + a \approx 1.5$ Å typical of Cu-N or Cu-O nearest neighbor scattering, with pronounced outer-shell scattering typical of rigid ligands such as imidazole. Quantitative fitting (Figure III-5, Table III-2) confirms this structure. The nearest-neighbor distance of 1.93 Å is typical of three-coordinate Cu(I), and the outer-shell scattering can be modeled using three imidazole ligands, results that are quantitatively consistent with structural parameters reported previously for Cu(I)(TRIW-H)$_3$.[16] Attempts to fit the data with a Cu-O shell in addition to, or in place of one of the Cu-imidazole interactions did not give any improvement in the fit. The three peptides investigated here include the parent peptide of the TRIW-EH series, the peptide with the largest and the smallest Δ_{charge} in the series. They all bind Cu(I) in a trigonal planar environment. One might notice that there are small differences

in the fitting parameters for these peptides (Debye-Waller factors, outer-shell distances), which could be reflective of subtle geometry changes of the first coordination sphere or the orientation of the imidazole ring. These changes, however, do not exceed the difference between the TRIW-EH series peptides and TRIW-H. For example, for TRIW-EH series of peptides, the Debye-Waller factors are between 0.0067 and 0.0072, ~0.002 smaller than that of TRIW-H, suggesting a more ordered environment for TRIW-EH peptides. Since the two ends of the TRIW-EH series as well as the "mid-point" peptide TRIW-EH are examined, it is a logical assumption that the other two peptides TRIW-EHK24Q and TRIW-EHK24E also adopt the same Cu(I) coordination.

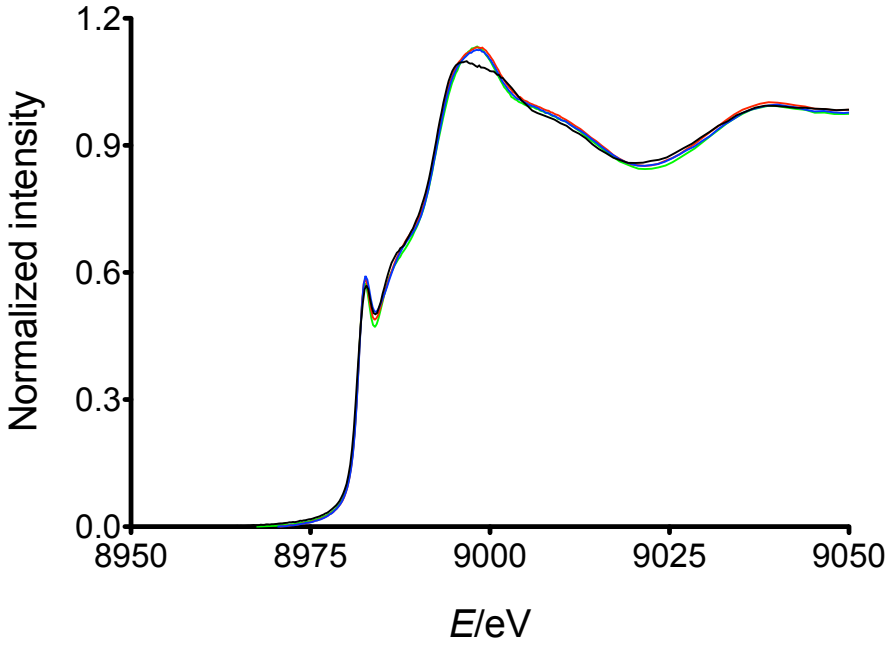

Figure III-4. XANES of Cu(I)(TRIW-H)$_3^+$ (black spectrum), Cu(I)(TRIW-EHE27K)$_3^+$ (green spectrum), Cu(I)(TRIW-EH)$_3^+$ (red spectrum), and Cu(I)(TRIW-EHK24E)$_3^+$ (blue spectrum) at pH 5.8.

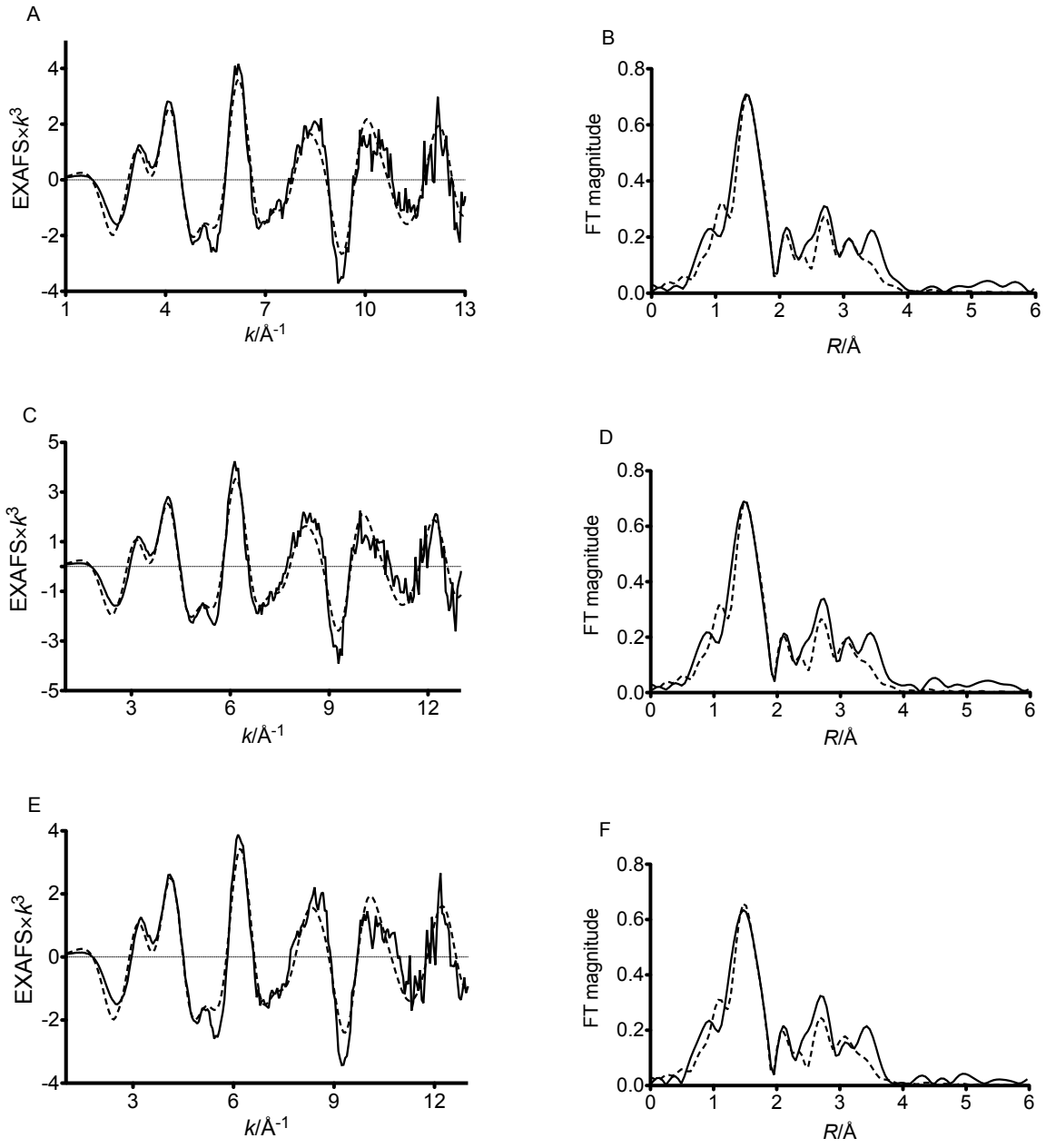

Figure III-5. EXAFS and FT data (solid line) and fitting (dashed line) for (A)(B) Cu(I)(TRIW-EHE27K)$_3^+$, (C)(D) Cu(I)(TRIW-EH)$_3^+$, (E)(F) Cu(I)(TRIW-EHK24E)$_3^+$ at pH 5.8.

Table III-2. EXAFS fitting parameters

Peptide	First shell	R/Å	σ^2/Å^2	Outer shells	R/Å	σ^2/Å^2	N_{var}	$F^2/(N_{free}) \times 10^{-2}$
$Cu(I)(TRIW\text{-}EHE27K)_3^+$	3 Cu(I)-N$^{(1)}$	1.930	0.0067	3 Cu-C$^{(1)}$	2.917	0.0101	2	4.5
				3 Cu-C$^{(2)}$	2.951	0.0102		
				3 Cu-N$^{(2)}$	4.058	0.0140		
				3 Cu-C$^{(3)}$	4.071	0.0141		
$Cu(I)(TRIW\text{-}EH)_3^+$	3 Cu(I)-N$^{(1)}$	1.934	0.0068	3 Cu-C$^{(1)}$	2.923	0.0103	2	3.8
				3 Cu-C$^{(2)}$	2.958	0.0104		
				3 Cu-N$^{(2)}$	4.002	0.0141		
				3 Cu-C$^{(3)}$	4.066	0.0143		
$Cu(I)(TRIW\text{-}EHK24E)_3^+$	3 Cu(I)-N$^{(1)}$	1.926	0.0072	3 Cu-C$^{(1)}$	2.911	0.0109	2	4.2
				3 Cu-C$^{(2)}$	2.946	0.0110		
				3 Cu-N$^{(2)}$	4.050	0.0152		
				3 Cu-C$^{(3)}$	4.063	0.0152		
$Cu(I)(TRIW\text{-}HK24E)_3^+$	3 Cu(I)-N$^{(1)}$	1.943	0.0081	3 Cu-C$^{(1)}$	2.937	0.0122	2	1.2
				3 Cu-C$^{(2)}$	2.972	0.0124		
				3 Cu-N$^{(2)}$	4.086	0.0170		
				3 Cu-C$^{(3)}$	4.099	0.0171		

1. R: absorber-backscatterer distance; σ^2: Debye-Waller factor. ΔE_0 is fixed at -10 eV. R (distance) and σ^2 (Debye-Waller

factor) are the only freely variable parameters (in red). Linked variables are in blue.

2. $N_{idp} = 2\Delta k \Delta R/\pi \sim 19$, $N_{free} = N_{idp} - N_{var}$. The outer shell parameters are calculated assuming a rigid imidazole ring.
3. The goodness of the fit is evaluated by $F' = F^2/(N_{free}) \times 10^{-2}$. The smaller the value, the better the fit.

XAS of Cu(I)(TRIW-HK24E)$_3^+$.

XANES of Cu(I)(TRIW-HK24E)$_3^+$ (Figure III-6) indicate that Cu(I) is three-coordinate, the same coordination number as the Cu(I) centers described above. The metrical parameters are similar to those of the TRIW-EH series of peptides as well as TRIW-H peptide (Table III-2, Figure III-7).

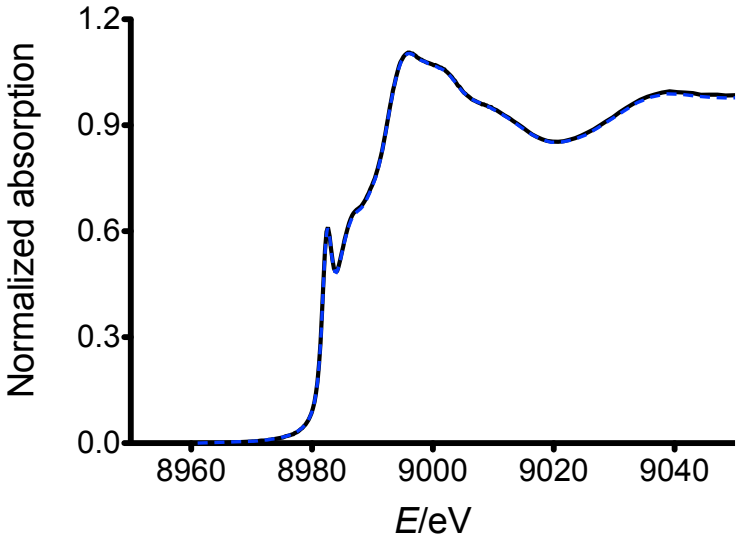

Figure III-6. XANES of Cu(I)(TRIW-HK24E)$_3^+$ at pH 5.8 (black spectrum) and 7.4 (dashed blue spectrum).

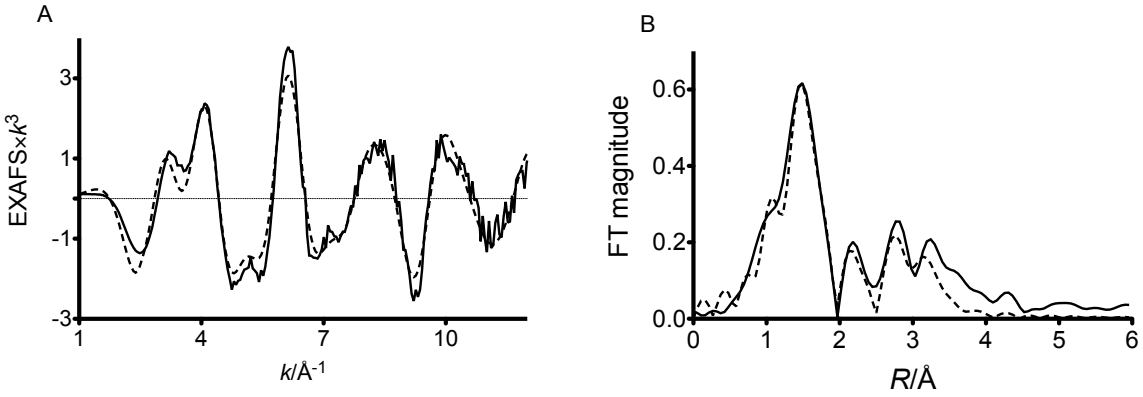

Figure III-7. EXAFS (A) and Fourier transform (B) of Cu(I)(TRIW-HK24E)$_3^+$. Experimental data are represented in solid lines and fittings are shown in dashed lines.

pK_a of Cu(II)-peptides.

As shown in Chapter II, Cu(II)(TRIW-H)$_3^{2+}$ has a deprotonation equilibrium reflected by the change of Cu(II) *d-d* band, which is most likely to be associated with the deprotonation of the Cu(II)-bound water molecule. The pK_a of this equilibrium is 8.53(2), corresponding to a one-proton process. Interestingly, the pH titration of Cu(II)(TRIW-EH)$_3^{2+}$ results in a pK_a distinctively different from the parent peptide (Table III-3). Similar to Cu(II)(TRIW-H)$_3^{2+}$, from the pH region 2.97-5.57, the increase of absorbance at 659 nm is indicative of copper binding to the peptide (Figure III-8A). However, when the pH is raised from 5.33 to 7.87, the absorbance at 659 nm decreases slightly (Figure III-8B), resulting in a pK_a = 6.33. This deprotonation event fits best to a 1.65(23) proton process (Figure III-8D), which suggested that the nature of this deprotonation might be different from the one for Cu(II)(TRIW-H)$_3^{2+}$. In a higher pH region, another set of spectral transformation is observed, which resembles that of Cu(II)(TRIW-H)$_3^{2+}$ (Figure III-8C). Similar effects are also observed for Cu(II)(TRIW-EHK24E)$_3$ (Figure III-9).

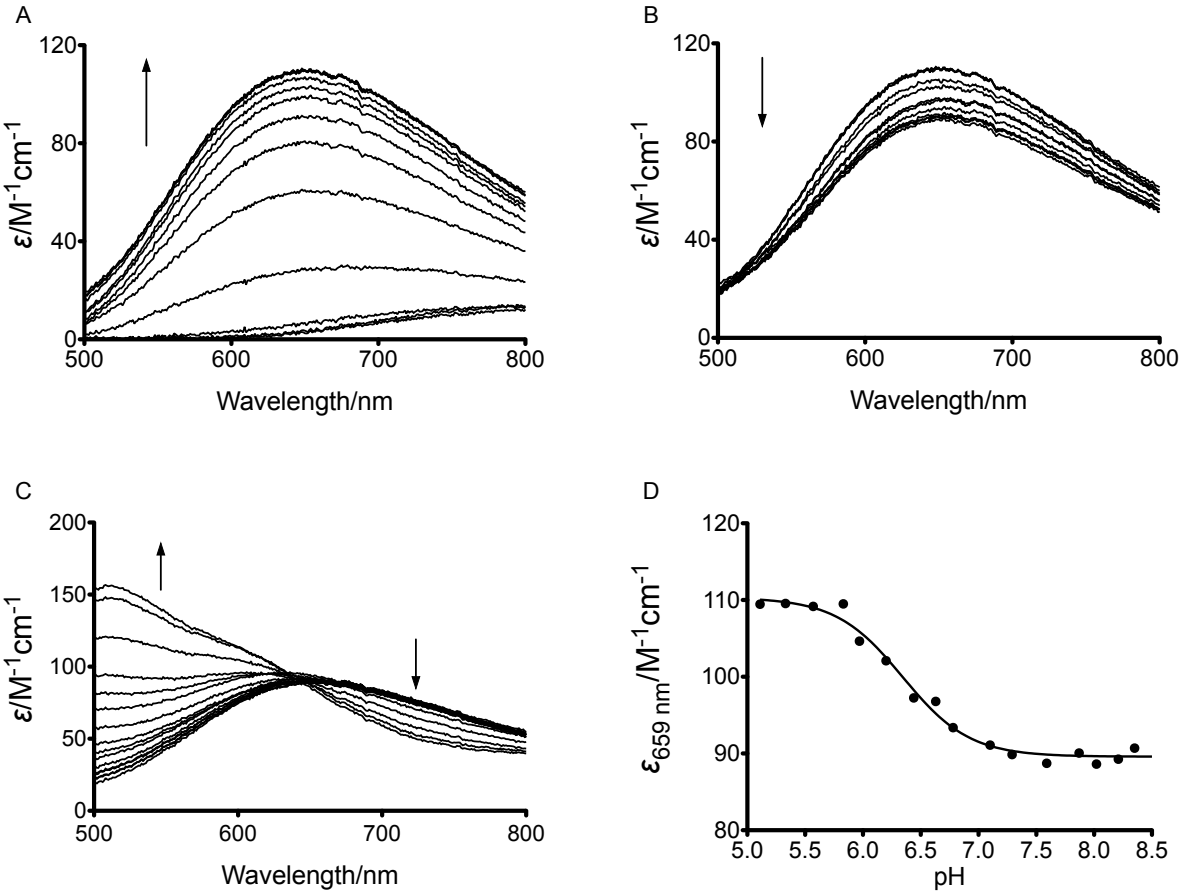

Figure III-8. pH titration spectra of Cu(II)(TRIW-EH)$_3^{2+}$ at (A) pH 2.92 to 5.57; (B) pH 5.33 to 7.87; (C) pH 7.59 to 10.65; (D) d-d band absorbance in pH 5–8.5 fitted to Equation II-3, pK_a = 6.33(4), n = 1.65(23).

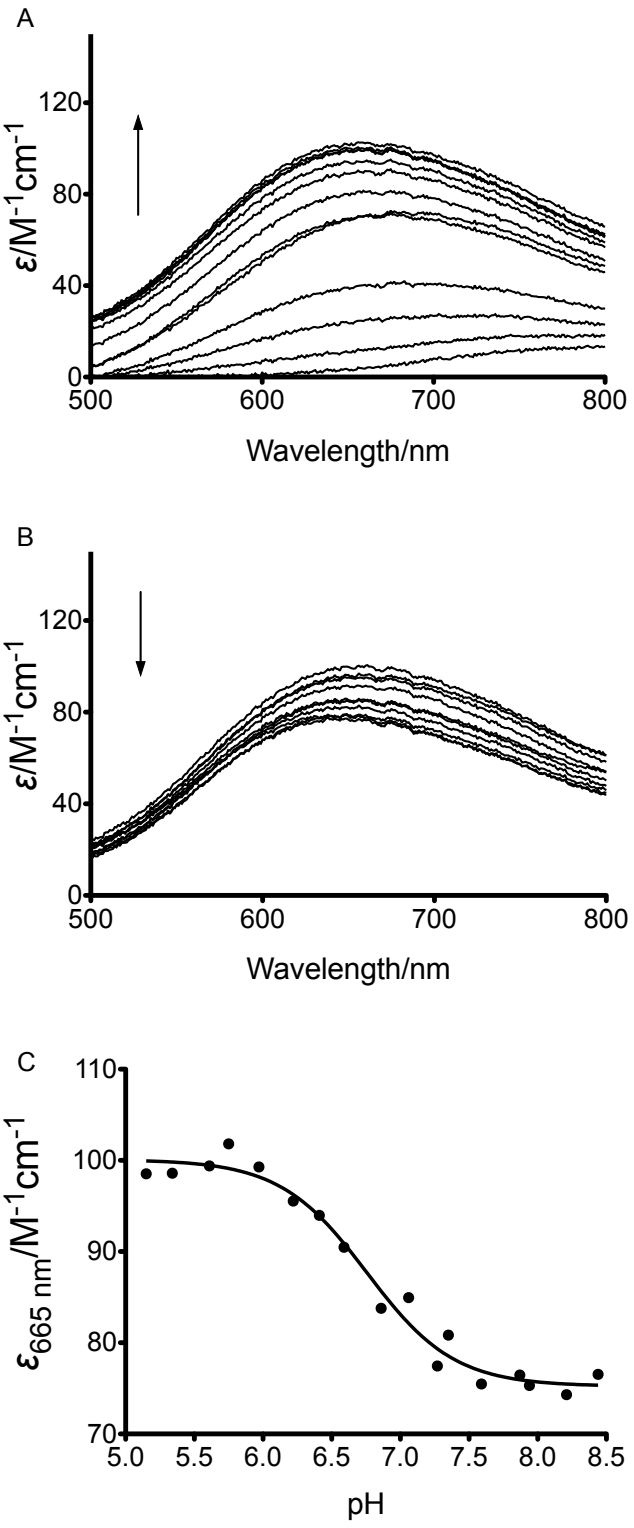

Figure III-9. pH titration spectra of Cu(II)(TRIW-EHK24E)$_3^{2+}$ at (A) pH 2.99-5.75; (B) pH 5.97-7.87; (C) d-d band absorbance fitted to Equation II-3, pK_a = 6.76(6), n = 1.37(25).

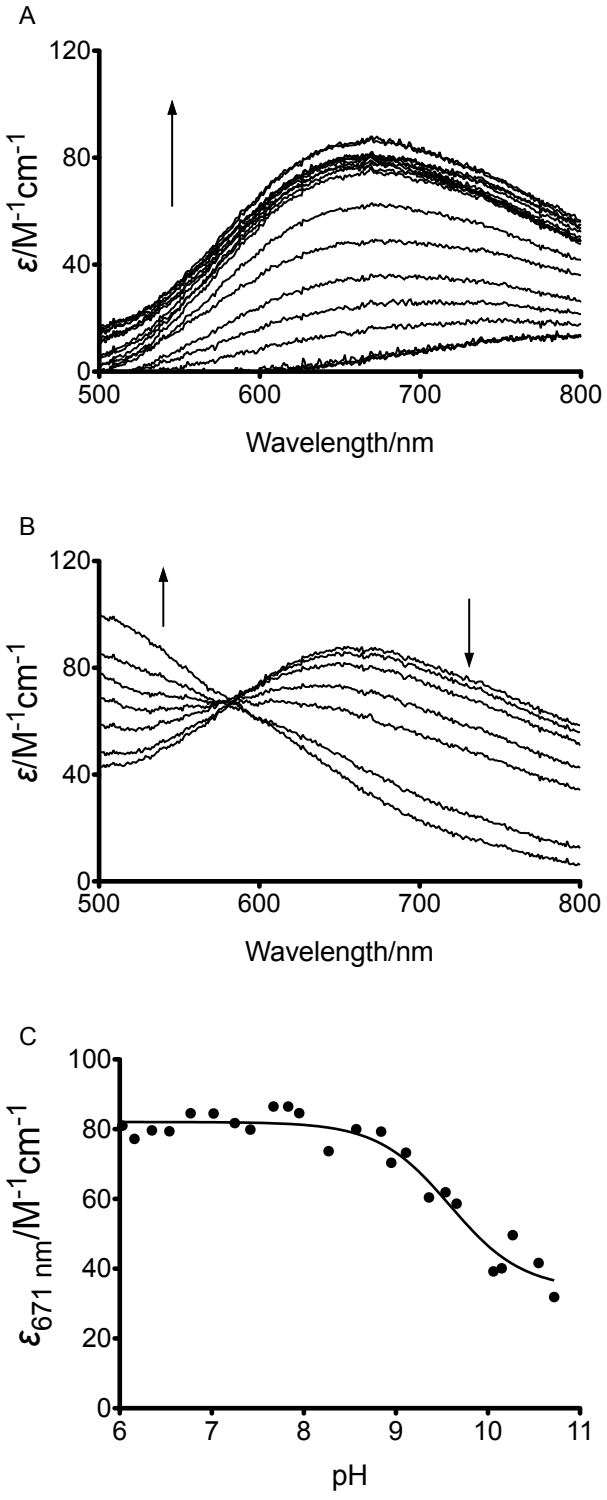

Figure III-10. pH titration spectra of Cu(II)(TRIW-EHE27K)$_3^{2+}$ at (A) pH 2.96-6.54; (B) pH 7.83-10.72; (C) d-d band absorbance fitted to Equation II-3, pK_a = 9.59(15), n = 1.10(31)

Different from the spectral evolution for Cu(II)(TRIW-EH)$_3^{2+}$ and Cu(II)(TRIW-EHK24E)$_3^{2+}$, the pH-dependent *d-d* absorption spectra for Cu(II)(TRIW-EHE27K)$_3^{2+}$ do not have a decrease in absorbance in the pH range of 5.8-7.4 (Figure III-10A and B). Only one deprotonation event is observed at a higher pH range, which is reminiscent of the Cu(II)-bound water deprotonation process (Figure III-10B).

pH titrations were also carried out for Cu(II)(TRIW-E$_M$H)$_3^{2+}$ and Cu(II)(TRIW-HK24E)$_3^{2+}$ as a comparison to peptides within the TRIW-EH series (Figure III-11, Figure III-12). These titrations share the common feature of increased *d-d* band absorption at pH below 5.5 and unvaried extinction coefficients when pH increases from 5.8 to 7.4.

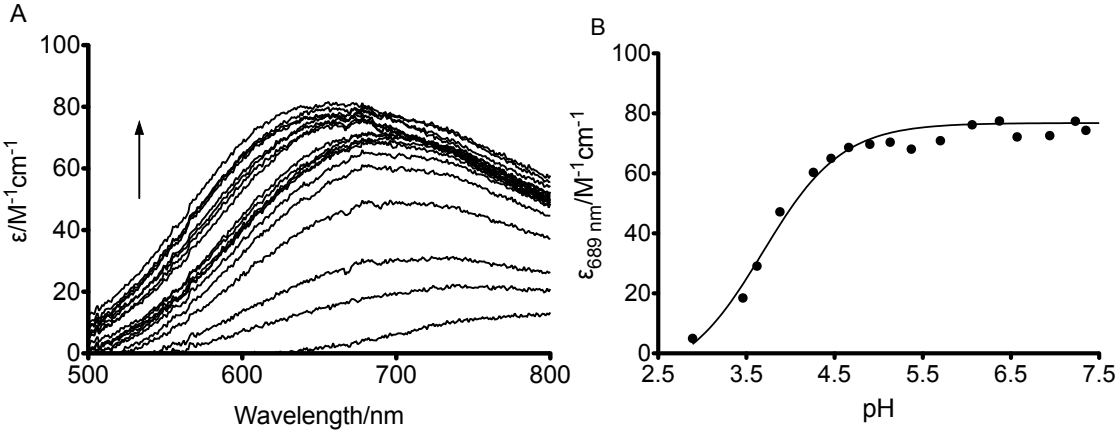

Figure III-11. pH titration for Cu(II)(TRIW-E$_M$H)$_3^{2+}$. (A) titration spectra at pH 2.89-7.81. (B) d-d band extinction coefficient at pH below 7.5, showing no decrease going from 5.8 to 7.4.

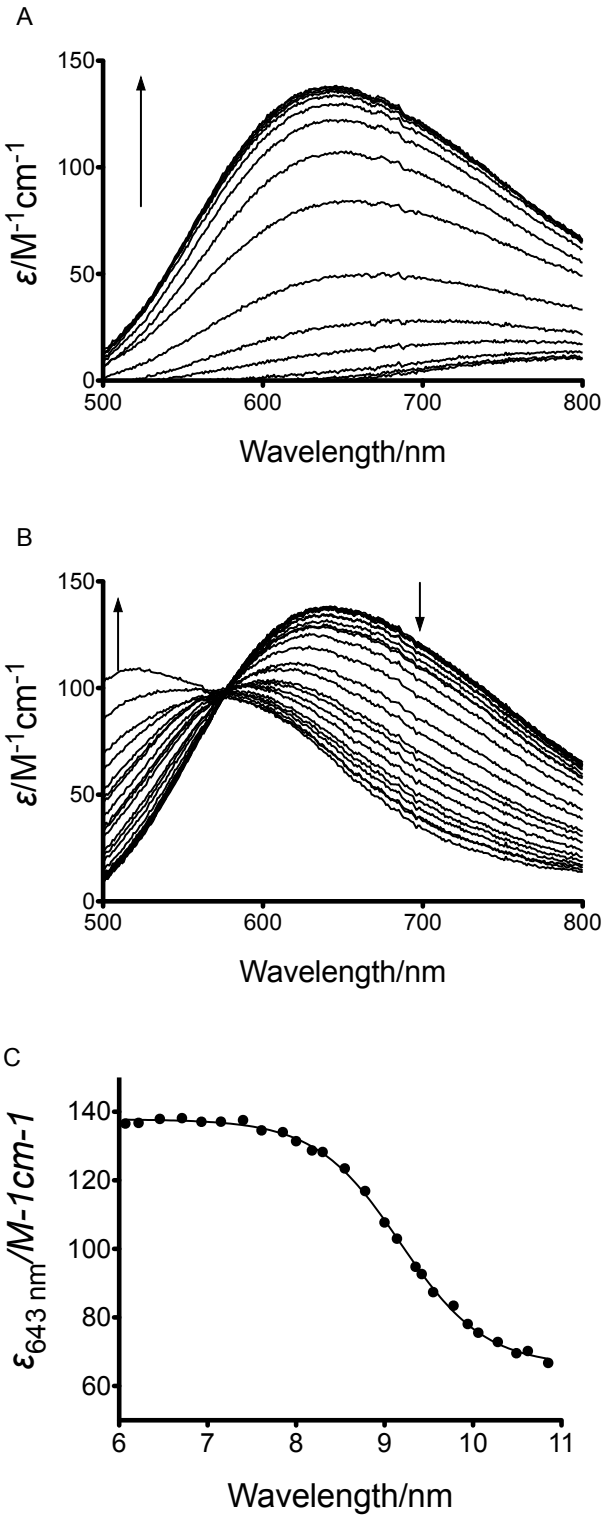

Figure III-12. pH titration spectra for Cu(II)(TRIW-HK24E)$_3^{2+}$. (A) pH 2.92 ~ 6.07; (B) pH 6.07 ~ 10.85; (C) d-d band absorbance fitted to Equation II-3, pK_a = 9.18(1), n = 0.91(3)

The Cu(II) *d-d* band evolves differently upon pH increase for different peptides within the pH region (5.8–7.4) that we are interested in (Figure III-13). In summary, Cu(II) *d-d* band appears when bound to different peptides and the transformations of the spectra are pH-dependent due to various deprotonation events.

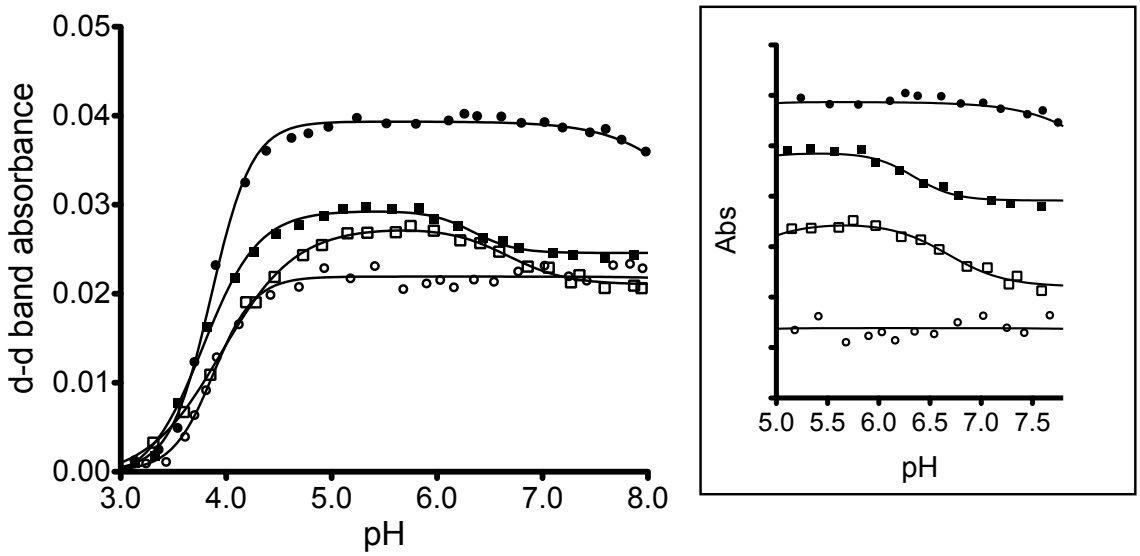

Figure III-13. Changes in Cu(II) *d-d* band absorbance when bound to TRIW-H (Δ_{charge} = 0), filled circles; TRIW-EHE27K (Δ_{charge} = 0), hollow circles; TRIW-EH (Δ_{charge} = -6), filled squares; and TRIW-EHK24E (Δ_{charge} = -12), hollow squares; insert: differences between the evolution of Cu(II)-peptide d-d band reveal different pK_a values (same symbols)

Table III-3. pK_a values and spectroscopic parameters of selected Cu(II)-peptides

Peptide	pK_a^E	pK_a^W	λ_{max}(ε/M^{-1} cm^{-1})/nm at pH 5.8	λ_{max}(ε/M^{-1} cm^{-1})/nm at pH 7.4
TRIW-H	-	8.53(2)	644(143)	644(143)
TRIW-EHE27K		9.59(15)	671(80)	671(79)
TRIW-EH	6.33(4)	9.86(5)	659(110)	659(89)
TRIW-EHK24E	6.76(6)	9.81(5)	665(101)	657(81)

The two pK_a values correspond to two different deprotonation processes. pK_a^E is associated with Glu22 and pK_a^w is associated with the Cu(II)-bound water.

Cu(I) and Cu(II) affinities, the free energy of binding and calculated reduction potentials.

Dissociation constants for the complexation of either Cu(I) or Cu(II) at pH 5.8 and 7.4 for the peptides studied in this work are provided in Table III-4. The first point to recognize is that the reversal of the position of the Lys and Glu groups going from TRIW-H to TRIW-EHE27K leads to a marked change in the Cu(I) affinity (a factor of 100 in favor of the reversed peptide), while the corresponding Cu(II) affinities are higher for the original parent peptide. In an effort to isolate the effects, peptides solely with modifications at the 22 position, which is much closer to the copper site than the 27 position (Table III-1) were examined. At pH 7.4, for the series TRIW-EH, TRIW-HK22Q, and TRIW-H corresponding to Δ_{charge} = -6, -3, and 0, respectively, the Cu(I) affinity changed only modestly (a factor of 5 less stable for TRIW-HK22Q and essentially identical for TRIW-EH) and the Cu(II) affinities were essentially invariant. At pH 5.8, the mutated peptides TRIW-HK22Q, TRIW-EH have very similar affinities and reduction potentials (Table III-5), although they have higher Cu(I) affinities and lower Cu(II) affinities compared to the parent peptide TRIW-H. It is worth noticing that TRIW-H behaves quite differently compared to the mutated peptides at pH 5.8, possibility due to the lower pK_a that the mutated peptides have; however, it appears that Δ_{charge} of the residues at the 22nd position (one residue above the binding site His23) does not have a dramatic influence on the affinities and redox properties of the peptide. Based on these observations, I chose to examine a series of peptide substitutions that occur below the copper-binding site (positions 24 and 27) using the K22E derived peptides as this would allow for the widest range of Δ_{charge} (from 0 to -12).

Table III-4. Cu(I) and Cu(II) dissociation constants at pH 5.8 and pH 7.4

Peptide	Δ_{Charge}	K_d(Cu(I))/M		K_d(Cu(II))/M	
		pH 5.8	pH 7.4	pH 5.8	pH 7.4
TRIW-H[16]*	--	$3.09(66) \times 10^{-12}$	$2.00(61) \times 10^{-13}$	$4.04(83) \times 10^{-8}$	$8.69(112) \times 10^{-9}$
TRIW-HK22Q	-3	$2.37(27) \times 10^{-14}$	$4.12(114) \times 10^{-14}$	$4.44(59) \times 10^{-7}$	$3.80(106) \times 10^{-9}$
TRIW-EHE27K	0	$1.36(56) \times 10^{-14}$	$2.07(27) \times 10^{-15}$	$3.47(104) \times 10^{-7}$	$1.45(71) \times 10^{-9}$
TRIW-EHE27Q	-3	$2.42(118) \times 10^{-14}$	$1.76(41) \times 10^{-14}$	$1.26(32) \times 10^{-7}$	$3.76(72) \times 10^{-9}$
TRIW-EH	-6	$4.17(19) \times 10^{-14}$	$1.12(43) \times 10^{-13}$	$7.38(324) \times 10^{-7}$	$6.39(258) \times 10^{-9}$
TRIW-EHK24Q	-9	$5.38(323) \times 10^{-13}$	$8.06(509) \times 10^{-14}$	$2.18(104) \times 10^{-7}$	$3.73(203) \times 10^{-9}$
TRIW-EHK24E	-12	$3.52(9) \times 10^{-13}$	$4.23(292) \times 10^{-13}$	$4.92\ (225) \times 10^{-7}$	$4.98(173) \times 10^{-9}$

*For TRIW-H, data were collected at pH 5.9 and 7.4

Table III-5. Calculated reduction potentials based on Cu(I) and Cu(II) affinities

Peptide	Δ_{Charge}	E^o(Cu-pep$_3$) at pH 5.8/mV	E^o(Cu-pep$_3$) at pH 7.4/mV
TRIW-H	--	402(8)	433(8)
TRIW-HK22Q	-3	589(5)	450(10)
TRIW-EHE27K	0	597(13)	504(13)
TRIW-EHE27Q	-3	556(14)	474(8)
TRIW-EH	-6	587(11)	440(14)
TRIW-EHK24Q	-9	491(20)	435(21)
TRIW-EHK24E	-12	522(12)	400(20)

For TRIW-H, calculations were based on affinities at pH 5.9 and 7.4

As shown in Figure III-14A, the Cu(I) affinities for the series of peptides containing a K22E substitution are related to the total charge around the copper binding site at both pH 5.8 and 7.4. As the total negative charge is increased, going from Δ_{charge} = 0 (TRIW-EHE27K) to Δ_{charge} = -12 (TRIW-EHK24E), the Cu(I) affinity decreases by about two orders of magnitude, which occurs under both pH conditions. However, the Cu(II) affinities seems to be relatively immune to the change of total charge. As shown in Figure III-14B, at both pH 5.8 and pH 7.4, the change of Cu(II) affinities to the peptides is minimal at a particular pH across the series of peptides with different total charge. It is interesting to notice that unlike Cu(I), whose affinities remains essentially the same for a particular peptide at different pH conditions with dissociation constants ranging from picomolar to femtomolar, Cu(II) is destabilized by at least two orders of magnitude when the pH decreases from 7.4 to 5.8, as shown in Figure III-14B. The difference between Cu(I) and Cu(II) can be described more clearly when one compares the free energy of binding at a particular pH (Figure III-15, Table III-6). The free energy of binding is calculated using the equation $\Delta G^{o} = 2.303RT\lg K_d$.

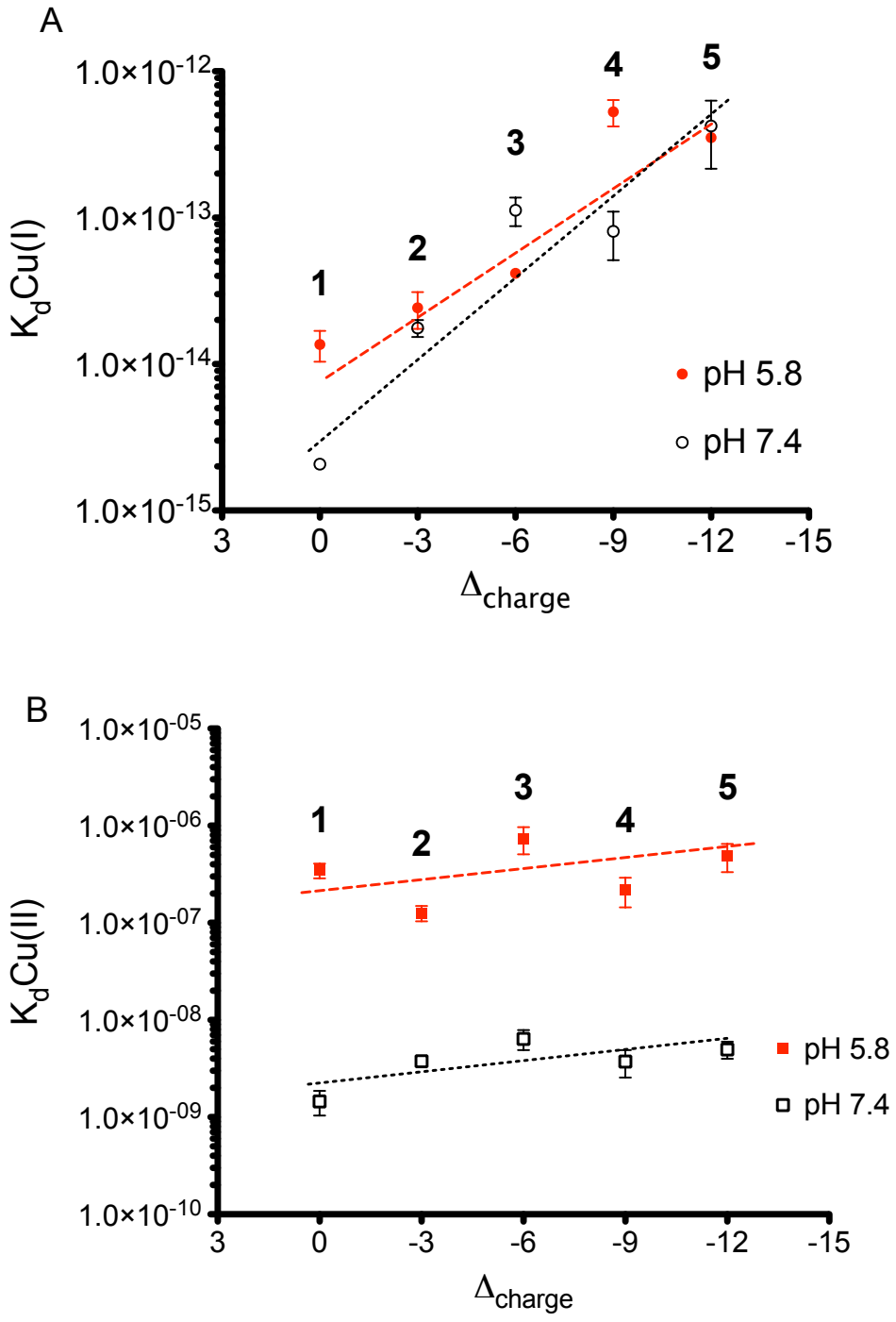

Figure III-14 (A) Cu(I) dissociation constants and (B) Cu(II) dissociation constants with respect to Δ_{charge} at pH 5.8 and pH 7.4. Peptides: 1) TRIW-EHE27K; 2) TRIW-EHE27Q; 3) TRIW-EH; 4) TRIW-EHK24Q; 5) TRIW-EHK24E. Note: the y-axis is on log scales.

Table III-6. The free energy of binding for Cu(I) and Cu(II) at pH 5.8 and 7.4

Peptide	ΔG^{o}(Cu(I)) at pH 5.8 kcal•mol^{-1}	ΔG^{o}(Cu(II)) at pH 5.8 kcal•mol^{-1}	ΔG^{o}(Cu(I)) at pH 7.4 kcal•mol^{-1}	ΔG^{o}(Cu(II)) at pH 7.4 kcal•mol^{-1}
TRIW-EHE27K	-18.91(24)	-8.81(18)	-20.02(8)	-12.05(29)
TRIW-EHE27Q	-18.57(29)	-9.41(15)	-18.75(14)	-11.49(11)
TRIW-EH	-18.25(3)	-8.36(26)	-17.66(23)	-11.17(24)
TRIW-EHK24Q	-16.74(36)	-9.08(28)	-17.86(37)	-11.49(32)
TRIW-EHK24E	-16.98(1)	-8.60(27)	-16.87(41)	-11.32(20)

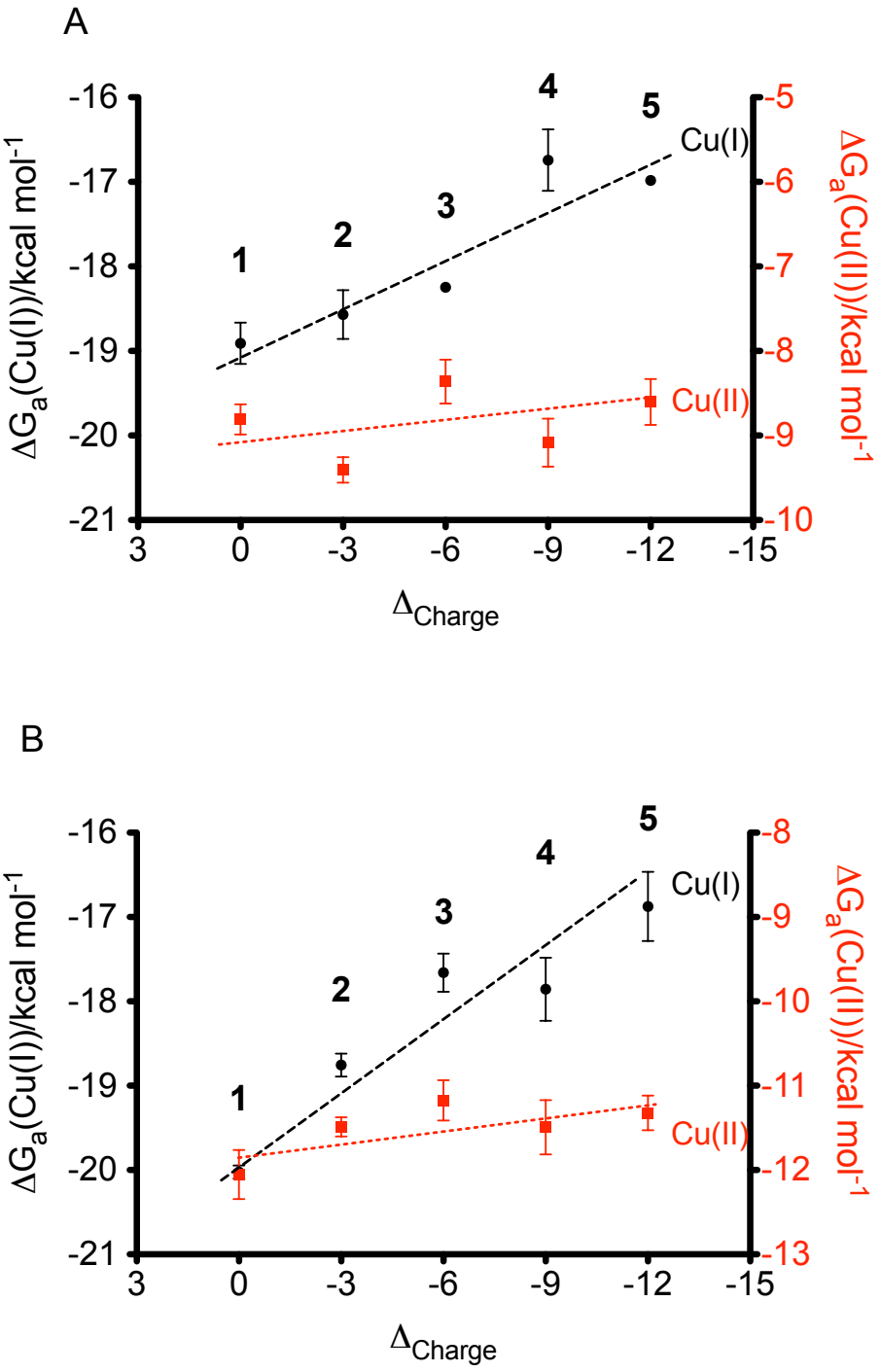

Figure III-15. The free energy of binding for both Cu(I) and Cu(II) at (A) pH 5.8; (B) pH 7.4. Peptides: 1) TRIW-EHE27K; 2) TRIW-EHE27Q; 3) TRIW-EH; 4) TRIW-EHK24Q; 5) TRIW-EHK24E

While reduction potentials for metalloproteins and small molecules are often determined by direct electrochemical methods, one may extract the same information by determining the binding affinities of the metals in both oxidation states to the proteins and applying the Nernst Equation. This approach has the added benefit that it allows one to track directly the behavior of interest (*e.g.,* reaction rates) not only against the reduction potential, but also to see if correlations exist associated with a specific oxidation level. The reduction potentials of the Cu(II)/Cu(I)-peptide system are calculated using the methodology shown in Scheme 2-1 and Equation II-1, where $E^{o}_{(Cu, aq)}$ = 0.159 V *vs*. NHE is utilized (Table III-5).[16,32] Since the free energy of binding for Cu(I) varies with amino acid substitution more than that of Cu(II) (Figure III-15), the change in the calculated reduction potential is dominated by the variation of Cu(I) affinities. This is true at both pH conditions; however, the change in potential between pH conditions is due to the stabilization of the Cu(II) upon acidification. The linear regressions for the trends following amino acid substitutions result in two parallel lines, the distance between which is about 100 mV. This value corresponds to a 1 H^+ per electron change in potential, which is consistent with a difference of 1.6 pH units for these measurements. (Figure III-16)

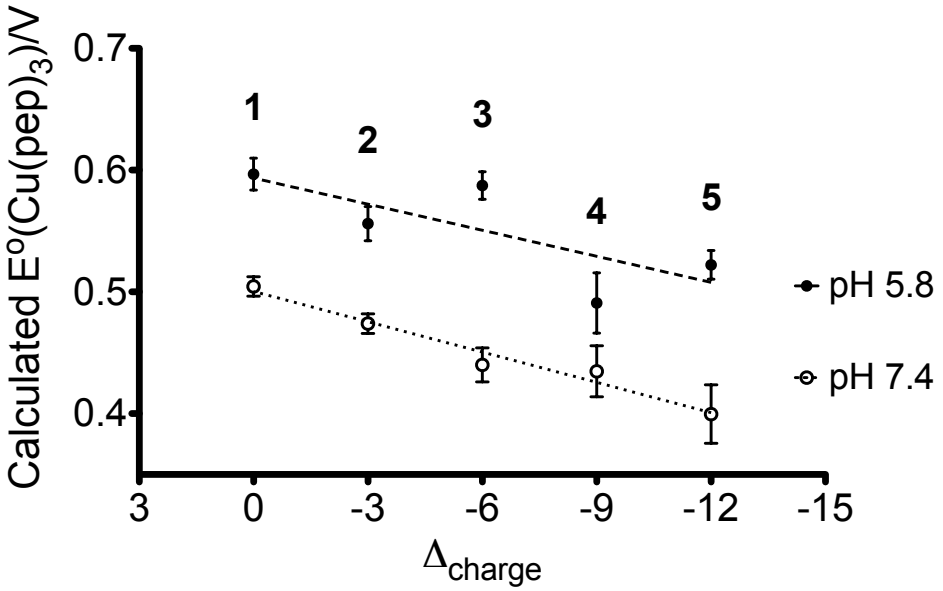

Figure III-16. Calculated reduction potentials in relation to the changes of the local charge at pH 5.8 and 7.4. Peptides: 1) TRIW-EHE27K; 2) TRIW-EHE27Q; 3) TRIW-EH; 4) TRIW-EHK24Q; 5) TRIW-EHK24E

EPR analyses of Cu(II) peptides.

The EPR parameters of Cu(II)(TRIW-EHE27K)$_3^{2+}$, Cu(II)(TRIW-EH)$_3^{2+}$, and Cu(II)(TRIW-EHK24E)$_3^{2+}$ at both pH 5.8 and 7.4 are in the same range as the parent peptide complex (Table III-7). The $g_\perp$ is smaller than the g_{II}, representing a typical $d_{x^2-y^2}$ ground state, and the A_{II} of all these complexes are in the range of 17 – 19 mT, indicative of an axial type 2 copper center with a high coordination number (4 or 5), which is consistent with the observed *d-d* band absorption spectra.

Table III-7. EPR parameters of Cu(II)(3SCC)$_3$ at pH 5.8 and 7.4

			pH 5.8		
Peptide	$g_\perp$	g_{II}	$A_\perp$/mT	A_{II}/mT	A_{iso}/mT
Cu(II)(TRIW-H)$_3^{2+}$	2.05	2.28	0.64	18.58	6.62
Cu(II)(TRIW-EHE27K)$_3^{2+}$	2.06	2.27	0.68	17.36	6.24
Cu(II)(TRIW-EH)$_3^{2+}$	2.06	2.27	0.36	18.33	6.35
Cu(II)(TRIW-EHK24E)$_3^{2+}$	2.06	2.28	0.18	18.33	6.23
			pH 7.4		
Peptide	$g_\perp$	g_{II}	$A_\perp$/mT	A_{II}/mT	A_{iso}/mT
Cu(II)(TRIW-H)$_3^{2+}$	2.05	2.27	0.64	18.58	6.62
Cu(II)(TRIW-EHE27K)$_3^{2+}$	2.05	2.27	1.07	17.50	6.55
Cu(II)(TRIW-EH)$_3^{2+}$	2.06	2.27	1.07	18.15	6.76
Cu(II)(TRIW-EHK24E)$_3^{2+}$	2.05	2.27	0.71	17.68	6.37

NiR activity.

The copper-peptide complexes exhibit NiR activity with different rates (Figure III-17), all of which are pH dependent. As the total negative charge goes from 0 to –12, the rates of the reaction increase by about four fold. Moreover, the rates are also correlated to the calculated reduction potentials at pH 5.8, as shown in Figure III-18: as the calculated reduction potentials increase, the rates decrease. The turnover numbers (TONs) for these reactions, expressed as moles of electrons per mole of copper, were obtained. The TONs in one hour are linearly correlated to the local negative charge (Figure III-19). As Δ_{charge} goes from 0 (TRIW-EHE27K) to -12 (TRIW-EHK24E), the TONs at pH 5.8 increase by one. For all of the NiR reactions, no degradation of the enzyme is observed 1.5 h after the reaction is initiated, which indicates that neither the copper center nor the protein undergoes degradation during this time period.

Nitric oxide production is examined for the peptides showing the lowest and highest rates [Cu(II)(TRIW-EHE27K)$_3^{2+}$ and Cu(II)(TRIW-EHK24E)$_3^{2+}$, respectively] at pH 5.8. The reaction catalyzed by Cu(II)(TRIW-EHE27K)$_3^{2+}$ produced 8.19×10^{-7} mol NO and that catalyzed by Cu(II)(TRIW-EHK24E)$_3^{2+}$ produced 1.53×10^{-6} mol NO (Figure III-20).

Table III-8. NiR rates of Cu-peptides at different pH conditions. Rate constants are reported in s^{-1}.

Peptide	pH = 5.8	pH = 6.0	pH = 6.25	pH = 6.50	pH = 6.75	pH = 7.00
TRIW-H	$2.04(14) \times 10^{-4}$	$1.43(25) \times 10^{-4}$	$7.46(98) \times 10^{-5}$	$4.86(12) \times 10^{-5}$	$2.90(35) \times 10^{-5}$	$2.11(52) \times 10^{-5}$
TRIW-EHE27K	$9.94(60) \times 10^{-5}$	$4.01(15) \times 10^{-5}$	$2.67(261) \times 10^{-5}$	$4.01(448) \times 10^{-6}$	$1.18(71) \times 10^{-5}$	$1.06(46) \times 10^{-5}$
TRIW-EHE27Q	$1.16(85) \times 10^{-4}$	$1.17(54) \times 10^{-4}$	$5.04(210) \times 10^{-5}$	$2.67(137) \times 10^{-5}$	$1.73(151) \times 10^{-5}$	$1.63(101) \times 10^{-5}$
TRIW-EH	$1.89(31) \times 10^{-4}$	$2.05(61) \times 10^{-4}$	$9.09(209) \times 10^{-5}$	$4.51(62) \times 10^{-5}$	$3.08(170) \times 10^{-5}$	$1.51(19) \times 10^{-5}$
TRIW-EHK24Q	$3.48(70) \times 10^{-4}$	$2.96(4) \times 10^{-4}$	$1.57(22) \times 10^{-4}$	$1.03(13) \times 10^{-4}$	$5.40(70) \times 10^{-5}$	$2.70(66) \times 10^{-5}$
TRIW-EHK24E	$3.29(56) \times 10^{-4}$	$2.88(54) \times 10^{-4}$	$1.68(17) \times 10^{-4}$	$1.33(15) \times 10^{-4}$	$7.90(31) \times 10^{-5}$	$1.99(112) \times 10^{-5}$

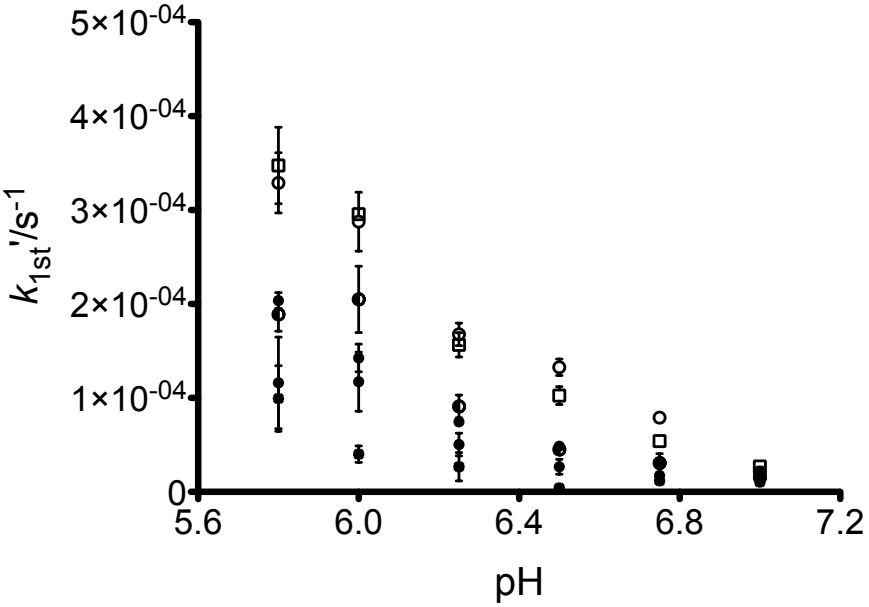

Figure III-17. pH dependence of nitrite reduction rate constants. Peptides: ○ TRIW-EHK24E (Δ_{charge} = -12), □ TRIW-EHK24Q (Δ_{charge} = -9), ◐ TRIW-EH (Δ_{charge} = -6), ● TRIW-EHE27Q (Δ_{charge} = -3), ✱ TRIW-EHE27K (Δ_{charge} = 0).

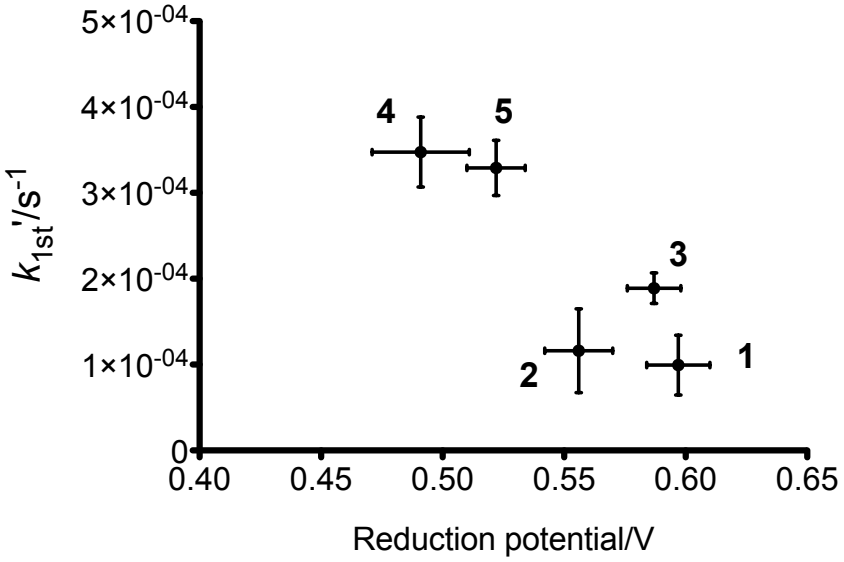

Figure III-18. Rates at pH 5.8 in relation to the calculated reduction potentials at pH 5.8. Peptides: 1) TRIW-EHE27K; 2) TRIW-EHE27Q; 3) TRIW-EH; 4) TRIW-EHK24Q; 5) TRIW-EHK24E

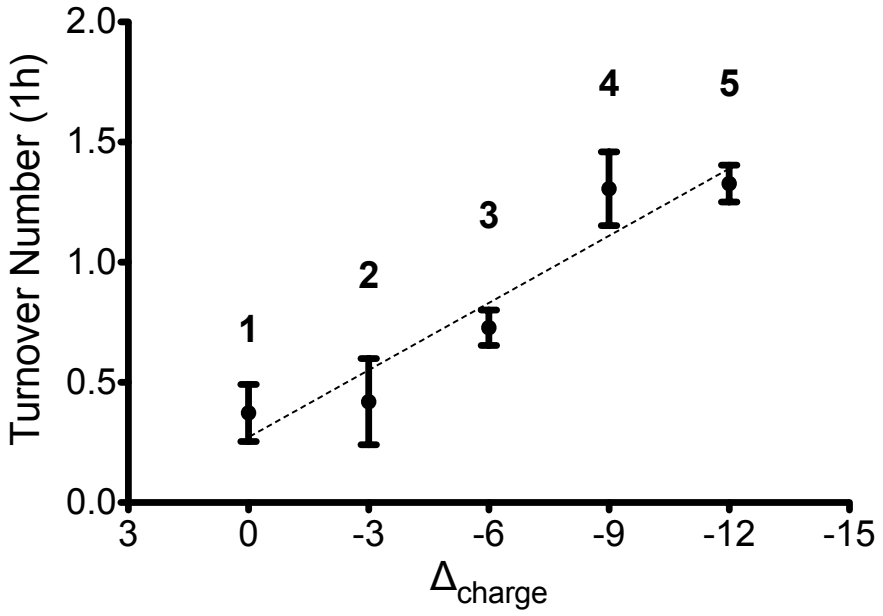

Figure III-19. Turnover numbers of NiR reactions by Cu-peptides related to Δ_{charge}. Peptides: 1) TRIW-EHE27K; 2) TRIW-EHE27Q; 3) TRIW-EH; 4) TRIW-EHK24Q; 5) TRIW-EHK24E

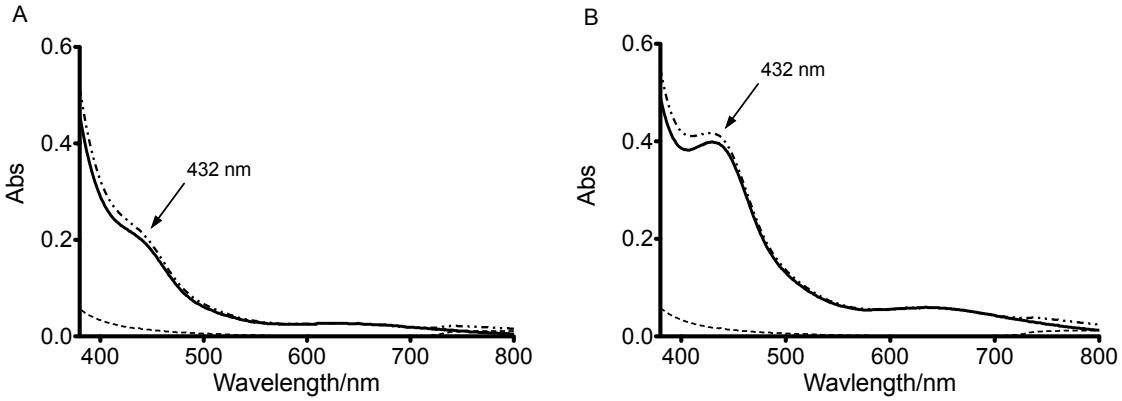

Figure III-20. Spectra of a 0.01 M $[Fe(EDTA)]^{2-}$ solution before (dashed line) and after (dashed dot line) the cannula transfer of the headspace gas from the reaction vessel. The difference spectrum is shown in solid lines. (A) Enzyme: $Cu(II)(TRIW\text{-}EHE27K)_3^{2+}$, 3 h; (B) Enzyme: $Cu(II)(TRIW\text{-}EHK24E)_3^{2+}$, 2.5 h.

Discussion

The environment that surrounds redox sites plays a critical role in determining the reduction potentials and pathways for electron flow in proteins, however, in most cases,

multiple factors exert influence on the reduction potential simultaneously, complicating the understanding of the structure-function relationship of a particular system. In general, the energy associated with the redox process can be conceptualized as the sum of the inner-sphere contributions, which directly point to the energy needed to add or remove an electron to the redox site, outer-sphere contributions, which are related to the interaction of the redox site with the protein and solvent environment during the redox process, the relative distances between the redox centers, and the solvating/desolvating of the metal cetners.[33] In reality, more often than not, one change around the active site may lead to a cascade of events that will eventually modify the redox properties, but it is challenging to track down the specific roles of each event.

A significant amount of work has been done to understand the redox property modulations on systems containing heme cofactors or cupredoxin sites. It was reported, as early as 1989, that mutating the valine (Val) residue into charged or polar residues such as Glu, aspartate (Asp) and asparagine (Asn) led to a decrease in the mid-point redox potential of recombinant myoglobin at 25 ºC, which demonstrated that changing the electric field around the redox center resulted in a substantial change in the redox thermodynamics of a particular system.[10] The substitution of Val68 close to the distal site of the heme center into a Glu or an Asp led to about 200 mV decrease in the reduction potential whereas Val68Asn resulted in an 80 mV decrease. Furthermore, the Dutton and Gibney groups showed that by varying the burial of heme in the hydrophobic core, heme peripheral substituents, heme-hydrophobic amino acids, *et al*., they were able to modulate rationally the heme-protein redox potential over a range of a few hundred mV.[34–37] More recently, Yi Lu and coworkers demonstrated that the redox potential of a cupredoxin site in azurin could be tuned by modifying two important secondary coordination sphere interactions: hydrophobicity and H-bonding. Their work showed an astounding shift in redox potentials, in some cases by as much as 700 mV, which extended even beyond the natural redox potential range of the protein.[38,39] Despite its importance in the electron transfer or catalytic functions in native proteins, there had been no systematic studies on the redox property modulations of $Cu(His)_3$ site in a protein environment until this work was published in 2013.

Design rationale.

Taking advantage of a *de novo* protein design approach, I took a known functional peptide Cu(TRIW-H)$_3$ (Chapter II), and modified the local charge in a stepwise manner in order to observe changes in the reduction potentials and NiR rates of a series of peptides (Table III-1). The rationale of the design is first to invert the charged residues Glu27 and Lys22, yielding TRIW-EHE27K. Compared to the parent peptide TRIW-H, the change in the overall charge, or Δ_{charge}, of this peptide is 0. While this double mutation leads to a significant shift in potential, no perturbation in the reduction potentials is observed between copper complexes of TRIW-H and TRIW-EH at pH 7.4. I used the K22E mutation (TRIW-EH scaffold) to evaluate a broader range of charge effects than would be available with TRIW-H. The residues below the copper-binding site of TRIW-EH are substituted in a stepwise manner from positively-charged residues into neutral and then negatively-charged residues. Since three strands of peptides self-assemble in aqueous solutions above pH 5,[40] the resulting series of peptides have a Δ_{charge} of 0, -3, -6, -9, and -12.

None of the residues (Lys22, Lys24 and Glu27 in TRIW-H) involved in the mutations are inside the helix bundle, neither can they directly coordinate to the copper center (according to the pymol models shown in Figure III-1), hence the first coordination sphere effects on the properties of the copper center are not expected. This *de novo* design strategy allows one to vary the charge systematically in order to probe the subtle influence of surface charged residues on the stability constants of Cu(I) and Cu(II)-peptides and, subsequently, upon the redox properties and catalytic activities of these type 2 copper centers.

Coordination environment of Cu(I).

To my expectation, the first coordination sphere of Cu(I)(TRIW-EH)$_3^+$ is not modified when the residues at the helical interface are mutated. The XAS data of Cu(I)(TRIW-EHE27K)$_3^+$, Cu(I)(TRIW-EH)$_3^+$, and Cu(I)(TRIW-EHK24E)$_3^+$ indicate that Cu(I) still binds to three imidazoles in a trigonal planar coordination with typical trigonal Cu(I)-N bond distances.[22,41,42] Since the EXAFS data do not provide information on the orientation of the imidazole rings (whether they are perpendicular or parallel to the

helical axis), it is possible that the aromatic rings might adopt different orientations based on other types of interactions such as H-bonds or salt bridges. As shown in Scheme III-1, assuming that all three imidazoles bind Cu(I) with their $^{\varepsilon}$N, Cu(I) is in the same plane as the three $^{\varepsilon}$N, which is true for all three peptides investigated here. As marked by the red arrows, the orientations of the imidazoles can be different for these peptides, depending on the packing of the aromatics and the potential interactions between the proton on the $^{\delta}$N with the charged residues. The differences in the orientations, consequently, would influence the orbital overlap between the $^{\varepsilon}$N and Cu(I), which might have an effect on the energetics of Cu(I) binding.

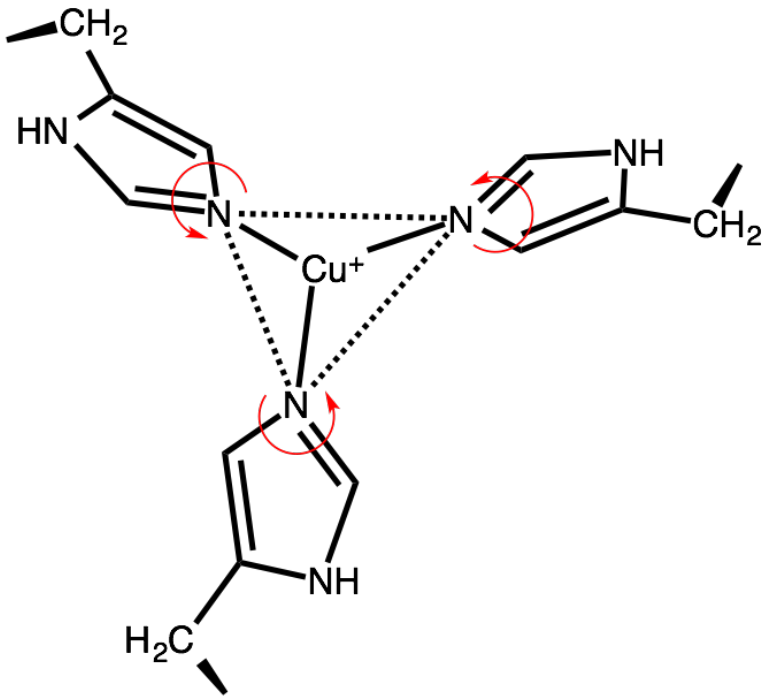

Scheme III-1

Deprotonation equilibria of Cu(II)(3SCC).

I then characterized the binding of the Cu(II) ion to the peptide as a function of pH using UV-Vis spectroscopy. As demonstrated in the last chapter, for Cu(II)(TRIW-H)$_3^{2+}$, the rise in the visible region when pH goes from ~3 to ~5 corresponds to the binding of Cu(II) to (TRIW-H)$_3$ and the spectral transformation in a higher pH range (7.5~10) relates to the deprotonation of Cu(II)-bound water. Besides these two equilibria,

the copper binding ligand can undergo deprotonation of the cationic imidazolium form, which does not bind copper, to a neutral imidazole, which binds copper.[43] A ^{1}H NMR titration of $(TRIW\text{-}H)_3$ has shown that this deprotonation event occurs over the pH range 5.5-8.0 in the absence of metal (Chapter II). Most likely, the presence of a Lewis Acid shifts the imidazolium to imidazole equilibrium in favor of the neutral metal binding ligand as has been reported for both zinc and copper complexes with $(TRIW\text{-}H)_3$.[16,25] Under higher pH conditions the imidazole may be converted to the negatively charged imidazolate form, which also binds copper efficiently. It is generally believed, however, that this equilibrium occurs at much higher pH values than investigated here. Additional carboxylic acid deprotonation events would be expected when Lys is substituted to Glu at the 22 and/or 24 positions for the mutated peptides. One would expect this deprotonation chemistry to occur in the general range of the pre-existing carboxylic acids at the *e* positions of the peptide. At very high pH conditions (again above pH 8), the deprotonation of the Lys side chain may become relevant, which could disrupt the 3SCCs; however, the conditions used in this study are unlikely to enter this basic range. The pK_a values involved are depicted in Figure III-21.

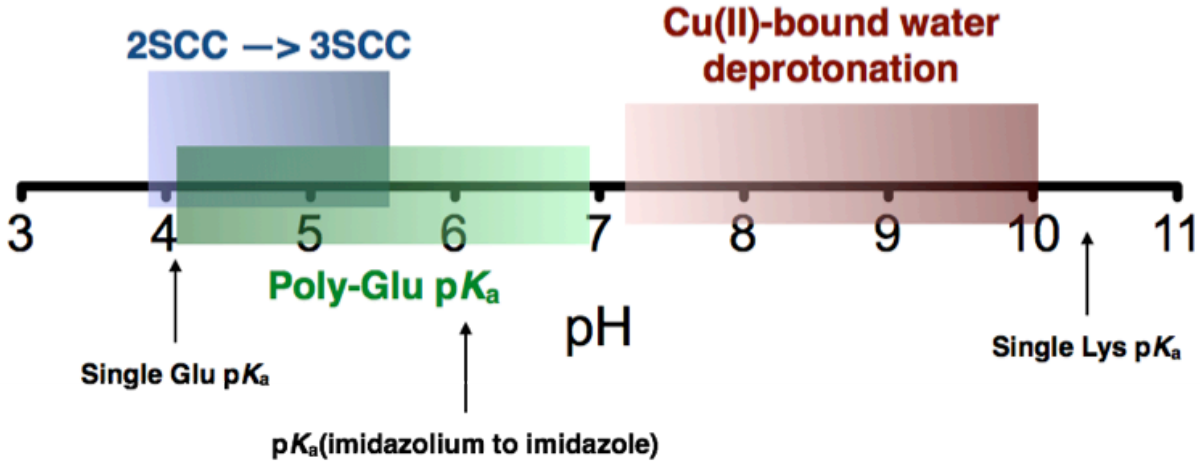

Figure III-21. Deprotonation events involved in the pH region of interest in this study

Similar to the first generation peptide TRIW-H, in the presence of Cu(II), TRIW-EHE27K, TRIW-EH, and TRIW-EHK24E all exhibit a sharp rise in absorbance moving from pH 3 until the spectra level out by ~pH 5 (Figure III-8, Figure III-9, Figure III-10). Again, this process corresponds to the binding of Cu(II) to the peptides, forming a Cu(II)

center with a high coordination number (*vide supra*). As the pH is raised to neutral conditions, peptides containing additional Glu (TRIW-EH, and TRIW-EHK24E) show an additional pH-dependent conversion (pK_a~6.5). Since this pK_a is about 2 pH units different from the that of Cu(II)-bound water deprotonation discussed in Chapter II, it is unlikely that this pK_a corresponds to the same equilibrium. This process could be due to either the complexation of Glu22 to Cu(II) or the deprotonation of the carboxylic acid on Glu22. Based on PyMol models, the position of Glu22 on the helix places it too far from the metal center to bind directly to the copper or to form a hydrogen bond with a Cu(II)-bound water. This observation leaves the most likely explanation for the pK_a in the 6~7 range for peptides containing the K22E mutations as the deprotonation of the glutamic acid leading to an H-bond formation between Glu22 and His23.

In the previous chapter, I presented the EPR spectra of Cu(II)(TRIW-H)$_3^{2+}$ at pH 5.2~7.8 (Figure II-12). showing that the EPR parameters are the same for a peptide without the K22E mutation in this pH range. In contrast, for the TRIW-EH series of peptides, the EPR parameters at pH 5.8 and 7.4 are different, signifying the perturbation derived from the K22E mutation. Specifically, for the charge "flipped" peptide Cu(II)(TRIW-EHE27K)$_3^{2+}$, g_{II} stayed the same, maintaining the $d_{x^2-y^2}$ ground state, while A_{II} increased by 0.14 mT and the isotropic hyperfine splitting constant A_{iso} increased by 0.31 mT (Table III-7). Similar changes of g_{II} and A_{iso} occurred for Cu(II)(TRIW-EH)$_3^{2+}$. For Cu(II)(TRIW-EHK24E)$_3^{2+}$, however, both g_{II} and A_{II} decreased significantly while $A_{\perp}$ increased, leading to an increased A_{iso}. In summary, the A_{iso} of the TRIW-EH series of copper-peptide complexes increased when pH rises from 5.8 to 7.4, indicating a higher spin-density at the copper center. The changes of the other EPR parameters are dissimilar to those of Cu(II)(TRIW-H)$_3^{2+}$ in a higher pH region (7.8~9.1, Figure II-20), which also supports the proposition that this equilibrium (corresponding to pK_a ~6.5) is not a Cu(II)-bound water deprotonation.

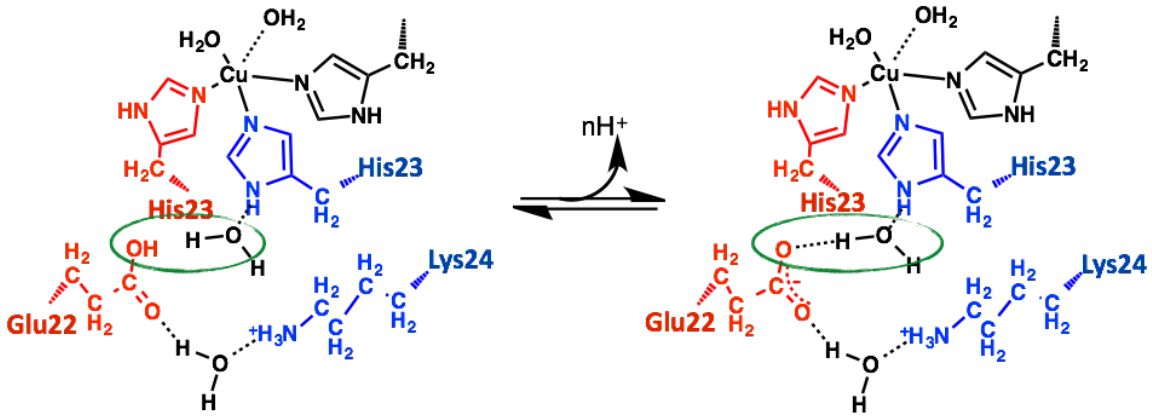

Scheme III-2. A possible scenario for the formation of an H-bond between Glu22 and His23 upon the deprotonation of the carboxylic acid for Cu(II)(TRIW-EH)$_3^{2+}$. Residues from the same helix are shown in the same color. Only key residues proposed to be involved in this deprotonation process are shown.

Considering the combined observations, the pK_a at ~6.5 for some of the TRIW-EH peptides is assigned to a deprotonation equilibrium of a glutamic acid side-chain (probably at the 22 position) which can become an H-bond acceptor for the imidazole proton at the 23 position or a bridging water molecule (Scheme III-2). This H-bond leads to the variance of both UV-Vis and EPR spectral parameters of the Cu(II) center when the pH increases from 5.8 to 7.4. Two control experiments were carried out to assess further whether this protonation equilibrium (pK_a~6.5) is associated with both Glu22 and His23. When the same pH titration was carried out for Cu(II)(TRIW-HK24E)$_3^{2+}$, where the Glu is placed at the 24th, instead of the 22nd position, no perturbation of the Cu(II) *d-d* band absorption is seen in this pH range (Figure III-12). As shown in the PyMol models (Figure III-1), the side chain of Glu at the 24th position in TRIW-HK24E is almost at the opposite side of the helix with regard to the His side chain, so it is very unlikely for Glu24 to form an H-bond with His23 (or with bridging water molecules). Even if there is deprotonation of the carboxylic acid side chain on Glu24, it is not reflected on the Cu(II) *d-d* absorption, which supports the conclusion that *the Glu has to be placed at the 22nd position to interact with His23* (Scheme III-3). In other words, Glu22 is necessary for this observed deprotonation event. The second control involves the substitution of the proton on the N$^{\delta}$ of the imidazole with a methyl group while Glu22 retains, yielding TRIW-E$_M$H. The d-d band absorption stays the same when pH increases from 5.5 to 7.5 (Figure

III-11), which indicates that *the presence of the proton on the imidazole is a must for one to observe this deprotonation event (pK_a~6.5)*. Again, even if there is a deprotonation within this pH range, it is not reflected on the Cu(II) absorption spectra (Scheme III-4).

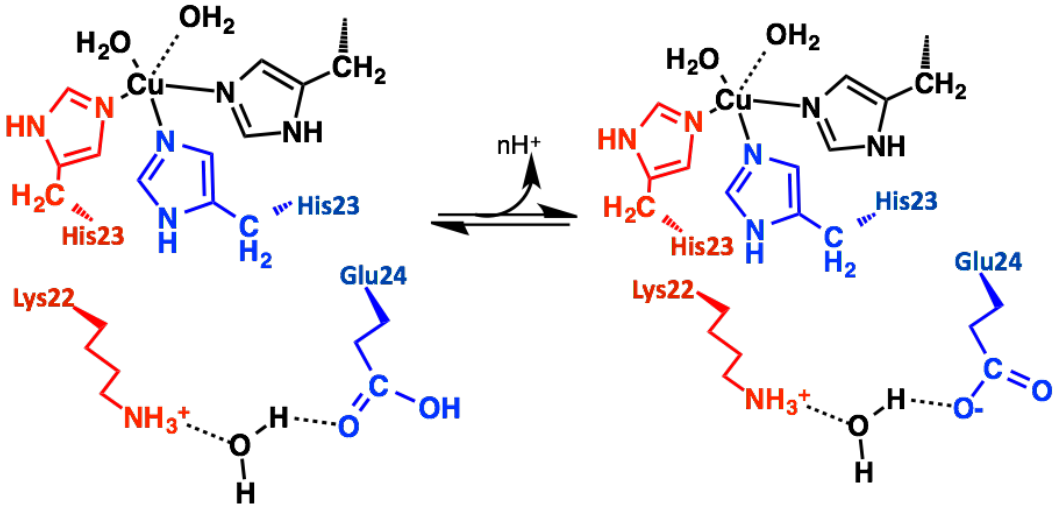

Scheme III-3. Possible deprotonation of Glu24, forming an H-bond with Lys22 for Cu(II)(TRIW-HK24E)$_3^{2+}$. Residues from the same helix are shown in the same color.

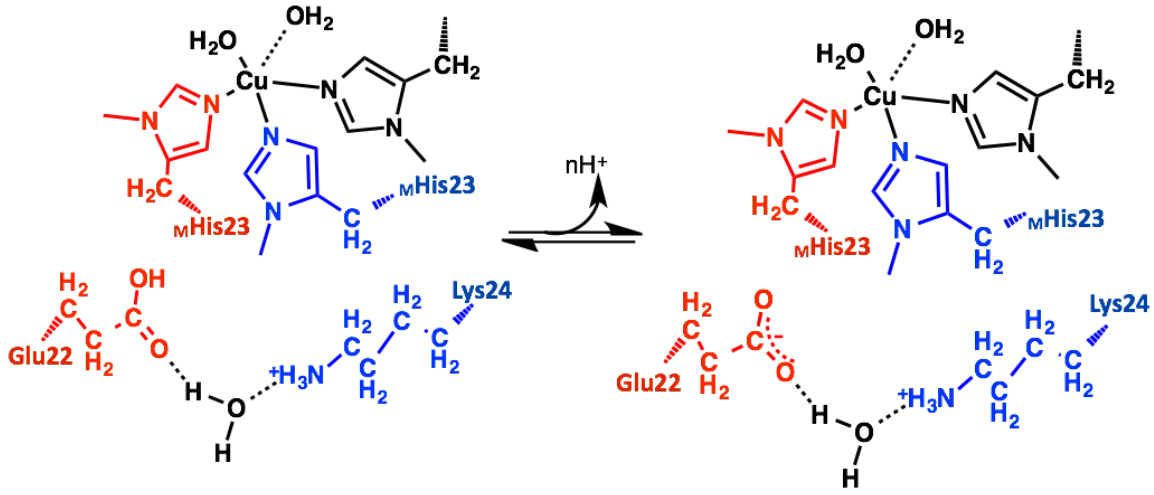

Scheme III-4.

Consistent with this assignment, For the charge "flipped" peptide Cu(II)(TRIW-EHE27K)$_3^{2+}$, one might have expected it to behave more similarly to the other TRIW-EH peptides having a lower pK_a; however, models suggest that Glu22 can interact with Lys27 in TRIW-EHE27K which would weaken the H-bonding interaction of Glu22 with His23 (Scheme III-5). This putative H-bond would lead to a less acidic Cu(II), which would

increase the pK_a for the Cu(II)-bound water deprotonation in these peptides. Correspondingly, a higher pK_a (9.6-9.8) for the TRIW-EH series of peptides is observed, which is assigned to the deprotonation of the Cu(II)-bound water (Table III-3).

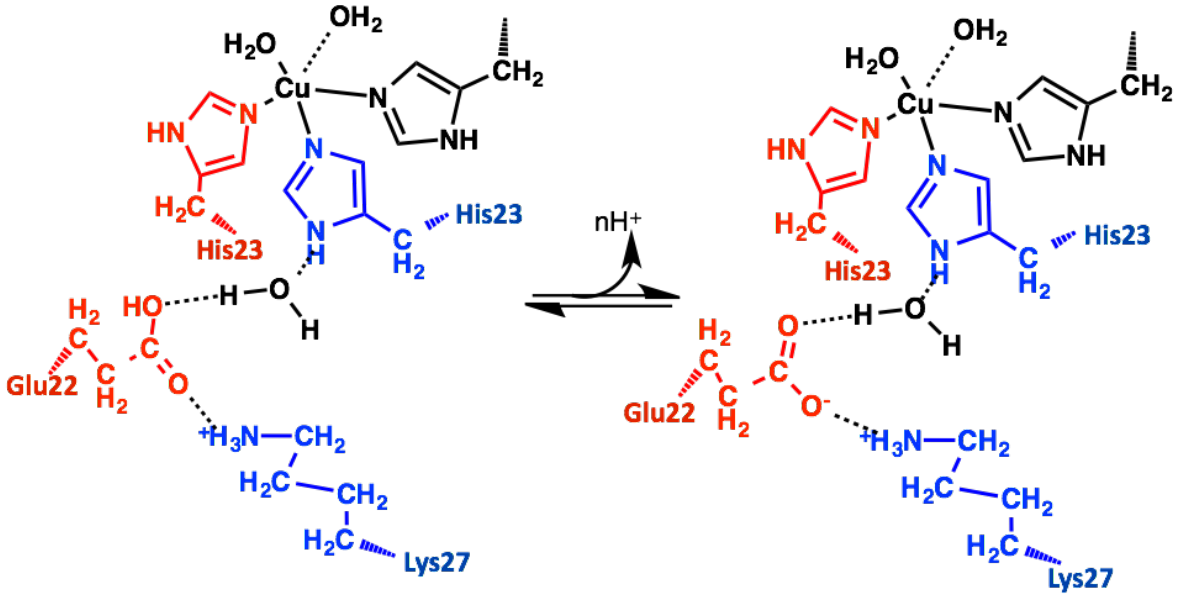

Scheme III-5. Possible deprotonation scheme for Cu(II)(TRIW-EHE27K)$_3^{2+}$. Residues from the same helix are shown in the same color.

Affinities and reduction potentials.

At pH 5.8 and 7.4, the binding affinities of Cu(I) and Cu(II) to the TRIW-EH series of peptides are determined in order to evaluate the reduction potentials and the impact of protein mutations at both oxidation levels (Table III-4, Figure III-14, Figure III-16). These peptides are prepared in order to examine the effect of increased local negative charge on the stabilities of Cu(I) and Cu(II) within the hydrophobic core. It was originally thought that the Cu(II) state would be more greatly stabilized by higher negative charge, decreasing the reduction potential of the system. While the reduction potentials (Table III-5) were made less positive by increasing the local negative charge, contrary to this expectation, the shift occurred as a result of Cu(I) destabilization rather than Cu(II) stabilization. These results are most clearly visualized when comparing the free energy of binding shown in Figure III-15.

In contrast, Rorabacher and coworkers have reported a series of potentially tetradentate copper complexes which vary neutral nitrogen or sulfur donors over the range N_4 to NS_3 (Figure III-22). The reduction potentials of these compounds are strongly influenced by the stability constants of the Cu(II) oxidation level rather than those of the Cu(I) complexes.[44,45] In particular, an increase in the stability constants of Cu(II) complexes by as much as $10^4 \sim 10^5$-fold was observed when substituting thioether sulfurs for unsaturated nitrogens; at the same time, the stability constants of Cu(I) complexes were maintained in the range $10^{14} \sim 10^{16}$ M^{-1}. These changes lead to differences in the reduction potentials (Figure III-23).[44] The reduction potentials were also shown to be pH-dependent below pH 5 (and invariant above this pH) due to the acid-base chemistry of the ligand.[46] Important differences between these models and our system include the choice of ligands (neutral thioethers and pyridyl groups), the lack of potential H-bond acceptors (such as glutamate), the lack of charge variation across the series and the possibility of a tertiary amino nitrogen atom that could serve as a fourth ligand. Hence, our system provides a more biologically relevant example to assess how electrostatic and H-bonding influence copper protein reduction potentials.

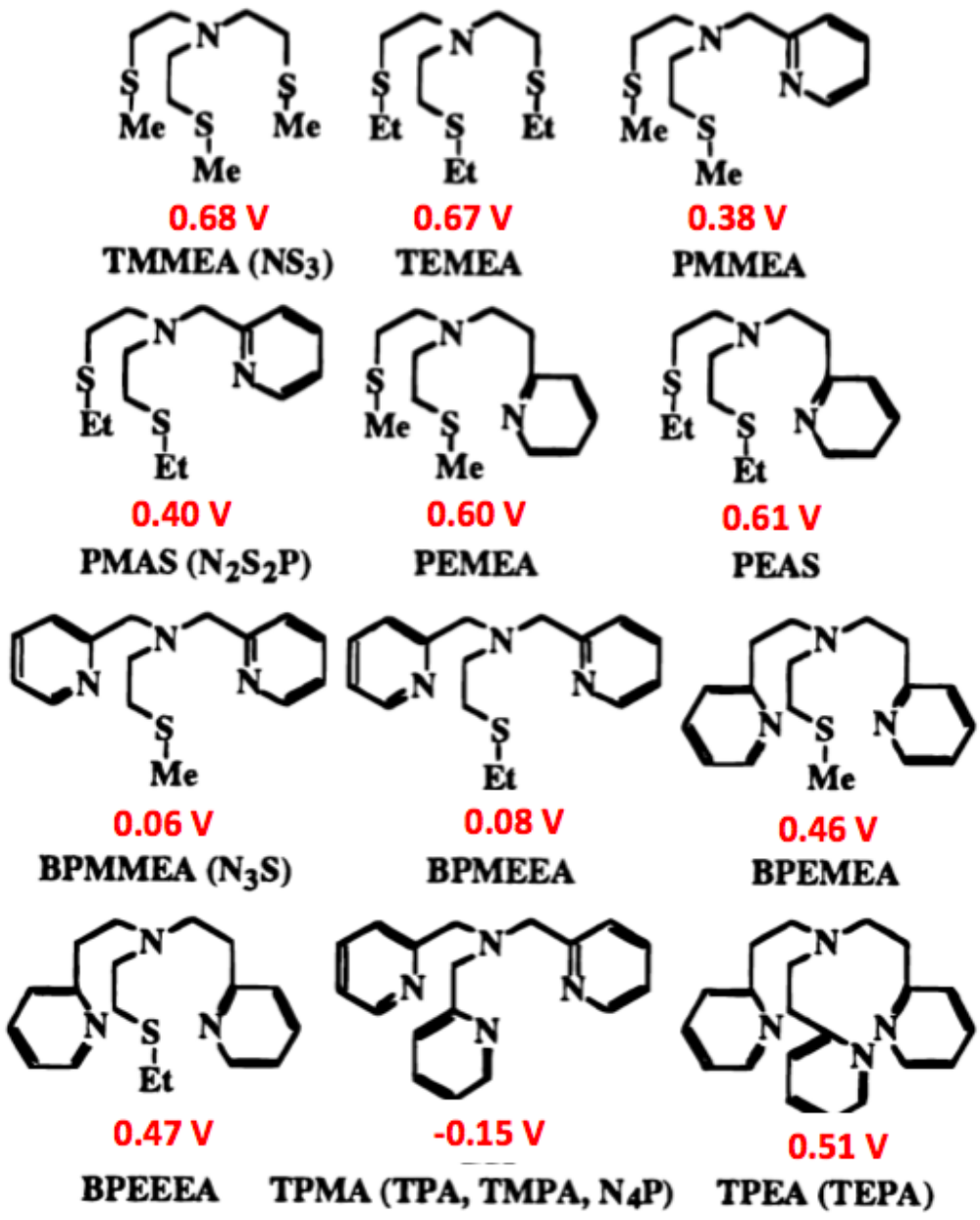

Figure III-22. Tetradendate ligands involved in Rorabacher's investigation. The numbers in red are the reduction potentials of the corresponding copper complexes (vs. NHE).

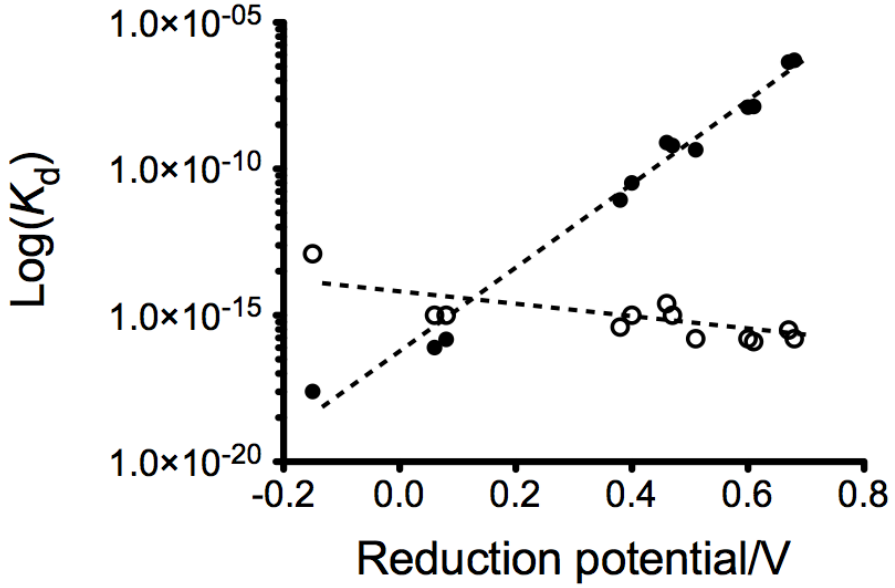

Figure III-23. Reduction potentials of the synthetic complexes investigated by Rorobacher and coworkers in relation to the Cu(II) and Cu(I) dissociation constants. Filled circles represent Cu(II) and hollow circles represent Cu(I). Note: the dissociation constants are on log scales.

As shown in Figure III-14, the relative Cu(I) or Cu(II) affinity change across the series of designed protein mutants is independent of pH as demonstrated by the invariant slopes of the lines for either oxidation state. This statement is not intended to suggest that the pH is not important in this system, as marked effects are seen both on Cu(II) stability and reduction potential. The Cu(I) stability is more sensitive to protein modification ($\Delta(\Delta G_a^{Cu(I)})$~ 2 kcal/mol *versus* $\Delta(\Delta G_a^{Cu(II)})$~ 0.7 kcal/mol), whereas one sees that the Cu(II) affinities are more sensitive to pH adjustment ($(\Delta G_a^{Cu(I)})_{pH\ 7.4} - (\Delta G_a^{Cu(I)})_{pH\ 5.8}$ ~ 0.5 kcal/mol *versus* $(\Delta G_a^{Cu(II)})_{pH\ 7.4} - (\Delta G_a^{Cu(II)})_{pH\ 5.8}$ ~ 3.5 kcal/mol). Thus, the trend is that as the negative charge around the copper center is increased via protein modification, Cu(I) is destabilized and the reduction potential becomes less positive. In contrast, as the pH is lowered, the Cu(II) affinity decreases and the reduction potential becomes more positive. Within the series there is an ~100 mV shift in potential from pH 7.4 to 5.8 for any peptide, providing a slope of ~ 60 mV/pH unit that indicates that the change in potential is dependent upon a single proton per electron. The differences between the copper affinities lead to the two parallel lines shown in Figure III-16. Thus, by controlling the

peptide sequence and the pH, one can systematically vary the reduction potential in this system by nearly 200 mV.

The observed trends can be explained by the change of H-bonding and salt bridge interactions around the copper center upon protein mutations under different pH conditions. The mutation of Lys at the 22 position into a Glu would likely lead to an H-bonding interaction between the carboxylic acid/carboxylate from Glu and the imidazole from His, therefore, pH-dependent Cu(II) affinities and reduction potentials are observed. Variations on the other charged residues would alter the salt-bridging interactions, leading to differences in the electron-donating abilities of the imidazoles or structural perturbations to the Cu(I) center, likely involving the change of the orientations of the imidazole ring. Consistent with this idea, TRIW-H only exhibits a modest shift to a less positive potential (Δ = - 30 mV) from pH 7.4 to 5.9 while all of the peptides with Gln or Glu in the 22 position show significant shifts to more positive potentials (Δ = + 60 to + 140 mV) as the pH is decreased (Table III-5). One possible H-bonding scheme that supports both the pH trends in Cu(II) binding and the impact of side chain mutations of the Cu(I) affinities is provided in Figure III-24.

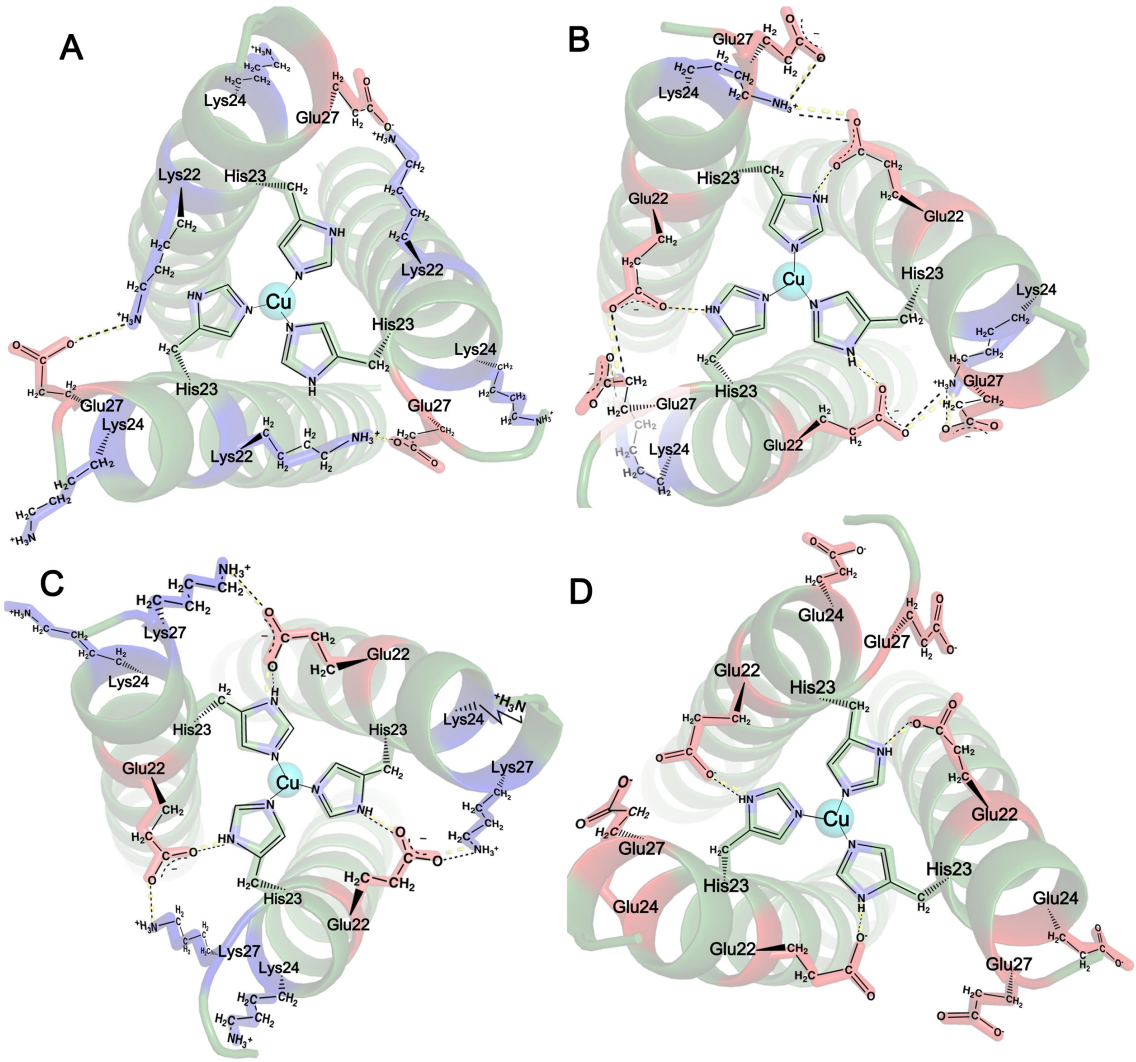

Figure III-24. Proposed H-bonding network formation in the mutated peptides compared to the parent peptide viewed from the C-terminus. (A) Parent peptide TRIW-H; (B) TRIW-EH when Glu22 is in its deprotonated state; (C) TRIW-EHE27K when Glu22 is in its deprotonated state; (D) TRIW-EHK24E when Glu22 is deprotonated. Water molecules are omitted for clarity; however, it is possible that a water molecule might exist between any of the salt bridges shown in the scheme. These PyMol models were made based on the crystal structure of $Hg(II)_SZn(II)_N(CSL9PenL23H)_3^-$ (PDB code: 3PBJ). With the 23rd position His as a reference point, mutations were made in the models into the real sequence of the corresponding TRI peptides. Specifically, the relevant amino acid sequence close to the His site in CSL9PenL23H is K**H**EALE (22–27). To make this short fragment the same sequence at the corresponding location in TRIW-H, Lys22 was mutated into a Glu and Glu24 was mutated into a Lys, yielding the sequence E**H**KALE (22–27). Additional mutations were then carried out to visualize the possible H-bonding and salt bridge interactions in the TRIW-EH family peptides.

The pymol models of TRIW-H, TRIW-EH, TRIW-EHE27K and TRIW-EHK24E illustrate the changes that may occur in salt bridge interactions as one modifies Glu and Lys residues in the *b*, *e* and *g* positions of the heptads. It appears that a neutral or charged acceptor side chain (Gln or Glu) can form an H-bond to the imidazole of His23 or having a water molecule bridging the two residues. One would expect that as the acidity of the solution increases, the negatively charged residue would decrease in charge and become a poorer H-bond acceptor. In addition, for some of the mutated peptides (TRIW-EH and TRIW-EHK24E), going from pH 7.4 to 5.8, Glu22 should experience protonation, which leads to the perturbation of the putative H-bond between Glu22 and His23. This effect will lead to less electron density on the imidazole of His23, thus result in a lower affinity for Cu(II). The extent of this influence though, varies for different peptides depending on the other possible interactions with Glu22, for example, the interaction between Lys24-Glu22 or Lys27-Glu22 for some of the mutated peptides. In contrast, Lys22 in TRIW-H cannot form such H-bonds with His23.

The likely key interactions in this system are the inter-helical H-bonds between Glu22 and His23 (or a water molecule bridging the two residues), salt bridges between Glu22 and Lys24, Lys24 and Glu27. The TRIW-EH peptide has available all three possibilities, meaning that Lys24 can spend part of its time salt bridged to either Glu22 or Glu27. When Lys24 is interacting with Glu27 with an average donor-acceptor distance of 3.0 Å based on the pymol model (Figure III-25), the Glu22 is free to H-bond with His23 (average donor-acceptor distance <2.7 Å, Figure III-25). This leads to an intermediate imidazole H-bonding situation (Figure III-24B). If Glu27 is converted to a Lys (TRIW-EHE27K), Lys27 would interact with Glu22 with an average donor-acceptor distance of 2.6 Å (Figure III-26), which would weaken the Glu22-His23 H-bond (Figure III-24C). For both situations, other rotamers of Lys24 can also interact with Glu20, Glu21 on the same strand with distances of <2.8 Å, which might also occur in the parent peptide TRIW-H. For residues above Glu22, The intra-helical salt-bridging interaction could happen between Glu20 and Lys15, Glu13 and Lys8. On the other hand, when Lys24 is converted to Glu24 (TRIW-EHK24E), Glu22 can then H-bond to His23 (average donor-acceptor distance <2.7 Å, Figure III-27), without the competition from the other potential

H-bond contributors (Figure III-24D). The situation with Gln substitution is expected to be intermediate between Lys and Glu substitution as is seen to be the case.

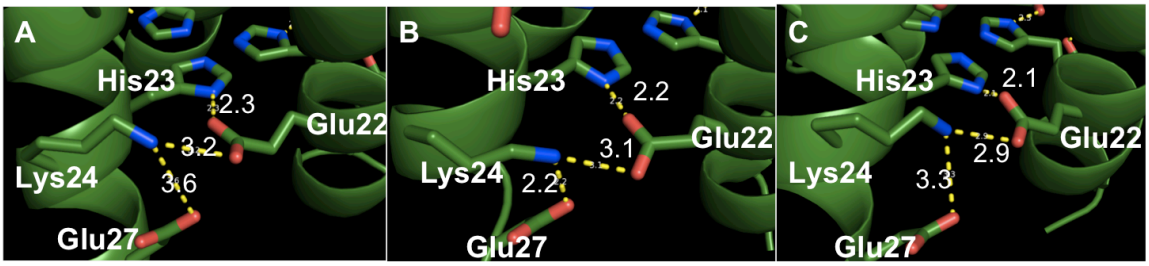

Figure III-25. PyMol models of TRIW-EH H-bond scheme (A, B, C represent the interactions on the three strands; the numbers represent distances measured directly from the pymol models in Å)

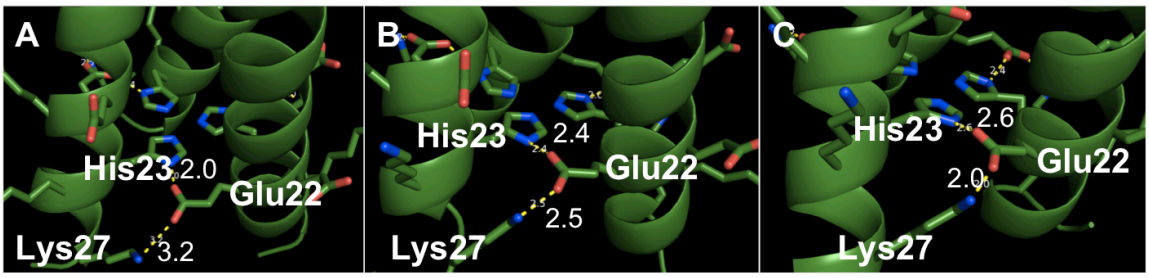

Figure III-26. PyMol models of TRIW-EHE27K H-bond scheme (A, B, C represent the interactions on the three strands; the numbers represent distances measured directly from the pymol models in Å)

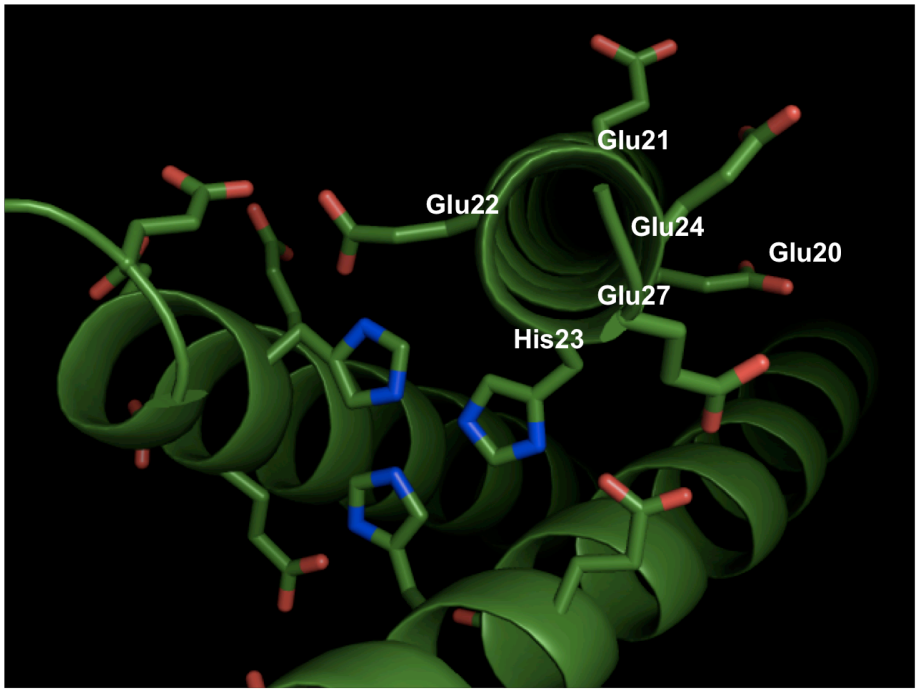

Figure III-27. TRIW-EHK24E helical wheel model representing the local negative charge around the binding site. The Glu22-His23 from the neighboring strands distances are 1.8, 2.2, 2.3 Å (Ave. < 2.7 Å).

Alteration of the amino acid residue in the layer above the copper site (22) has virtually no effect on the reduction potential of the system (at pH 7.4: TRIW-H E^0 = 433 mV; TRIW-HK22Q E^0 = 450 mV; TRIW-EH E^0 = 440 mV). In general, with peptides containing the K22E modification (i.e., those where mutations are made to TRIW-EH), one observes that increasing the side chain positive charge below the metal site causes significant stabilization of the Cu(I) oxidation level, while the Cu(II) state is mildly stabilized by the same mutation. Thus, if we take TRIW-EH as the parent peptide, replacing Lys at the 24 position with Gln and Glu progressively destabilizes Cu(I) binding, whereas converting Glu27 into Gln or Lys yields much higher Cu(I) affinities. If this were solely an electrostatic effect, one might expect the opposite trend for Cu(I) affinity (as more positive charge around the positive metal should destabilize binding) and that the greater effect would be observed for the Cu(II) level (as charge repulsion would be greater). These observations suggest an alternative explanation is required. The best explanation is that this may again reflect H-bonding and salt bridging interactions

between the different surface residues. In the case of Cu(I)-peptides, the dominant factor may be structural perturbations around the metal center.

In order to form an effective geometry for directional H-bonding and salt bridging interactions, the imidazoles may need to reorient to minimize the conformational changes on the peptide backbone. Cu(I) still adopts a trigonal planar coordination when bound to the TRIW-EH series of peptides. However, as shown in Scheme III-1, the orientations of the imidazoles might vary depending on the interactions between the charged residues and the imidazole protons. One may notice that the Debye-Waller factors of the TRIW-EH series are consistently smaller than that of TRIW-H (by 0.002 $Å^2$), which indicates that the Cu(I) trigonal environment in the TRIW-EH series of peptides is slightly less distorted than that for $Cu(I)(TRIW\text{-}H)_3^+$. This could be the result of the interactions described above, which would constrain the motions of the imidazole rings.

It seems that a more ordered trigonal plane possibly exists for TRIW-EHE27K because of the inter-helical H-bonding network formed, connecting His23-Glu22-Lys27 from the adjacent strands that would hold the copper coordinating ligand His in a relatively constrained environment (Figure III-24C). This is of great relevance to the rack-induced binding hypothesis proposed for blue copper electron transfer centers in native proteins.[47] This hypothesis suggests that the protein matrix is responsible for maintaining a proper metal coordination environment and fine-tuning the redox potential to facilitate electron transfer processes. A previous report demonstrates the importance of an H-bond close to the type 1 copper center in plastocyanin, which contributes to the rigidity of the coordinating environment of the type 1 copper center.[48] The higher reduction potential of $Cu(II)(TRIW\text{-}EHE27K)_3^{2+}$, is reflective of the rigidity at the copper centers that favors a trigonal Cu(I).

For TRIW-EHK24E, while Glu22 forms an H-bond with His23, the charge repulsion between Glu22, Glu24 and Glu27 on the neighboring helices might force the imidazoles to adopt a tetrahedral geometry. Such perturbations in geometry are not required for the Cu(II) site as it is believed that this ion is already five-coordinate with the imidazoles no longer planar. So for Cu(II), the influence of salt-bridging and H-bonding effects are not as pronounced. This point may be understood most simply. Cu(II) being much more Lewis acidic should lead to acidification of the coordinated imidazole proton.

Thus, regardless of competing salt bridges, the Glu22 substitution may lead to an H-bond of sufficient stability not to be diminished significantly by salt bridging effects and protein mutations.

NiR activity.

How side chain modifications would affect the known catalytic activity of this system is examined. The nitrite reductase (NiR) activity of these peptides is expressed as the rates of ascorbate consumption. The influence of reduction potential on the NiR rates is clearly revealed when examining the rates at a constant pH. At pH 5.8, for the TRIW-EH series of peptides, the higher the reduction potentials, the lower the rates (Figure III-18). The reduction potential changes from 597 mV (TRIW-EHE27K) to 491 mV (TRIW-EHK24Q), leading to a 3.5 fold increase in the rates (from $9.94(60) \times 10^{-5}$ s^{-1} to $3.48(71) \times 10^{-4}$ s^{-1}). While there is an impressive linear correlation between rates and reduction potential, one must use caution to ascribe this effect to electron transfer since our studies show that the rapid reduction of Cu(II) to Cu(I) by ascorbate can not be rate limiting. More likely, the significant reorganization energy due to the change of coordination geometry from Cu(I) (3-coordinate) to Cu(II) (5-coordinate) limits the observed rates.

The nitrite reduction rates also increase markedly with decreasing pH, which was observed for both the parent peptide[16] and the mutated peptides (Table III-8). The native CuNiR is also reported to exhibit pH-dependent activities that are proposed to be closely related to both the electron transfer process and the nitrite binding step at the catalytic site.[49] In this case, since a type 1 electron transfer site does not exist, and the reduction of the Cu(II) by ascorbate is much faster than the catalytic reaction, the observed pH-dependence is likely correlated to steps during the nitrite reduction catalytic cycle. It is not surprising to see that at a lower pH, the reaction rates are higher, as the full chemical reaction requires two equivalents of protons. Quantitatively, when the pH decreases from 7.0 to 5.8, the proton concentration in the solution $[H^+]$ increases by about 16 times; the rates of the reaction, if directly proportional to $[H^+]^2$, should have increased by 256 fold. Instead, an increase in rate of ~10-fold is observed for TRIW-H. The rates for the TRIW-EH series of peptides similarly increased by about 10-16 fold when the pH changed from

7.0 to 5.8 (Table III-8). If one plots Log(Initial rate) = a -b·pH for TRIW-H, the b coefficient which corresponds to the proton order of the reaction is 0.85. Thus, while the stoichiometric reaction requires two protons, the rate-limiting step is dependent on a single proton. The second proton is necessary once the hydroxide leaving group is formed.[50–52] Similar linear correlations are observed for peptides in the TRIW-EH series as well (Figure III-28), with a slope of 0.85~0.98.

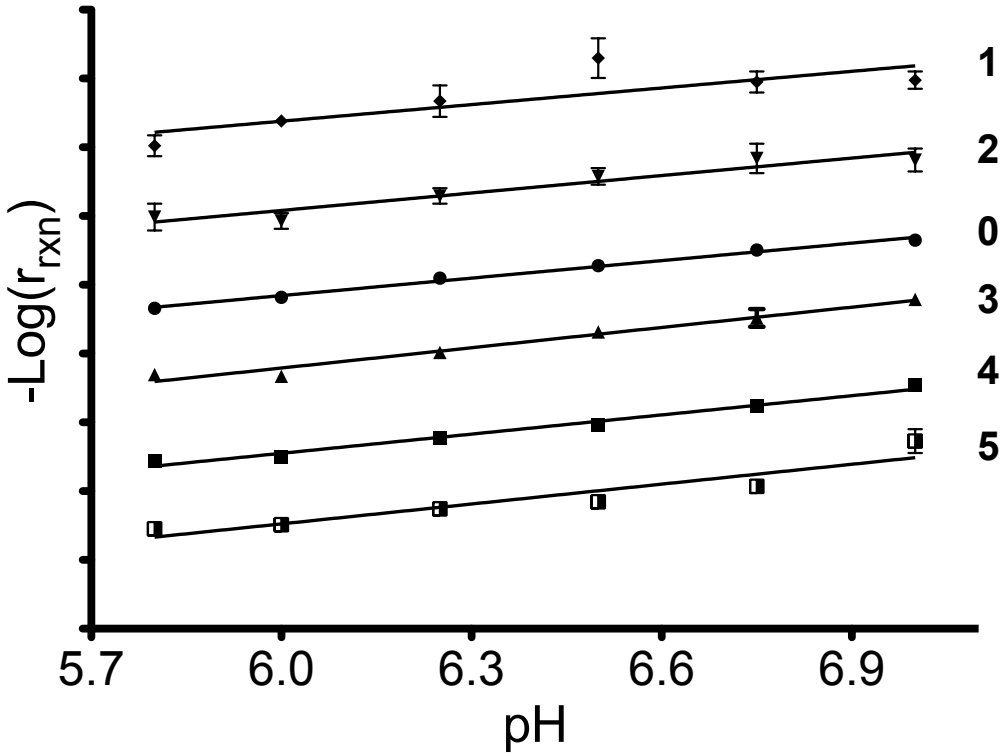

Figure III-28. The correlation between NiR rates and the pH. The rates are on log scales. For a clear presentation, the data points for different peptides are nudged, so there are no absolute values on the y-axis. Peptide: 0. TRIW-H; 1. TRIW-EHE27K; 2. TRIW-EHE27Q; 3. TRIW-EH; 4. TRIW-EHK24Q; 5. TRIW-EHK24E.

For all the TRIW-EH peptides, when the pH decreases from 7.4 to 5.8, the reduction potential increases by about 100 mV. If this is the only factor influencing the rates, the NiR reaction rate should have decreased. It is worth noticing that the rates are very low at pH 7.0, so the NiR rates are only analyzed at pH 5.8. As a result, for a specific peptide, when pH decreases from 7.0 to 5.8, the participation of a proton in the rate-limiting step directly enhances the rate, while the significant structural change upon

converting from Cu(I) to Cu(II) (reflected as an increased reduction potential) impedes the reaction. This is consistent with the trends observed when comparing the peptides at a fixed proton concentration. Combining these two opposite effects, a 10-16 fold rate increase is observed when the pH decreases from 7.0 to 5.8.

It should be noted that the NiR rate vs. reduction potential correlation at a constant pH should be interpreted with caution as it only compares peptides within the TRIW-EH series. If one compares the parent peptide TRIW-H and the charge "flipped" peptide TRIW-EHE27K at pH 5.8 the situation is different. The reduction potential of TRIW-EHE27K is about 200 mV more positive than that of TRIW-H, but its NiR rate is only 2 times less than that of the parent peptide. Using the correlation in Figure III-18, one would have expected a 6-fold differential between these two peptides if reduction potential *alone* were the determining factor. In general, despite the TRIW-EH peptides having much more positive reduction potentials, they have, as a group, comparable rates to TRIW-H. In the next chapter, I will discuss a few peptides that that involve the K22E mutation and demonstrate that Glu22 either does not influence or lowers the reaction rates. Among the TRIW-EH series of peptides presented in this chapter, interactions of Glu22 with other charged residues at the helical interface (*vide supra*) moderate the impact on catalysis of Glu22.

Conclusion

I have presented here a systematic approach of modulating the reduction potentials and NiR activity within a self-assembled peptidic framework by stepwise modifications that influence the local charge. These modifications are carried out for residues at the helical interface. Varied deprotonation equilibria of Cu(II)-peptides are observed, which have a direct impact on the Cu(II) affinities to the *apo*-peptide at different pH conditions. At a specific pH, the influence of the mutations is reflected from the linearly correlated Cu(I)-peptide affinities and Δ_{charge}. Reduction potentials are calculated based on the Cu(I) and Cu(II) affinities to the *apo*-peptides. For a particular peptide, the difference of reduction potentials at different pH conditions originates from the change in Cu(II) affinities; at a specific pH, the difference of reduction potentials for TRIW-EH series of peptides is dominated by the variance in Cu(I) affinities, which could

be the result of the variation in the orientations of imidazole rings upon the alteration of charged residues. Moreover, all of these copper-peptides exhibit pH-dependent NiR activities. Within the TRIW-EH series, the NiR rates are governed by the proton concentration and the reduction potentials. At a specific pH, the reduction potential correlates to the observed rates, however, other factors, such as the formation of substrate-enzyme complex, product-enzyme complex and product release, may also play a role in determining the NiR rates. The effects on the processes described above are likely the result of an H-bond between Glu22 and His23 (or a water molecule bridging the two residues), together with salt-bridging interactions of Glu22 with other charged residues.

This study demonstrates that even in highly simplified scaffolds, attempts to change the local charge around the active site may cause multiple interactions that can vary the redox properties and activities in distinct ways. Nevertheless, this *de novo* design approach allows one to begin to peel the onion layer by layer. One can isolate different factors (pH, affinities, reduction potentials, *et al*.) and to compare and analyze the effects in a multi-dimensional way. In conclusion, this work showcases the strength of *de novo* protein design to anchor the in-depth understanding of fundamental interactions that modulate the redox properties and NiR rates for a type 2 copper center, which provides interesting directions for future work on model chemistry in general.

References

(1) Prabhulkar, S.; Tian, H.; Wang, X.; Zhu, J.-J.; Li, C.-Z. *Antioxid. Redox Signal.* **2012**, *17*, 1796–1822.
(2) Fedurco, M. *Coord. Chem. Rev.* **2000**, *209*, 263–331.
(3) Groves, J. T. *Proc. Natl. Acad. Sci. U. S. A.* **2003**, *100*, 3569–3574.
(4) Umena, Y.; Kawakami, K.; Shen, J.-R.; Kamiya, N. *Nature* **2011**, *473*, 55–60.
(5) Castiglione, N.; Rinaldo, S.; Giardina, G.; Stelitano, V.; Cutruzzolà, F. *Antioxid. Redox Sign.* **2012**, *17*, 684–716.
(6) Gray, H. B.; Malmström, B. G.; Williams, R. J. P. *J. Biol. Inorg. Chem.* **2000**, *5*, 551–559.
(7) Saab-Rincón, G.; Valderrama, B. *Antioxid. Redox Signal.* **2009**, *11*, 167–192.
(8) Matsuda, T.; Warshel, A. *Biochemistry* **1986**, *25*, 1675–1681.
(9) Kuila, D.; Fee, J. A. *J. Biol. Chem.* **1986**, *261*, 2768–2771.
(10) Varadarajan, R.; Zewert, T. E.; Gray, H. B.; Boxer, S. G. *Science* **1989**, *243*, 69–72.
(11) Hellwig, P.; Behr, J.; Ostermeier, C.; Richter, O. M.; Pfitzner, U.; Odenwald, a; Ludwig, B.; Michel, H.; Mäntele, W. *Biochemistry* **1998**, *37*, 7390–7399.
(12) Baltzer, L.; Nilsson, H.; Nilsson, J. *Chem. Rev.* **2001**, *101*, 3153–3163.
(13) DeGrado, W. F.; Summa, C. M.; Pavone, V.; Nastri, F.; Lombardi, A. *Annu. Rev. Biochem.* **1999**, *68*, 779–819.
(14) Bryson, J. W.; Betz, S. F.; Lu, H. S.; Suich, D. J.; Zhou, H. X.; O'Neil, K. T.; DeGrado, W. F. *Science* **1995**, *270*, 935–941.
(15) Ghosh, D.; Pecoraro, V. L. *Inorg. Chem.* **2004**, *43*, 7902–7915.
(16) Tegoni, M.; Yu, F.; Bersellini, M.; Penner-Hahn, J. E.; Pecoraro, V. L. *Proc. Natl. Acad. Sci. U. S. A.* **2012**, *109*, 21234–21239.
(17) Ghadiri, M. R.; Case, M. A. *Angew. Chem. Int. Ed. Engl.* **1993**, *32*, 1594–1597.
(18) Tanaka, T.; Mizuno, T.; Fukui, S.; Hiroaki, H.; Oku, J.-I.; Kanaori, K.; Tajima, K.; Shirakawa, M. *J. Am. Chem. Soc.* **2004**, *126*, 14023–14028.
(19) Kiyokawa, T.; Kanaori, K.; Tajima, K.; Koike, M.; Mizuno, T.; Oku, J. J.-I. I.; Tanaka, T. *J. Pept. Res.* **2004**, *63*, 347–353.
(20) Chufán, E. E.; Prigge, S. T.; Siebert, X.; Eipper, B. A.; Mains, R. E.; Amzel, L. M. *J. Am. Chem. Soc.* **2010**, *132*, 15565–15572.
(21) Evans, J. P.; Blackburn, N. J.; Klinman, J. P. *Biochemistry* **2006**, *45*, 15419–15429.
(22) Kline, C. D.; Mayfield, M.; Blackburn, N. J. *Biochemistry* **2013**, *52*, 2586–2596.
(23) Prigge, S. T.; Eipper, B. A.; Mains, R. E.; Amzel, L. M. *Science* **2004**, *304*, 864–867.
(24) Yu, F.; Penner-Hahn, J. E.; Pecoraro, V. L. *J. Am. Chem. Soc.* **2013**, *135*, 18096–18107.
(25) Zastrow, M. L.; Peacock, A. F. A.; Stuckey, J. A.; Pecoraro, V. L. *Nat. Chem.* **2012**, *4*, 118–123.
(26) *Fmoc Solid Phase Peptide Synthesis, A Practical Approach, Vol. 222*; Chan, W. C.; White, P. D., Eds.; Oxford University Press Inc.: New York, 2000.
(27) Farrer, B. T.; Harris, N. P.; Valchus, K. E.; Pecoraro, V. L. *Biochemistry* **2001**, *40*, 14696–14705.

(28) *The Protein Protocols Handbook*; Walker, J. M., Ed.; Second Edi.; Humana Press Inc.: Totowa, NJ, 2002.
(29) Dieckmann, G. R.; McRorie, D. K.; Lear, J. D.; Sharp, K. A.; DeGrado, W. F.; Pecoraro, V. L. *J. Mol. Biol.* **1998**, *280*, 897–912.
(30) Monzani, E.; Anthony, G. J.; Koolhaas, a; Spandre, a; Leggieri, E.; Casella, L.; Gullotti, M.; Nardin, G.; Randaccio, L.; Fontani, M.; Zanello, P.; Reedijk, J. *J. Biol. Inorg. Chem.* **2000**, *5*, 251–261.
(31) Kau, L. S.; Spira-Solomon, D. J.; Penner-Hahn, J. E.; Hodgson, K. O.; Solomon, E. I. *J. Am. Chem. Soc.* **1987**, *109*, 6433–6442.
(32) Atkins, P.; Overton, T.; Rourke, J.; Weller, M.; Armstrong, F.; Hagerman, M. *Inorganic Chemistry*; Fifth Edit.; Oxford University Press, W. H. Freeman and Company: New York, 2010.
(33) Perrin, B. S.; Ichiye, T. *J. Biol. Inorg. Chem.* **2013**, *18*, 103–110.
(34) Gibney, B. R.; Rabanal, F.; Reddy, K. S.; Dutton, P. L. *Biochemistry* **1998**, *37*, 4635–4643.
(35) Shifman, J. M.; Gibney, B. R.; Sharp, R. E.; Dutton, P. L. *Biochemistry* **2000**, *39*, 14813–14821.
(36) Gibney, B. R.; Isogai, Y.; Rabanal, F.; Reddy, K. S.; Grosset, a M.; Moser, C. C.; Dutton, P. L. *Biochemistry* **2000**, *39*, 11041–11049.
(37) Gibney, B. R.; Dutton, P. L. In *Advances in Inorganic Chemistry*; 2001; Vol. 68, pp. 409–456.
(38) Marshall, N. M.; Garner, D. K.; Wilson, T. D.; Gao, Y.-G.; Robinson, H.; Nilges, M. J.; Lu, Y. *Nature* **2009**, *462*, 113–116.
(39) New, S. Y.; Marshall, N. M.; Hor, T. S. A.; Xue, F.; Lu, Y. *Chem. Commun. (Camb).* **2012**, *48*, 4217–4219.
(40) Peacock, A. F. A.; Iranzo, O.; Pecoraro, V. L. *Dalton Trans.* **2009**, *9226*, 2271–2280.
(41) Dooley, D. M.; Scott, R. A.; Knowles, P. F.; Colangelo, C. M.; McGuirl, M. A.; Brown, D. E. *J. Am. Chem. Soc.* **1998**, *120*, 2599–2605.
(42) Sanyal, I.; Karlin, K. D.; Strange, R. W.; Blackburn, N. J. *J. Am. Chem. Soc.* **1993**, *115*, 11259–11270.
(43) Sundberg, R. J.; Martin, R. B. *Chem. Rev.* **1974**, *74*, 471–517.
(44) Ambundo, E. A.; Deydier, M.; Grall, A. J.; Aguera-vega, N.; Dressel, L. T.; Cooper, T. H.; Heeg, M. J.; Ochrymowycz, L. A.; Rorabacher, D. B. *Inorg. Chem.* **1999**, *38*, 4233–4242.
(45) Rorabacher, D. B. *Chem. Rev.* **2004**, *104*, 651–697.
(46) Bernardo, M. M.; Heeg, J.; Schroeder, I. R. R.; Ochrymowycz, L. A.; Rorabacher, D. B. *Inorg. Chem.* **1992**, *31*, 191–198.
(47) Gray, H. B.; Malmström, B. G. *Comments Inorg. Chem.* **1983**, *2*, 203–209.
(48) Dong, S.; Ybe, J. a; Hecht, M. H.; Spiro, T. G. *Biochemistry* **1999**, *38*, 3379–3385.
(49) Pinho, D.; Besson, S.; Brondino, C. D.; de Castro, B.; Moura, I. *Eur. J. Biochem.* **2004**, *271*, 2361–2369.
(50) Tocheva, E. I.; Rosell, F. I.; Mauk, a G.; Murphy, M. E. P. *Science* **2004**, *304*, 867–870.
(51) Antonyuk, S. V; Strange, R. W.; Sawers, G.; Eady, R. R.; Hasnain, S. S. *Proc. Natl. Acad. Sci. U. S. A.* **2005**, *102*, 12041–12046.

(52) Tavares, P.; Pereira, a S.; Moura, J. J. G.; Moura, I. *J. Inorg. Biochem.* **2006**, *100*, 2087–2100.

Chapter IV . Modifications of the interior of the coiled coils to achieve a better NiR model

Introduction

The fine-tuning of activities of a metal center involves interactions beyond the coordinating atoms. As discussed in Chapter I, the second coordination sphere interactions have an impact on the reactivity of metal centers through H-bonding, salt-bridges, packing patterns, and hydrophobicity in both redesigned and *de novo* designed systems. Significant efforts have been made to understand how the above-described interactions influence the activity of hydrolytic centers such as the zinc center in CA,[1–5] and electron transfer centers such as a cupredoxin center.[6] Again, no such study on a $Cu(His)_3$ center was precedent before this thesis work was begun. The crystal structure of NiR reveals a few important residues that are responsible for solvent and substrate binding, shaping the active site, as well as facilitating proton/electron transfer at the T2Cu center.[7–13] Mutagenesis studies have been carried out to probe the roles of these residues. For example, Asp98 in *Achromobacter cycloclastes* CuNiR forms an H-bond with the copper-coordinating water[14] or nitrite, playing a direct role in the protonation of intermediates. The mutation of Asp into an Asn significantly decreases the activity attributed to the loss of this H-bond or an alternative substrate binding mode due to a different orientation of the Asn side chain.[7,8] An Ile residue at position 257 is highly conserved in native NiRs. When Ile257 is mutated to Ala, Gly, Thr, and Met, nitrite binds to the T2Cu center in a monodendate mode revealed by crystal structures, leading to the decrease of specific activity of up to 100-fold.[9] Therefore, the residues beyond the first coordination sphere are essential for efficient nitrite reduction to occur at this copper site.

In the context of this thesis, I have constructed a model for the first coordination sphere of the T2Cu center in NiR as described in Chapter II. The cuprous state of this model is three-coordinate, the same coordination number as the ascorbate-reduced T2Cu

center in CuNiR.[15] The cupric state might have a higher coordination number than seen in the native T2Cu center. Although possessing a higher redox potential as compared to native CuNiR, this model can still catalyze nitrite reduction with 5 turnovers over 3.7 h. Then I explored the modification of the charged residues on the helical interface that yielded a series of peptides with reduction potentials spanning ~200 mV and NiR rates varying 4-fold (Chapter III). These modifications are thought to alter the electrostatics around the copper center, the H-bonding interactions, and the salt-bridges, which are all important facets of second coordination sphere interactions.[16] In this chapter, I will take a different design approach to modify the residues in the interior of the helical coiled coils in order to utilize a few other second coordination sphere interactions to tune the reactivity.

Two general strategies are undertaken: 1) the modification of the hydrophobic residues around the copper center; 2) the modification of the electronic environment of the imidazole ring by incorporating an unnatural amino acid N-methyl-histidine. In addition, the K22E mutation is also introduced combined with the two strategies mentioned above. Table IV-1 shows the peptide sequences involved in this chapter. The potential consequences of these modifications include the change of the coordination environment on either or both oxidation levels, the alteration of solvent/substrate access, the change of the H-bonding scheme around the copper center, and the variation of the Lewis acidity of the copper ions. All these possible effects might lead to altered reactivity.

Table IV-1. Peptide sequences involved in Chapter IV

Peptide[1]	Sequence
	a b c d e f g a b c d e f g a b c d e f g a b c d e f g
	1 2 8 9 15 16 19 23 29 30
TRIW-H	Ac-G WKALEEK LKALEEK LKALEEK HKALEEK G-NH_2
TRIW-HL19A	Ac-G WKALEEK LKALEEK LKA**A**EEK HKALEEK G-NH_2
TRIW-$_M$H[2]	Ac-G WKALEEK LKALEEK LKALEEK $_M$**H**KALEEK G-NH_2
TRIW-$_M$HL19A	Ac-G WKALEEK LKALEEK LKA**A**EEK $_M$**H**KALEEK G-NH_2
TRIW-EH	Ac-G WKALEEK LKALEEK LKALEE**E** **H**KALEEK G-NH_2
TRIW-E$_M$H	Ac-G WKALEEK LKALEEK LKALEE**E** $_M$**H**KALEEK G-NH_2
TRIW-EHL19A	Ac-G WKALEEK LKALEEK LKA**A**EE**E** HKALEEK G-NH_2

[1]The C-termini are capped by a –NH_2 group and the N-termini are capped by an acetyl (-Ac) group.

[2]$_M$H stands for N-methyl-histidine, which has a methyl group on the $^{\delta}$N of the imidazole.

Material and methods

All the general procedures and methods are the same as reported in the the previous chapters.

NiR rates at pH 5.8.

30 mM $NaNO_2$ was mixed with 19.4 μM Cu(II)(3SCC) and 80.6 μM apo-3SCC (to ensure that over 99% of Cu(II) is bound to the peptide) in 50 mM potassium phosphate buffer. The pH was adjusted to 5.8 by adding small amount of concentrated KOH or $KHSO_4$. The reaction was initiated by adding 1.1 mM sodium ascorbate (NaAsc). The consumption of sodium ascorbate (NaAsc) was monitored by UV-Visible spectroscopy. The control was a mixture of 30 mM $NaNO_2$ and 80.6 μM apo-3SCC with the same amount of NaAsc. The rates of the reaction were calculated by two times the different rates of NaAsc consumption (decrease of absorbance at 251 nm) between the sample and the control. To compare to the peptides presented in the previous chapters, the rates were then calibrated based on the first order dependence between peptide concentrations and rates.

Correlation between peptide concentrations and rates at pH 5.8.

A series of reactions with different Cu(II)(3SCC) concentrations were set up to establish the relationship between enzyme concentration and NiR rates. The samples contain 30 mM $NaNO_2$, varied concentrations of Cu(II)(3SCC) (0.5, 1, 5, 10, 15, and 20 μM), and corresponding concentrations of apo-peptides (3.5, 7, 35, 70, 105, 140 μM). The controls contain 30 mM $NaNO_2$ and apo-peptides (3.5, 7, 35, 70, 105, 140 μM). The pH of the solution was adjusted to 5.8 by adding concentration KOH/$KHSO_4$. The reactions were initiated by adding a solution of NaAsc. The final NaAsc concentration in the cuvette was 1.5 mM. The rates of the reaction were calculated the same way as discussed previously.

Michaelis-Menten kinetics.

Different concentrations of $NaNO_2$ (0.5, 1, 2.5, 5, 10, 20, 30, 40, 50, 100, 150, 200, 300 mM) were incubated with the peptides. Samples contained 10 μM Cu(II)(3SCC), 70 μM apo-peptide in 50 mM potassium phosphate buffer. Controls contained 70 μM apo-peptide. The pH was adjusted to 5.8. The reactions were initiated by injecting NaAsc to the reaction mixture. The final NaAsc concentration was 1.5 mM. The rates of the reactions were calculated the same way as discussed previously.. The rates were correlated to the substrate concentrations through fits to the Michaelis-Menten equation in Prism 5 (GraphPad software).

Results

Characterization of apo-peptides.

The CD spectra of apo-peptides are shown in Figure IV-1A. These peptides all have characteristic double-well spectra at 208 and 222 nm, signifying formation of coiled coils. It is worth noticing that with the introduction of the L19A mutation, the helical content of the apo-peptide decreases from ~70% to ~60%. In addition, the introduction of a methyl group on the imidazole does not alter the helical content or the stability of the peptide as compared to TRIW-H ($[GuaHCl]_{midpoint}$ = 2 M for both denaturation titrations). Since there is no plateau at the beginning of the titration curve, the unfolding process cannot be fitted to a two-state model.

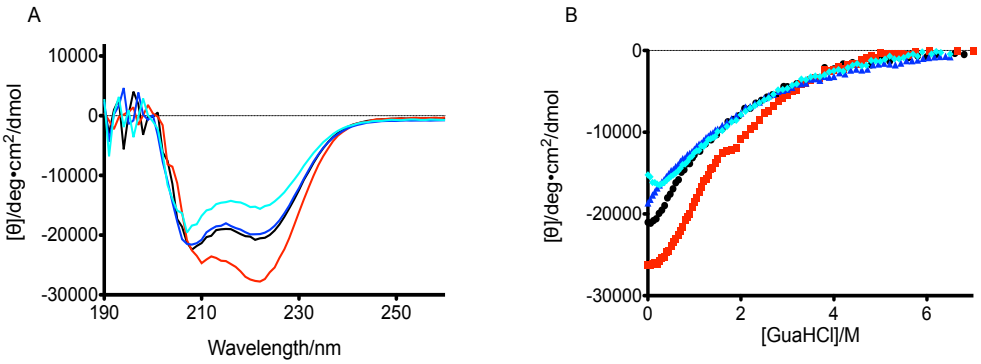

Figure IV-1. (A) CD spectra of TRIW-EHL19A (cyan spectrum), TRIW-HL19A (black spectrum), TRIW-$_M$H (red spectrum), and TRIW-$_M$HL19A (blue spectrum). (B) GuaHCl denaturation titration monitored by CD. The color-coding for peptides is the same as (A).

XAS of Cu(I)(TRIW-HL19A)$_3^+$.

The L19A mutation leads to a different Cu(I) coordination environment at pH 5.8. The XANES of Cu(I)(TRIW-HL19A)$_3^+$ has a relatively high intensity at ~8984 eV, typical of a two-coordinate Cu(I) center. As pH is increased from 5.8 to 7.4, this feature gradually decreases. At pH 7.4, the XANES resembles that of a three-coordinate Cu(I). The EXAFS fittings of Cu(I)(TRIW-HL19A)$_3^+$ at these two pH conditions are consistent with the change of coordination numbers (Figure IV-3, Table IV-2). Going from pH 5.8 to 7.4, the Cu-N_{imid} distance increases by 0.05 Å, which is smaller than one might expect for an increase of one in coordination number (~0.07-0.1 Å).

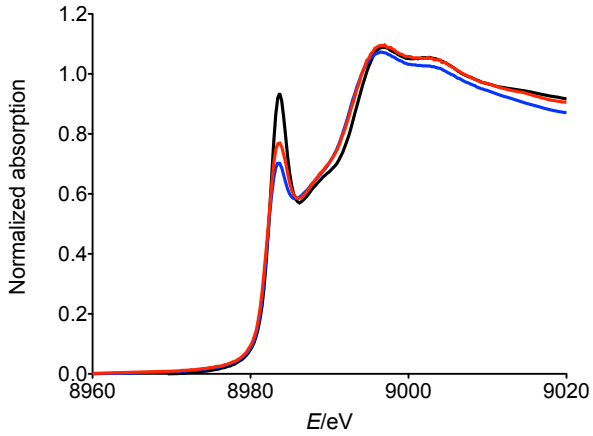

Figure IV-2. XANES of Cu(I)(TRIW-HL19A)$_3^+$ at pH 5.8 (black spectrum), 6.5 (red spectrum), and 7.4 (blue spectrum).

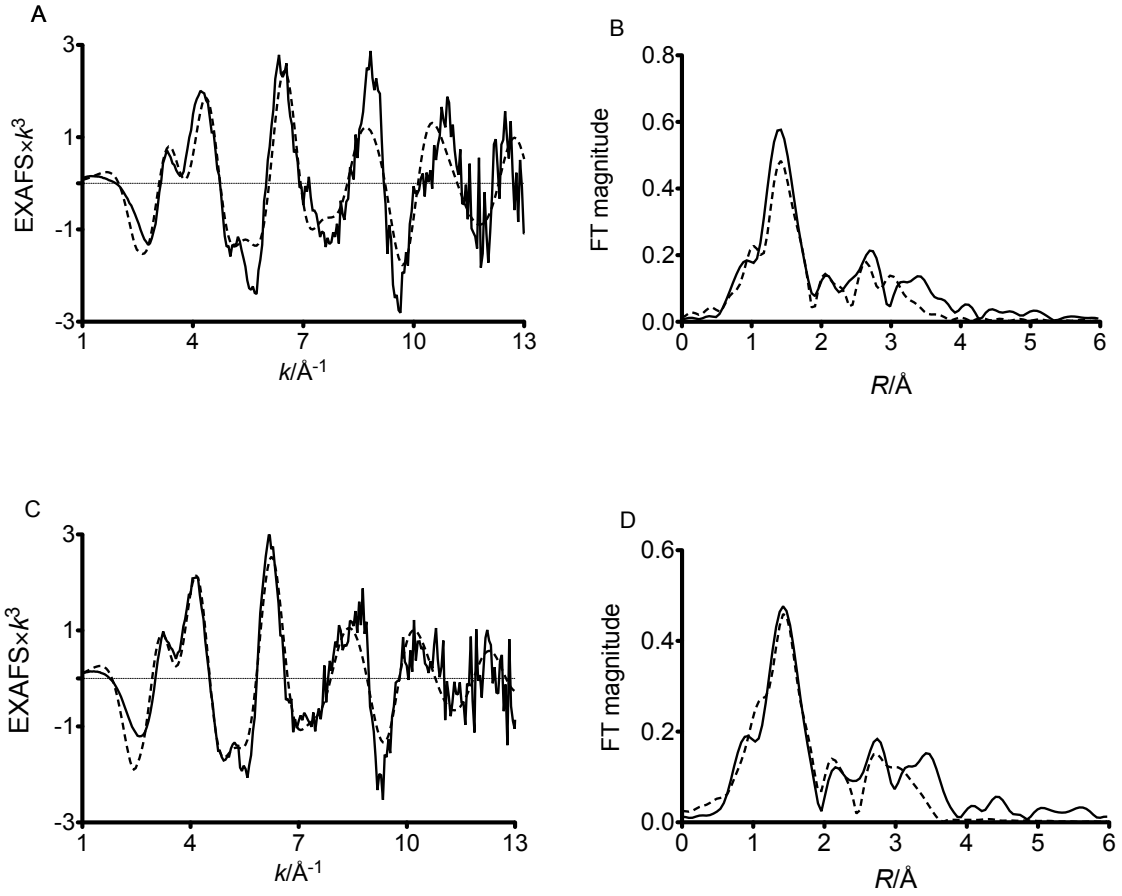

Figure IV-3. EXAFS of Cu(I)(TRIW-HL19A)$_3^+$ at pH 5.8 (A) and pH 7.4 (C). The Fourier transform of the EXAFS at pH 5.8 (B) and pH 7.4 (D). Experimental data are shown in solid lines and fittings are shown as dashed lines.

XAS of Cu(I)(TRIW-$_M$H)$_3^+$.

The XANES of Cu(I)(TRIW-$_M$H)$_3^+$ overlays very well with that of Cu(I)(TRIW-H)$_3^+$, indicating that Cu(I) is still three-coordinate. Subtle differences in the edge structures might reflect minimal geometrical perturbations. Also similar to Cu(I)(TRIW-H)$_3^+$, when the pH increases from 5.8 to 7.4, there is essentially no change in the XANES of Cu(I)(TRIW-$_M$H)$_3^+$ (Figure IV-4). EXAFS fitting results corroborate the assignment of coordination numbers. A typical three-coordinate Cu-N$_{imid}$ distance is seen (1.935 Å) with a smaller Debye-Waller factor as compared to that for Cu(I)(TRIW-H)$_3^+$ (Figure IV-5, Table IV-2).

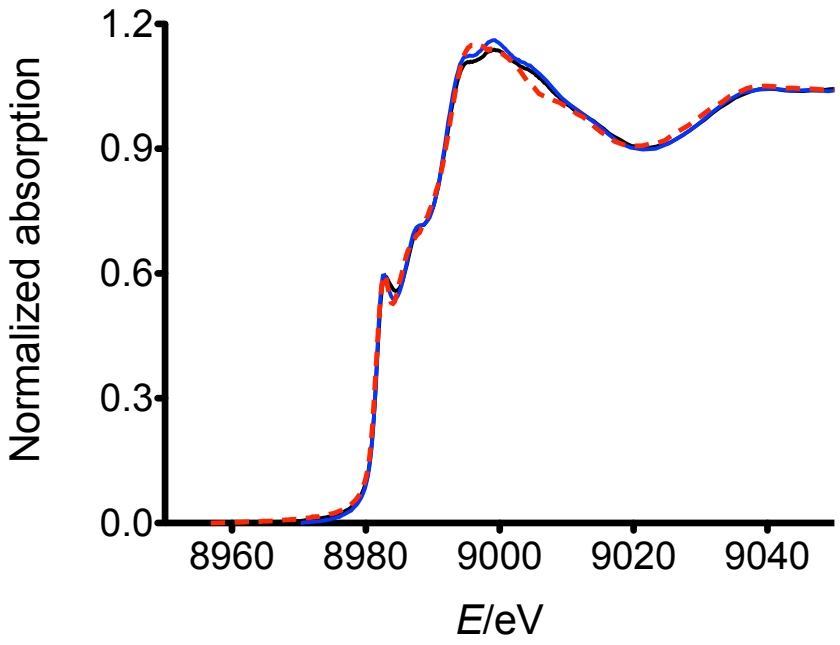

Figure IV-4. XANES of Cu(I)(TRIW-$_M$H)$_3^+$ at pH 5.8 (black solid line) and 7.4 (blue solid line) compared to that of Cu(I)(TRIW-H)$_3^+$ at pH 5.8 (red dashed line).

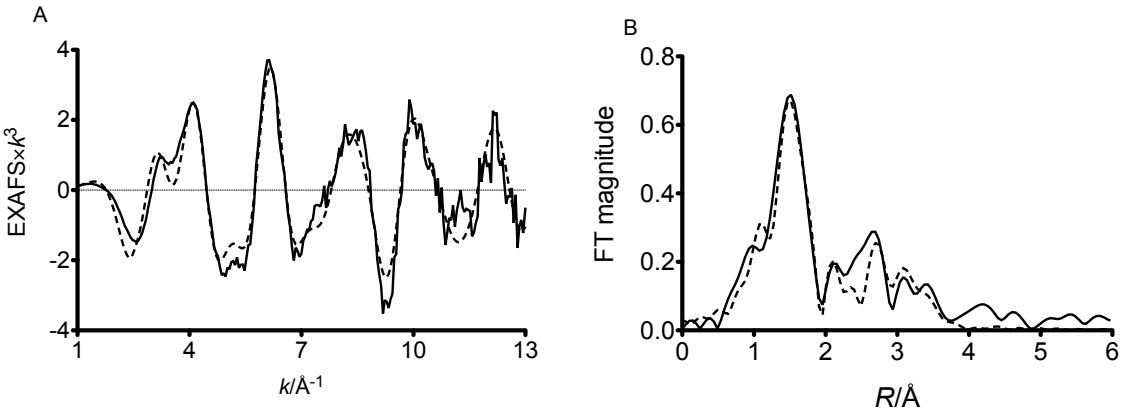

Figure IV-5. EXAFS (A) and Fourier transform (B) of Cu(I)(TRIW-$_M$H)$_3^+$. Experimental data are shown in solid lines and fittings are represented as dashed lines.

XAS of other peptides involved in this study.

The XANES of other peptides involved in this chapter are shown in Figure IV-6. They are presented in three groups. Group 1 (Figure IV-6A) includes two types of modifications: L19A and L23$_M$H, and their combination $_M$HL19A. As described above, at

pH 5.8, Cu(I)(TRIW-H19A)$_3^+$ is two-coordinate while Cu(I)(TRIW-$_M$H)$_3^+$ is three-coordinate. One sees an intermediary spectrum for Cu(I)(TRIW-$_M$HL19A)$_3^+$. Group 2 (Figure IV-6B) focuses on K22E and L19A mutations and a peptide combining these two features (TRIW-EHL19A). Cu(I) binds to three His in a distorted trigonal plane in TRIW-EH (Chapter III), however, when the L19A mutation is introduced, the coordination number of Cu(I) decreases from 3 to 2, as the XANES of Cu(I)(TRIW-EHL19A)$_3^+$ is the same as that of Cu(I)(TRIW-HL19A)$_3^+$. Group 3 (Figure IV-6C) contains peptides with only an $_M$H feature, K22E mutation with $_M$H, and L19A mutation with $_M$H feature. Again, one sees the tendency of forming a two-coordinate Cu(I) once L19A is introduced to TRIW-$_M$H. Interestingly, in the presence of a methyl group on imidazole, it seems that K22E mutation drives toward the formation of a two-coordinate Cu(I) as well. The EXAFS fittings of these peptides are mostly consistent with the assignment of coordination numbers, resulting in typical two- or three-coordinate Cu(I)-N_{imid} distances (Table IV-2, Figure IV-7, Figure IV-8, and Figure IV-9).

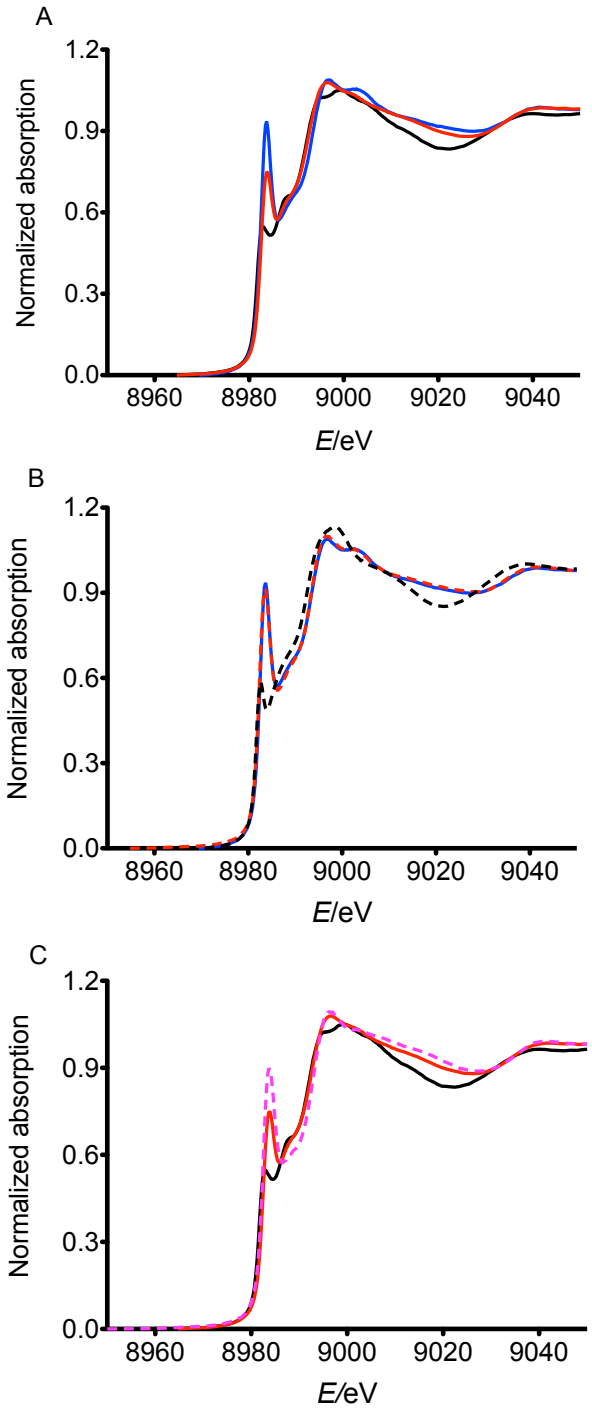

Figure IV-6. (A) XANES of Cu(I)(TRIW-HL19A)$_3^+$ (solid blue line), Cu(I)(TRIW-$_M$H)$_3^+$ (solid black line), and Cu(I)(TRIW-$_M$HL19A)$_3^+$ (solid red line) at pH 5.8; (B) XANES of Cu(I)(TRIW-HL19A)$_3^+$ (solid blue line), Cu(I)(TRIW-EHL19A)$_3^+$ (dashed red line), and Cu(I)(TRIW-EH)$_3^+$ (dashed black line) at pH 5.8; (C) XANES of Cu(I)(TRIW-$_M$H)$_3^+$ (solid black line), Cu(I)(TRIW-$_M$HL19A)$_3^+$ (solid red line), and Cu(I)(TRIW-E$_M$H)$_3^+$ (dashed purple line) at pH 5.8.

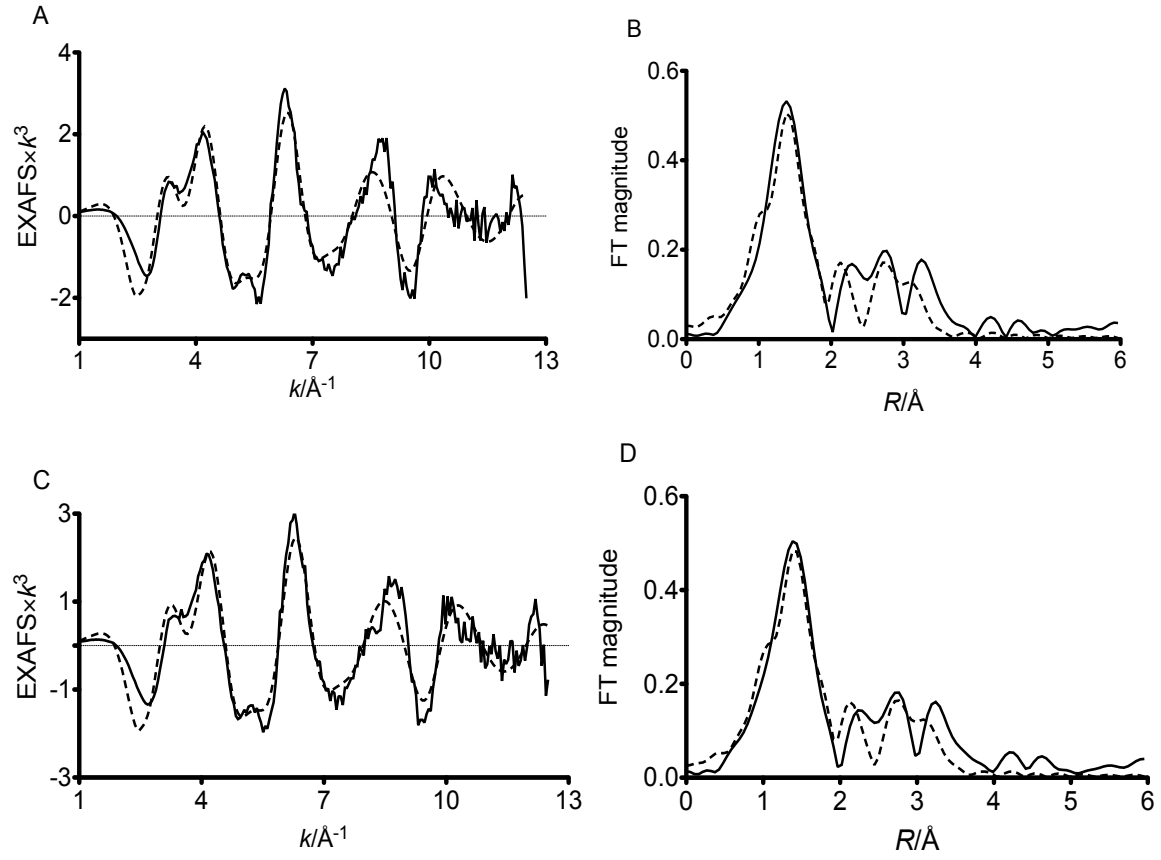

Figure IV-7. Cu(I)(TRIW-$_M$HL19A)$_3^+$ at pH 5.8 [EXAFS (A) and Fourier transform (B)] and 7.4 [EXAFS (C) and Fourier transform (D)]. Experimental data are shown in solid lines and fittings are shown as dashed lines.

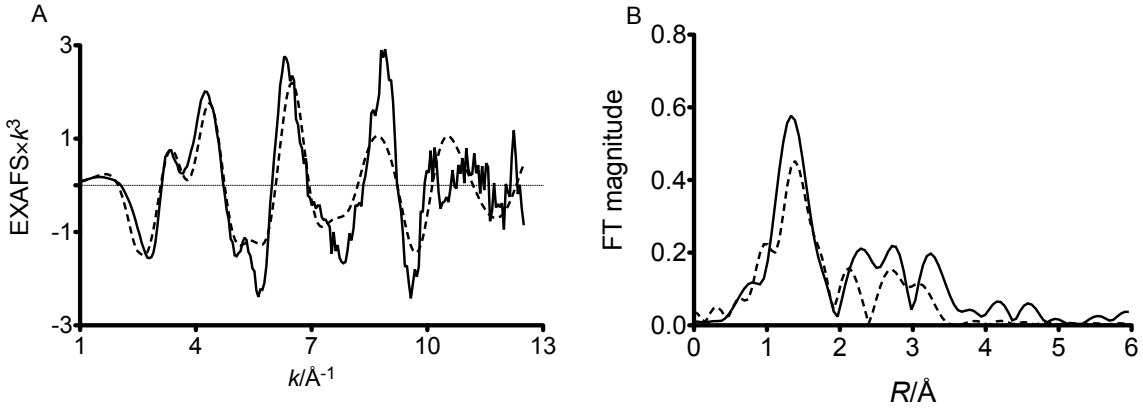

Figure IV-8. EXAFS (A) and Fourier transform of EXAFS of Cu(I)(TRIW-E$_M$H)$_3^+$ at pH 5.8. Experimental data are shown in solid lines and fittings are shown as dashed lines.

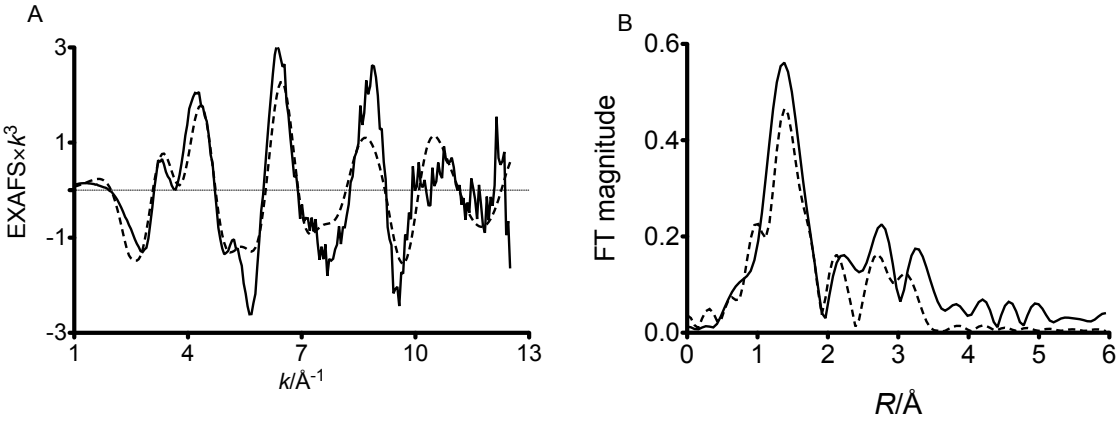

Figure IV-9. EXAFS (A) and Fourier transform of EXAFS of Cu(I)(TRIW-EHL19A)$_3^+$ at pH 5.8. Experimental data are shown in solid lines and fittings are shown as dashed lines.

Table IV-2. EXAFS fitting parameters

Peptide	First shell	R/Å	σ^2/Å^2	Outer shells	R/Å	σ^2/Å^2	N_{var}	$F^2/(N_{free}) \times 10^{-2}$
Cu(I)(TRIW-HL19A)$_3^+$, pH 5.8	2 Cu(I)-N$^{(1)}$	1.860	0.0072	2 Cu-C$^{(1)}$	2.812	0.0109	2	5.7
				2 Cu-C$^{(2)}$	2.845	0.0110		
				2 Cu-N$^{(2)}$	3.912	0.0152		
				2 Cu-C$^{(3)}$	3.924	0.0152		
Cu(I)(TRIW-HL19A)$_3^+$, pH 7.4	3 Cu(I)-N$^{(1)}$	1.914	0.0102	3 Cu-C$^{(1)}$	2.893	0.0154	2	1.7
				3 Cu-C$^{(2)}$	2.928	0.0156		
				3 Cu-N$^{(2)}$	4.025	0.0215		
				3 Cu-C$^{(3)}$	4.038	0.0215		
Cu(I)(TRIW-$_M$H)$_3^+$, pH 5.8	3 Cu(I)-N$^{(1)}$	1.935	0.0070	3 Cu-C$^{(1)}$	2.925	0.0105	2	4.1
				3 Cu-C$^{(2)}$	2.960	0.0107		
				3 Cu-N$^{(2)}$	4.070	0.0147		
				3 Cu-C$^{(3)}$	4.082	0.0147		
Cu(I)(TRIW-$_M$HL19A)$_3^+$, pH 5.8	3.00 Cu(I)-N$^{(1)}$	1.890	0.0103	3 Cu-C$^{(1)}$	2.857	0.0156	3	1.8
				3 Cu-C$^{(2)}$	2.891	0.0158		
				3 Cu-N$^{(2)}$	3.975	0.0212		
				3 Cu-C$^{(3)}$	3.988	0.0218		
Cu(I)(TRIW-$_M$HL19A)$_3^+$,	2.87 Cu(I)-N$^{(1)}$	1.900	0.0102	2.87 Cu-C$^{(1)}$	2.872	0.0154	3	1.0

pH 7.4				2.87 Cu-$C^{(2)}$	2.906	0.0156		
				2.87 Cu-$N^{(2)}$	3.995	0.0214		
				2.87 Cu-$C^{(3)}$	4.008	0.0216		
$Cu(I)(TRIW\text{-}E_MH)_3^+$, pH 5.8	2 Cu(I)-$N^{(1)}$	1.859	0.0081	2 Cu-$C^{(1)}$	2.810	0.0123	2	4.9
				2 Cu-$C^{(2)}$	2.844	0.0124		
				2 Cu-$N^{(2)}$	3.910	0.0171		
				2 Cu-$C^{(3)}$	3.922	0.0172		
$Cu(I)(TRIW\text{-}EHL19A)_3^+$, pH 5.8	2 Cu(I)-$N^{(1)}$	1.864	0.0078	2 Cu-$C^{(1)}$	2.818	0.0118	2	4.2
				2 Cu-$C^{(2)}$	2.851	0.0119		
				2 Cu-$N^{(2)}$	3.920	0.0164		
				2 Cu-$C^{(3)}$	3.933	0.0164		

4. R: absorber-backscatterer distance; σ^2: Debye-Waller factor. ΔE_0 is fixed at -10 eV. R (distance) and σ^2 (Debye-Waller factor) are the only freely variable parameters (in red). Linked variables are in blue.
5. $N_{idp} = 2\Delta k \Delta R/\pi \sim 19$, $N_{free} = N_{idp} - N_{var}$. The outer shell parameters are calculated assuming a rigid imidazole ring.
6. The goodness of the fit is evaluated by $F' = F^2/(N_{free}) \times 10^{-2}$. The smaller the value, the better the fit.

CO adduct of Cu(I)(TRIW-HL19A)$_3^+$ at pH 5.8.

In Chapter II, I presented the characterization of the CO adduct of Cu(I)(TRIW-H)$_3^+$. As a probe molecule, CO is widely used to study the coordination environment of Cu(I) in synthetic small molecules and native copper centers.[17–23] If this method can be applied to the case of Cu(I)(TRIW-HL19A)$_3^+$ (pH 5.8), one would expect to see a very different CO stretching frequency (~2100 cm^{-1})[20] since Cu(I) is two-coordinate at this pH. Surprisingly, the CO adduct of Cu(I)(TRIW-HL19A)$_3^+$ exhibits a C-O stretching frequency of 2064.6 cm^{-1}, suggesting the formation of a tetrahedral Cu(I) center where Cu(I) is coordinated to three His and a CO in a terminal binding mode (Chapter II).[19,22] The XANES of Cu(I)(CO)(TRIW-HL19A)$_3^+$ is different from those of Cu(I)(TRIW-HL19A)$_3^+$, which has a two-coordinate Cu(I), and from Cu(I)(TRIW-H)$_3^+$ with a three-coordinate Cu(I). The decreased intensity of the ~8984 eV peak indicates the formation of a four-coordinate Cu(I) center, consistent with the FTIR analysis.

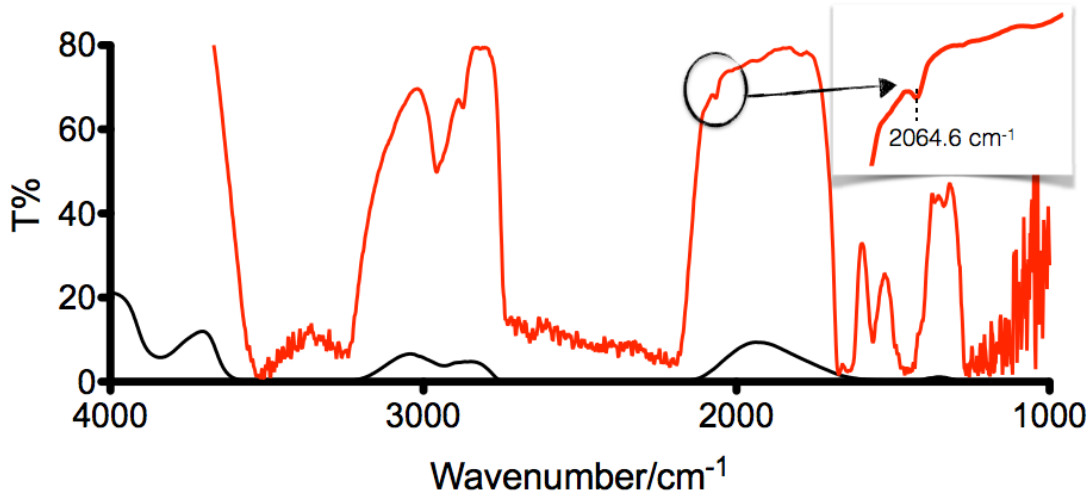

Figure IV-10. FTIR spectrum of the CO adduct of Cu(I)(TRIW-HL19A)$_3^+$ at pH 5.8.

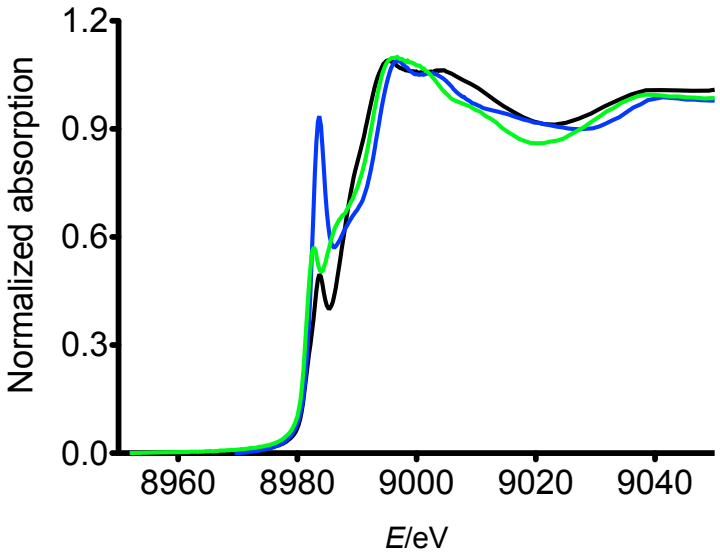

Figure IV-11. XANES of Cu(I)(TRIW-HL19A)$_3^+$ (blue spectrum), Cu(I)(CO)(TRIW-HL19A)$_3^+$ (black spectrum), and Cu(I)(TRIW-H)$_3^+$ (green spectrum) at pH 5.8.

Spectroscopies of Cu(II)-peptides.

The absorption spectra of Cu(II)(3SCC) exhibit typical T2Cu features, with broad absorption bands and low extinction coefficients (Table IV-3). These absorption features are typical of $N_{2\text{-}3}O_{2\text{-}3}$ coordination to Cu(II). Together with EPR parameters (Table IV-4), Cu(II) spectroscopy studies indicate that Cu(II) is coordinated to multiple nitrogen atoms (presumably from imidazoles) and oxygen atoms (from solvent) with a relatively high coordination number (4~5).

Table IV-3. *d-d* absorption features of Cu(II)(3SCC)

Peptide	λ_{max}(ε/M^{-1} cm^{-1})/nm, pH 5.8	λ_{max}(ε/M^{-1} cm^{-1})/nm, pH 7.4
Cu(II)(TRIW-HL19A)$_3^{2+}$	652(94)	646(100)
Cu(II)(TRIW-$_M$H)$_3^{2+}$	670(67)	666(72)
Cu(II)(TRIW-$_M$HL19A)$_3^{2+}$	659(74)	645(82)
Cu(II)(TRIW-E$_M$H)$_3^{2+}$	689(71)	657(76)
Cu(II)(TRIW-EHL19A)$_3^{2+}$	677(75)	664(74)

Table IV-4. EPR parameters of selected Cu(II)(3SCC) at pH 5.8

Peptide	g_x	g_y	g_z	A_z/mT
$Cu(II)(TRIW\text{-}HL19A)_3^{2+}$	2.050	2.060	2.278	18.93
$Cu(II)(TRIW\text{-}_MH)_3^{2+}$	2.054	2.058	2.292	18.65
$Cu(II)(TRIW\text{-}_MHL19A)_3^{2+}$	2.048	2.058	2.285	18.93

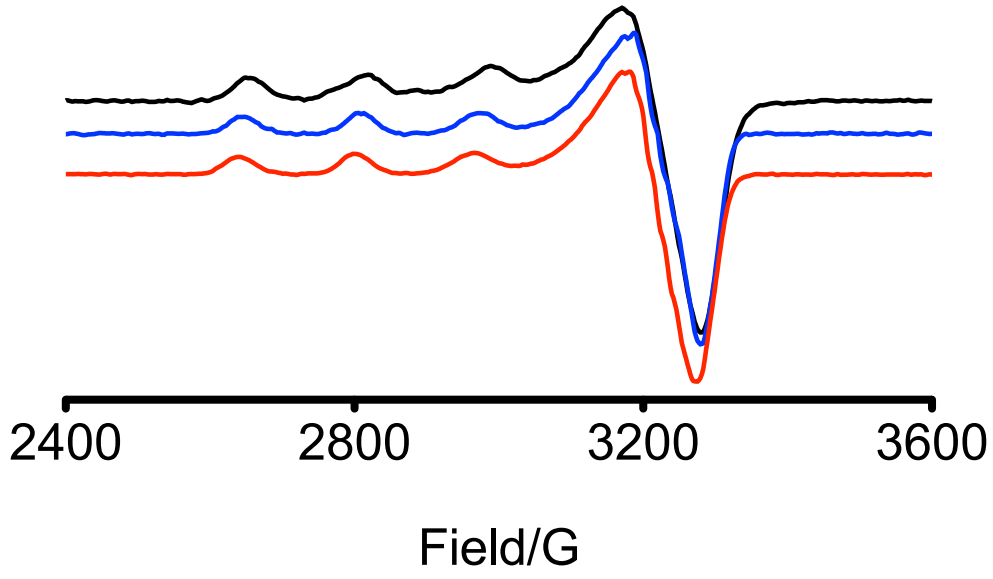

Figure IV-12. EPR spectra of $Cu(II)(TRIW\text{-}HL19A)_3^{2+}$ (black spectrum), $Cu(II)(TRIW\text{-}_MHL19A)_3^{2+}$ (blue spectrum), and $Cu(II)(TRIW\text{-}_MH)_3^{2+}$ (red spectrum).

pK_a of Cu(II)(3SCC).

pH titrations were carried out for Cu(II)(3SCC) to probe how the Cu(II) coordination environment changes upon changing pH and to understand the nature of the coordination environment based on the deprotonation events observed for a specific peptide. For each system, as pH is increased from ~3 to ~5, a *d-d* band grows in at 650 – 690 nm. After this conversion, the *d-d* band evolves differently for different peptides.

For $Cu(II)(TRIW\text{-}HL19A)_3^{2+}$, from pH 5.60 to 7.95, the *d-d* band is essentially unvaried (Figure IV-13A). As the pH keeps increasing, the spectra transform into

another set with a maximum centered at 516 nm (Figure IV-13B). This conversion can be fitted into a protonation equilibrium with a pK_a = 9.08(3), n = 0.99(7) (Figure IV-14).

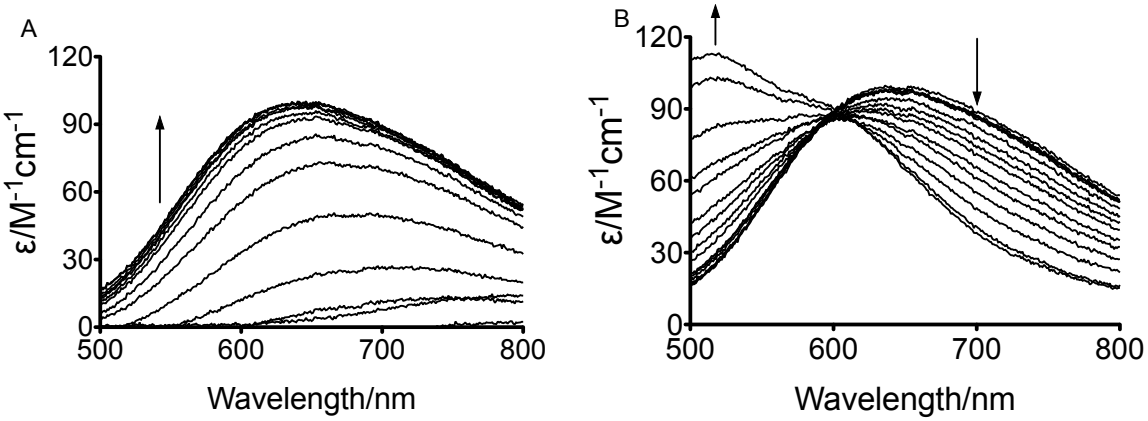

Figure IV-13. pH titration of Cu(II)(TRIW-HL19A)$_3^+$. (A) pH 2.94 – 7.26; (B) pH 7.26 – 9.93.

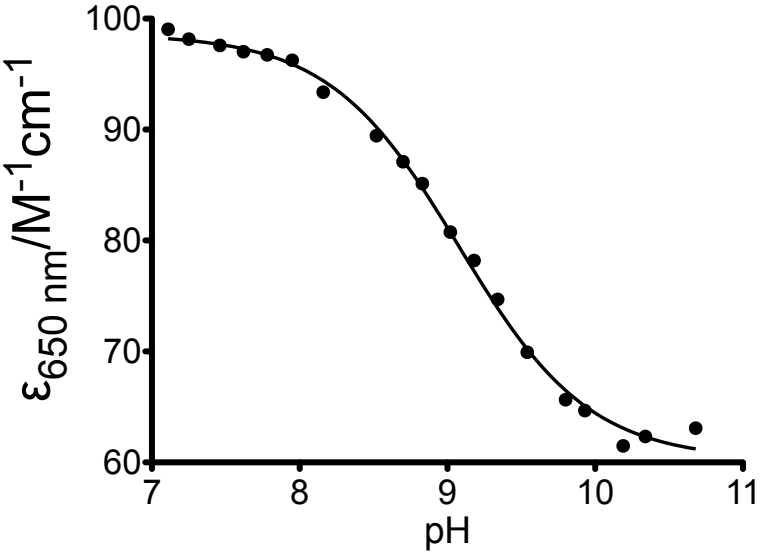

Figure IV-14. The *d-d* band extinction coefficient of Cu(II)(TRIW-HL19A)$_3^+$ fitted to Equation II-3 at pH 7 – 11.

When a methyl group is introduced onto the imidazole, one more protonation equilibrium is observed in the neutral pH range. When the pH is raised from 5.99 to 9.07, the Cu(II) *d-d* band shifts from 660 nm to 625 nm, with an increased extinction coefficient (Figure IV-15A). This conversion can be fitted to Equation II-3, yielding a

pK_a = 7.53(5), n = 1.18(14). Furthermore, in an even higher pH range (9.07 – 10.79), a similar transformation is observed.

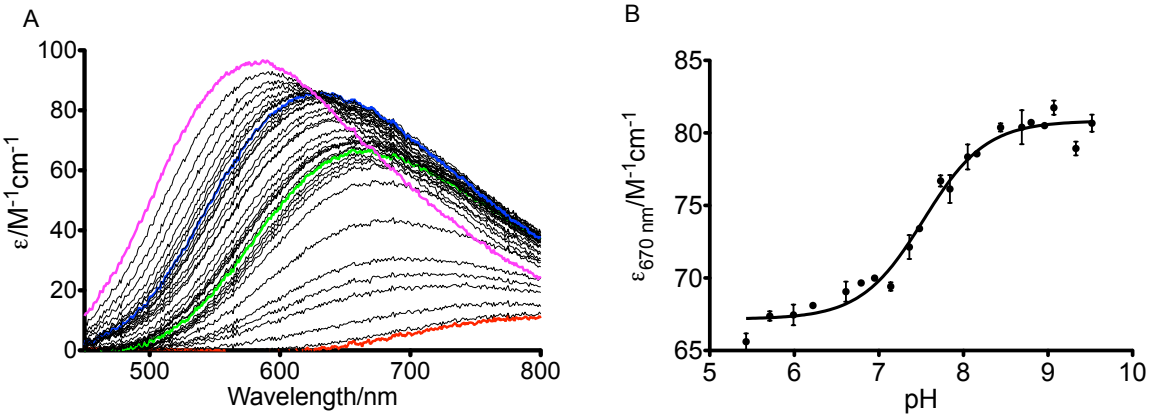

Figure IV-15. (A) pH titration spectra of Cu(II)(TRIW-$_M$H)$_3^{2+}$. Red spectrum: pH 2.89; green spectrum: pH 5.99; blue spectrum: pH 9.07; magenta spectrum: pH 10.79. (B) Cu(II) *d-d* band extinction coefficient fitted toEquation II-3.

Cu(II)(TRIW-$_M$HL19A)$_3^{2+}$, the peptide combining the two features described above, *i.e.* L19A mutation and $_M$H, shows similar behavior as Cu(II)(TRIW-$_M$H)$_3^{2+}$ (Figure IV-16A). However, the equilibria in this case are not well-defined, as one sees an increased absorbance going from pH ~3 to ~10, without distinct steps as seen in other Cu(II)(3SCC). The titration curve cannot be fitted properly toEquation II-3.

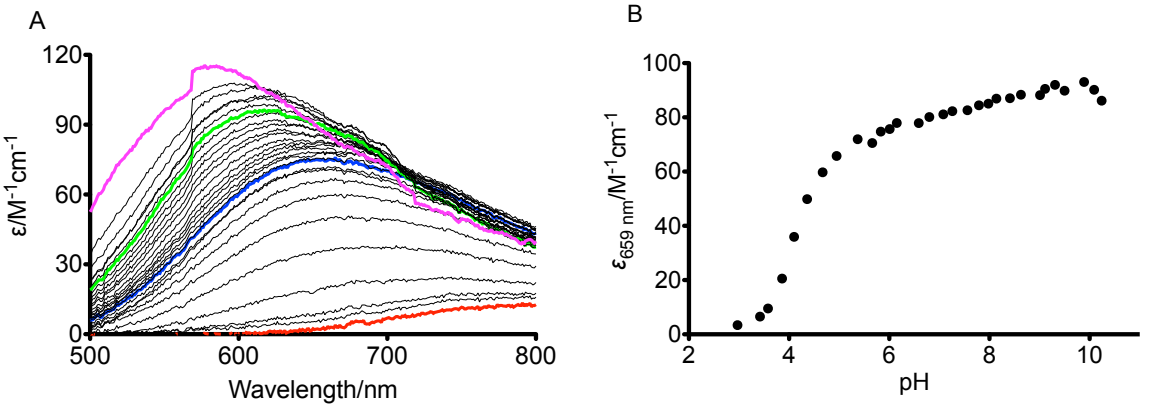

Figure IV-16. (A) pH titration spectra of Cu(II)(TRIW-$_M$HL19A)$_3^{2+}$. Red spectrum: pH 2.97; glue spectrum: pH 5.83; green spectrum: pH 9.01; magenta spectrum: pH 10.24. (B) the change of $\varepsilon_{\text{d-d band}}$ upon pH change.

The spectral evolution of Cu(II)(TRIW-EHL19A)$_3^{2+}$ as a function of pH is shown in Figure IV-17. Two equilibria are observed after the formation of Cu(II)(3SCC)

complex. At pH 6.98 – 8.73, the absorption maximum shifts from 664 nm to 625 nm. An isosbestic point is observed, indicating a conversion from one species to another (Figure IV-17B). As pH is raised above 9, a few new species show up in a higher energy region (~510 nm) (Figure IV-17C). Since the pK_a values of these deprotonation equilibria are too close to each other, they cannot be defined by fitting the titration curve to Equation II-3.

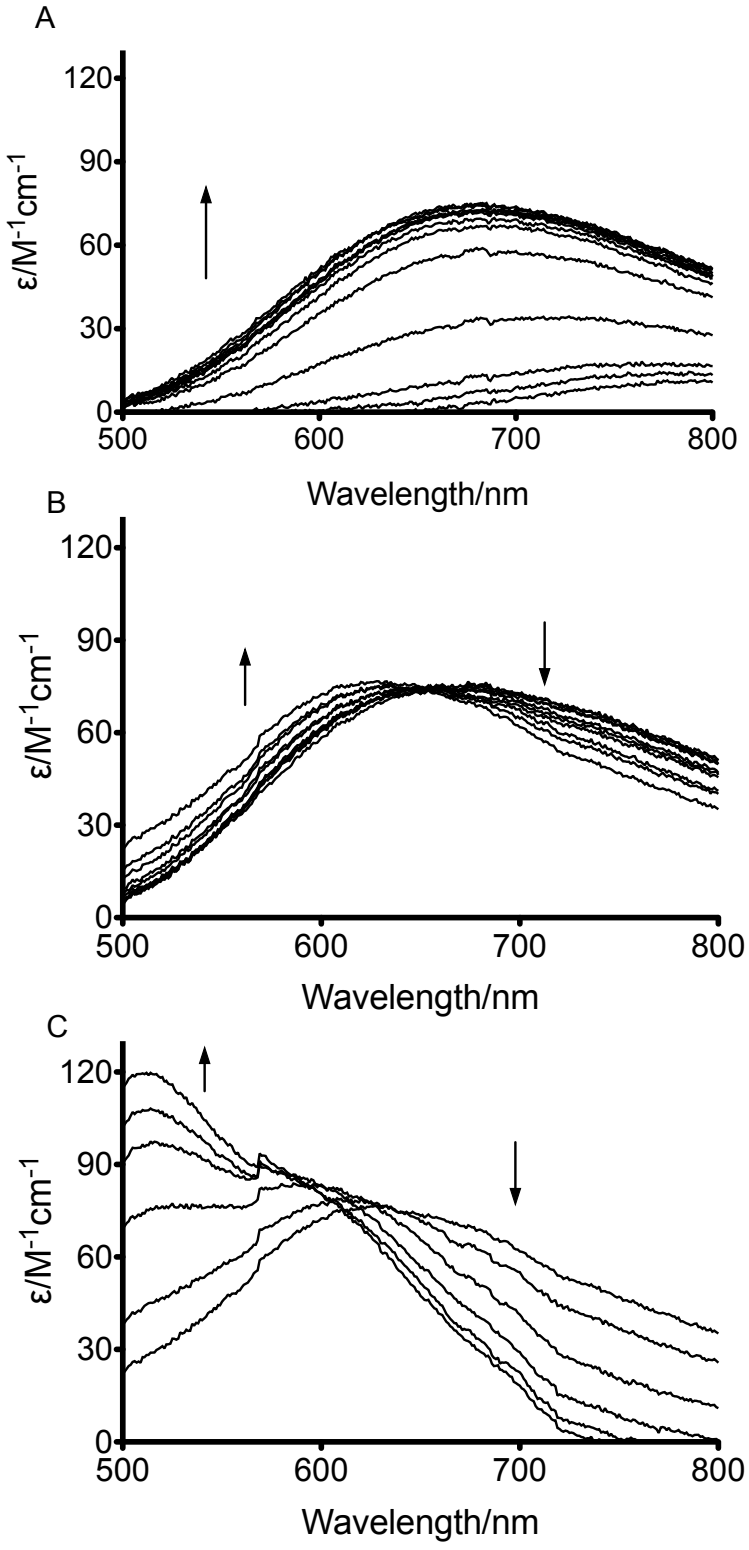

Figure IV-17. pH titration of Cu(II)(TRIW-EHL19A)$_3^{2+}$. (A) pH 2.91 – 6.19; (B) pH 6.98 – 8.73; (C) pH 8.73 – 10.10.

NO_2^- titration monitored by EPR.

NO_2^- titrations were carried out for Cu(II)(TRIW-HL19A)$_3^{2+}$, Cu(II)(TRIW-$_M$H)$_3^{2+}$, and Cu(II)(TRIW-$_M$HL19A)$_3^{2+}$ at pH 5.8 monitored by EPR. No spectral change is observed for Cu(II)(TRIW-HL19A)$_3^{2+}$ or Cu(II)(TRIW-$_M$HL19A)$_3^{2+}$ after 20 eq. of NO_2^- is added (Figure IV-18, Figure IV-19). For Cu(II)(TRIW-$_M$H)$_3^{2+}$, however, as NO_2^- is titrated in small aliquots, A_{II} decreases (Figure IV-20). The correlation of A_{II} to the concentration of NO_2^- yields a NO_2^- dissociation constant of 8.8 mM (Figure IV-21).

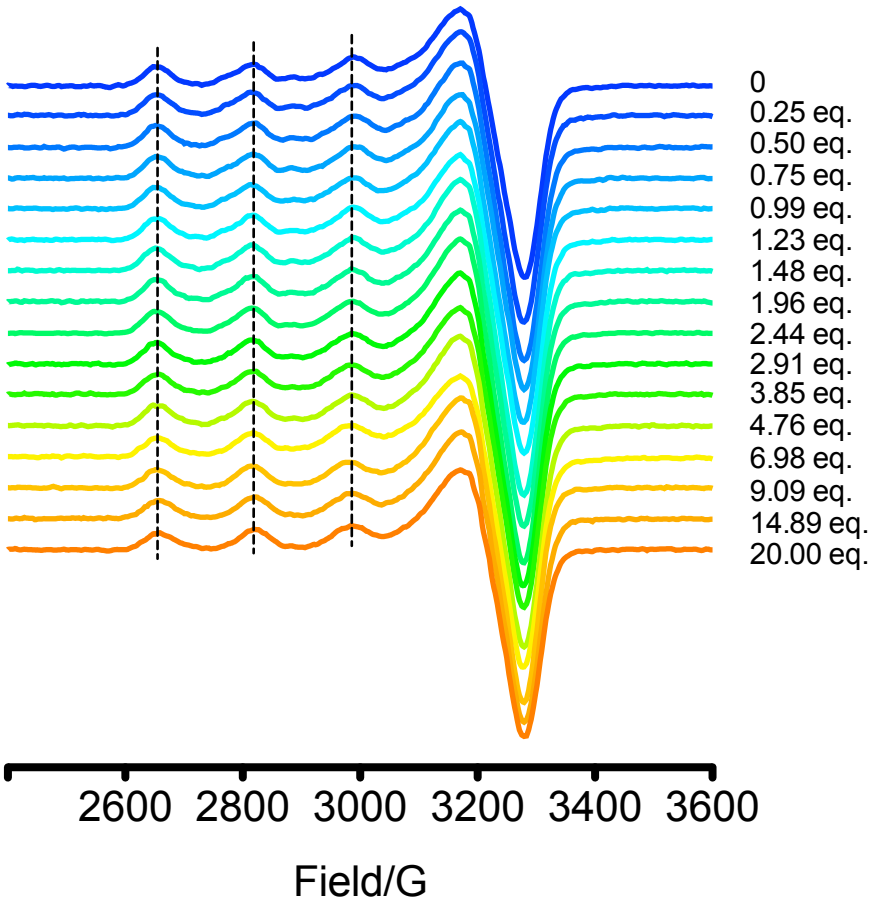

Figure IV-18. NO_2^- titration of Cu(II)(TRIW-HL19A)$_3^{2+}$ at pH 5.8 ([Cu(II)] = 1 mM, [3SCC] = 1.5 mM, 50 mM MES). The numbers on the right side of the spectra represent the equivalents of NO_2^- with respect to Cu(II).

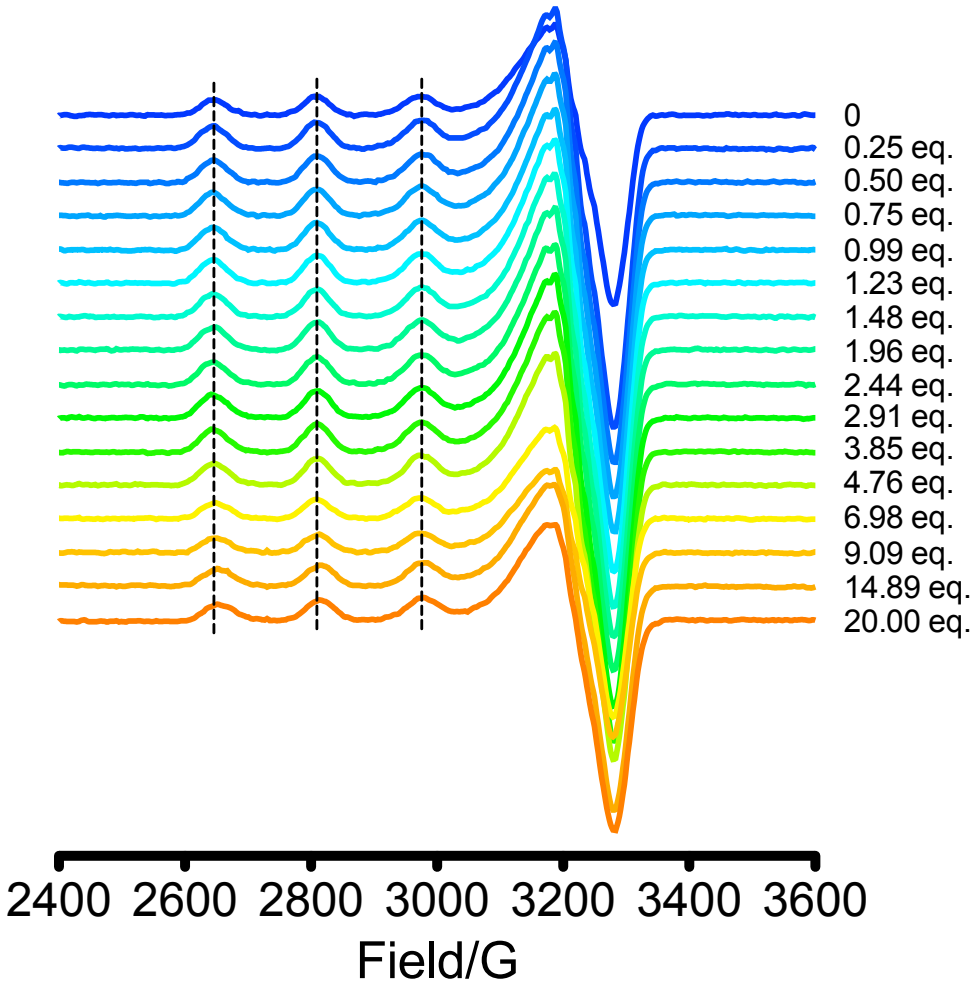

Figure IV-19. NO_2^- titration of Cu(II)(TRIW-$_M$HL19A)$_3^{2+}$ at pH 5.8 ([Cu(II)] = 1 mM, [3SCC] = 1.5 mM, 50 mM MES). The numbers on the right side of the spectra represent the equivalents of NO_2^- with respect to Cu(II).

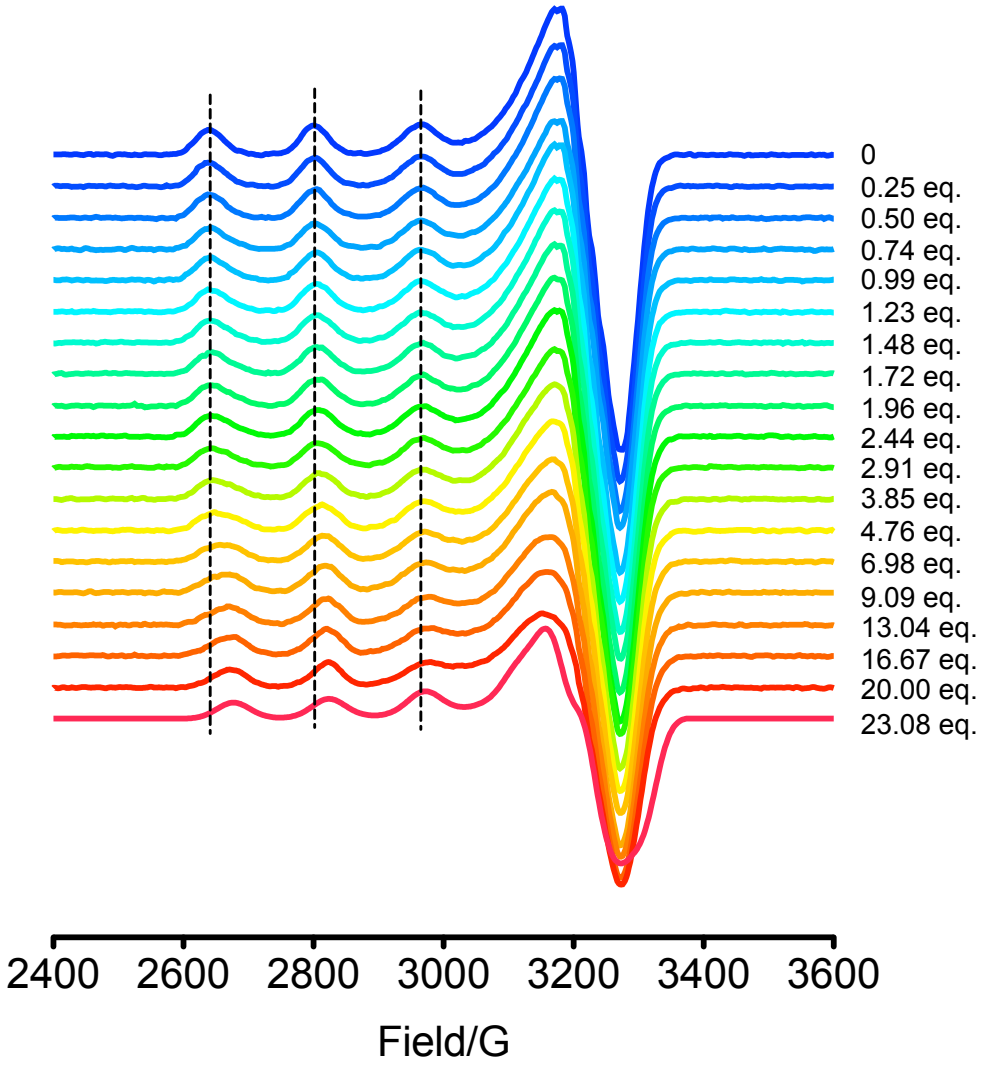

Figure IV-20. NO_2^- titration of Cu(II)(TRIW-$_M$H)$_3^{2+}$ at pH 5.8 ([Cu(II)] = 1 mM, [3SCC] = 1.5 mM, 50 mM MES). The numbers on the right side of the spectra represent the equivalents of NO_2^- with respect to Cu(II).

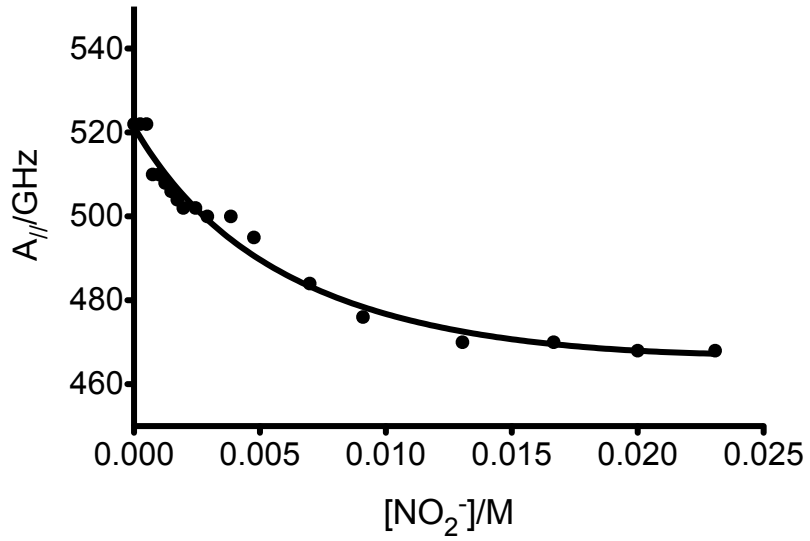

Figure IV-21. A_{II} of Cu(II)(TRIW-$_M$H)$_3^{2+}$ with solid line representing the fit to Equation II-2.

Azide binding to Cu(II)(3SCC).

Azide binding titrations monitored by UV-Vis spectroscopy were carried out for selected peptides in this study. When azide is titrated into a solution of Cu(II)(TRIW-HL19A)$_3^{2+}$, a peak at 382 nm starts to grow when azide is below 30 eq. with respect to Cu(II). After 30 eq., the peak shifts to a higher wavelength (Figure IV-22A). A red-shifted *d-d* band is observed for both processes. This is tentatively conceived as sequential azide binding, the chemical reactions of which are represented by:

$$[Cu(3SCC)(N_3)]^+ \rightleftharpoons Cu(3SCC)^{2+} + N_3^- \qquad K_{d_1}^{N_3^-} = \frac{[Cu(3SCC)^{2+}][N_3^-]}{[Cu(3SCC)(N_3)^+]}$$

$$Cu(3SCC)(N_3)_2 \rightleftharpoons [Cu(3SCC)(N_3)]^+ + N_3^- \qquad K_{d_2}^{N_3^-} = \frac{[Cu(3SCC)(N_3)^+][N_3^-]}{[Cu(3SCC)(N_3)_2]}$$

$$Cu(3SCC)^{2+} + 2\ N_3^- \rightleftharpoons Cu(3SCC)(N_3)_2 \qquad K_f^{N_3^-} = \frac{[Cu(3SCC)(N_3)_2]}{[Cu(3SCC)^{2+}][N_3^-]^2}$$

The $K_{d_1}^{N_3^-}$ and $K_f^{N_3^-}$ values can be extracted by fitting the titration spectra into these equilibria, and $K_{d_2}^{N_3^-}$ is calculated from the equation $K_{d_2}^{N_3^-} = \frac{1}{K_f^{N_3^-} \bullet K_{d_1}^{N_3^-}}$ (Table IV-5).

Table IV-5. Azide binding at pH 5.8

Peptide	λ_{LMCT} (ε/M cm^{-1})/nm	$\lambda_{d\text{-}d}$ (ε/M cm^{-1})/nm	$K_{d_1}^{N_3^-}$ /mM	$K_{d_2}^{N_3^-}$ /mM	$K_f^{N_3^-}$ /M^{-1}
Cu(II)(TRIW-HL19A)$_3^{2+}$	382(1850), 424(5240)	696(195), 749(318)	17.4	78.7	7.30×10^2
Cu(II)(TRIW-$_M$H)$_3^{2+}$	390(3550)	670(381)	26.3	-	-
Cu(II)(TRIW-$_M$HL19A)$_3^{2+}$	375(1500), 387(4540)	674(184), 692(319)	8.92	132	8.47×10^2

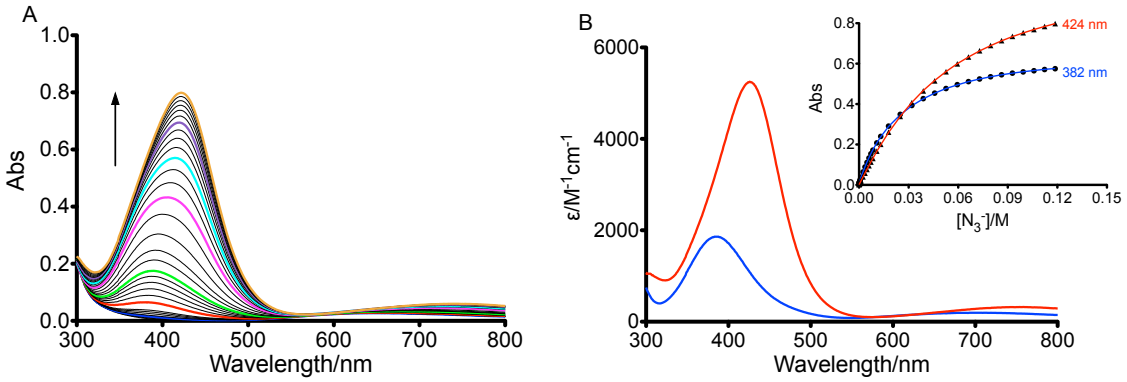

Figure IV-22. Azide titration of Cu(II)(TRIW-HL19A)$_3^{2+}$ monitored by UV-Vis spectroscopy. (A) Titration spectra. The blue, red, green, magenta, cyan, purple, and orange spectra correspond to 1, 10, 30, 120, 200, 300, and 460 eq. of azide with respect to Cu(II). (B) The absorption spectra of two types of azide-Cu(II)(TRIW-HL19A)$_3^{2+}$ adduct. Insert: fitting of the two species. Dots: data points; solid lines: calculated titration curves. The colors of the calculated curves correspond to the color of the specific spectrum, representing the formation of that species.

For Cu(II)(TRIW-$_M$H)$_3^{2+}$, only one type of azide adduct is produced when azide is added (Figure IV-23A). This species corresponds to an absorption maximum at 390 nm. With a model of one azide binding to the Cu(II)-peptide complex, the absorbance at 390 nm can be fitted to yield a dissociation constant of 26.3 mM (Table IV-5).

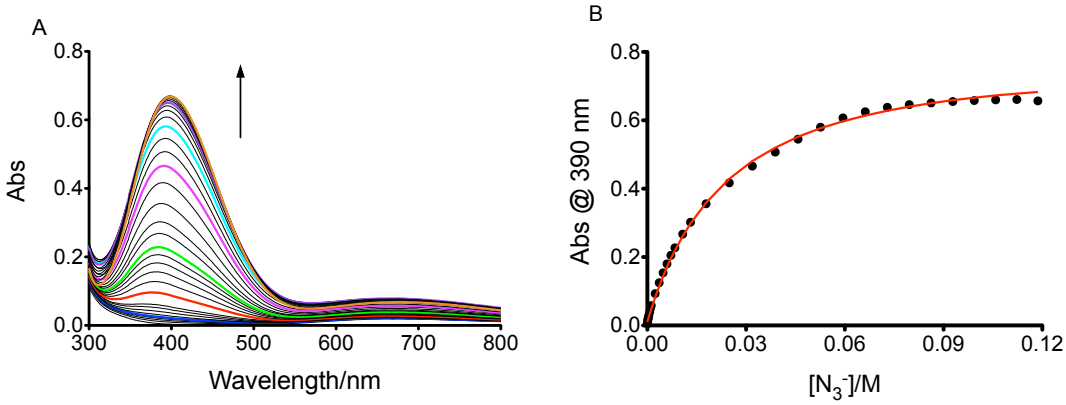

Figure IV-23. Azide titration of Cu(II)(TRIW-$_M$H)$_3^{2+}$ monitored by UV-Vis spectroscopy. (A) Titration spectra. The blue, red, green, magenta, cyan, purple, and orange spectra correspond to 1, 10, 30, 120, 200, 300, and 460 eq. of azide with respect to Cu(II). (B) Calculated titration curve (solid red line) and experimental data (black dots, absorbance at 390 nm).

Azide also binds to the peptide with combined features of L19A and $_M$H mutations. A slight shift of absorption maximum is observed as azide reaches higher equivalents (Figure IV-24A). The titration spectra can be fitted to two equilibria as shown for Cu(II)(TRIW-HL19A)$_3^{2+}$ (Table IV-5).

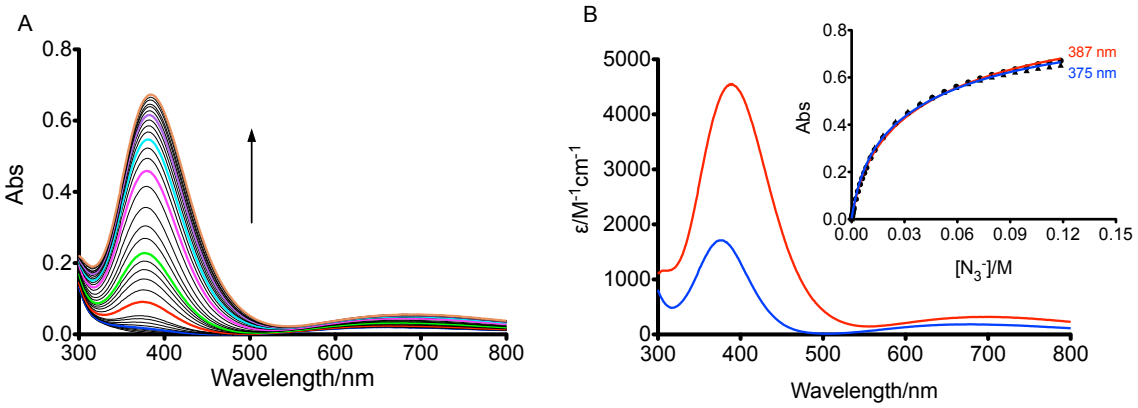

Figure IV-24. Azide titration of Cu(II)(TRIW-$_M$HL19A)$_3^{2+}$ monitored by UV-Vis spectroscopy. (A) Titration spectra. The blue, red, green, magenta, cyan, purple, and orange spectra correspond to 1, 10, 30, 120, 200, 300, and 460 eq. of azide with respect to Cu(II). (B) The absorption spectra of two types of azide-Cu(II)(TRIW-$_M$HL19A)$_3^{2+}$ adduct. Insert: fitting of the two species. Dots: data points; solid lines: calculated titration curves. The colors of the calculated curves correspond to the color of the specific spectrum, representing the formation of that species.

Affinities and reduction potentials.

The affinity of Cu(I) to selected peptides were determined based on the procedures described in the previous chapters (Chapter II, Experimental section). For the peptide Cu(I)(TRIW-HL19A)$_3^+$, when small aliquots of Na_2BCA were first added to the solution, a peak centered at 508 nm grew in. With the addition of more BCA^{2-}, the absorption spectra gradually transformed to a new set centered at 562 nm, which is consistent with the reported Cu(BCA)$_2^{3-}$ species. The titration spectra can be fitted to a model with two equilibria:

$$Cu(3SCC)(BCA)^{-} \rightleftharpoons Cu(3SCC)^{+} + BCA^{2-} \qquad K_d^{ternary} = \frac{[Cu(3SCC)^+][BCA_2^-]_{free}}{[Cu(3SCC)(BCA)^-]}$$

$$Cu(3SCC)^{+} \rightleftharpoons Cu^{+} + 3SCC \qquad K_d^{Cu^+} = \frac{[Cu^+]_{free}[3SCC]_{free}}{[Cu(3SCC)^+]}$$

$$Cu(3SCC)^{+} + 2\,BCA^{2-} \rightleftharpoons Cu(BCA)_2^{3-} + 3SCC \qquad K_e = \frac{[Cu(BCA)_2^{3-}][3SCC]_{free}}{[BCA_2^-]_{free}^2[Cu(3SCC)^+]} = \frac{K_d^{Cu^+}}{K_d^{Cu(BCA)_2^{3-}}}$$

where $K_d^{Cu(BCA)_2^{3-}} = \frac{[Cu^+][BCA^{2-}]^2}{[Cu(BCA)_2^{3-}]}$.

Data fitting was carried out in the global fitting program Hyperquad.[24] As shown in Figure 25B, both processes contribute to the increase in absorbance simultaneously. The dissociation constants and reduction potentials are listed in Table IV-6. TRIW-$_M$HL19A experiences slow kinetics for BCA^{2-} chelation. As a result, the competition assay cannot be used for this peptide.

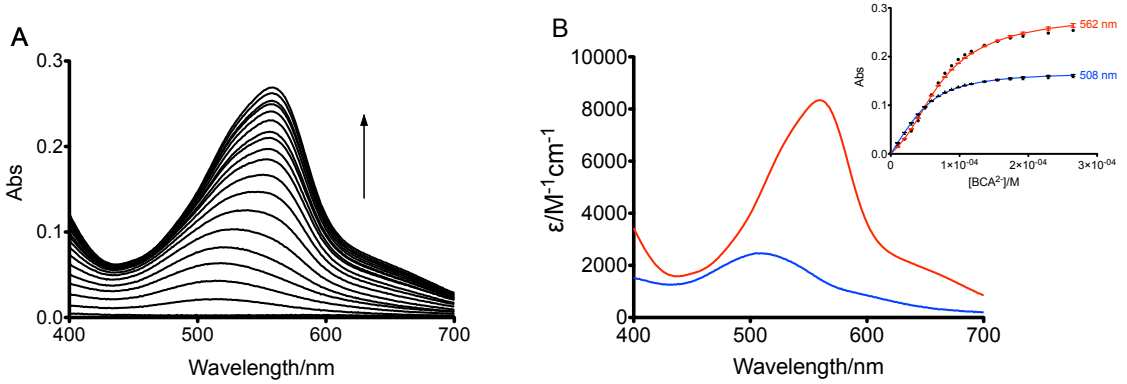

Figure IV-25. BCA^{2-} competitive chelation titration of $Cu(I)(TRIW\text{-}HL19A)_3^+$ at pH 5.8. (A) Titration spectra. (B) Two species extracted from spectral fitting. Red spectrum: $Cu(BCA)_2^{3-}$; blue spectrum: $CuP(BCA)^-$. Insert: data points and fitting curves for the two colored species.

Table IV-6. Cu(I) and Cu(II) dissociation constants and reduction potentials of selected peptides at pH 5.8

Peptide	K_d(Cu(I))/M	K_d(Cu(II))/M	E/mV vs. NHE
TRIW-HL19A	$K_d^{ternary} = 6.12(10) \times 10^{-18}$ $K_d^{CuP} = 2.28(68) \times 10^{-12}$	$1.33(19) \times 10^{-5}$	559(8)
TRIW-$_M$H	$1.70(23) \times 10^{-12}$	$3.29(100) \times 10^{-6}$	530(8)
TRIW-$_M$HL19A	-	$5.66(38) \times 10^{-6}$	-

NiR activity.

NiR rates at pH 5.8. It has been demonstrated in the previous chapters that NiR rates increase as the pH decreases. At pH 5.8, the rates are the highest for all the peptides presented so far. Herein, I collected data on NiR rates at pH 5.8 for the peptides involved in this chapter. In general, the peptides containing the L19A and $_M$H features exhibit much higher NiR rates than the previous generations (Figure IV-26). Compared to TRIW-H, the L19A mutation introduced ~150-fold increase in rates, the $_M$H mutation ~500-fold, and the peptide with both features ~1300-fold. The K22E mutation, on the other hand, tends to decrease the rates, as is seen for the cases of TRIW-EHL19A versus TRIW-HL19A, and TRIW-E$_M$H versus TRIW-$_M$H. The peptides on the right side of the plot (from TRIW-EHL19A to the right) have significantly higher rates than the ones on the left side of the plot, suggesting that the modifications of the interior of the helical coiled coils might be more effective in influencing the NiR rates.

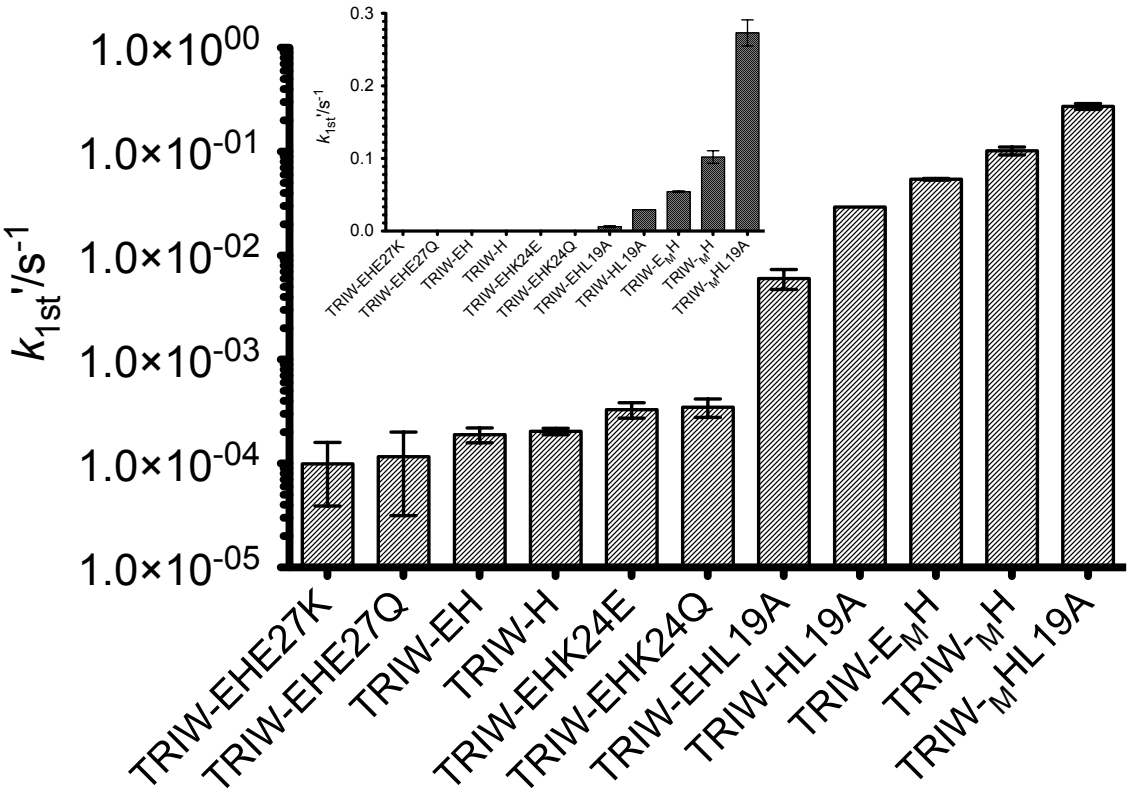

Figure IV-26. NiR pseudo-first order rate constants at pH 5.8 for Cu(II)(3SCC). The y-axis is on a logarithmic scale. Insert: the same plot on a linear scale.

Since the rates are much higher for some of the peptides in this chapter, for a direct comparison to TRIW-H and TRIW-EH series of peptides, I would have to decrease the enzyme concentration to obtain a valid initial rate, and proportionally scale up the rates to compare to the other peptides. The NiR rates are linearly dependent on the peptide concentrations (Figure IV-27), allowing me to carry out this process for comparison.

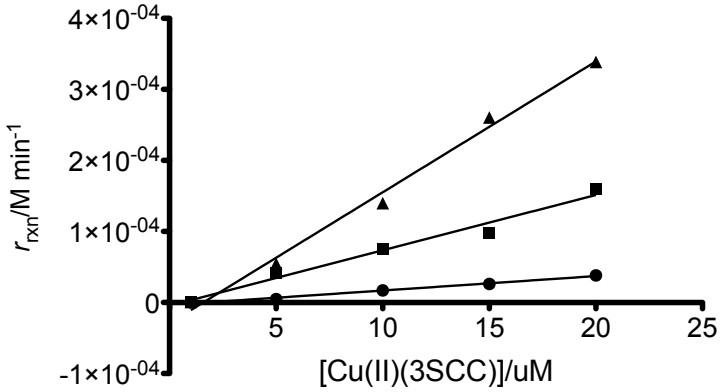

Figure IV-27. Linear correlations between peptide concentrations and NiR rates at pH 5.8. Filled triangles: TRIW-$_M$HL19A; filled squares: TRIW-$_M$H; filled circles: TRIW-HL19A.

Michaelis-Menten kinetics. Michaelis-Menten kinetic studies were carried out for TRIW-HL19A, TRIW-$_M$H, and TRIW-$_M$HL19A. The parameters are shown in Table IV-7.

Table IV-7. Kinetic parameters at pH 5.8

Peptide	v_{max} (M min^{-1})	K_M (M)	k_{cat} (min^{-1})	k_{cat}/K_M (min^{-1} M^{-1})
Cu(II)(TRIW-HL19A)$_3^{2+}$	1.4(2) × 10^{-4}	0.24(5)	14(2)	60(15)
Cu(II)(TRIW-$_M$H)$_3^{2+}$	8.9(7) × 10^{-4}	0.18(2)	89(7)	4.9(7) × 10^2
Cu(II)(TRIW-$_M$HL19A)$_3^{2+}$	8.8(3) × 10^{-4}	0.13(1)	88(3)	6.8(6) × 10^2

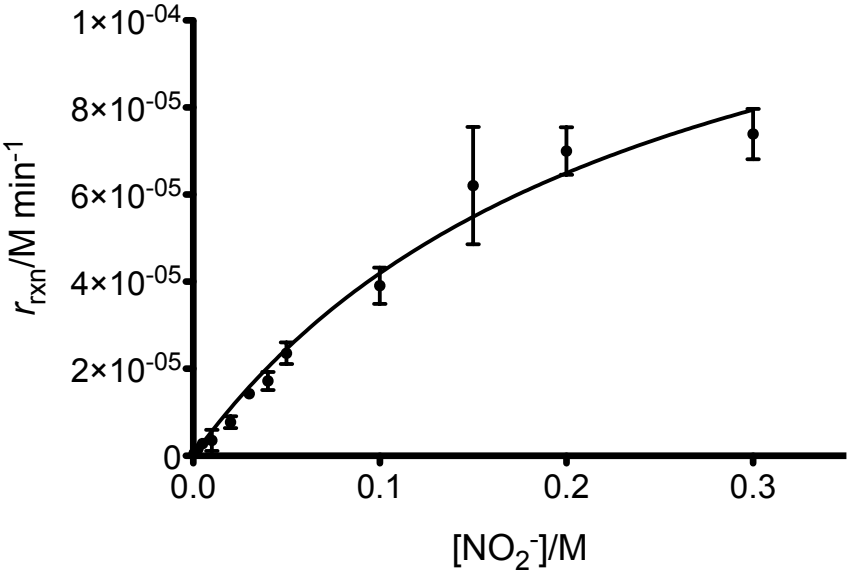

Figure IV-28. Michaelis-Menten kinetics of Cu(II)(TRIW-HL19A)$_3^{2+}$ at pH 5.8.

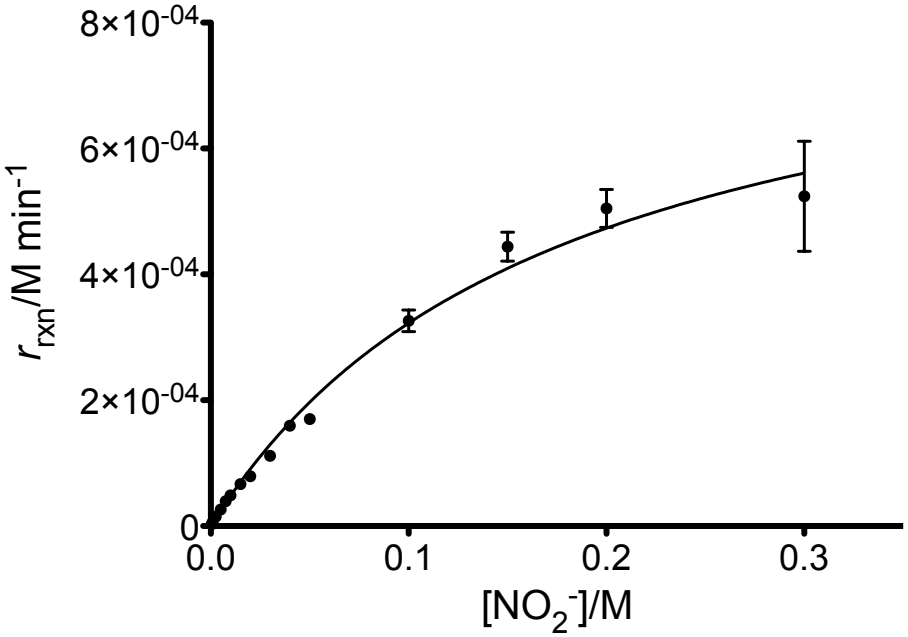

Figure IV-29. Michaelis-Menten kinetics of Cu(II)(TRIW-$_M$H)$_3^{2+}$ at pH 5.8.

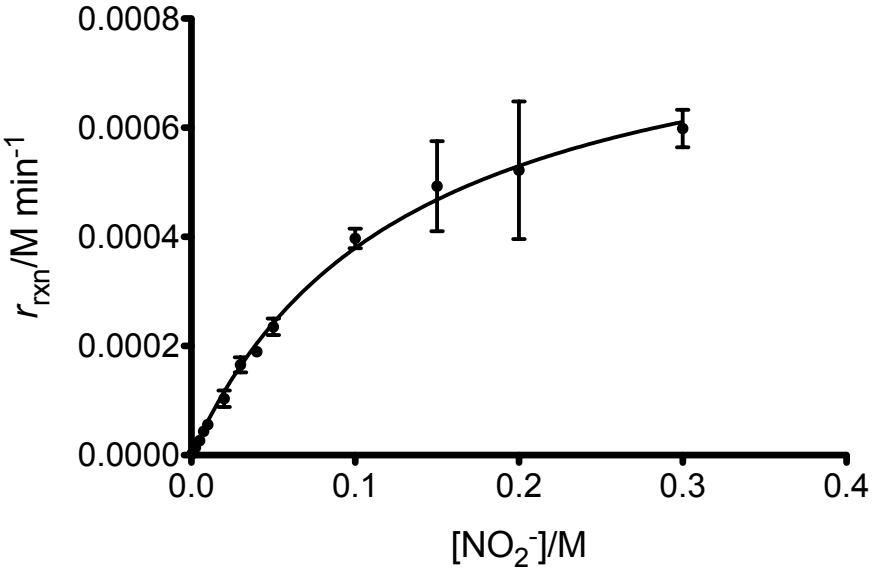

Figure IV-30. Michaelis-Menten kinetics of Cu(II)(TRIW-$_M$HL19A)$_3^{2+}$ at pH 5.8.

Discussion

To obtain a desired metal coordination environment, protein designers can either directly change the first coordination sphere of the metal center or the area immediately surrounding the catalytic center (second coordination sphere). In the first case, one may incorporate an exogenous ligand or modify/add a coordinating residue. The second coordination sphere may be controlled by changing the packing of the hydrophobes, including H-bonding, changing local dielectric, building channels and even altering the grand topology of the protein. In native metalloenzymes, the complex architecture of substrate channel, proton-electron transfer chain, and the proper shaping and packing of amino acid side chains is responsible for the outstanding efficiency and selectivity which is observed. It is generally believed that the modification of the second coordination sphere only leads to a limited level of influence on the metal center; however, sometimes, changes in the second coordination sphere directly gives rise to alterations of the first coordination sphere, as is the case described here.

The designs introduced in this chapter focus on the interior of the helical coiled coils. The first strategy is to mutate a Leu a layer above the copper-binding site into an Ala in order to change the substrate/solvent access to the copper center. It has been demonstrated that the peptide TRIL16C binds Cd(II) with three sulfurs from the Cys residue. This Cd(II)-peptide complex contains a mixture of a four-coordinate $Cd(II)S_3O$, where the oxygen presumably comes from a coordinating water molecules, and a three-coordinate $Cd(II)S_3$. The mutation of a ***d*** site (***a*** site versus ***d*** site, see Chapter I) right above the Cd(II)-binding site (TRIL12AL16C) leads to a 100% four-coordinate $Cd(II)S_3O$ species.[25,26] This change of coordination number is attributed to the smaller side chain of Ala, which opens a "hole" above the Cd(II)-binding site to accommodate the coordinating solvent molecule. My design is similar to this in the distance between the Ala mutation site and the metal-binding residue, but the residues involved here are one heptad repeat closer to the C-terminus. Based on the known effect of having an Ala residue one hydrophobic layer above the Cd(II)-binding residue, L19A mutation is introduced with the intention of modifying the solvent/substrate access to the copper center (Figure IV-31).

The second strategy is to replace the copper-binding His by N^{δ}-methyl-histidine in order to utilize the steric bulk introduced by the methyl group. The intention was to increase the coordination number of Cu(I) by forcing the copper ion out of the trigonal plane ($3N_{imid}$) (Figure IV-32), so as to decrease the reorganizational energy upon electron transfer. In addition, the electronic effect of the methyl group can potentially influence the binding properties of both cuprous and cupric forms, thus changing the redox properties and activity.

Based on these two strategies and the K22E mutation introduced in Chapter III, I then prepared a few peptides that have two features incorporated in the same peptide: TRIW-EHL19A, TRIW-E_MH, TRIW-$_MHL19A$. Basic characterizations such as copper binding and spectroscopic studies were carried out for all of these peptides to investigate how these changes influence copper coordination on both oxidation levels.

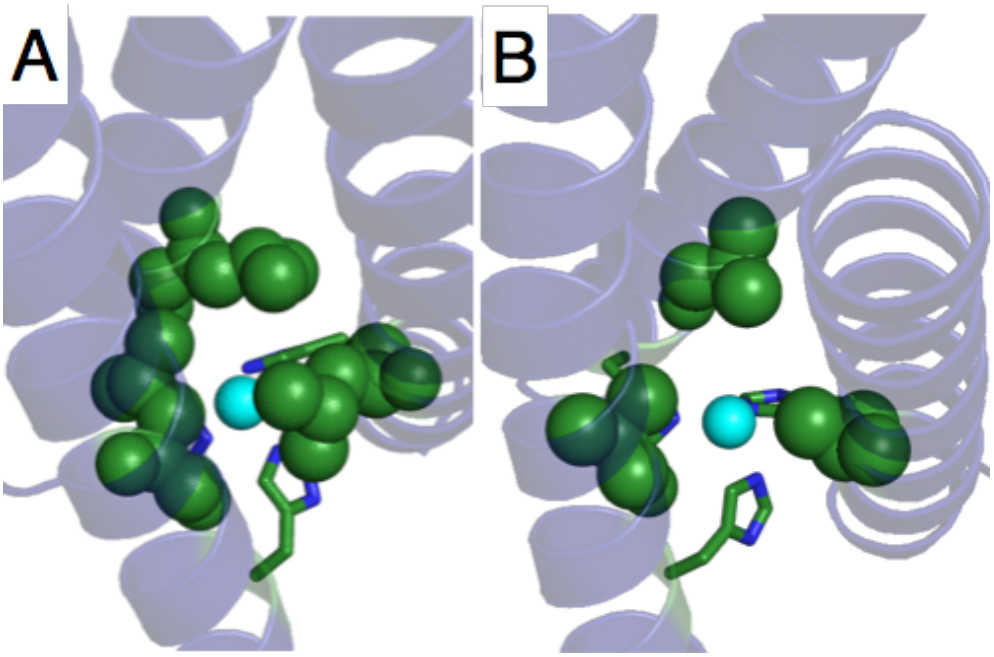

Figure IV-31. Space-filling model of TRIW-H (A) and TRIW-HL19A (B) illustrating that the L19A mutation opens space above the copper-binding site. The PyMol models are made based on the crystal structure of $Hg(II)_SZn(II)_N(CSL9PenL23H)_3^-$ (PDB code: 3PBJ).

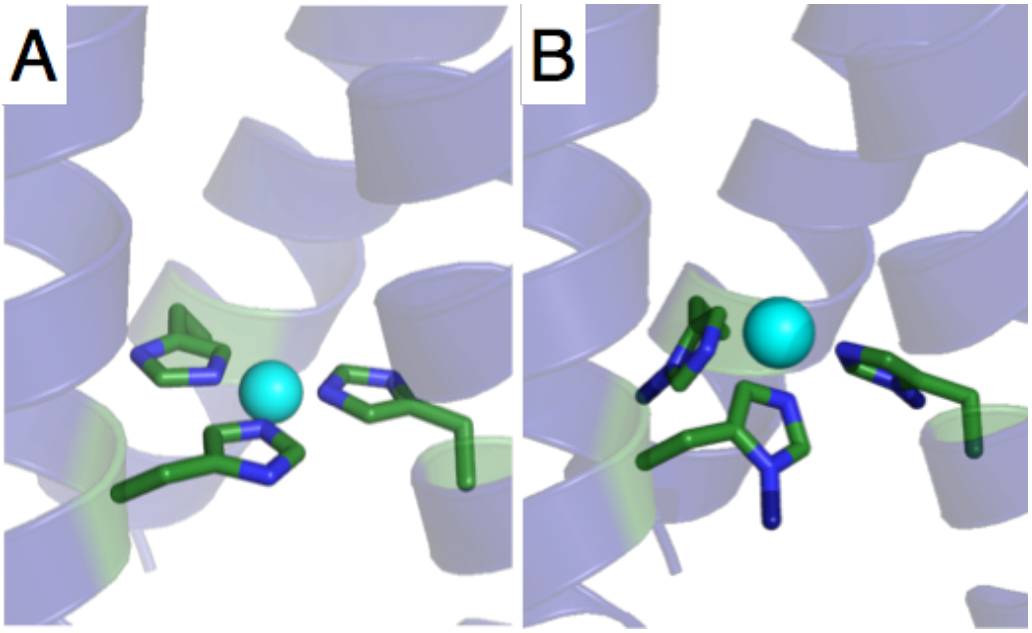

Figure IV-32. Predicted coordination of Cu(I) in TRIW-$_M$H (B) compared to the TRIW-H (A). The PyMol models are made based on the crystal structure of $Hg(II)_SZn(II)_N(CSL9PenL23H)_3^-$ (PDB code: 3PBJ).

Cu(I) coordination.

The modifications directly influence Cu(I) coordination, possibly through the change of packing of the side chains and H-bonding scheme around the copper center. Contrary to the expectation of potentially increasing the coordination number, Cu(I) is only coordinated to two His when bound to TRIW-HL19A at pH 5.8, as XANES shows a typical two-coordinate Cu(I) edge structure and EXAFS fitting parameters are consistent with those of the reported two-coordinate Cu(I) sites (Table IV-8, blue blocks). When the pH is increased to 6.5 and 7.4, a gradual decrease in the pre-edge peak intensity is observed, while the peak positions do not shift. This indicates that the pH change is directly correlated to the change of coordination numbers of Cu(I), the pK_a of which is between 5.7 to 6.3 depending on whether it is a one- or two-proton related process. This transformation is linked with either the association of 2SCC into 3SCC (Figure IV-33A) or the deprotonation of His (Figure IV-33B). As shown in Figure 3-21, the pK_a corresponding to route Figure IV-33A is generally smaller than 5.5 and an isolated His imidazole has a pK_a of ~6, so route B (Figure IV-33) is a more favored explanation. At pH 5.8, Cu(I) is coordinated to two His residues, the third His is in its protonated form, i.e. imidazolium form. When the pH is increased, the remaining imidazolium is deprotonated into an imidazole, which then binds Cu(I), forming a trigonal cuprous center (Scheme IV-2).

Table IV-8. Two-coordinate and three-coordinate Cu(I) centers

Sample	Shell	*R*(Å)	σ^2(Å^2)	Ref
Cu(I)(TRIW-HL19A)$_3^+$, pH 5.8	2 N_{imid}	1.86	0.007	This work
Aβ16Cu(I), pH 7.2	2 N_{imid}	1.88	0.006	[27]
L_ε-Cu(I)[a]	2 N_{imid}	1.86	0.009	[20]
$(Met_2Im)_2Cu(I)$[b]	2 N_{imid}	1.86	0.003	[28]
Cu(I)(TRIW-HL19A)$_3^+$, pH 7.4	3 N_{imid}	1.91	0.010	This work
Cu(I)(TRIW-H)$_3^+$, pH 5.9	3 N_{imid}	1.93	0.009	[29]
Reduced psAO	3 N_{imid}	1.94	0.006	[30]
Reduced PHM*cc* (pH 7.5)	2.5 N_{imid}	1.92	0.017	[31]
	0.5 S_{Met}	2.24	0.012	
$(Met_2Im)_3Cu(I)$	2N_{imid}	1.89	0.01	[28]
	1N	2.08	0.003	

The Chemdraw schemes for compound *a* and *b* are shown in Scheme IV-1.

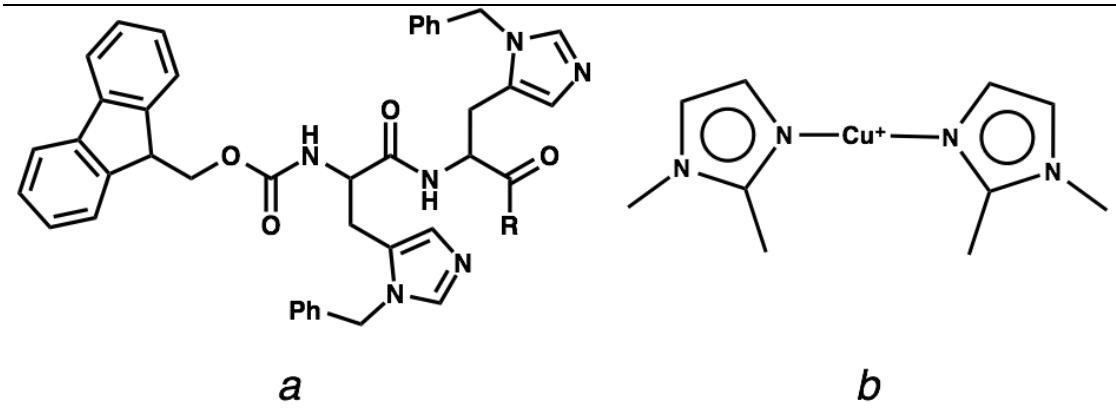

Scheme IV-1. (a) L_ε; (b) $(Met_2Im)_2Cu(I)$

Based on this analysis, at pH 5.8, the linear coordination of Cu(I) possibly reflects the change of packing patterns in the interior of the helical coiled coils. For example, it is

possible that the extra space created by Ala19 can accommodate an imidazolium from His23, leaving two imidazoles from the other strands coordinated to Cu(I) (Figure IV-34A). It is also reasonable that the linear Cu(I)(imid)$_2$ center shifts to the N-terminus, packing into the extra space from Ala19 (Figure IV-34B). I cannot distinguish one model versus the other without a crystal structure. Whichever is the case, the results here possibly allude to the preference for a linear coordination of Cu(I). As shown in the previous chapters, the peptides without the L19A mutation all bind Cu(I) into a trigonal planar geometry, which might attribute to the bulky Leu side chains that would not accommodate either an imidazolium or a Cu(I)(imid)$_2$ center. Once this layer of Leu is removed, Cu(I) readily adopts a linear coordination geometry, as seen in the case of TRIW-HL19A.

It is worth noticing that at pH 7.4, the Cu-N_{imid} distance is 0.02 Å shorter than those from the previous chapters (1.91 Å for Cu(I)(TRIW-HL19A)$_3^+$ versus 1.93 Å for peptides presented in the previous chapters), and the Debye-Waller factor is 20~30% larger than the previous cases. This could be due to either the incomplete deprotonation of imidazolium (a mixture of two- and three-coordinate Cu(I)) or a T-shaped structure. XAS data at a higher pH condition can help clarify this.

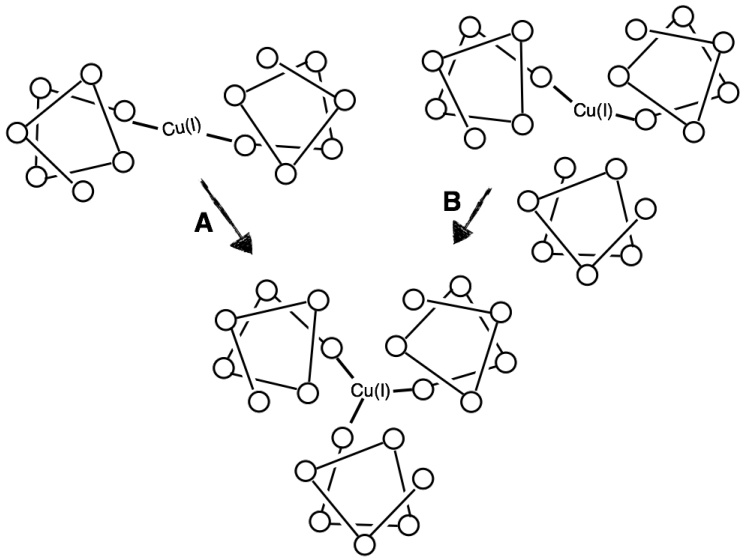

Figure IV-33. Two possible routes for the transformation from linear Cu(I) to trignoal Cu(I).

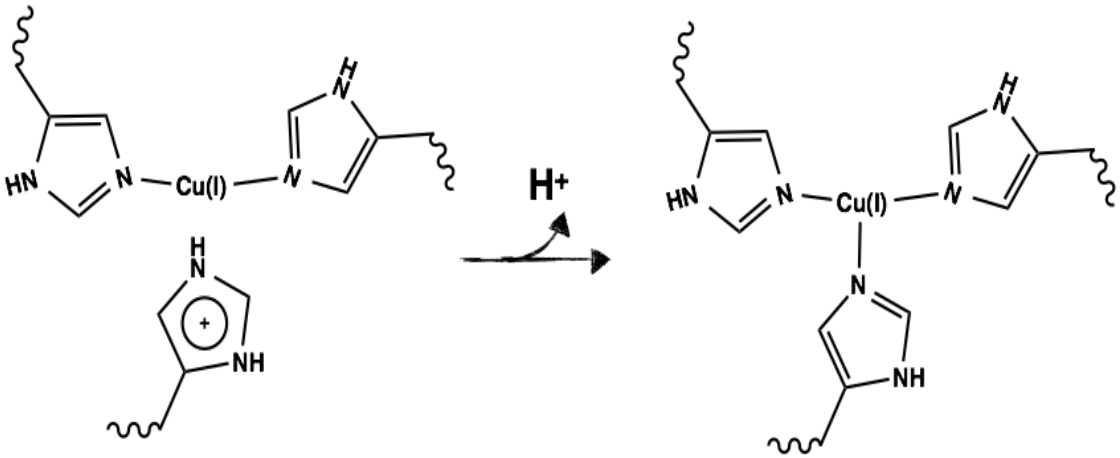

Scheme IV-2

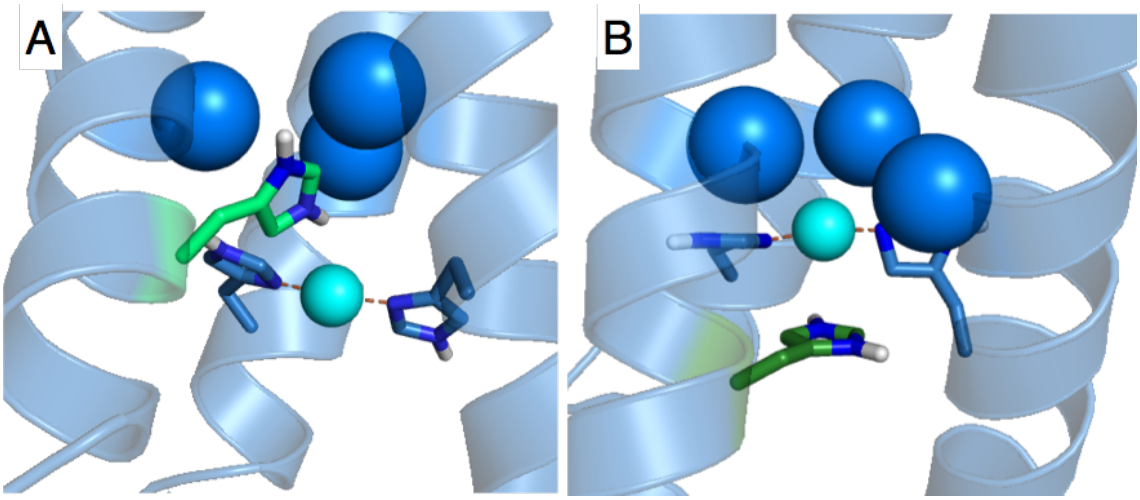

Figure IV-34. Possible packing model of Ala19 (space-filling spheres) directing the formation of a linear Cu(I)$(imid)_2$ center. (A) Imidazolium filling in the extra space created by Ala19; (B) linear Cu(I)$(imid)_2$ filling the space.

The peptide TRIW-$_M$H, involving the introduction of a methyl group on the imidazole, is expected to also modify the Cu(I) coordination. Contrary to this expectation, both the XANSE and EXAFS data are consistent with a three-coordinate Cu(I) center. Notably, in the EXAFS fitting process, if one fixes the coordination number to four, the fitting still yields Cu-N_{imid} distances at around 1.93 Å, which is too short for a four-coordinate Cu(I)-N distance (Table IV-9). The Debye-Waller factor of the best fit (Table IV-2) is 0.002 $Å^2$ smaller than that of Cu(I)$(TRIW\text{-}H)_3^+$ at the same pH, indicating that the introduction of the methyl group reduces the dynamic motions of the copper

center. There are two facets that can contribute to the decreased Debye-Waller factor. The incorporation of the methyl group eliminates N^{δ} from binding to Cu(I) in the case of TRIW-$_{M}$H, whereas in TRIW-H, there are potentially four possible binding modes depending on whether it is N^{ε} or N^{δ} of the imidazole that binds to Cu(I) (Figure 2-28). The sterics of the methyl group may also limit the wobbling motion of the imidazole plane along the Cu(I)-N^{ε} axis, creating a less dynamic Cu(I) site.

Table IV-9. Relevant distances in four-coordinate Cu(I) complexes

Complex	Cu(I)-N distance/ Å	Geometry description	Ref
$[Cu(Meim)_4]^+[ClO_4]^{-a}$	2.054	Tetrahedral	[32]
$[OP(3\text{-}t\text{-}Bupz)^3Cu(NCMe)]^+[PF_6]^{-b}$	2.101, 2.135, 2.089, 1.910 (Cu-NCMe)	Pyramidal	[33]
$[Cu(dbp)(dmp)]^{+c}$	2.087, 2.087, 2.052, 2.095	Pseudo-tetrahedral	[34]
The Chemdraw schemes of compounds *a*, *b*, and *c* are shown in Scheme IV-3			

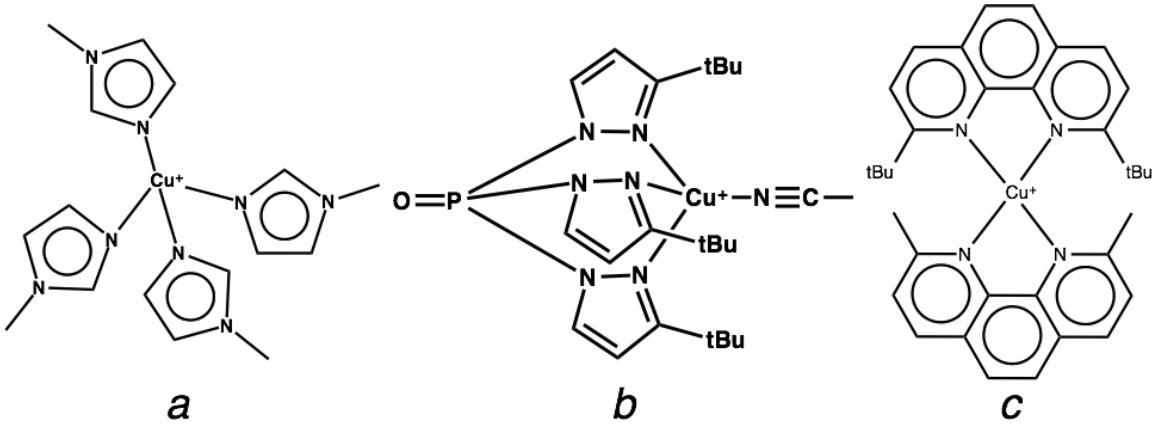

Scheme IV-3

TRIW-$_{M}$HL19A contains both the L19A and the $_{M}$H mutations, exhibiting combined Cu(I) coordination features. The pre-edge peak of Cu(I)(TRIW-$_{M}$HL19A)$_3^+$ is in between those of Cu(I)(TRIW-HL19A)$_3^+$ and Cu(I)(TRIW-$_{M}$H)$_3^+$, and is more similar to that of Cu(I)(TRIW-HL19A)$_3^+$, indicating that there might be a mixed two- and three-coordinate species or a pure species with a T-shaped Cu(I) center. In an effort to solve

this ambiguity, in the multi-scattering EXAFS fitting process, I let the coordination number of the imidazoles float, with the intention of resolving the best fitted coordination number. The best fit yielded a coordination number of 3 (Table IV-2). Considering that there is ~25% error in coordination number for EXAFS fittings, the coordination number alone cannot distinguish whether this site is a two- or three-coordinate mixture or a three-coordinate T-shaped pure species. The Cu(I)-N_{imid} distance of 1.890 Å can also be derived from both cases. If this is a pure T-shaped species with Cu-N distances of 1.86, 1.86, and 1.95 Å, the averaged bond distance is 1.89 Å. If, for example, this is a 50/50 mixture of two- and three-coordinate Cu(I), with linear Cu(I)-N_{imid} distance of 1.86 Å and trigonal Cu(I)-N_{imid} distance of 1.93 Å, the averaged bond distance is 1.90 Å, within the error of the fitting parameters. However, if this site is a mixture of two- and three-coordinate species, when the pH is increased, the uncoordinated methyl-imidazolium is expected to bind Cu(I), with a pK_a possibly similar to that of Cu(I)(TRIW-HL19A)$_3^+$ for the same process. So I examined the EXAFS of Cu(I)(TRIW-$_M$HL19A)$_3^+$ at pH 7.4. With the coordination number set to float freely, a coordination number and bond distances essentially the same as those of pH 5.8 were obtained from a multi-scattering fitting, suggesting that it is unlikely that 50% of the Cu(I) center changed from two-coordinate two three-coordinate. Based on these analyses, the best description of the Cu(I) coordination so far is T-shaped three-coordinate, with Cu(I)-N_{imid} distances of ~1.86, ~1.86, and ~ 1.95 Å.

At this point, I have analyzed peptides with K22E, L19A, and $_M$H mutations. One might have noticed that the L19A mutation tends to drive the formation of linear or T-shaped (possessing a linear component) Cu(I) centers at pH 5.8. For example, going from Cu(I)(TRIW-H)$_3^+$ to Cu(I)(TRIW-HL19A)$_3^+$, a trigonal to linear coordination change is observed; from Cu(I)(TRIW-$_M$H)$_3^+$ to Cu(I)(TRIW-$_M$HL19A)$_3^+$, there is a change from a trigonal to arguably a T-shaped Cu(I) center; from Cu(I)(TRIW-EH)$_3^+$ to Cu(I)(TRIW-EHL19A)$_3^+$, the coordination number also changes from three to two. Both K22E and $_M$H mutations tend to maintain the trigonal coordination environment of Cu(I), however, when these two features are present together, both XANES and EXAFS indicate a two-coordinate Cu(I) center in Cu(I)(TRIW-E$_M$H)$_3^+$ (Figure IV-6C, Table IV-2). The best possible explanation for the coordination environment and H-bonding scheme around the

Cu(I) center is shown in Scheme IV-4. It is possible that the formation of an H-bond between Glu22 and $_{M}$His23 lowers the total energy of this structure, making it a more favored coordination than Cu(I)($_{M}$His)$_3$.

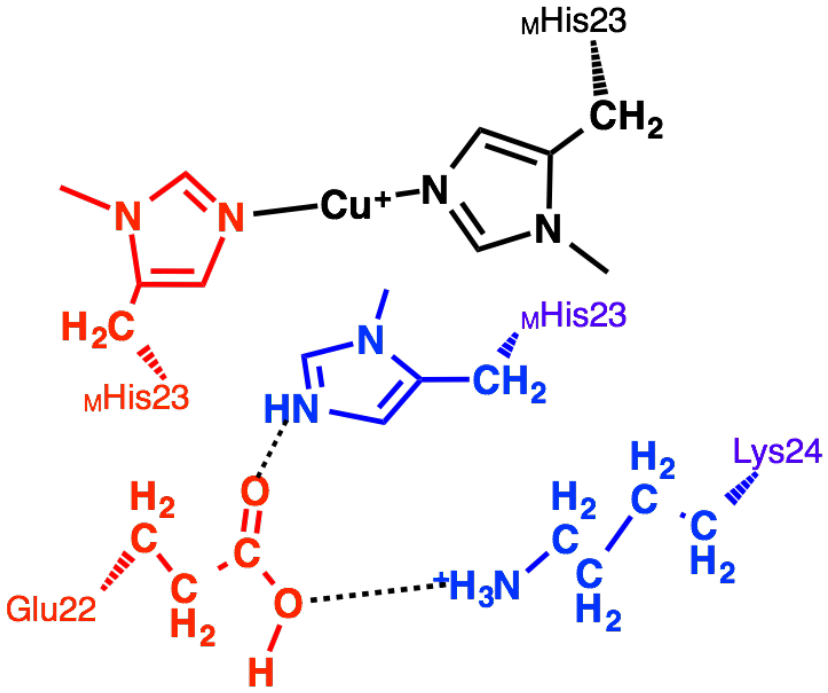

Scheme IV-4. Possible coordination environment of Cu(I)(TRIW-E$_M$H)$_3^+$ at pH 5.8. Residues of the same color are from the same strand.

Cu(II) coordination.

Similar to the effects on the Cu(I) coordination environment, the modifications introduced here might change the primary coordination sphere of Cu(II). Spectroscopic parameters all point to a typical T2Cu center with slight differences in the coordination environment. As compared to Cu(II)(TRIW-H)$_3^{2+}$, the *d-d* bands of the Cu(II)-peptide complexes introduced here shift to lower energy, with smaller extinction coefficients. Although I do not have crystal structures of any of these complexes, I will use a five-coordinate Cu(II) center as the basis for my analyses here for these two reasons: 1) in copper literature, pentacoordinate Cu(II) complexes are just as abundant as the hexacoorindate rhombically elongated stereochemistry; 2) based on my discussion in the previous chapters, it is unlikely that the coordination number of these Cu(II) centers is less than four, so I will use coordination number five as a starting point.

In general, the geometry of pentacoordinate Cu(II) centers range from trigonal bipyramidal (D_{3h}) to square pyramidal (C_{4v}). The conversion between these two forms is usually follows a distortion coordinate along the Berry pseudorotation.[35] Due to the structural plasticity and the variety of donor ligands of Cu(II), researchers have experienced significant difficulties trying to establish a structure-spectroscopy correlation.[36–39] Taking the approach adapted by Addison *et al.*,[40] in a pentacoordinate metal center, τ is introduced to measure the degree of square pyramidal versus trigonal bipyramidal stereochemistry, which is defined as the $(\beta - \alpha)/60^{\circ}$ (angle α and β are shown in Scheme IV-5). The closer τ is to zero, the more square pyramidal character the metal center possesses; the closer τ is to one, the more trigonal bipyramidal character. Again, since I do not have crystal structure of these Cu(II)-peptide complexes, my analyses will be qualitatively based on spectroscopic parameters.

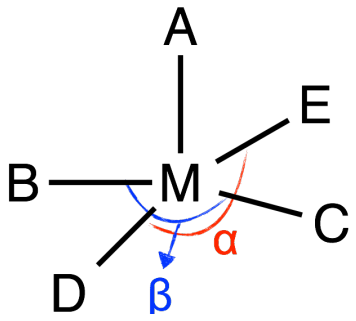

Scheme IV-5. A pentacoordinate metal center. A is the axial ligand. Angle $\alpha = \angle$DME, $\beta = \angle$BMC. When $\alpha = \beta = 180^{\circ}$, this center has square pyramidal geometry. When $\alpha = 120^{\circ}$ and $\beta = 180^{\circ}$, BMC becomes the principle axis, so that it adopts trigonal bipyramidal geometry.

As lower extinction coefficients are observed for Cu(II)(TRIW-HL19A)$_3^{2+}$, Cu(II)(TRIW-$_M$H)$_3^{2+}$, Cu(II)(TRIW-$_M$HL19A)$_3^{2+}$, Cu(II)(TRIW-E$_M$H)$_3^{2+}$, and Cu(II)(TRIW-EHL19A)$_3^{2+}$, an inversion center is introduced as a symmetry component. A possible scenario of Cu(II) coordination is shown in Table IV-10. Cu(II)(TRIW-H)$_3^{2+}$ is most likely to be square planar as compared to all the other peptides as it has the largest extinction coefficient, so it has the smallest τ value, probably close to zero. Within the group of Cu(II)(TRIW-HL19A)$_3^{2+}$, Cu(II)(TRIW-$_M$HL19A)$_3^{2+}$, and Cu(II)(TRIW-$_M$HL19A)$_3^{2+}$, Cu(II)(TRIW-HL19A)$_3^{2+}$ has the most similar spectroscopic parameters as

Cu(II)(TRIW-H)$_3^{2+}$. A smaller extinction coefficient of Cu(II)(TRIW-HL19A)$_3^{2+}$ indicates that there is an axial component of another ligand that points to the opposite direction from the axial O_W (Table IV-10). This is a case where the Cu(II) geometry is in between square planar and trigonal bipyramidal ($0 < \tau_a < 1$). Cu(II)(TRIW-$_M$H)$_3^{2+}$ has the smallest extinction coefficient and the lowest energy *d-d* band within these three peptides. The significant decrease in extinction coefficient and a slight decrease in *d-d* band energy of Cu(II)(TRIW-$_M$H)$_3^{2+}$ as compared to that of Cu(II)(TRIW-H)$_3^{2+}$ suggests Cu(II)(TRIW-$_M$H)$_3^{2+}$ that might have an (elongated) octahedral center. The absorption parameters of Cu(II)(TRIW-$_M$HL19A)$_3^{2+}$ lie in between the above-described two cases in both the absorption wavelength and extinction coefficient, which indicates that the Cu(II) geometry is probably between these two cases. The coordination in Table IV-10 shows one possibility: Cu(II) adopts a geometry close to trigonal bipyramidal so that the integration is small when one applies the dipole transition operator on the *d*-orbitals, although this effect is not as pronounced as the case of an octahedral Cu(II). Using similar analogies, the possible Cu(II) coordinations for Cu(II)(TRIW-EHL19A)$_3^{2+}$ and Cu(II)(TRIW-E$_M$H)$_3^{2+}$ are provided in Table IV-10. The EPR parameters of selected Cu(II)-peptide complexes further indicate that the they have a $d_{x^2-y^2}$ ground state, consistent with the geometric assignments here.

The pH titrations of these Cu(II)-peptide complexes show different deprotonation equilibria, only some of which have pK_a values that can be defined. Considering the Jahn-Teller effect of Cu(II) centers, one would expect that the equatorial water oxygens (O_W) to have more orbital overlap than the axial O_W, so the equatorially coordinated water would have a lower pK_a than the axial water. After inspecting the pK_a values (Table IV-10), one realizes that the pK_a difference between Cu(II)(TRIW-HL19A)$_3^{2+}$ and Cu(II)(TRIW-$_M$H)$_3^{2+}$ (first deprotonation equilibrium) is 1.5 pH unit. The difference in pK_a values might derive from the position of the coordinated water that is deprotonated. In the case of Cu(II)(TRIW-HL19A)$_3^{2+}$, it is possible that the deprotonation occurs at the axial water with a larger pK_a while in Cu(II)(TRIW-$_M$H)$_3^{2+}$, an equatorial water might be deprotonated when the pH is increased. A spectral conversion at a higher pH region is observed for Cu(II)(TRIW-$_M$H)$_3^{2+}$, which might correspond to the combined effects of axial water deprotonation and Lys side chain deprotonation. One might wonder about the

equatorial water in Cu(II)(TRIW-HL19A)$_3^{2+}$. My current best explanation is that the equatorial water might have already been deprotonated along with Cu(II) binding. If one were to fit the titration points below pH 6 for Cu(II)(TRIW-HL19A)$_3^{2+}$, a pK_a of 4.47 (n = 1.57) is observed. This pK_a might correspond to combined effects of Cu(II) binding to 3SCC and equatorial water deprotonation because it is larger than the previously observed pK_a for Cu(II) binding (~3.8). The other peptides involved in this study do not yield well-defined deprotonation equilibria, possibly because the energies of the two coordinated water molecules are very similar or the involvement of carboxylic acid deprotonation, which might occur for the peptides containing K22E mutation.

Table IV-10. Proposed Cu(II) coordination at pH 5.8 based on spectroscopic parameters

Peptide	TRIW-H	TRIW-HL19A	TRIW-$_M$HL19A	TRIW-$_M$H	TRIW-EHL19A	TRIW-E$_M$H
Coordinating atom	1-2O_W, 3N_{imid}	1-2O_W, 2-3N_{imid}	1-2O_W, 2-3N_{imid}	2-3O_W, 2-3N_{imid}	2-3O_W, 2-3N_{imid}	2-3O_W, 2-3N_{imid}
Possible coordination	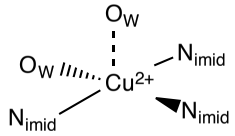	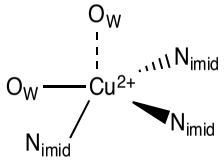	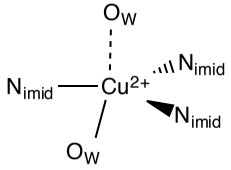	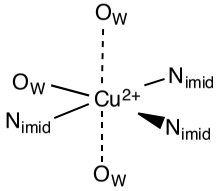	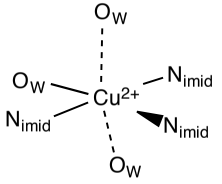	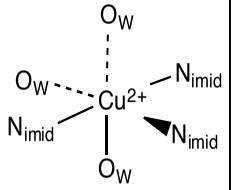
Closest geometric description	Square planar, τ_0 close to zero	Between square planar and trigonal bipyramidal, $\tau_a > \tau_0$	Closer to trigonal bipyramidal, $\tau_{ma} > \tau_a$	Octahedral with elongated axial ligands	Distorted octahedral	Octahedral or trigonal bipyramidal
λmax(ε/M cm^{-1})/nm	643(135)	652(94)	659(74)	670(67)	677(75)	689(71)
pK_a^W	8.53 (n = 1)	9.08 (n = 1)	-	7.53 (n = 1) > 9	6~8 > 9	> 9.5

NO_2^- binding.

EPR is used to monitor NO_2^- binding to Cu(II)-peptide complexes. No spectral change was observed for Cu(II)(TRIW-HL19A)$_3^{2+}$ or Cu(II)(TRIW-$_M$HL19A)$_3^{2+}$, which means either nitrite does not bind to these two peptides or the binding cannot be detected by EPR spectroscopy. I favor the latter but cannot rule out the former possibility. The introduction of L19A mutation is likely to induce easier access of the substrate, if it changes the substrate binding at all. The fact that no spectral change is observed possibly means that the symmetry of the site does not vary upon NO_2^- binding. In particular, the O-Cu-O (Scheme IV-6) angle might or might not change depending on the peptides and the geometry of the Cu(II) center prior to NO_2^- binding. One can infer that the orbital overlap between the oxygen *p*-orbitals and copper *d*-orbitals changes upon the variation of this angle (Scheme IV-6).

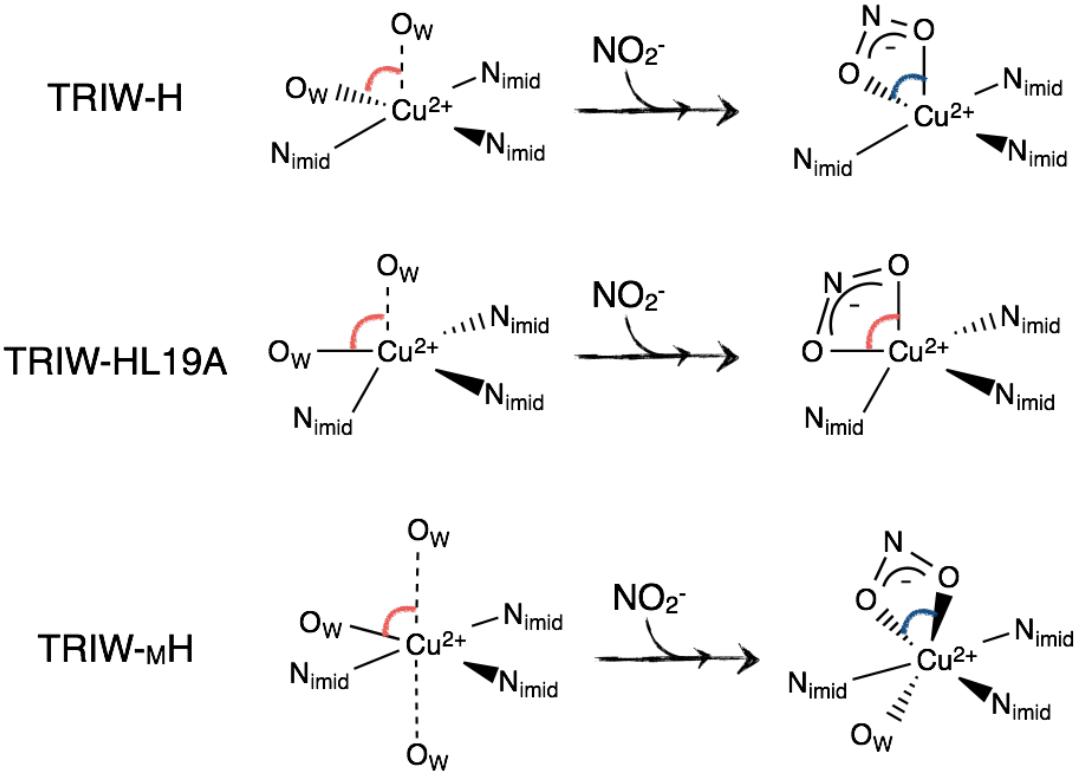

Scheme IV-6. A possible scheme to explain the EPR spectral evolution upon NO_2^- binding. For TRIW-H and TRIW-$_M$H, upon binding to NO_2^-, the O-Cu-O angle varies, leading to the change of symmetry, thus the EPR spectra change. It is possible that due to the altered packing around the copper center, the O-Cu-O angle in TRIW-HL19A does

not vary much, so that EPR spectroscopy cannot detect the binding. TRIW-$_M$HL19A might be similar to TRIW-HL19A in this regard.

Azide binding.

Azide is widely used as a structural and mechanistic probe for copper enzymes and synthetic copper complexes.[41–47] Due to the potential for a Jahn-Teller distortion, there are potentially two different binding sites for azide: equatorial and axial, although that some of the Cu(II) centers in this study might not have a strictly defined equatorial plane. Usually, the equatorial coordination of azide anion to a Cu(II) center results in a LMCT with moderate intensity and a blue-shifted *d-d* band, and the axially coordinated azide-Cu(II) adduct has a LMCT with reduced intensity and red-shifted *d-d* band.[44] Casella and coworkers have investigated azide binding to a series of Cu(II) complexes with tridentate ligands (N_2O to N_3 donor set). They observed that when the equatorial donors are dinegatively charged, azide prefers to bind at the axial position; while it binds at the equatorial position when the donors are neutral or mononegatively charged.[44] Of course, the spectroscopic features of Cu(II)-azide adducts are markedly influenced by the nature of other coordinating ligands and the special arrangements of the ligands, so the trend cannot be generalized in all the cases.

For Cu(II)(TRIW-$_M$H)$_3^{2+}$, the binding of azide leads to a *d-d* band with increased intensity, but the position of the peak remains the same, which suggests that azide weakly interacts with the Cu(II) center, most likely by binding at the axial position. A relatively large dissociation constant is consistent with this assignment. The relatively large extinction coefficient for LMCT indicates the significant orbital overlap between the $\Pi^{nb}(\pi)$, $\Pi^{nb}(\sigma)$ from azide with $d_{x^2-y^2}$ of Cu(II).[46] In contrast, two binding events are observed for both Cu(II)(TRIW-HL19A)$_3^{2+}$ and Cu(II)(TRIW-$_M$HL19A)$_3^{2+}$. Take Cu(II)(TRIW-HL19A)$_3^{2+}$ as an example, the second equivalent of azide seems to be competitive with the first equivalent, which might be due to the formation of a neutral complex after binding to two azide anions. The first equilibrium involves 1:1 binding of azide to Cu(II), which occurs at the axial position (less intense LMCT band and red-shifted *d-d* band) with weaker affinity. The second equivalent of azide binds almost

simultaneously at a position that is not strictly axial or equatorial. Both N_3^- interact with the $d_{x^2-y^2}$ orbital of Cu(II), resulting in an increased intensity of LMCT.

NiR activity.

The NiR rates of peptides with modifications inside the helical coiled coils are compared to those presented in the previous chapters (Figure IV-26). A few general trends are observed: 1) L19A mutation introduces rate enhancements. Three groups of peptides [(TRIW-H, TRIW-HL19A), (TRIW-EH, TRIW-EHL19A), and (TRIW-$_M$H, TRIW-$_M$HL19A)] all have higher rates for those with L19A mutation than those without; 2) $_M$H helps increase the rates, which is seen by comparing the rates of TRIW-H with TRIW-$_M$H, TRIW-EH with TRIW-E$_M$H, and TRWI-HL19A with TRIW-$_M$HL19A; 3) K22E mutation tends to decrease the rates, possibly through the interference of the proton transfer process by Glu22.

Based on the previous discussions on the possible mechanism (Chapter II), the reaction is likely to be initiated at the Cu(I) state, which is different from native NiRs.[10,12,48] The rate enhancement described for the peptides involved in this chapter is likely related to the ***change of the binding modes of Cu(I)-NO_2^- adduct***. Nearly all of the reported Cu(I)-NO_2^- complexes are N-ligation nitrites (η^1-N mode),[49–55] indicating that this form has a relatively low energy. In some of the synthetic complexes, Cu(I)-η^1-N and Cu(I)-η^1−O linkage isomers are observed in the same crystal structure, consistent with the DFT calculation results, which suggest that the energies of these two isomers are similar, although the η^1–N linkage seems to be slightly more favorable.[54] In my case, possible different binding modes of NO_2^- to Cu(I) can explain the enhanced reactivity for the mutants discussed in this chapter.

At the beginning of the reaction, since the Cu(II)-peptide complex is incubated with NO_2^-, under the conditions that I carried out the assay, almost all the Cu(II) is bound to NO_2^-. When NaAsc is injected to initiate the reaction, the first equivalent of NaAsc directly reduces Cu(II)(NO_2^-)(3SCC)$^+$ complex into Cu(I)(NO_2^-)(3SCC), followed by inner-sphere electron transfer between Cu(I) and NO_2^-. With the dissociation of nitric oxide aided by a proton, the copper-peptide complex goes back to the

Cu(II)(3SCC)$(OH_2)_x$ state (Scheme IV-7, route 1). This sequence of substrate-binding, electron transfer is similar to one of the proposed mechanisms for the native T2Cu center in CuNiR and is thought to be a fast process.[56] After the first equivalent of NaAsc is consumed, the peptide goes back to the cupric form. As there is excess NaAsc in the system and electron transfer step is fast, the reduction of Cu(II)-peptide occurs before the binding of NO_2^- to Cu(II), producing the corresponding cuprous form. For different peptides, depending on the coordination environment of Cu(I), they might go through different routes, which differentiate the reaction rates. A copper-nitrosyl complex is proposed to be an important intermediate in the final stage of nitric oxide production in native CuNiR.[11,48,57,58] The fate of these Cu(I)-NO_2^- adducts is the formation of the corresponding copper-nitrosyl complexes, thus the binding modes of NO_2^- and the energetics of the adducts are important determinants for the reaction rates.

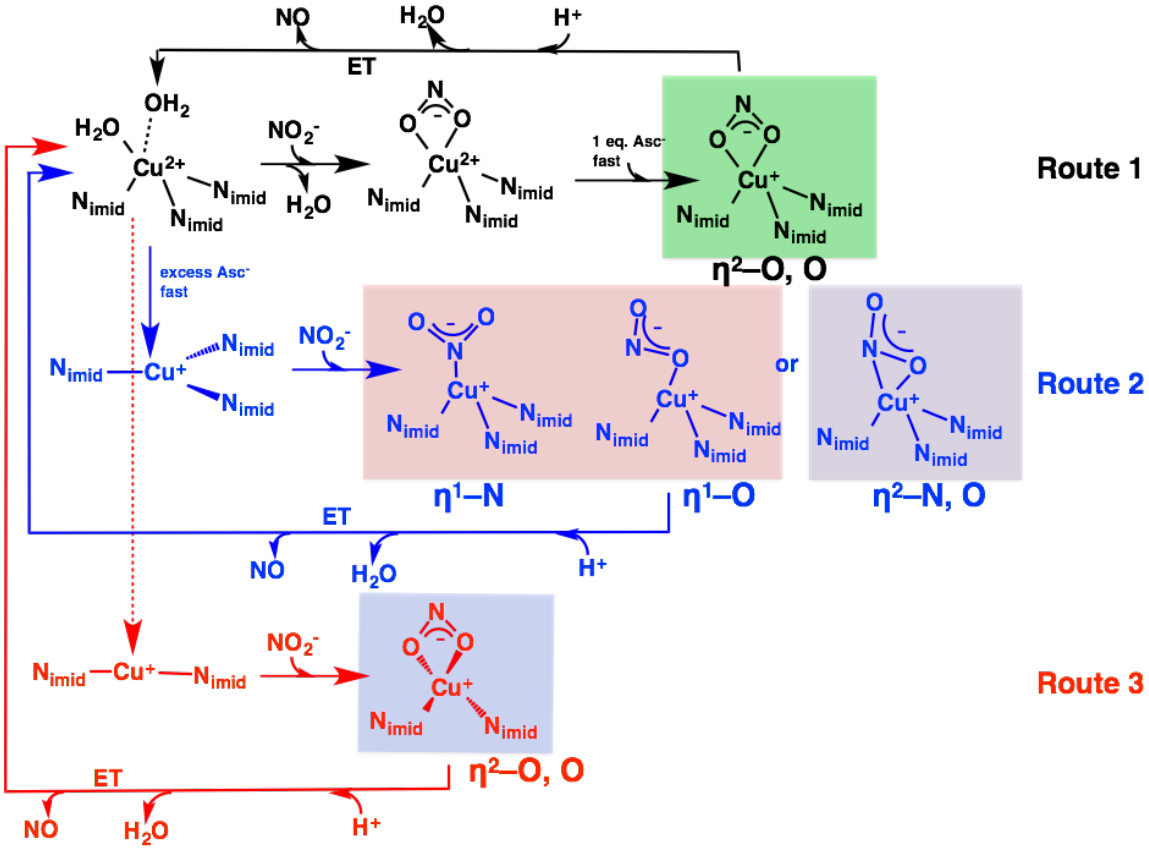

Scheme IV-7

For peptides that have three-coordinate Cu(I) centers, the reaction may follow route 2 (Scheme IV-7), with NO_2^- then coordinating to Cu(I), forming η^1-N, η^1-O, or η^2-N, O adduct, which might go through different processes to yield the product. Again, based on synthetic small molecule models, the η^1-N mode adduct is the most stable,[52,55,58–60] however, the possibility of η^1-O binding mode should not be eliminated since it has a similar energy based on DFT calculations. The bidendate η^2-N, O adduct, in the presence of protons, is higher in energy than the monodendate adduct, and the energy gap between the η^2-N, O adduct and the copper-nitrosyl complex is smaller than that between the monodendate Cu(I)-NO_2^- adduct and the copper-nitrosyl complex.[55] For those peptides with $_M$H mutation that have trigonal Cu(I) coordination, it is possible that a bidentate η^2-N, O binding mode is adopted by NO_2^-. This assignment is consistent with the fact that the rate of the nitrite reduction catalyzed by $_M$H-containing mutants is not as high as that of native CuNiR (not in a η^2-O, O mode), but much higher than those without $_M$H (monodendate binding mode).

On the other hand, for peptides with linear Cu(I) coordination (or T-shaped with a weakly coordinating imidazole), NO_2^- may also bind in a bidentate η^2-O, O mode, forming a four-coordinate Cu(I)$(N_{imid})_2$(η^2-O, O) center, which then follows route 3 (Scheme IV-7). A larger K_M is observed for TRIW-HL19A (Table IV-7), suggesting that the increase in coordination number upon NO_2^- binding might not be preferred by this Cu(I) center, which leads to elevated energy of the Cu(I)-NO_2^- adduct. Since the resulting adduct is still a four-coordinate Cu(I) complex, it is expected to have similar energy as the other four-coordinate adducts (Scheme IV-8). The unbound imidazolium at pH 5.8 might also contribute to the rate enhancement in the case of TRIW-HL19A. The protonation of nitrite when bound to the copper center is important for the elongation of the HO-NO bond, therefore efficient proton transfer to the active site is a crucial factor to maintain the high activity of nitrite reduction.[10,58,61] The imidazolium in TRIW-HL19A can serve as a general acid catalyst, assisting the protonation of the Cu(I)-NO_2^- adduct, thus increasing the nitrite reduction rate. For TRIW-$_M$HL19A, since Cu(I) forms a T-shaped coordination, the effect of general acid catalysis from imidazolium is not available. As a result, the effect of rate enhancement cannot simply be added. The Cu(I)-

NO_2^- adduct might be more energetically favorable than that of TRIW-$_M$H, possibly more similar to the η^2-O, O form due to the extra space created by the L19A substitution.

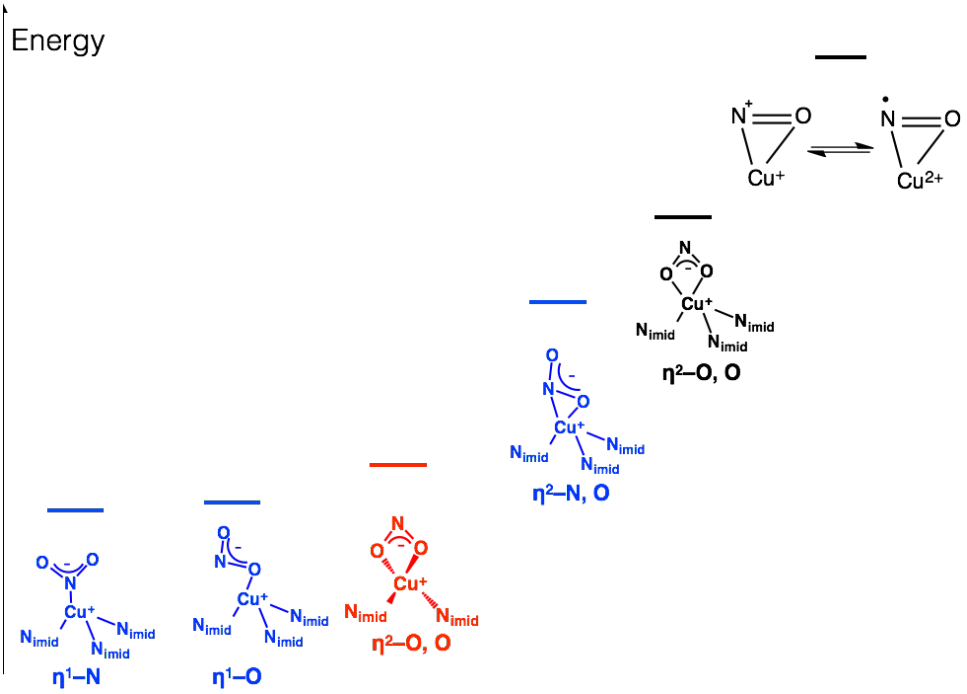

Scheme IV-8. A relative energy diagram of the possible Cu(I)-NO_2^- adduct in relation to the copper-nitrosyl complex.

The rate for TRIW-E$_M$H is ~2-fold lower than that of TRIW-$_M$H, and the rate for TRIW-EHL19A is ~5-fold lower than that of TRIW-HL19A. This is tentatively attributed to the interference of the proton transfer process by Glu22. At pH 5.8, for peptides with K22E mutation, due to the existence of multiple Glu residues, the pK_a for the carboxylic acid spans a wide range (Figure 3-21). The glutamate might compete with the Cu(I)-NO_2^- adduct for protons, leading to lower rates. For TRIW-E$_M$H, one of the imidazoles possibly forms an H-bond with Glu22 (Scheme IV-4), however, the other two Glu22 can still interfere the protonation of NO_2^-. As a result, the rate of TRIW-E$_M$H is lower than that without Glu22. In the case of TRIW-EHL19A, it is possible that since Cu(I) adopts a linear coordination, the way that the imidazole plane orients makes it difficult to form an H-bond with Glu22, thus glutamates compete with NO_2^- for protons. This effect is not as evident in the case of TRIW-EH and TRIW-H possibly because Glu22 forms an H-bond with the imidazole $^\delta$N (Chapter III), which elevated the pK_a of of the carboxylic acid to ~

6.5, so most of the Glu22 is in its protonated form. Granted that this is the pK_a for the cupric form, one can still expect a similar influence on the cuprous form.

It has been demonstrated that in native NiR, the reaction goes through a step-wise mechanism.[10,48,56] The timing of substrate-binding and electron transfer is crucial for this reaction to occur efficiently. The order of these two steps has originated two different proposed reaction pathways: Suzuki/Hasnain mechanism[11,48,62] and Averill mechanism[57,63]. The energetics of different reaction intermediates might lead to distinct pathways. A recent study using protein film voltammetry revealed that the three-coordinate Cu(I) is an inactive reduced state in native CuNiR, the reactivation of which is still possible.[64] As analyzed above, the major portion of the reaction (other than the first equivalent) in my system goes through the less-active Cu(I) state as the starting point, which might explain why this system has rates that are much lower than the native T2Cu center. The protein design strategies described here change the Cu(I) coordination or possibly the Cu(I)-NO_2^- adduct to influence the reaction rates, which has proved to be successful. Another approach can be taken by properly timing the influx of electrons to make sure that the reaction always starts with the substrate-bound cupric form. This will be discussed in Chapter 4.

Compared to the best model CuNiR in the literature, the copper-peptide model has a comparable catalytic efficiency (Table IV-11). The higher efficiency of the synthetic small molecule mainly originates from a relatively low K_M, which could be explained by the heterogeneous catalytic nature of this system that leads to easy access of substrate. It was estimated that if the same reaction were to be carried out in a homogeneous solution, the efficiency would decrease by three orders of magnitude,[65] much lower than my model. The current methods for setting up the reaction yield catalytic efficiencies that are six-orders of magnitude smaller than that of the native CuNiR (Table IV-11). The discrepancy of the catalytic efficiency reflects the importance of the sequence of Cu(II) reduction and substrate binding in this particular system, and the crucial role of the proton-electron transfer chain around the T2Cu center. Laser flash-photolysis experiments have been employed to investigate the efficacy of several residues around a native T2Cu center in CuNiR in the proton-coupled electron transfer (PCET) process.[66] It was demonstrated that Asn90 route is the main proton delivery channel for

*Ax*NiR, but even if this channel is disrupted, there are other possible routes for proton delivery.[66] This is one of the most profound benefits of possessing an extended H-bonding network in native metalloenzymes, which has not been assimilated in *de novo* designed system quite yet.

Table IV-11. Kinetic parameters

	k_{cat} (min^{-1})	K_M (M)	k_{cat}/K_M (min^{-1} M^{-1})	Notes	Ref
$Cu(II)(TRIW\text{-}_MHL19A)_3^{2+}$	87.9(30)	0.13(1)	$6.8(6) \times 10^2$	pH 5.8, homogeneous aqueous solution	This work
$[CuMe_2bpa(H_2O)(ClO_4)]^{+a}$	3.8	$1.1(2) \times 10^{-3}$	3.4×10^3	Reaction occurs on a collagen film coated electrode, pH 5.5	65
	3.2×10^{-3}	$2.5(6) \times 10^{-3}$	1.3	Homogeneous, pH 5.5	
*Af*NiR	$3.72(6) \times 10^4$	$1.5(1) \times 10^{-4}$	$2.5(1) \times 10^8$	pH 6.5, aqueous	12
*Ax*NiR	$5.34(18) \times 10^3$	$2.68(49) \times 10^{-5}$	$2.0(4) \times 10^8$	pH 7.0, 4 °C	66

[a]The Chemdraw scheme of this compound is shown in Scheme IV-9

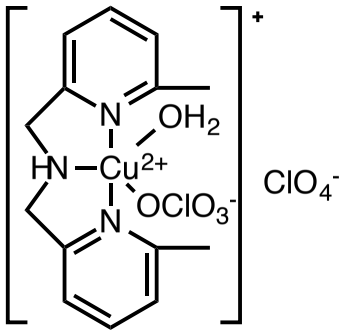

Scheme IV-9

Conclusion

I have presented in this chapter a series of peptides with modifications on the interior of the helical coiled coils. Parallel to the designs described in Chapter 3, the approach taken here is focused on altering the packing of the hydrophobic residues and the putative H-bonding schemes, in order to achieve higher NiR activity. Two mutations, L19A and $L23_MH$, have been described, along with the K22E mutation introduced in Chapter III, lead to the third generation of CuNiR models. Although the modifications are carried out on the second coordination sphere, the alteration on the first coordination sphere of the copper centers is observed, especially for peptides with the L19A mutation, which tend to bind Cu(I) into a linear coordination at pH 5.8. Additional insight into the coordination environment of both oxidation levels is obtained by small molecule binding studies monitored by FTIR, EPR, or UV-Vis spectroscopies.

Based on the previous analysis of the possible reaction routes, one realizes that the cuprous state is likely the starting point of the catalytic reaction. This generation of models exhibits NiR rates up to ~1300-fold better than TRIW-H, which is tentatively explained by the alternative binding modes of NO_2^- to Cu(I)-3SCC, forming intermediates that are energetically more accessible to facilitate the intramolecular electron transfer. The higher rates allow me to carry out Michaelis-Menten kinetic studies for these peptides. They are by far the best CuNiR models in homogeneous aqueous conditions with high enzyme stability. Overall, this work suggests that modifying the interior of the helical coiled coils is an effective design strategy to achieve a better CuNiR model. Future work will focus on the timing of electron flux and substrate binding, as well as building a H-bonding network to facilitate PCET.

References

(1) Kiefer, L. L.; Krebs, J. F.; Paterno, S. A.; Fierke, C. A. *Biochemistry* **1993**, *32*, 9896–9900.
(2) Krebs, J. F.; Fierke, C. A.; Alexander, R. S.; Christianson, D. W. *Biochemistry* **1991**, *30*, 9153–9160.
(3) Kiefer, L. L.; Paterno, S. A.; Fierke, C. A. *J. Am. Chem. Soc.* **1995**, *117*, 6831–6837.
(4) Lesburg, C. A.; Christianson, D. W. *J. Am. Chem. Soc.* **1995**, *117*, 6838–6844.
(5) Ippolito, J. A.; Baird, T. T.; McGee, S. A.; Christianson, D. W.; Fierke, C. A. *Proc. Natl. Acad. Sci. U. S. A.* **1995**, *92*, 5017–5021.
(6) Marshall, N. M.; Garner, D. K.; Wilson, T. D.; Gao, Y.-G.; Robinson, H.; Nilges, M. J.; Lu, Y. *Nature* **2009**, *462*, 113–116.
(7) Boulanger, M. J.; Kukimoto, M.; Nishiyama, M.; Horinouchi, S.; Murphy, M. E. *J. Biol. Chem.* **2000**, *275*, 23957–23964.
(8) Boulanger, M. J.; Murphy, M. E. P. *Biochemistry* **2001**, *40*, 9132–9141.
(9) Boulanger, M. J.; Murphy, M. E. P. *Protein Sci.* **2003**, *12*, 248–256.
(10) Tocheva, E. I.; Rosell, F. I.; Mauk, a G.; Murphy, M. E. P. *Science* **2004**, *304*, 867–870.
(11) Antonyuk, S. V; Strange, R. W.; Sawers, G.; Eady, R. R.; Hasnain, S. S. *Proc. Natl. Acad. Sci. U. S. A.* **2005**, *102*, 12041–12046.
(12) Tocheva, E. I.; Eltis, L. D.; Murphy, M. E. *Biochemistry* **2008**, *47*, 4452–4460.
(13) Antonyuk, S. V; Han, C.; Eady, R. R.; Hasnain, S. S. *Nature* **2013**, *496*, 123–126.
(14) Godden, J.; Turley, S.; Teller, D.; Adman, E.; Liu, M.; Payne, W.; LeGall, J. *Science (80-.).* **1991**, *253*, 438–442.
(15) Murphy, M. E.; Turley, S.; Adman, E. T. *J. Biol. Chem.* **1997**, *272*, 28455–28460.
(16) Yu, F.; Penner-Hahn, J. E.; Pecoraro, V. L. *J. Am. Chem. Soc.* **2013**, *135*, 18096–18107.
(17) Costas, M.; Xifra, R.; Llobet, A.; Solà, M.; Robles, J.; Parella, T.; Stoeckli-Evans, H.; Neuburger, M. *Inorg. Chem.* **2003**, *42*, 4456–4468.
(18) Ebrahimpour, P.; Cushion, M.; Haddow, M. F.; Hallett, A. J.; Wass, D. F. *Dalton Trans.* **2010**, *39*, 10910–10919.
(19) Matsumoto, J.; Kajita, Y.; Masuda, H. *Eur. J. Inorg. Chem.* **2012**, *2012*, 4149–4158.
(20) Himes, R. A.; Park, G. Y.; Barry, A. N.; Blackburn, N. J.; Karlin, K. D. *J. Am. Chem. Soc.* **2007**, *129*, 5352–5353.
(21) Zhang, H.; Boulanger, M. J.; Mauk, A. G.; Murphy, M. E. P. *J. Phys. Chem. B* **2000**, *104*, 10738–10742.
(22) Hirota, S.; Iwamoto, T.; Tanizawa, K.; Adachi, O.; Yamauchi, O. *Biochemistry* **1999**, *38*, 14256–14263.
(23) Jaron, S.; Blackburn, N. J. *Biochemistry* **2001**, *40*, 6867–6875.
(24) Gans, P.; Sabatini, A.; Vacca, A. *Talanta* **1996**, *43*, 1739–1753.
(25) Lee, K.-H.; Matzapetakis, M.; Mitra, S.; Marsh, E. N. G.; Pecoraro, V. L. *J. Am. Chem. Soc.* **2004**, *126*, 9178–9179.
(26) Lee, K.-H.; Cabello, C.; Hemmingsen, L.; Marsh, E. N. G.; Pecoraro, V. L. *Angew. Chem. Int. Ed. Engl.* **2006**, *45*, 2864–2868.

(27) Shearer, J.; Szalai, V. A. *J. Am. Chem. Soc.* **2008**, *130*, 17826–17835.
(28) Sanyal, I.; Karlin, K. D.; Strange, R. W.; Blackburn, N. J. *J. Am. Chem. Soc.* **1993**, *115*, 11259–11270.
(29) Tegoni, M.; Yu, F.; Bersellini, M.; Penner-Hahn, J. E.; Pecoraro, V. L. *Proc. Natl. Acad. Sci. U. S. A.* **2012**, *109*, 21234–21239.
(30) Dooley, D. M.; Scott, R. A.; Knowles, P. F.; Colangelo, C. M.; McGuirl, M. A.; Brown, D. E. *J. Am. Chem. Soc.* **1998**, *120*, 2599–2605.
(31) Kline, C. D.; Mayfield, M.; Blackburn, N. J. *Biochemistry* **2013**, *52*, 2586–2596.
(32) Clegg, W.; Acott, S. R.; Garner, C. D. *Acta Crystallogr. Sect. C Cryst. Struct. Commun.* **1984**, *40*, 768–769.
(33) Tazelaar, C. G. J.; Lyaskovskyy, V.; Dijk, T. Van; Broere, D. L. J.; Kolfschoten, L. a.; Khiar, R. O. H.; Lutz, M.; Slootweg, J. C.; Lammertsma, K. *Organometallics* **2012**, *31*, 3308–3315.
(34) Miller, M. T.; Gantzel, P. K.; Karpishin, T. B. *J. Am. Chem. Soc.* **1999**, *121*, 4292–4293.
(35) Berry, R. S. *J. Chem. Phys.* **1960**, *32*, 933.
(36) Murphy, G.; O'Sullivan, C.; Murphy, B.; Hathaway, B. *Inorg. Chem.* **1998**, *37*, 240–248.
(37) O'Sullivan, C.; Murphy, G.; Murphy, B.; Hathaway, B. *J. Chem. Soc. Dalt. Trans.* **1999**, 1835–1844.
(38) Muetterties, E. L.; Guggenberger, L. J. *J. Am. Chem. Soc.* **1974**, *96*, 1748–1756.
(39) Mukherjee, R. *Comprehensive Coordination Chemistry II*; Elsevier, **2004**; pp. 747–910.
(40) Addison, A. W.; Rao, T. N.; Reedijk, J.; van Rijn, J.; Verschoor, G. C. *J. Chem. Soc. Dalt. Trans.* **1984**, 1349.
(41) Banci, L.; Bertini, I.; Borsari, M.; Viezzoli, M. S.; Hallewell, R. A. *Eur. J. Biochem.* **1995**, *232*, 220–225.
(42) Deligeer; Kataoka, K.; Suzuki, S. *Bull. Chem. Soc. Jpn.* **2001**, *74*, 183–184.
(43) Chufán, E. E.; Prigge, S. T.; Siebert, X.; Eipper, B. A.; Mains, R. E.; Amzel, L. M. *J. Am. Chem. Soc.* **2010**, *132*, 15565–15572.
(44) Casella, L.; Gullotti, M.; Pallanza, G.; Buga, M. *Inorg. Chem.* **1991**, *30*, 221–227.
(45) Casella, L.; Carugo, O.; Gullotti, M.; Doldi, S.; Frassoni, M. *Inorg. Chem.* **1996**, *35*, 1101–1113.
(46) Chen, J.; Russo, R.; Chao, W.; Margerum, L. D.; Malachowski, M. R.; White, R.; Thawley, Z.; Thayer, A.; Rheingold, A. L.; Zakharov, L. N. *Dalton Trans.* **2007**, 2571–2579.
(47) Kunishita, A.; Ertem, M. Z.; Okubo, Y.; Tano, T.; Sugimoto, H.; Ohkubo, K.; Fujieda, N.; Fukuzumi, S.; Cramer, C. J.; Itoh, S. *Inorg. Chem.* **2012**, *51*, 9465–9480.
(48) Kataoka, K.; Furusawa, H.; Takagi, K.; Yamaguchi, K.; Suzuki, S. *J. Biochem.* **2000**, *127*, 345–350.
(49) Halfen, J. A.; Mahapatra, S.; Wilkinson, E. C.; Gengenbach, A. J.; Young, V. G.; Que, L.; Tolman, W. B.; August, R. *J. Am. Chem. Soc.* **1996**, *118*, 763–776.
(50) Yokoyama, H.; Yamaguchi, K.; Sugimoto, M.; Suzuki, S. *Eur. J. Inorg. Chem.* **2005**, *2005*, 1435–1441.

(51) Nairn, A. K.; Archibald, S. J.; Bhalla, R.; Boxwell, C. J.; Whitwood, A. C.; Walton, P. H. *Dalton Trans.* **2006**, 1790–1795.
(52) Kujime, M.; Izumi, C.; Tomura, M.; Hada, M.; Fujii, H. *J. Am. Chem. Soc.* **2008**, *130*, 6088–6098.
(53) Chuang, W.-J.; Lin, I.-J.; Chen, H.-Y.; Chang, Y.-L.; Hsu, S. C. N. *Inorg. Chem.* **2010**, *49*, 5377–5384.
(54) Woollard-Shore, J. G.; Holland, J. P.; Jones, M. W.; Dilworth, J. R. *Dalton Trans.* **2010**, *39*, 1576–1585.
(55) Hsu, S. C. N.; Chang, Y.; Chuang, W.; Chen, H.; Lin, I.; Chiang, M. Y.; Kao, C.; Chen, H. *Inorg. Chem.* **2012**, *51*, 9297–9308.
(56) Suzuki, S.; Kataoka, K.; Tamaguchi, K. *Acc. Chem. Res.* **2000**, *33*, 728–735.
(57) Averill, B. A. *Chem. Rev.* **1996**, *96*, 2951–2964.
(58) Merkle, A. C.; Lehnert, N. *Dalton Trans.* **2012**, *41*, 3355–3368.
(59) Komeda, N.; Nagao, H.; Kushi, Y.; Adachi, G.; Suzuki, M.; Uehara, A.; Tanaka, K. *Bull. Chem. Soc. Jpn.* **1995**, *68*, 581–589.
(60) Fujisawa, K.; Tateda, A.; Miyashita, Y.; Okamoto, K.; Paulat, F.; Praneeth, V. K. K.; Merkle, A.; Lehnert, N. *J. Am. Chem. Soc.* **2008**, *130*, 1205–1213.
(61) Ghosh, S.; Dey, A.; Sun, Y.; Scholes, C. P.; Solomon, E. I. *J. Am. Chem. Soc.* **2009**, *131*, 277–288.
(62) Strange, R. W.; Murphy, L. M.; Dodd, F. E.; Abraham, Z. H.; Eady, R. R.; Smith, B. E.; Hasnain, S. S. *J. Mol. Biol.* **1999**, *287*, 1001–1009.
(63) Hulse, C. L.; Tiedje, J. M.; Averill, B. A. *J. Am. Chem. Soc.* **1989**, *111*, 2322–2323.
(64) Wijma, H. J.; Jeuken, L. J. C.; Verbeet, M. P.; Armstrong, F. a; Canters, G. W. *J. Am. Chem. Soc.* **2007**, *129*, 8557–8565.
(65) Isoda, N.; Yokoyama, H.; Nojiri, M.; Suzuki, S.; Yamaguchi, K. *Bioelectrochemistry* **2010**, *77*, 82–88.
(66) Leferink, N. G. H.; Han, C.; Antonyuk, S. V; Heyes, D. J.; Rigby, S. E. J.; Hough, M. A.; Eady, R. R.; Scrutton, N. S.; Hasnain, S. S. *Biochemistry* **2011**, *50*, 4121–4131.

Chapter V . X-ray absorption spectroscopy and its applications on *de novo* designed metallopeptides

An overview of X-ray absorption spectroscopy

X-ray absorption spectroscopy (XAS) has become one of the most important tools to understand the structural details of metal centers in metalloproteins. In the X-ray absorption process, a core electron is ejected to an outer empty orbital or the continuum, absorbing certain energy of X-ray radiation. Although this phenomenon has been known since the 1920s,[1,2] the interest in X-ray absorption reoccurred in the 1970s when the Stanford Positron Electron Accelerating Ring (SPEAR) was first employed as a synchrotron radiation source. Unlike X-ray crystallography, which requires a well-defined periodic structure of the sample, this technique can be used to study non-crystalline materials thus making it very convenient to investigate the metal coordination environment in diluted protein samples. In addition, XAS techniques are element specific, which is especially important for the study of heterometallic systems. The two most commonly used spectroscopic techniques are X-ray absorption near-edge structure (XANES) and extended X-ray absorption fine structure (EXAFS), both of which are based on the scattering of the X-ray photoelectrons by the surrounding atoms.[3] In my previous data chapters, I used XAS techniques to determine the Cu(I) coordination environment in an NiR model. I present herein a brief overview of this technique and my data fitting procedures for future reference. Two other *de novo* designed systems using XAS for structural assignment will also be presented.

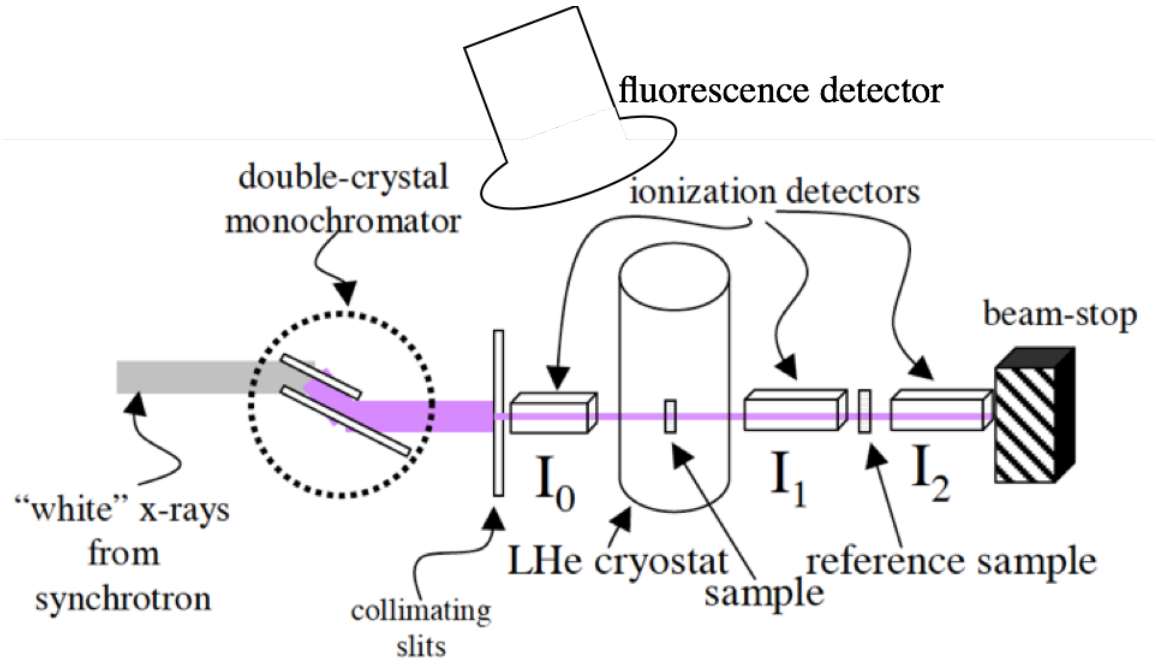

Figure V-1. Experimental setup for XAS

An X-ray beam goes through a monochromator and three ionization chambers (Figure V-1). The reference sample and experimental sample are placed in between I_1 and I_2, I_0 and I_1, respectively. Data are collected as fluorescence exciation spectra and transformed to desired formats depending on the specific technique. An electron can be ejected from an atom by X-ray. The mathematical description of X-ray absorption process is discussed in an exhaustive review by de Groot.[4] When core electrons are ejected, there is an abrupt increase in the absorption, which is called an absorption "edge". The nomenclature of the X-ray absorption derives from its core orbital. The most common XAS experiments focus on the K-edge of the sample, which refers to the excitation of an electron from the innermost *s* orbital. For first row transition metals, the K-edge energy is in the hard X-ray region (5 – 10 keV, or *ca*. 2 – 1 Å).[3]

XANES refers to the range of the X-ray absorption spectrum within about 30 eV of the energy threshold where scattering is very strong and inelastic losses are relatively weak.[5] The edge structure provides information on the geometry and oxidation state of the metal center. Recent advancement in the theoretical aspects and quantitative interpretation of XANES is reviewed by Rehr *et al*.[5] In this dissertation, I use XANES to

investigate the geometry and coordination number of spectroscopically silent metal such as Zn(II) and Cu(I).

For X-ray energy beyond the initial ~30 – 50 eV threshold, the photoelectron kinetic energy increases as described in Equation V-1

$E = E_o + E_k = E_o + 1/2m_e v^2$,

Equation V-1

The wavelength of the ejected photoelectron can be expressed as Equation V-2.

$$\lambda = \frac{h}{m_e v} = \frac{h}{\sqrt{2m_e(E - E_o)}},$$

Equation V-2

The energy is converted into *k* space (photoelectron wave-vector), which refers to the inverse photoelectron wavelength described in Equation V-3.

$$k = \frac{2\pi}{\lambda} = \frac{2\pi\sqrt{2m_e(E - E_o)}}{h} = \frac{\sqrt{2m_e(E - E_o)}}{\hbar},$$

Equation V-3

The ejected electron interacts with the neighboring atoms (back-scatterers), creating backscattered waves, which interfere with the original electrons, creating oscillating patterns. EXAFS is defined as the oscillatory part of the absorption coefficient, which is described by the difference between the observed absorption coefficient and the free-atom absorption coefficient, normalized to the free-atom absorption coefficient, as shown in Equation V-4.

$$\chi(k) = \frac{\mu(k) - \mu_0(k)}{\mu_0(k)},$$

Equation V-4.

Quantitatively, between a single absorber-backscatterer, EXAFS can be written as Equation V-5, where N_s stands for the number of scattering atoms; $A_s(k)$ stands for the contribution of this specific interaction to the amplitude; R_{as} is the distance between the

absorber and the backscatterer; σ_{as}^2 is the mean-square disorder of the distance between the absorber and the backscatterer, usually referred to as the Debye-Waller factor, which accounts for disorder, both thermal and structural, of the relevant scattering paths;[6] $\phi_{as}(k)$ is the phase component.

$$\chi_i(k) = \frac{N_s A_s(k)}{R_{as}^2} \exp(-2k^2\sigma_{as}^2) \sin(2kR_{as} + \phi_{as}(k)),$$

Equation V-5

For systems with multiple components of backscatterers, the total EXAFS is the sum of all these components, as shown in Equation V-6.

$$\chi(k) = \sum_{i=1}^{n} \chi_i(k),$$

Equation V-6.

Single scattering and multiple scattering fitting procedures.

The XAS data are collected on line 7-3 at Stanford National Accelerator Laboratory (SLAC). The program for data collection was written by Martin J. George at SSRL and the user manual can be downloaded at http://ssrl.slac.stanford.edu/~xas/xas-man.html. The same file can also be found in the Pecoraro group D-drive under "XAS documents" folder. The raw XAS data are viewed, calibrated, averaged, baseline subtracted, and normalized using the EXAFSPAK program suite, which can be downloaded at http://www-ssrl.slac.stanford.edu/exafspak.html with a user manual. Scheme V-1 shows the general procedure for the EXAFS data fitting process. The steps for single scattering fitting are described in details in the EXAFSPAK manual, so I will omit the description here and focus on multiple scattering fitting.

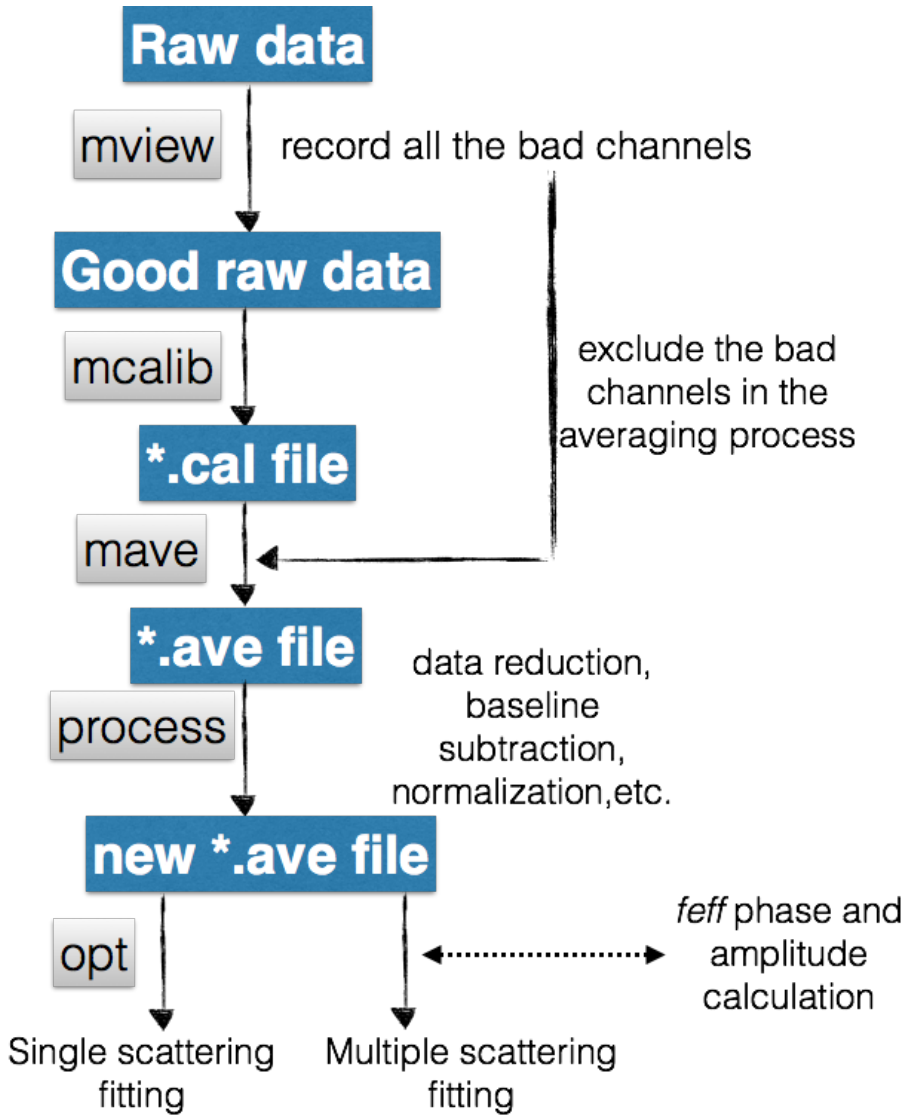

Scheme V-1. EXAFS data fitting process. Blue blocks represent files; gray blocks represent the commands.

For metal centers with ligands such as imidazoles, significant Fourier transform peaks from the outer shells are observed, which is attributed to the multiple scattering processes occurring within the atoms from the imidazole ring and the metal center. Multiple scattering effects are sensitive to the geometry of the ligands. Atoms closer to a 180° angle with respect to the axis created by the metal center and the primary scatterer have greater contributions to the scattering amplitude. To map out the multiple scattering paths, a model has to be built based on the known crystal structures of similar coordination environments. For example, based on XANES and single scattering fitting,

$Cu(I)(TRIW\text{-}H)_3^+$ has a coordination number of 3 (maybe 4), so I searched for three- or four-coordinate Cu(I) centers with imidazoles as ligands, averaged the bond distances and angles, and built a model of Cu-imidazole into Cartesian coordinates (Figure V-2).

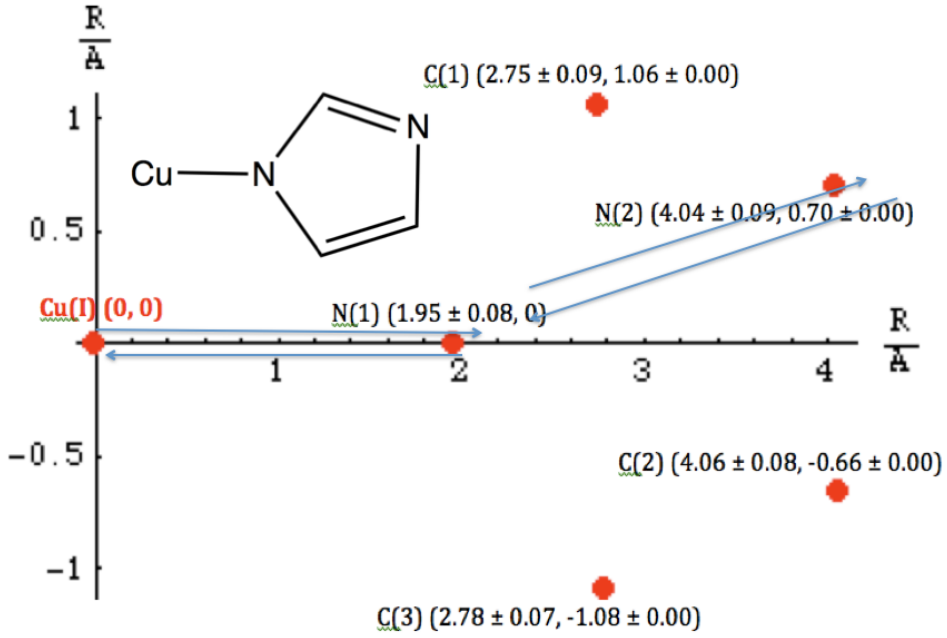

Figure V-2. The Cu-imid model. Red spheres represent atoms.

The coordinates of relevant atoms are then written into a text file, which is named as "*.inp". This *.inp file is used as an input file for ATOMS, a program for generating a list of atomic coordinates from crystallographic data. The primary use of ATOMS is to create input files suitable for running the *ab initio* program FEFF. An online version of ATOMS can be found at http://cars9.uchicago.edu/cgi-bin/atoms/atoms.cgi. There is a copy of ATOMS on the Pecoraro lab computer. For installation on personal computers, the relevant files can be downloaded at http://cars9.uchicago.edu/ifeffit/Downloads. The file that ATOMS creates is named feff.inp by the program.

The phase and amplitude calculation for multiple scattering fitting is carried out on a remote server (brd-ts2.adsroot.itcs.umich.edu). A remote desktop app can be used to access this server. For this calculation, one needs the feff.inp file that is generated by ATOMS. Once this file is downloaded onto the remote server, one can find the JFEFF program on the desktop, and load the feff.inp file into the program for calculations. It is worth mentioning that for different versions of ATOMS and JFEFF, the coding might not

necessarily be the same. So there might be errors in the assignment of potentials for different atoms. One needs to double-check the potential surface as well as the coordination by clicking the "Edit" tab in the JFEFF program. In addition, one can monitor what specific files to generate after the calculation by changing the numbers under "print level". The manual of the GUI version of JFEFF is under the same folder on the Pecoraro lab computer.

After the JFEFF calculation, one should see a group of files including paths, chi, as well as specific path files (feff0001, 0002, etc.) under the same folder as the initial feff.inp file. These files can then be used to carry out multiple scattering fitting. The JFEFF calculation is the only step that requires the biophysics server. After this step, one can copy these files into a local folder, and continue the multiple scattering fitting from a personal computer or the lab computer. It is essential that all the files generated from JFEFF and the data file (*.ave) are in the same folder before any further pursuit. Under Command Prompt (or terminal), type "feff_hld825 *.ave", where "*.ave" is the averaged, processed EXAFS data file to fit. This operation will generate a file called "paths.hld" under the same directory as all the other files. Now a command needs to be executed to change the name of this "paths.hld" file into "*.hld", where the * should be the same as that in "*.ave" to ensure that the program can correctly extract the right .hld file. After all these files are taken care of, one can type "opt *.ave" to carry out multiple scattering fitting. The operations under the opt program are similar to those for single scattering fitting. I have written a multiple scattering fitting protocol, which is in the "XAS documents" folder on the Pecoraro lab computer.

De novo designed copper-peptides as a model for a key intermediate in copper transfer by metallochaperones

Copper is an important trace metal that is indispensible for essentially all aerobic organisms. The hallmark of copper reactivity in biological systems are its redox properties, which leads to a variety of copper proteins that catalyze oxidoreductase reactions or carry out electron transfer.[7–17] These reactions are critical for many cellular functions; however, copper is a potential toxin if not regulated properly. Free copper ions carry out Fenton-type reactions that produce deleterious reactive oxygen species, which

can cause lipid, nucleic acid, and protein damage.[18,19] These effects demand a tight homeostatic regulation of copper acquisition, distribution and use. For example, the most common copper deficiency disorders in humans are Menkes and Wilson diseases, which are related to defects of human P_{1B}-type ATPase ATP7A and ATP7B, respectively.[20–25] The uptake and transport of copper ions involve cell surface transporters (Ctr1)[26] and copper chaperones. Three pathways with three distinct metallochaperones have been proposed to deliver copper to the mitochondria (Cox17 pathway), the Golgi (Atx1 pathway), and the cytosolic superoxide dismutase (CCS pathway).[27–30] The Cu(I) binding sites of these metallochaperones are generally cysteine rich with a highly conserved CXXC motif. Intracellular copper trafficking is achieved through ligand exchange of these metallochaperones with their delivery target via thermodynamic and kinetic control. The mechanistic details of transfer, however, are not completely understood on the molecular level. Over the years, two- and three-coordinate copper-thiol/thiolate species have been proposed to be key intermediates,[29–32] but the protonation states of the coordinating cysteine residues have not been elucidated experimentally.

De novo protein design has been utilized to understand the interactions between metal ions and proteins.[33–38] The Pecoraro group has demonstrated the design of thiolate environments amenable for Hg(II), Pb(II), Cd(II), and As(III) binding to address heavy metal selectivity, specificity, and coordination preferences in a protein environment.[39–53] Cu(I)-thiol/thiolate interactions under physiologically relevant pH conditions in a peptidic environment are investigated here. A thiol-rich site is embedded in a *de novo* designed scaffold TRIW-C (sequence: Ac-G WKALEEK LKALEEK CKALEEK LKALEEK G-NH_2). Cu(I) is then introduced to study its coordination preference in a thiol-rich environment. The resulting Cu(I)S_xO_y ($x, y \geq 0$) center serves as a model for the intermediates in the copper transfer process, providing key insight into the delivery mechanism. XAS data were collected at pH 6.5, 7.5, and 9.0 for Cu(I)(TRIW-C)$_3^x$ ($x = -1$ or -2 depending on the protonation state of the Cys). Sample preparation and data collection were carried out according to the previously described procedures.

A relatively intense pre-edge peak is observed for the XANES at all three pH conditions (Figure V-3). Subtle variations in the edge structure are observed: the ratio of the normalized intensity of the pre-edge peak and edge peak increases as the pH is raised

from 6.5 to 9.0. One should use caution when interpreting this set of XANES data based on the previous experience for the Cu(I)-N_{imid} coordination environment. Since the pre-edge of Cu(I) corresponds to a 1*s* → 4*p* transition, the intensity of this peak is influenced by the geometry (orbital degeneracy) and the nature of the ligand (energy level). Due to different ligand field created by N_{imid} and S_{Cys}, the relative ratio of the pre-edge/edge intensity to determine the coordination number of Cu(I)$(N_{imid})_x$ does not apply to the Cu$(S_{Cys})_y$ environment. Compared to reported CuS_x centers (Table V-1), the I_a/I_b ratio of Cu(I)(TRIW-C)$_3^x$ falls in between those of the linear and trigonal Cu(I) centers. This, however, does not exclude the possibility of Cu(I) binding to other coordinating atoms such as an oxygen from solvent water.

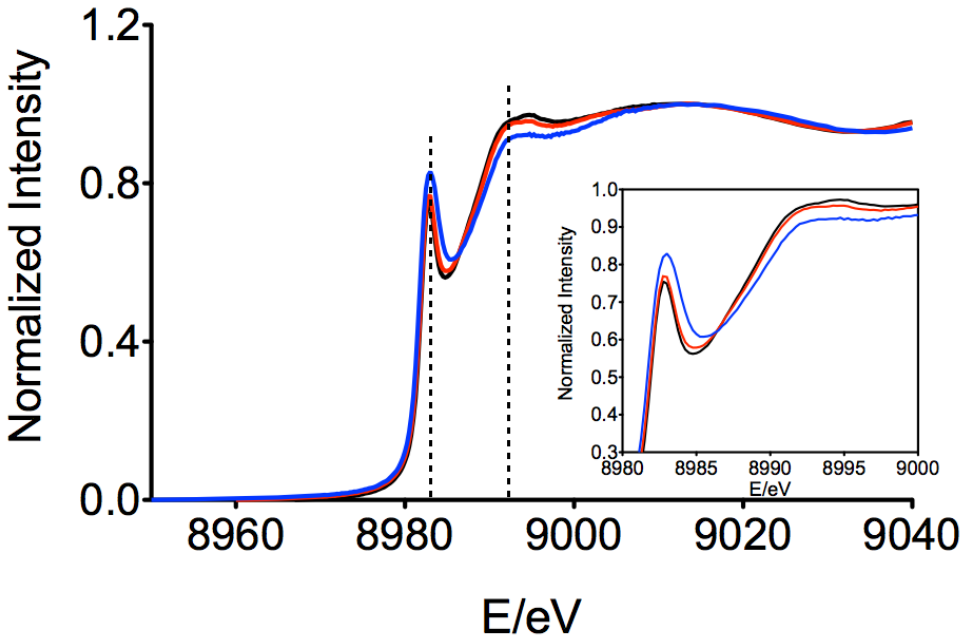

Figure V-3. XANES of Cu(I)(TRIW-C)$_3^x$ at pH 6.5 (black line), pH 7.5 (red line), and pH 9.0 (blue line). Insert: detail of the edge. The dashed lines indicate the positions of the pre-edge and edge peaks.

Table V-1. Ratio of pre-edge/edge intensity for Cu(I) XANES

Complex	I_a/I_b	Comments	Ref
Cu(I)(TRIW-C)$_3^x$	0.8–0.9	I_a/I_b increases slightly as the pH goes up	This work
$[Cu(SC_{10}H_{12})_2]^{2-}$	~1.1	Digonally coordinated by two sulfurs	54
$[Cu_4(SPh)_6]^{2-}$	0.5–0.6	Trigonally coordinated cuprous cluster	
Cu-CueR	~1.1	Digonal coordination	55
Cu-HAH1	~1.1	Linear CuS_2 center	56
$[Cu(SC_6H_5)_3]^{2-}$	~0.7	Trigonal Cu(I)S_3	30
Cu-CopZ	~0.7	Three coordinate	57

I_a, I_b represent the normalized intensity of the pre-edge and edge peaks, respectively

EXAFS data were collected for all three pH conditions and Fourier transformation was carried out. A transition is observed when the pH is raised from 6.5 to 9.0. Two major peaks are observed for pH 6.5 and 7.5 samples; at pH 9.0, a shoulder at $R + \alpha$ ~2.3 Å is observed (Figure V-4). Plotting the ratio of the intensities corresponding to the two major peaks, one sees an increasing trend as the pH increases. This, together with XANES data, suggests a transition between two species that is correlated with pH change. At pH 7.5, it is highly likely that the sample contains a mixture of two species. Since EXAFS can only provide information of an "averaged" coordination, fitting EXAFS data at pH 6.5 and 9.0 is more likely to yield useful metric parameters.

Table V-2 and Figure V-5 show the current best fits. At pH 6.5, the fitting model suggests that Cu(I) is coordinated to sulfur at two short distances [R(Cu-S) = 2.24 Å], one sulfur at a longer distance [R(Cu-S) = 2.45 Å], and a low Z scatter such as an oxygen or nitrogen atom [R(Cu-O) = 1.96 Å]. During the fitting process, the Debye-Waller factor of Cu-O/N and long Cu-S components have to be fixed, otherwise the simulation generates unphysical parameters. As shown in Figure V-5B, the component at $R + a$ ~2.3 Å is not well-simulated. At pH 9.0, the current best model is a Cu(I) center that coordinates to three sulfurs at short distances (consistent with thiolates) and an oxygen, however, the comparison between this model and copper centers in a similar coordination environment

(Table V-3) reveals that the Cu-S distance of 2.13 Å is too short for such a copper center. All of these observations reflect the inherent inconsistency of the data, possibly due to impurity in the samples, which could lead to an incorrect chemical interpretation. At this point, before we can reproduce this experiment, further analysis on this set of XAS data is unwarranted.

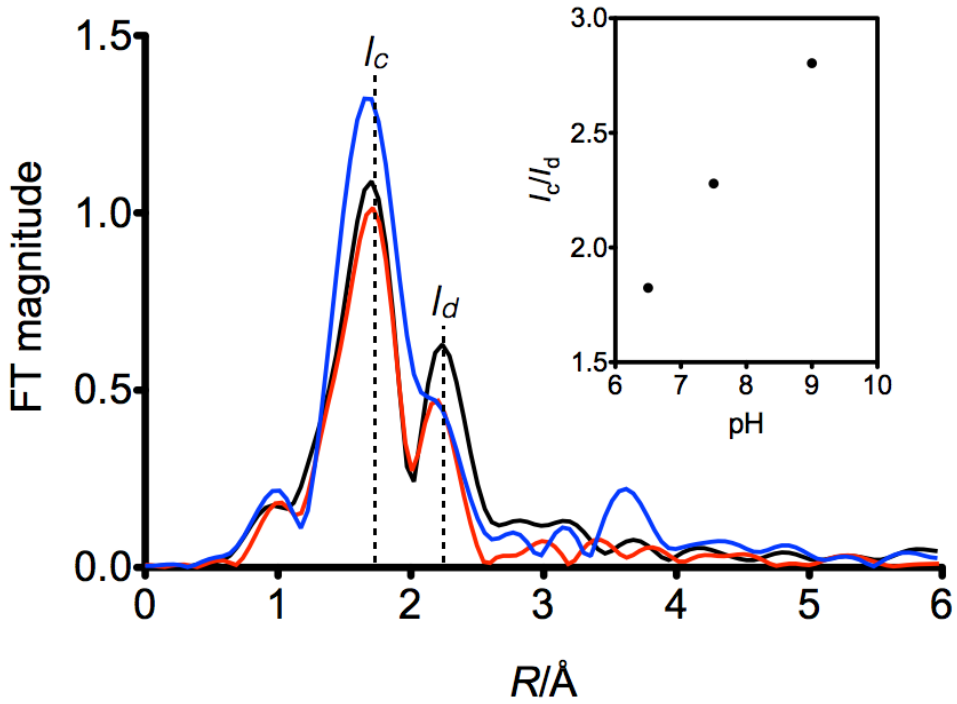

Figure V-4. Fourier transform of the EXAFS at pH 6.5 (black spectrum), 7.5 (red spectrum), and 9.0 (blue spectrum). Insert: I_c/I_d in relation to the pH.

Table V-2. EXAFS parameters of Cu(I)(TRIW-C)$_3^x$.

pH	Component	*CN*	*R*/Å	σ^2/Å	E^o/eV	*F*	N_{var}	$F^2/(N_{free}) \times 10^{-2}$
6.5	Cu-O	1	1.96	0.0010	-10	69	4	4.0
	Cu-S	2	2.24	0.0032				
	Cu-S	1	2.45	0.0010				
9.0	Cu-O	1	2.08	0.0010	-10	157	3	19
	Cu-S	3	2.13	0.0051				

1. CN: coordination number; R: distance; σ^2: Debye-Waller factor;
2. Variable parameters in red;
3. Assuming $N_{idp} = 2\Delta k \Delta R/\pi \sim 16$ and $N_{free} = N_{idp} - N_{var}$;
4. The goodness of the fit is evaluated by $F' = F^2/(N_{free}) \times 10^{-2}$. The smaller the value, the better the fit.

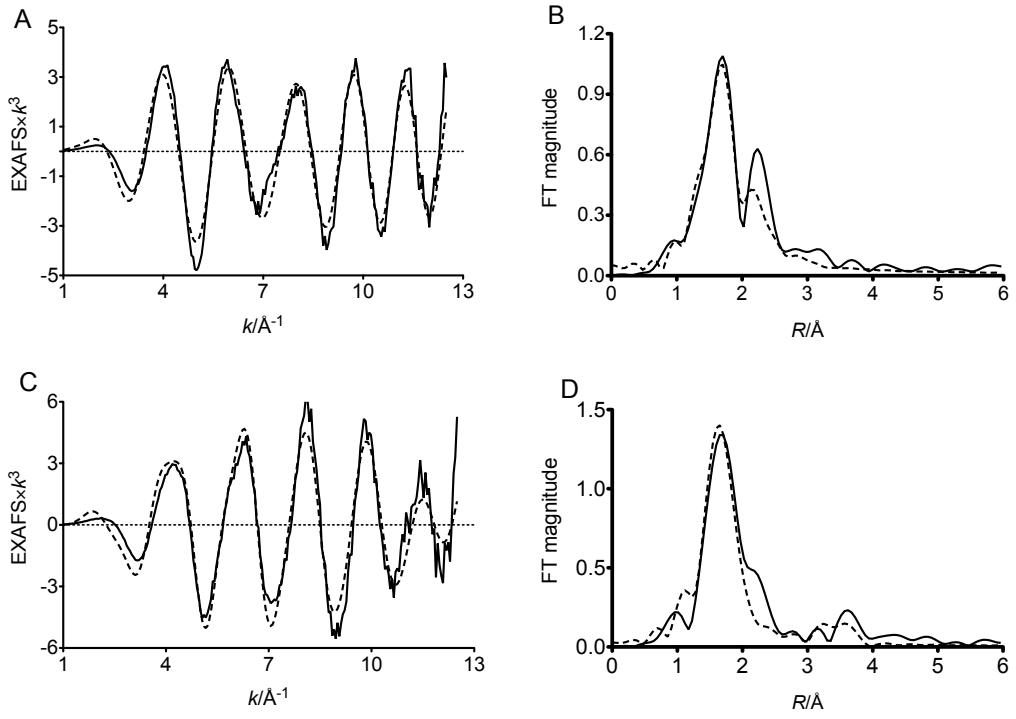

Figure V-5. EXAFS and Fourier transforms of Cu(I)(TRIW-C)$_3^x$ at (A)(B) pH 6.5; (C)(D) pH 9.0. Solid lines: data; dashed lines: fitting.

Table V-3. Bond distances in relevant complexes

Complex	*R*(Cu(I)-S)/Å	*R*(Cu(I)-O)/Å	Ref
$[Cu(1,4\text{-}TOX)_3OH_2]BF_4$[a]	2.291, 2.261, 2.272	2.235	60
$[Cu(Vn_3S_3)(CH_3OH)]O_3SCF_3 \bullet MeOH$[b]	2.299, 2.300, 2.279	1.980	61
$[Cu(\mathbf{L^1})(OH_2)(ClO_4)]ClO_4 \bullet$acetone[c]	2.344, 2.271, 2.329	1.956(OH_2), 2.759(ClO_4)	62
[Et4N]2[Cu{S(*p*-*t*BuC_6H_4)}$_3$][d]	2.234, 2.244, 2.257	-	63
The Chemdraw scheme of complexes a, b, c, d are shown in Scheme V-2			

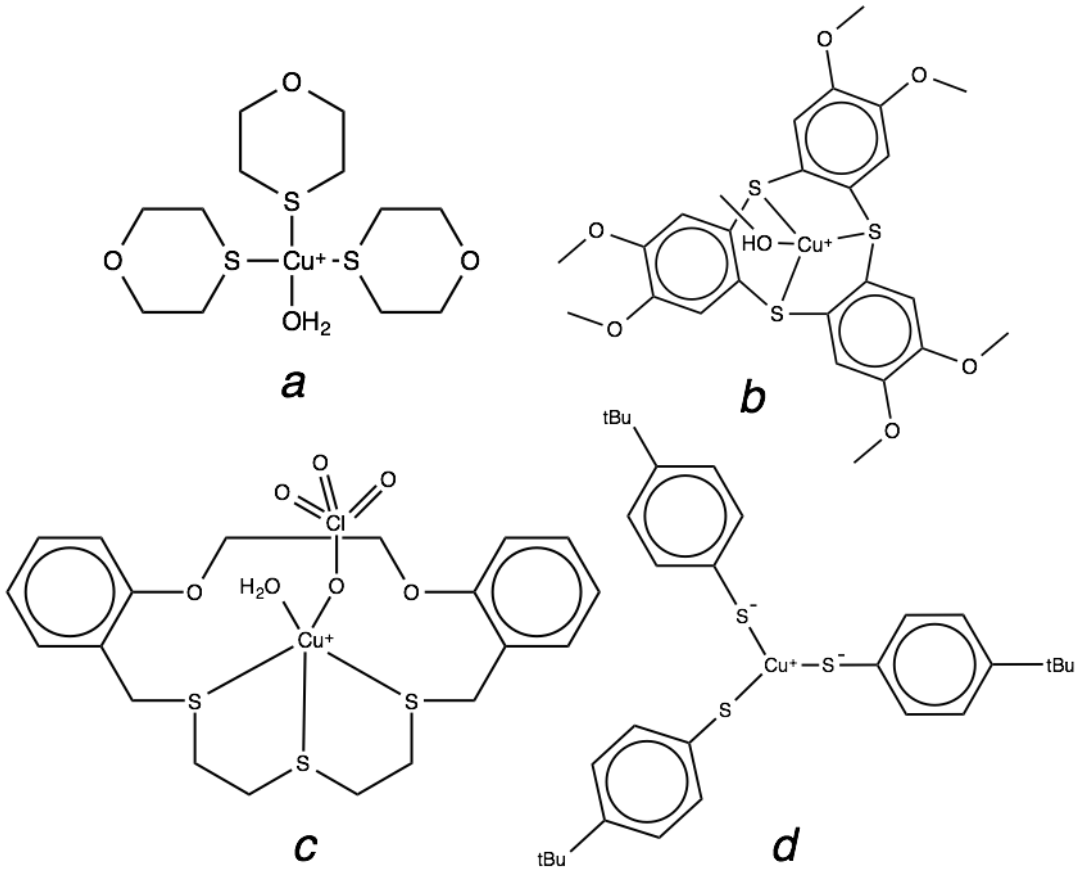

Scheme V-2

The Cu(I) affinities to TRIW-C were determined using the previously described procedures.[64,65] As expected, Cu(I) binds to this peptide with a high affinity, with K_d in the range of 10^{-15}~10^{-16} M. The dissociation constants are generally smaller than the reported values for Atx1s, HAH1, and MNK1 (Table V-4), which might reflect the strong stabilization effect of a linear S-Cu(I)-S coordination. One sees a ~3-fold decrease in K_d when the pH increases from 6.5 to 9.0. A similar pH-dependent affinity variation of Cu(I) to HAH1 and MNK1 has been reported previously.[66] For HAH1 in particular, the affinities vary from $10^{19.3}$ at pH 10.8 to $10^{16.8}$ at pH 6.1. Fitting the change of affinities results in a pK_a of 8.5, which corresponds to the deprotonation equilibrium of the cysteine thiol.[66]

Table V-4. Cu(I) affinities

Protein/peptide	K_d/M (pH)
TRIW-C	[a]$4.80(280) \times 10^{-15}$ (6.5), $1.31(50) \times 10^{-15}$ (7.5), $4.50(12) \times 10^{-17}$ (9.0)
Atx1 (*Saccharomyces cerevisiae*)	$4.2–7.1 \times 10^{-19}$ (8.0)[67], 10^{-16} (6.0)[68]
HAH1 (*homo sapiens*)	1.8×10^{-18} (7.0)[66]
MNK1[b] (*homo sapiens*)	2.8×10^{-18} (7.0)[66]
Wilson protein MBDs 1–6[c] (*homo sapiens*)	$1.6–4.5 \times 10^{-11}$ (7.5)[69]; 2.1×10^{-7}–4.8×10^{-6} (6.5)[70]
Ccc2ac (*Saccharomyces cerevisiae*)	$1.4–1.6 \times 10^{-19}$ (8.0)[67]

[a]The dissociation constants at pH 6.5 and 7.5 were determined by Catherine S. Mocny.
[b]MNK: Menkes protein ATP7A that has six MBDs; MNK1 refers to the first MBD.
[c]Wilson protein: ATP7B. CCcc2a: the first MBD of Ccc2, a yeast Golgi pump.

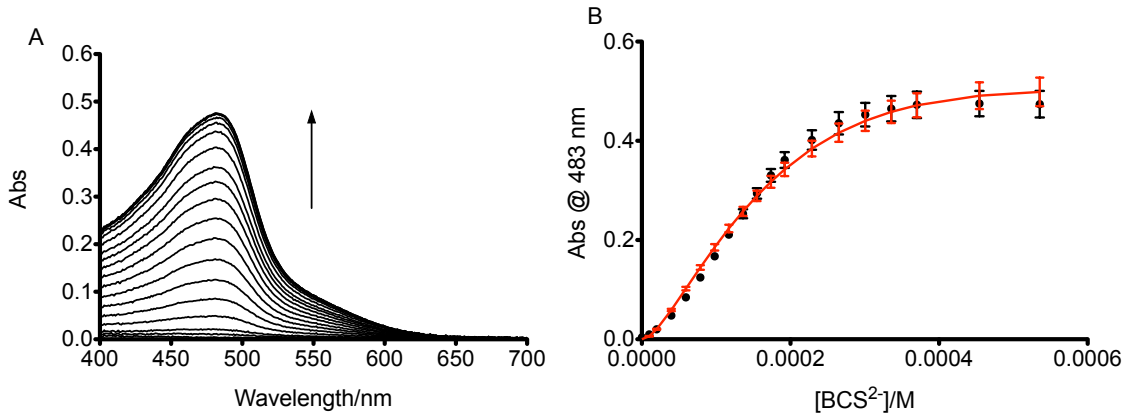

Figure V-6. BCS^{2-} competitive chelation of $Cu(I)(TRIW\text{-}C)_3^{2-}$ at pH 9.0 (50 mM TAPS buffer). (A) titration spectra; [Cu(I)] = 40 μM, [3SCC] = 80 μM, $[BCS^{2-}]$ = 5.00 mM (B) maximum absorbance corresponding to $Cu(I)(BCS)_2^{3-}$ with respect to the total concentration of BCS^{2-}. Experimental data are shown in black dots and fitting is shown in red line.

This study might potentially provide insight into the mechanism for Cu(I) transfer from copper chaperones to the corresponding cuproproteins. However, before the collection of another set of XAS data, the copper coordination environment cannot be described convincingly. The inability to distinguish possible impurities substantiates the importance of having a pure species for XAS samples for correct data interpretation.

XAS to probe the Zn(II) coordination environment in a *de novo* designed construct

The Pecoraro lab has been interested in the hydrolytic chemistry conferred by a *de novo* designed zinc peptide.[72,73] This construct represents one of the most advanced CA models, with catalytic efficiency only ~100-fold lower than that of CAII. Crystallography reveals a four-coordinate zinc center at pH 8.5, with Zn(II) coordinated to three His and an oxygen atom from either water or hydroxide.[72] The hydroxide species has been demonstrated to be the active species in hydrolysis. One would expect a decrease in Zn-O distance (≤0.1 Å) when the Zn(II)-bound water is deprotonated into a Zn(II)-bound hydroxide, however, the resolution of protein crystallography cannot usually discern such a small change in bond distance. The goal of this study was to evaluate whether the use of XAS techniques to distinguish zinc-bound water versus zinc-bound hydroxide species at different pH would allow such differentiation.

Samples were prepared according to the previously described procedures. The XANES of Zn(II)(TRI-H)$_3^{2+}$ are shown in Figure V-7. Minimal perturbation is observed for the edge structure, indicating the coordination number or geometry of the zinc center does not change under these conditions. Based on the kinetic studies, the chemical model going from pH 7.5 to 9.5 is that [Zn(II)(His)$_3$(OH$_2$)]$^{2+}$ deprotonates into [Zn(II)(His)$_3$(OH)]$^+$, with no change in coordination number, consistent with the XANES data.

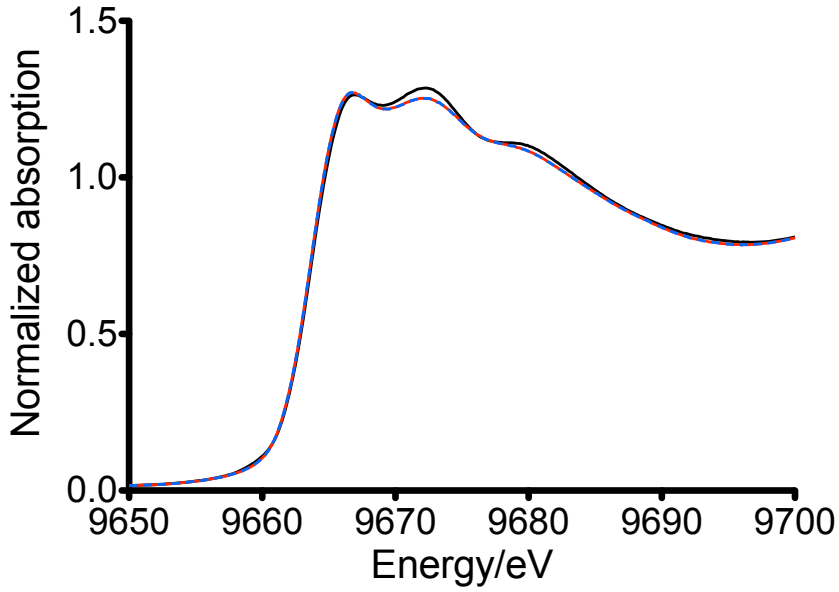

Figure V-7. XANES of Zn(II)(TRI-H)$_3$ at pH 7.5, black solid line; pH 8.5, red solid line; pH 9.5, blue dashed line.

Theoretically, EXAFS would be able to distinguish the change in bond distances upon deprotonation as long as the data are collected to a high energy with good quality. Unfortunately, there are glitches in the higher energy region. The *k* region needs to be truncated to (1.5, 12.5) Å to yield a decent signal to noise ratio. Multiple scattering fitting was carried out to distinguish the imidazole ring versus oxygen atom scattering (Table V-5). At pH 7.5, the best fit yields a 3N1O coordination with bond distances slightly shorter than the four-coordinate small molecule zinc complexes (Table V-5, Table V-6). At pH 8.5, two fits have the same level of goodness, one with 3N1O coordination and the other 2N2O. Since Dr. Melissa Zastrow has obtained a crystal

structure at pH 8.5, showing that Zn(II) is coordinated to three His and one oxygen (from water or hydroxide) or chloride, the coordination environment corresponding to fit1 (Table V-5) is more reasonable. At pH 9.5, both 3N1O and 1N3O have a similar level of goodness (Table V-5). Again, the 3N1O coordination makes more sense chemically.

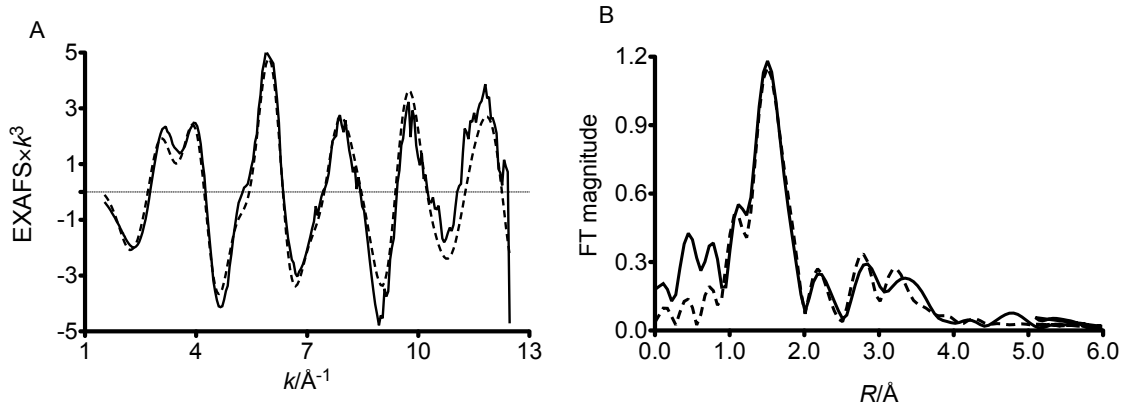

Figure V-8. EXAFS (A) and Fourier transform of the EXAFS (B) of Zn(II)(TRI-H)$_3^{2+}$ at pH 7.5.

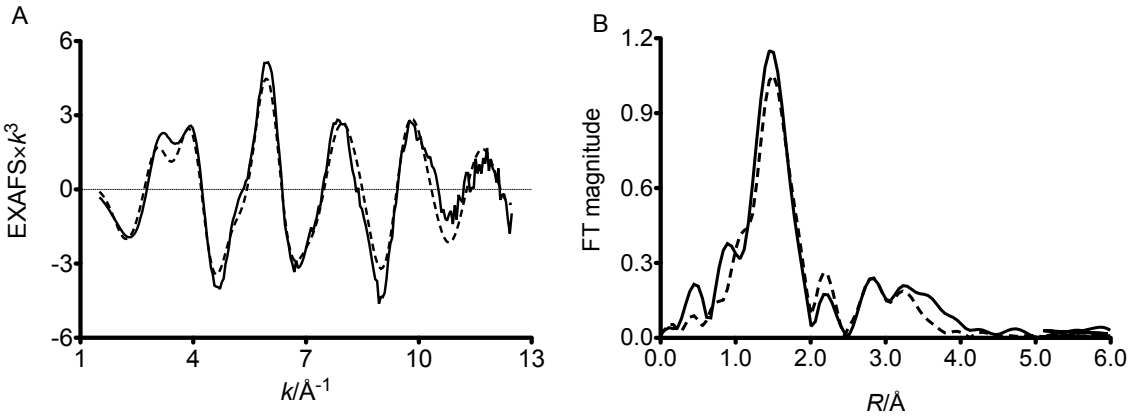

Figure V-9. EXAFS (A) and Fourier transform of the EXAFS (B) of Zn(II)(TRI-H)$_3^{2+}$ at pH 8.5 corresponding to fit1.

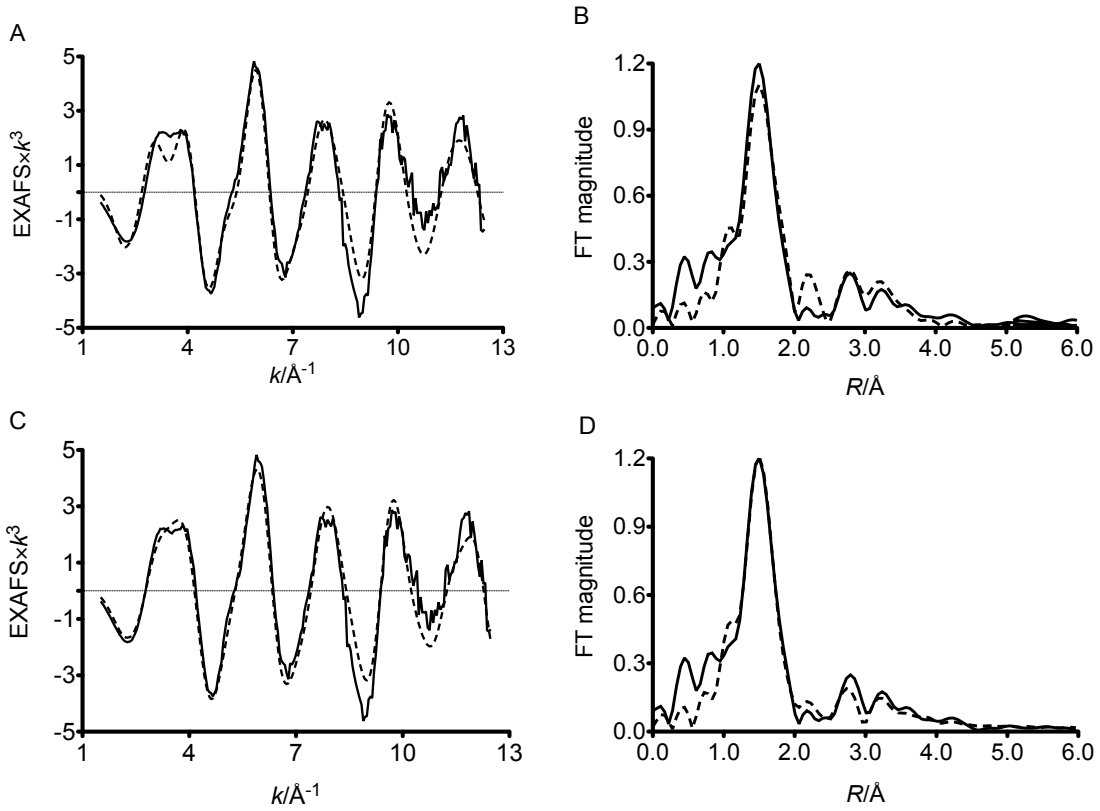

Figure V-10. EXAFS (A) and Fourier transform of the EXAFS (B) of Zn(II)(TRI-H)$_3^{2+}$ at pH 9.5 corresponding to fit1. EXAFS (C) and Fourier transform of the EXAFS (D) of Zn(II)(TRI-H)$_3^{2+}$ at pH 9.5 corresponding to fit2.

Table V-5. EXAFS fitting parameters for Zn(II)(TRI-H)$_3^{2+}$

pH	First shell	R/Å	σ^2/Å^2	Outer shells	R/Å	σ^2/Å^2	N_{var}	$F^2/(N_{free}) \times 10^{-2}$
7.5	3 Zn(II)-N$^{(1)}$	1.977	0.0062	3 Zn(II)-C$^{(1)}$	2.974	0.0093	4	7.5
				3 Zn(II)-C$^{(2)}$	3.117	0.0097		
	1 Zn(II)-O$_w$	1.975	0.0027	3 Zn(II)-N$^{(2)}$	4.121	0.0128		
				3 Zn(II)-C$^{(3)}$	4.131	0.0129		
8.5 fit1	3 Zn(II)-N$^{(1)}$	1.984	0.0081	3 Zn(II)-C$^{(1)}$	2.984	0.0122	4	3.2
				3 Zn(II)-C$^{(2)}$	2.986	0.0122		
	1 Zn(II)-O$_w$	1.953	0.0002	3 Zn(II)-N$^{(2)}$	4.146	0.0169		
				3 Zn(II)-C$^{(3)}$	4.162	0.0170		
8.5 fit2	2.13 Zn(II)-N$^{(1)}$	1.981	0.0077	3 Zn(II)-C$^{(1)}$	2.980	0.0116	6	2.3
				3 Zn(II)-C$^{(2)}$	2.982	0.0116		
	2.26 Zn(II)-O$_w$	1.962	0.0040	3 Zn(II)-N$^{(2)}$	4.129	0.0161		
				3 Zn(II)-C$^{(3)}$	4.139	0.0161		
9.5 fit1	3 Cu(I)-N$^{(1)}$	1.981	0.0074	3 Zn(II)-C$^{(1)}$	2.979	0.0111	4	4.8
				3 Zn(II)-C$^{(2)}$	2.981	0.0111		
	1 Zn(II)-O$_w$	1.978	0.0009	3 Zn(II)-N$^{(2)}$	4.128	0.0154		
				3 Zn(II)-C$^{(3)}$	4.138	0.0154		
9.5	1 Cu(I)-N$^{(1)}$	1.980	0.0036	3 Zn(II)-C$^{(1)}$	2.978	0.0054	4	3.6

fit2				3 Zn(II)-$C^{(2)}$	2.979	0.0054
	3 Zn(II)-O_w	1.976	0.0053	3 Zn(II)-$N^{(2)}$	4.126	0.0075
				3 Zn(II)-$C^{(3)}$	4.136	0.0075

7. R: absorber-backscatterer distance; σ^2: Debye-Waller factor. ΔE_0 is fixed at -10 eV. R (distance) and σ^2 (Debye-Waller factor) are the only freely variable parameters (in red). Linked variables are in blue.
8. $N_{idp} = 2\Delta k \Delta R/\pi \sim 21$, $N_{free} = N_{idp} - N_{var}$. The outer shell parameters are calculated assuming a rigid imidazole ring.
9. The goodness of the fit is evaluated by $F' = F^2/(N_{free}) \times 10^{-2}$. The smaller the value, the better the fit.

Table V-6. Bond distances of relevant zinc complexes

Compounds	*R*(Zn-N)/Å	*R*(Zn-O)/Å	Ref
$\{[Pim^{Pr^i,Bu^t}]ZnOH\}(ClO_4)^a$	2.072, 2.086, 2.087	1.860 (OH)	74
$[L1Zn(OH_2)](BNPP)_2 \bullet 6H_2O^b$	2.035, 2.015, 2.034	1.984 (OH_2)	75
$[L1hZn(OH)]ClO_4 \bullet 1.5H_2O^c$	2.015, 2.016, 2.014	2.046 (OH)	
$[(TriMIm)Zn(OH_2)](BF_4)_2^d$	1.997, 2.000, 2.012	2.129 (OH_2)	76
The Chemdraw schemes of compound *a, b, c, d* are shown in Scheme V-3			

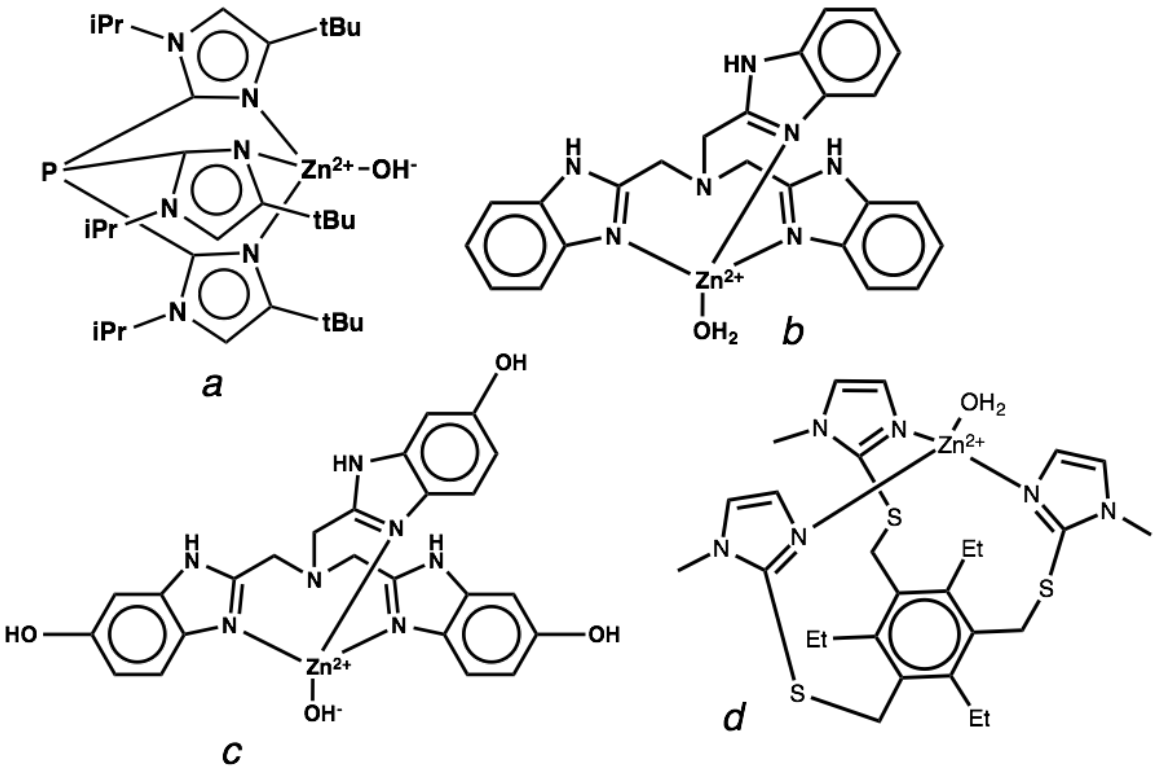

Scheme V-3

The bond distances based on EXAFS fits do not increase or decrease significantly to indicate a deprotonation process; however, this does not exclude the possibility of deprotonation. XANES data suggest that there is a change in the zinc coordination upon pH change. If $\overline{R}$ stays the same, as in our case, the EXAFS resolution needs to be good enough so that the fitting should still be able to distinguish the change in bond distances.

As shown in Table V-6, the bond distances of Zn-O (water or hydroxide) span a range of 1.86~2.05 Å, the assignment of water or hydroxide coordination simply based on bond distances is difficult. The challenge in interpreting the present data might derive from the fact that the pK_a value of this water deprotonation is 9.2(1).[73] The highest pH in this study is 9.5, which, based on the Henderson-Hasselbalch equation, would have ~67% hydroxide and ~33% water. Not having enough hydroxide species would lessen the change in bond lengths to an extent that might not be observable in this system. This could lead to unvaried bond lengths seen in this study. In addition, the pK_a of both the buffer and peptide might change upon freezing. We used 50 mM CHES buffer for pH 8.5 and 9.5 samples. At room temperature (25 ºC), the pK_a of CHES is 9.50. Based on the temperature dependence of CHES $d(pK_a)/dT = -0.011$ ºC^{-1},[77] the pK_a of CHES at 0 ºC is estimated to be ~9.2. In the frozen state, the conjugate base of CHES is more than 50%, which might have an impact on the protonation state of the Zn(II)-bound water. On the other hand, how temperature influences the pK_a of Zn(II)-bound water is still unknown. The uncertainty in the conditions of the solution adds on to the difficulty of data interpretation. It is worth noticing that the variation of conditions such as the change in buffer pK_a upon freezing exists in all the XAS studies, but this is only critical in this case as the goal is to investigate the protonation equilibrium.

Based on the present data, it is difficult to judge which specific scenario described above is more plausible. Future studies involve obtaining a crystal structure at pH 9.5 to investigate the active form of this catalyst.

Conclusion

In this chapter, I present the detailed EXAFS data fitting procedure for future reference. Using XAS techniques to probe the coordination environment of spectroscopically inert metals is prevalent in the study of metalloproteins. I have used XAS to investigate the coordination environment of a NiR model in the previous chapters. I describe a thiol-rich environment for Cu(I) binding in this chapter, using XAS aided by binding studies to understand the coordination preference of Cu(I) at different pH conditions. Unfortunately, the EXAFS data cannot be fitted to a reasonable model,

suggesting that the sample might contain mixed species. The XAS data need to be reproduced before further analysis.

XAS has been used to study the coordination environment of a hydrolytic zinc center in Zn(II)(TRI-H)$_3^{2+}$. This study aims to distinguish the Zn(II)-bound water from Zn(II)-bound hydroxide by the bond distances from EXAFS fitting. The Zn(II)-N and Zn(II)-O distances remain the same going from pH 7.5 to 9.5, which spans over the pK_a of 9.0~9.5 obtained by kinetic studies of *p*-NPA hydrolysis and CO_2 hydration.[73,78] The invariant bond lengths could mean that the hydroxide ratio is not high enough to cause a difference or that the conditions (variation of pK_a values) may not allow for the effects to be observed via XAS techniques.

References

(1) Kossel, W. *Zeitschrift für Phys*. **1920**, *1*, 119–134.
(2) Siegbahn, M. *The Spectroscopy of X-rays*; Oxford University Press, H. Milford, 1925; pp. 1–287.
(3) Penner-Hahn, J. E. *Coord. Chem. Rev*. **2005**, *249*, 161–177.
(4) De Groot, F. *Chem. Rev*. **2001**, *101*, 1779–1808.
(5) Rehr, J. J.; Ankudinov, A. L. *Coord. Chem. Rev*. **2005**, *249*, 131–140.
(6) Dimakis, N.; Bunker, G. *Phys. Rev. B* **2002**, *65*, 201103.
(7) Klinman, J. P. *Chem. Rev*. **1996**, *96*, 2541–2562.
(8) Averill, B. A. *Chem. Rev*. **1996**, *96*, 2951–2964.
(9) Crichton, R. R.; Pierre, J. L. *Biometals* **2001**, *14*, 99–112.
(10) Solomon, E. I.; Szilagyi, R. K.; DeBeer George, S.; Basumallick, L. *Chem. Rev*. **2004**, *104*, 419–458.
(11) Rosenzweig, A. C.; Sazinsky, M. H. *Curr. Opin. Struct. Biol*. **2006**, *16*, 729–735.
(12) MacPherson, I. S.; Murphy, M. E. P. *Cell. Mol. Life Sci*. **2007**, *64*, 2887–2899.
(13) Solomon, E. I.; Sundaram, U. M.; Machonkin, T. E. *Chem. Rev*. **1996**, *96*, 2563–2606.
(14) Solomon, E. I.; Ginsbach, J. W.; Heppner, D. E.; Kieber-Emmons, M. T.; Kjaergaard, C. H.; Smeets, P. J.; Tian, L.; Woertink, J. S. *Faraday Discuss*. **2011**, *148*, 11.
(15) Solomon, E. I.; Hadt, R. G. *Coord. Chem. Rev*. **2011**, *255*, 774–789.
(16) Solomon, E. I.; Chen, P.; Metz, M.; Lee, S.-K.; Palmer, A. E. *Angew. Chem. Int. Ed. Engl*. **2001**, *40*, 4570–4590.
(17) Hannan, J. P.; Busch, J. L. H.; Breton, J.; James, R.; Thomson, A. J.; Moore, G. R.; Davy, S. L. *J. Biol. Inorg. Chem*. **2000**, *5*, 432–447.
(18) Halliwell, B.; Gutteridge, J. M. *Methods Enzymol*. **1990**, *186*, 1–85.
(19) Halliwell, B.; Gutteridge, J. M. *FEBS Lett*. **1992**, *307*, 108–112.
(20) Menkes, J. H.; Alter, M.; Steigleder, G. K.; Weakley, D. R.; Sung, J. H. *Pediatrics* **1962**, *29*, 764–779.
(21) Vulpe, C. D.; Packman, S. *Annu. Rev. Nutr*. **1995**, *15*, 293–322.
(22) Bull, P. C.; Cox, D. W. *Trends Genet*. **1994**, *10*, 246–252.
(23) Solioz, M.; Vulpe, C. *Trends Biochem. Sci*. **1996**, *21*, 237–241.
(24) Wernimont, A. K.; Huffman, D. L.; Lamb, A. L.; Halloran, T. V. O.; Rosenzweig, A. C. *Nat. Struct. Biol*. **2000**, *7*, 766–771.
(25) Gupta, A.; Lutsenko, S. *Future Med. Chem*. **2009**, *1*, 1125–1142.
(26) Dancis, a; Yuan, D. S.; Haile, D.; Askwith, C.; Eide, D.; Moehle, C.; Kaplan, J.; Klausner, R. D. *Cell* **1994**, *76*, 393–402.
(27) O'Halloran, T. V; Culotta, V. C. *J. Biol. Chem*. **2000**, *275*, 25057–25060.
(28) Harrison, M. D.; Jones, C. E.; Solioz, M.; Dameron, C. T. *Trends Biochem. Sci*. **2000**, *25*, 29–32.
(29) Robinson, N. J.; Winge, D. R. *Annu. Rev. Biochem*. **2010**, *79*, 537–562.
(30) Pufahl, R. a.; Singer, C. P.; Peariso, K. L.; Lin, S. J.; Schmidt, P. J.; Fahrni, C. J.; Culotta, V. C.; Penner-Hahn, J. E.; O'Halloran, T. V. *Science* **1997**, *278*, 853–856.
(31) Huffman, D. L.; O'Halloran, T. V. *J. Biol. Chem*. **2000**, *275*, 18611–18614.

(32) Banci, L.; Bertini, I.; Cantini, F.; Felli, I. C.; Gonnelli, L.; Hadjiliadis, N.; Pierattelli, R.; Rosato, A.; Voulgaris, P. *Nat. Chem. Biol.* **2006**, *2*, 367–368.
(33) Yu, F.; Cangelosi, V. M.; Zastrow, M. L.; Tegoni, M.; Plegaria, J. S.; Tebo, A. G.; Mocny, C. S.; Ruckthong, L.; Qayyum, H.; Pecoraro, V. L. *Chem. Rev.* **2014**, *114*, 3495–3578.
(34) Zastrow, M. L.; Pecoraro, V. L. *Biochemistry* **2014**, *53*, 957–978.
(35) Zastrow, M. L.; Pecoraro, V. L. *Coord. Chem. Rev.* **2013**, 1–24.
(36) DeGrado, W. F.; Summa, C. M.; Pavone, V.; Nastri, F.; Lombardi, A. *Annu. Rev. Biochem.* **1999**, *68*, 779–819.
(37) Hill, R. B.; Raleigh, D. P.; Lombardi, A.; DeGrado, W. F. *Acc. Chem. Res.* **2000**, *33*, 745–754.
(38) Ghosh, D.; Pecoraro, V. L. *Curr. Opin. Chem. Biol.* **2005**, *9*, 97–103.
(39) Dieckmann, G. R.; McRorie, D. K.; Tierney, D. L.; Utschig, L. M.; Singer, C. P.; O'Halloran, T. V; Penner-Hahn, J. E.; Degrado, W. F.; Pecoraro, V. L. *J. Am. Chem. Soc.* **1997**, *119*, 6195–6196.
(40) Dieckmann, G. R.; McRorie, D. K.; Lear, J. D.; Sharp, K. A.; DeGrado, W. F.; Pecoraro, V. L. *J. Mol. Biol.* **1998**, *280*, 897–912.
(41) Farrer, B. T.; McClure, C. P.; Penner-Hahn, J. E.; Pecoraro, V. L. *Inorg. Chem.* **2000**, *39*, 5422–5423.
(42) Farrer, B. T.; Harris, N. P.; Valchus, K. E.; Pecoraro, V. L. *Biochemistry* **2001**, *40*, 14696–14705.
(43) Matzapetakis, M.; Farrer, B. T.; Weng, T.-C.; Hemmingsen, L.; Penner-Hahn, J. E.; Pecoraro, V. L. *J. Am. Chem. Soc.* **2002**, *124*, 8042–8054.
(44) Farrer, B. T.; Pecoraro, V. L. *Proc. Natl. Acad. Sci. U. S. A.* **2003**, *100*, 3760–3765.
(45) Lee, K.-H.; Cabello, C.; Hemmingsen, L.; Marsh, E. N. G.; Pecoraro, V. L. *Angew. Chem. Int. Ed. Engl.* **2006**, *45*, 2864–2868.
(46) Iranzo, O.; Ghosh, D.; Pecoraro, V. L. *Inorg. Chem.* **2006**, *45*, 342–345.
(47) Matzapetakis, M.; Ghosh, D.; Weng, T.-C.; Penner-Hahn, J. E.; Pecoraro, V. L. *J. Biol. Inorg. Chem.* **2006**, *11*, 876–890.
(48) Iranzo, O.; Cabello, C.; Pecoraro, V. L. *Angew. Chem. Int. Ed. Engl.* **2007**, *46*, 6688–6691.
(49) Iranzo, O.; Thulstrup, P. W.; Ryu, S.-B.; Hemmingsen, L.; Pecoraro, V. L. *Chem. --Eur. J.* **2007**, *13*, 9178–9190.
(50) Touw, D. S.; Nordman, C. E.; Stuckey, J. A.; Pecoraro, V. L. *Proc. Natl. Acad. Sci. U. S. A.* **2007**, *104*, 11969–11974.
(51) Pecoraro, V. L.; Peacock, A. F. A.; Iranzo, O.; Luczkowski, M. In *ACS Symposium Series*; American Chemical Society, **2009**; pp. 183–197.
(52) Neupane, K. P.; Pecoraro, V. L. *Angew. Chem. Int. Ed. Engl.* **2010**, *49*, 8177–8180.
(53) Chakraborty, S.; Iranzo, O.; Zuiderweg, E. R. P.; Pecoraro, V. L. *J. Am. Chem. Soc.* **2012**, *134*, 6191–6203.
(54) Pushie, M. J.; Zhang, L.; Pickering, I. J.; George, G. N. *Biochim. Biophys. Acta* **2012**, *1817*, 938–947.
(55) Chen, K.; Yuldasheva, S.; Penner-Hahn, J. E.; O'Halloran, T. V. *J. Am. Chem. Soc.* **2003**, *125*, 12088–12089.

(56) Ralle, M.; Lutsenko, S.; Blackburn, N. J. *J. Biol. Chem.* **2003**, *278*, 23163–23170.
(57) Cobine, P. a; George, G. N.; Jones, C. E.; Wickramasinghe, W. a; Solioz, M.; Dameron, C. T. *Biochemistry* **2002**, *41*, 5822–5829.
(58) Ghosh, D.; Lee, K.-H.; Demeler, B.; Pecoraro, V. L. *Biochemistry* **2005**, *44*, 10732–10740.
(59) Ghosh, D.; Pecoraro, V. L. *Inorg. Chem.* **2004**, *43*, 7902–7915.
(60) Olmstead, M. M.; Musker, W. K.; Kessler, R. M. *Transit. Met. Chem.* **1982**, *7*, 140–146.
(61) Behrens, J.; Arnold, S.; Klar, G.; Hinrichs, W. *Transit. Met. Chem.* **1991**, *16*, 76–81.
(62) Jo, M.; Seo, J.; Seo, M. L.; Choi, K. S.; Cha, S. K.; Lindoy, L. F.; Lee, S. S. *Inorg. Chem.* **2009**, *48*, 8186–8191.
(63) Zeevi, S.; Tshuva, E. Y. *Eur. J. Inorg. Chem.* **2007**, *2007*, 5369–5376.
(64) Tegoni, M.; Yu, F.; Bersellini, M.; Penner-Hahn, J. E.; Pecoraro, V. L. *Proc. Natl. Acad. Sci. U. S. A.* **2012**, *109*, 21234–21239.
(65) Yu, F.; Penner-Hahn, J. E.; Pecoraro, V. L. *J. Am. Chem. Soc.* **2013**, *135*, 18096–18107.
(66) Badarau, A.; Dennison, C. *J. Am. Chem. Soc.* **2011**, *133*, 2983–2988.
(67) Xiao, Z.; Loughlin, F.; George, G. N.; Howlett, G. J.; Wedd, A. G. *J. Am. Chem. Soc.* **2004**, *126*, 3081–3090.
(68) Miras, R.; Morin, I.; Jacquin, O.; Cuillel, M.; Guillain, F.; Mintz, E. *J. Biol. Inorg. Chem.* **2008**, *13*, 195–205.
(69) Yatsunyk, L. A.; Rosenzweig, A. C. *J. Biol. Chem.* **2007**, *282*, 8622–8631.
(70) Wernimont, A. K.; Yatsunyk, L. a; Rosenzweig, A. C. *J. Biol. Chem.* **2004**, *279*, 12269–12276.
(71) Peacock, A. F. A.; Iranzo, O.; Pecoraro, V. L. *Dalton Trans.* **2009**, *9226*, 2271–2280.
(72) Zastrow, M. L.; Peacock, A. F. A.; Stuckey, J. A.; Pecoraro, V. L. *Nat. Chem.* **2012**, *4*, 118–123.
(73) Zastrow, M. L.; Pecoraro, V. L. *J. Am. Chem. Soc.* **2013**, *135*, 5895–5903.
(74) Kimblin, C.; Allen, W. E.; Parkin, G. *J. Chem. Soc. Chem. Commun.* **1995**, *1*, 1813.
(75) Echizen, T.; Ibrahim, M. M.; Nakata, K.; Izumi, M.; Ichikawa, K.; Shiro, M. *J. Inorg. Biochem.* **2004**, *98*, 1347–1360.
(76) Voo, J. K.; Incarvito, C. D.; Yap, G. P. a.; Rheingold, A. L.; Riordan, C. G. *Polyhedron* **2004**, *23*, 405–412.
(77) Ellis, K. J.; Morrison, J. F. *Methods Enzymol.* **1982**, *87*, 405–426.
(78) Zastrow, M. L. De novo designed metalloenzymes: structural stabilization and hydrolytic catalysis in a family of alpha-helical coiled coils, University of Michigan, 2013.

Chapter VI . Conclusions

De novo protein design is an advanced strategy to create functional protein constructs.[1–8] Taking a minimalist approach, de novo designed constructs maintain sufficient level of complexity while focusing on the core coordination environment of a metal center. Significant progress is seen in the past few decades in incorporating a stable metal site into a designed construct. The next challenge is to build a functional metal-binding protein from scratch with minimal coordination factors to convey optimal activity. The Pecoraro group has used a highly modular peptide TRI to understand heavy metal sequestration and toxicity by binding metal ions to thiol-rich coordination environment. Based on a solid understanding of how metal ions interact with these de novo designed peptides, we started to focus on transition metal ions and their physiological roles.

In the context of model chemistry, the 13 well-characterized copper-peptide complexes presented in Chapter II, III, and IV of this thesis represent an advanced stage of designing structural and functional models of a native metal center. The amphipathic nature of helices allows for the co-existence of a hydrophobic core for metal binding and a hydrophilic exterior for solvation. The reaction is carried out in homogeneous aqueous solutions in a neutral pH region, more physiologically relevant than most of the synthetic small molecule models. Taking advantage of a highly modular scaffold, I have utilized two novel strategies to develop two more generations of models, which have advanced the understanding of the structure-function relationship of a $Cu(His)_3$ center and has produced catalysts with higher rates.

While the copper center is embedded in an α-helical coiled coil, a scaffold completely different from that in native CuNiR, a certain level of structural integrity and reactivity is still retained for the $Cu(His)_3$ centers described in this thesis. The coordination environment for Cu(I) is the same as that for the reduced form of the T2Cu

in native CuNiR,[9] whereas Cu(II) in the current scaffold likely has a higher coordination number than the native center. Both oxidation levels have relatively high affinities to the peptide, which suggests that the α-helical coiled coil environment can accommodate a redox-active metal center with appropriate choice of coordinating ligands. The active site of CuNiR lies in the interface between two domains,[9,10] whereas the copper center described in this thesis is situated inside the helical coiled coil. The dissimilarity of reactivity between this family of constructs and the T2Cu in CuNiR could be partially due to the level of substrate access and the hydrophobicity around the copper center, which is an inherent difference between the two protein scaffolds. The first generation construct can be viewed as a "reference point" of how much reactivity a $Cu(His)_3$ center can confer. As described in Chapter II, although this peptide is capable of multiple turnovers, the rate is very limited.

Changing the second coordination sphere interactions leads to variation of copper binding properties, reduction potentials, deprotonation equilibria, and NiR rates. Comparison between the peptides described in Chapter III (second generation) and Chapter IV (third generation) suggests that interior modifications are way more effective in modulating the catalysis than the modifications of the charged residues at the helical interface, although both types of modifications show a similar level of impact on the reduction potentials. Specifically, the third generation peptides have a significant increase in NiR rates as compared to the previous two generations, reflecting the efficacy of interior modifications in tuning the rates. The NiR rates for the second generation models with Δ_{charge} from 0 to –12 only vary by 4-fold at pH 5.8, whereas the third generation has a rate enhancement of up to 1300-fold. On the other hand, the series of peptides described in Chapter III have reduction potentials that span ~200 mV at different pH conditions with +400 mV being the lowest reduction potential [Cu(II)/(I)$(TRIW\text{-}EHK24E)_3^{2+/+}$ at pH 7.4] and +597(13) the highest [Cu(II)/(I)$(TRIW\text{-}EHE27K)_3^{2+/+}$ at pH 5.8]; the peptides with interior modifications (Chapter IV) have reduction potentials of ~550 mV, which, compared to TRIW-H, is ~100–150 mV higher. This indicates that the ~200 mV range variation of reduction potentials is probably as much as one can achieve with these two types of modifications in the TRI family. All peptides considered, the reduction potentials

of Cu(II)/(I)-3SCC do not directly correlate to the NiR rates, so efforts to decrease the reduction potential would not necessarily increase the catalytic activity.

To enhance the NiR rates, a few factors need to be considered based on the results presented in this thesis. Since the major portion of the substrate reduction starts with Cu(I)-3SCC, one should focus on altering the cuprous state. When Cu(I) coordination number decreases from three (TRIW-H) to two (TRIW-HL19A), a 150-fold increase in rate is observed, which seems to suggest that this could be a strategy to create a better catalyst; however, TRIW-$_{M}$H has a 500-fold rate enhancement as compared to TRIW-H, but both peptides bind Cu(I) in a (distorted) trigonal geometry. This analysis indicates that the *Cu(I) coordination number is not the dominant factor for rate enhancement*. A possible explanation for rate enhancement is the different binding modes of nitrite to Cu(I), which might lead to different intermediates. Some of these intermediates might be better than others for proton and electron transfer. The current data do not pertain information of these intermediates, but it is necessary to investigate these species and their relative energies. A two-dimensional potential energy surface based on a synthetic small molecule model shows that the electron transfer from Cu(I) to NO_2^- is energetically unfavorable.[11] The protonation of the intermediate is a key step to shift the reduction potential. The incorporation of a general acid catalyst, for example, the imdiazolium in the case of TRIW-HL19A, can enhance the NiR rates by facilitating proton transfer.

In addition, the methylation of the imidazole probably plays a role in changing the electron density on the copper center, as seen in the modulated reduction potentials of TRIW-$_{M}$H as compared to that of TRIW-H. It is worth mentioning that the methylation of the $_{M}$His in this work all occurs on the $^{\delta}$N of the imidazole. This design is based on the crystal structure of $Hg(II)_{S}Zn(II)_{N}(CSL9PenL23H)_3^+$, which reveals that Zn(II) is coordinated to three $^{\varepsilon}$N.[12] This does not necessarily mean that copper would all bind to three $^{\varepsilon}$N, although $Cu(^{\varepsilon}N_{imid})_3$ might be a preferred scenario. In a case where all the $^{\varepsilon}$Ns are methylated, leaving only $^{\delta}$N for copper binding, it would require a significant change in the orientation of the His side chains to form an appropriate binding pocket and the resulting triangle from the coordinating $^{\delta}$Ns is going to be larger than that formed by $^{\varepsilon}$Ns (Figure VI-1). Since copper and zinc are similar in size, a larger binding pocket from $^{\delta}$Ns might not be optimal for copper binding.

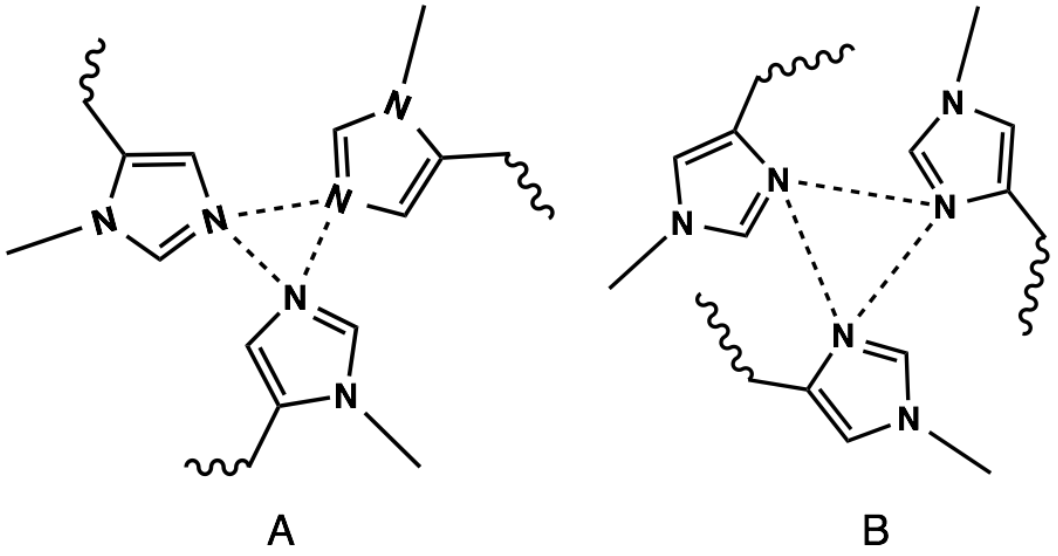

Figure VI-1. Possible Chemdraw schemes of $^{\varepsilon}$N coordination (A) versus $^{\delta}$N coordination (B).

Modifications of charged residues at the helical interface do not have a great impact on rates, but certain functionalities are still worth considering. For example, as compared to peptides with K22X or E27X mutations (X = Q or E), a more evident increase in NiR rate is observed for peptides with the K24X mutation (X = Q or E), although the side chain of Glu22 is closer to the copper center than that of the residue on the 24th position based on the PyMol models. The enhancement in rate is probably due to the appropriate distance of the carboxylate (Glu) or the amide group (Gln) on the 24th position residue in assisting either the proton transfer to the substrate-enzyme complex or the proper positioning of the substrate (a similar effect as the Asp98 in CuNiR[13]).

As introduced in Chapter II, a Cu(His)$_3$ center is highly versatile in native metalloproteins, with functions ranging from electron transfer, catalysis, to oxygen activation (with the assist of other cofactors).[14–31] It is the local environment that fine-tunes the reduction potentials of these sites to afford their proper functions. The understanding of how different factors (electrostatics, H-bonding, salt bridges, *etc*.) in the protein matrix influence the behavior of the metal center is of great importance and is the foundation of designing redox-active models. In general, within the TRI family peptide models, most of the Cu(I) centers are three-coordinate, except for two scenarios: 1) peptides with L19A mutations; 2) when K22E and $_M$H are simultaneous present in one

peptide. This might reflect the inherent preference of Cu(I) for a linear coordination. When the environment allows, be it extra room above the copper center or the putative H-bond between Glu22 and $_{M}$H (Chapter IV), Cu(I) readily adopts a linear Cu(I)(N_{imid})$_2$ coordination. Cu(II)-3SCC is photo-reduced upon exposure to X-ray within 20 min: the corresponding reduced state is usually observed at the second scan. As a result, compared to Cu(I), the Cu(II) forms are not as well-defined due to the unavailability of XAS techniques. Spectroscopic studies indicate that the cupric forms of this family of peptides have higher coordination numbers with different geometries depending on the peripheral residues. Changing the residues on the second coordination sphere possibly leads to variations of geometry or the coordination number for Cu(II) so that the modifications have a significant impact on Cu(II) affinities and the reduction potentials calculated based on the affinities. So if one wants to create an electron transfer center based on this scaffold, changing the coordination environment of Cu(II) is the key to modulate the reduction potentials.

From the perspective of protein design, the strategies of tuning the coordination and the properties of the metal center can potentially inspire a plethora of functional protein-based catalysts. The models discussed in this thesis not only address the question of how much activity a primary coordination sphere can convey, but also push forward the design of extended outer coordination sphere, with the ultimate goal of constructing the most critical interactions to achieve the catalytic efficiency of the native T2Cu center.

The success of designing generations of structural and functional NiR models leads to numerous possibilities for future designs. I can envision two broad directions for future projects based on the major portion of this thesis. The first direction aims to understand the other possible factors that might influence the affinities, redox properties, and reactivity of the copper center, with the ultimate goal of improving the NiR activity. For example, since the L19A mutation confers higher rates, one can ask the question of whether a L26A mutation (the Leu layer below the copper binding His) would also lead to altered copper coordination and higher rates. In Chapter III, I described that the mutations toward the C-terminus of the copper-binding site lead to varied properties, more so than those toward the N-terminus. For example, if one compares TRIW-H, TRIW-HK22Q and TRIW-EH, one realizes that the reduction potentials and NiR rates

are similar; on the other hand, the TRIW-EH family peptides with different mutations toward the C-terminus exhibit distinct properties. This observation alludes to the possibility of water/substrate access from the C-terminus because of fraying. One can expect the L26A mutation to accommodate the imidazolium and to alter the solvent/substrate access to a higher degree than L19A. In extension, TRIW-$_M$HL26A can be prepared, which may lead to a catalytically more favorable η^2–N, O or η^2–O, O Cu(I)-NO_2^- intermediate. At the same time, the general acid catalysis is expected to be retained, which assists in proton transfer.

The next step is to incorporate some other important residues into this construct. For example, an Asp close to the T2Cu center is important in the positioning of nitrite by forming an H-bond.[32] In addition, an Ile residue creates the steric bulk to alter the inhibition profile by small anionic ligands in the native enzyme.[32] The limit of the current scaffold is that these residues would have to be introduced in copies of three due to the self-assembly nature of the 3SCC. Recently, the Pecoraro group has demonstrated the design of heterotrimeric peptides.[33] With this strategy, one can use one strand containing the Asp or Ile functionality, together with the copper-coordinating His, and two strands without the extra functional residues but His, to assemble a heterotrimeric coiled coil. For example, peptide (GRW-CHL26D)(GRW-ACH)$_2$ can be prepared (sequence of GRW-CHL26D: Ac-G WKALEEK LKALEEK LKACEEK LKADEEK HKALEEK G-NH_2, sequence of GRW-ACH: Ac-G WKALEEK LKALEEK AKACEEK LKALEEK HKALEEK G-NH_2,) to create an Asp(His)$_3$ pocket (Figure VI-2A), where the Asp is expect to H-bond to nitrite in the Cu(I)-NO_2^- adduct, playing a similar role as Asp98 in native CuNiR. Obviously, if the above-described L26A mutation results in higher enhancement in rates, one can consider placing the Asp below the His. An Ile residue can be placed analogously as the Asp, assisting in the positioning of the substrate (Figure VI-2B). In addition, the "L19A" mutation can be incorporated in this design to include general acid catalysis, creating a heterotrimer that contains one Ile and two Ala on the same layer (Figure VI-2C).

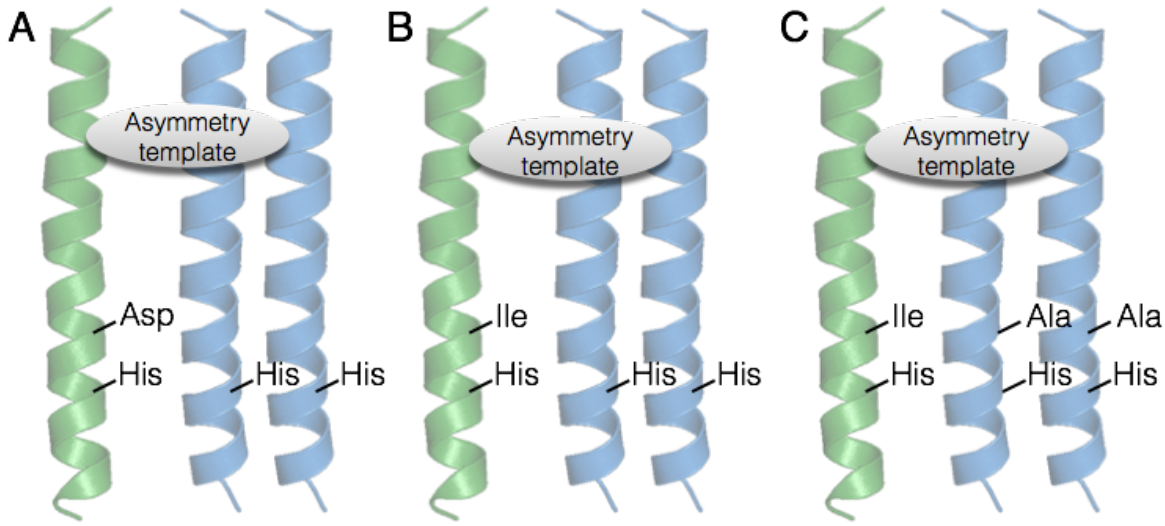

Figure VI-2. Schemes of heterotrimeric coiled coils. (A) Asp$(His)_3$; (B) Ile$(His)_3$; (C) Ile$(Ala)_2(His)_3$.

Another piece of insight gained from the constructs in this thesis is the possibility of a different reaction route. As discussed extensively in Chapter II, III, and IV, the sequence of substrate binding and Cu(II) reduction via electron transfer is essential to determine the reaction intermediates thus the reaction rates. Up to this point, all the reactions have been run in such a way that the majority of the copper-peptide reacts from the cuprous form, *i.e*. Cu(II) reduction happens before substrate binding. On one hand, this allows one to evaluate experimentally the reactivity of an alternative route from the proposed catalytic cycle in native NiR; on the other, it would be ideal if this system can also carry out reactions following the same route of native NiR for comparison. Tethering a $[Ru(bpy)_3]^{2+}$ complex onto a strand of TRI peptide as a photosensitizer is currently being pursued in the Pecoraro group with promising preliminary results. One can imagine attaching a photosensitizing complex onto one of the three strands in a heterotrimeric coiled coil with a $Cu(His)_3$ site to carry out NiR reaction (Figure VI-3). A sacrificial reductant with a reduction potential higher than that of Cu(II)/(I)-peptide couple (*e.g*. $[Co(NH_3)_5Cl]^{2+}$)[34] should be selected to reduced Ru(III). Scheme VI-1 shows a possible reaction scheme to carry out the light-driven NiR reaction.

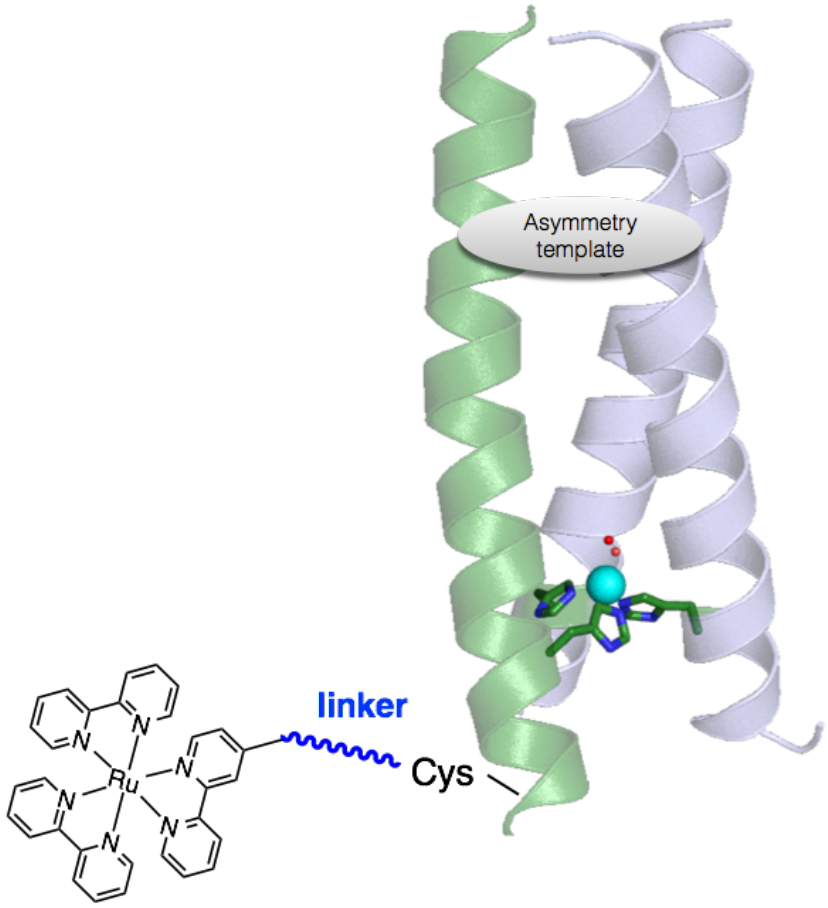

Figure VI-3. A PyMol model of the proposed catalyst. Different colors of the peptides represent different sequences. The green helix has a Cys at the C-terminus for the attachment of the Ru complex.

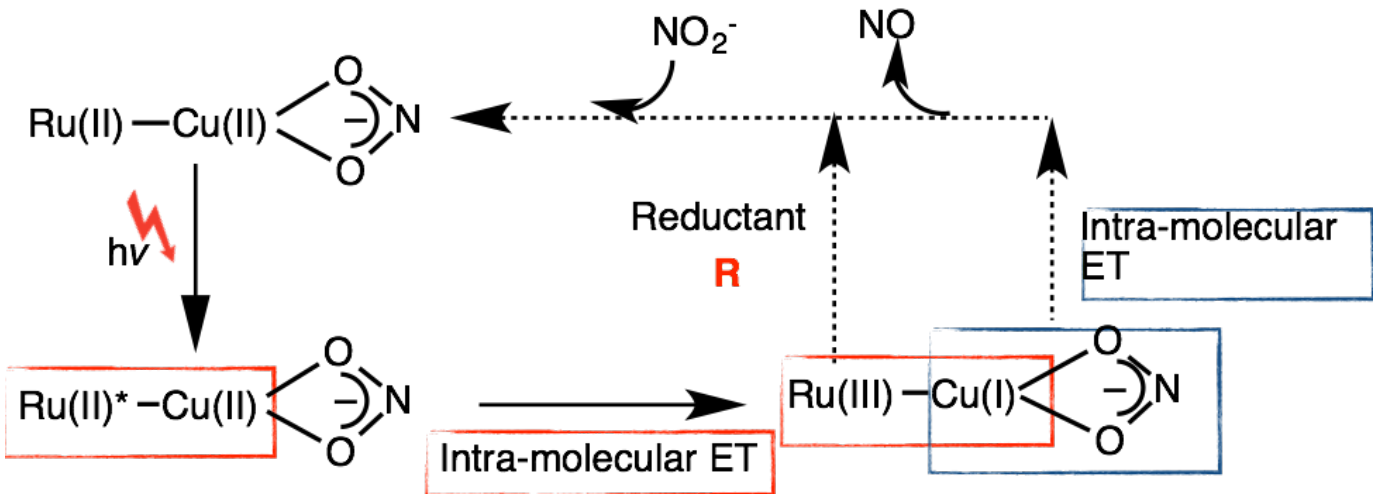
NO2-
NO
Ru(II) —Cu(II)
hν
Reductant
R
Intra-molecular
ET
Ru(II)* —Cu(II)
Intra-molecular ET
Ru(III) —Cu(I)

Scheme VI-1

The second direction for future projects should focus on expanding the realm of reactions that this T2Cu center can catalyze. As is discussed earlier (Chapter II), depending on the protein environment and other cofactors, a $Cu(His)_3$ center can carry out electron transfer, oxygen activation, and other types of oxidoreductase reactions. The electron transfer capability can be examined by photophysical studies. Inter- and intra-molecular electron transfer in these constructs will provide insight into the nature of electron transfer pathways and the influence of protein secondary structures on electron transfer rates.

Regarding the oxygen activation capability of these constructs, I have obtained preliminary data on O_2 and H_2O_2 oxidation of $Cu(I)(TRIW\text{-}H)_3^+$ and a few of its derivatives. The oxidation of $Cu(I)(TRIW\text{-}H)_3^+$ by H_2O_2 leads to an increased absorbance at ~640–660 nm, indicating the production of $Cu(II)(TRIW\text{-}H)_3^{2+}$ (Figure VI-4). Both the oxidation rate and the yield are low (initial rate ~4×10^{-6} M•s^{-1}, ~25%). To model an oxygen activation center for the purpose of substrate oxidation, the reduction potential of the metal center needs to be low enough to reduce oxygen, and the metal-oxygen active species has to be a relatively long-lived intermediate or the production of this intermediate has to be fast so that the system can accumulate a certain amount of the active species.

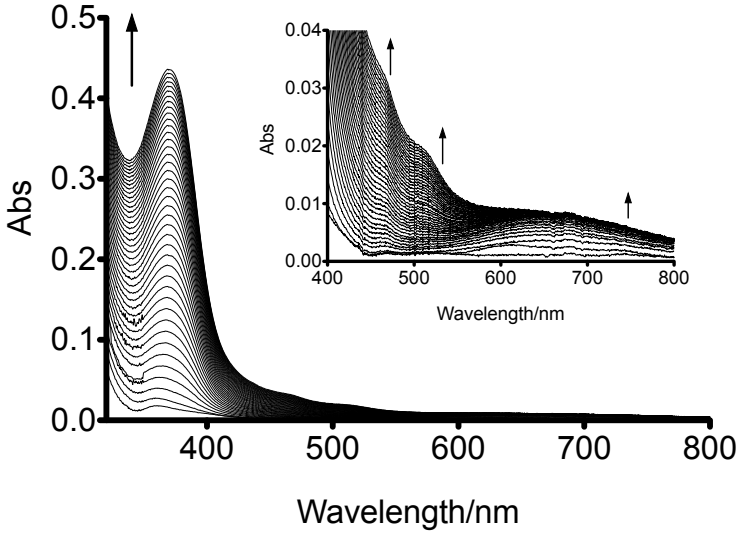

Figure VI-4. The oxidation of 0.23 mM $Cu(I)(TRIW\text{-}H)_3^+$ at pH 6.0 (50 mM MES) by 5 eq. H_2O_2. Spectra were collected every 2 min.

The study of copper coordination complexes has demonstrated that the diverse nature of copper-oxygen reactivity derives from the ligand donor type, chelate ring size, denticity, and aromatic substitutions (if applicable).[35–38] As shown in the previous chapters, the reduction potentials of the T2Cu centers in the present constructs are generally above +400 mV. Lowering the reduction potential should be one of the most important considerations to create a functional oxygen activation center. One approach is to use unnatural amino acids with imidazole-like side chains as copper-binding residues. For example, imidazoles can be substituted with a pyrazole, pyrrole, pyrazine, or pyridine. These modifications would have different electronic effects on the copper center, possibly lowering the reduction potential through the stabilization of the cupric form or the destabilization of the cuprous form. Since these aromatic groups might adopt different orientations inside the helical coiled coils, the influence on either oxidation state might also be different. Substitutions on the aromatics can further fine-tune the reduction potentials.

Overall, the work presented in this dissertation is the first example of a functional copper nitrite reductase model constructed within a three-stranded coiled coil. With the ultimate goal of achieving native-like reactivity within a minimal construct, this project progresses from designing the first coordination sphere to the systematic modifications of the second coordination sphere. Modulated binding properties, reduction potentials, protonation equilibria have been achieved; more importantly, some of these constructs exhibit the best catalytic efficiency among the NiR models under homogeneous aqueous conditions in the literature. The design strategies have advanced the understanding of the structure-function relationship of a redox-active metal center. Providing the importance of the nitrite reduction process in the terrestrial nitrogen cycle and the critical role that nitric oxide plays in human health and diseases,[19,39–41] my doctoral work lays a solid foundation for potential biotechnological and pharmaceutical applications. It is a benchmark against which all the future work on *de novo* designed redox-active catalytic centers will be evaluated.

References

(1) Yu, F.; Cangelosi, V. M.; Zastrow, M. L.; Tegoni, M.; Plegaria, J. S.; Tebo, A. G.; Mocny, C. S.; Ruckthong, L.; Qayyum, H.; Pecoraro, V. L. *Chem. Rev.* **2014**, *114*, 3495–3578.

(2) DeGrado, W. F.; Summa, C. M.; Pavone, V.; Nastri, F.; Lombardi, A. *Annu. Rev. Biochem.* **1999**, *68*, 779–819.

(3) Hill, R. B.; Raleigh, D. P.; Lombardi, A.; DeGrado, W. F. *Acc. Chem. Res.* **2000**, *33*, 745–754.

(4) Tegoni, M. *Eur. J. Inorg. Chem.* **2014**, *2014*, 2177–2193.

(5) Khoury, G. a; Smadbeck, J.; Kieslich, C. a; Floudas, C. a. *Trends Biotechnol.* **2014**, *32*, 99–109.

(6) Peacock, A. F. a. *Curr. Opin. Chem. Biol.* **2013**, *17*, 934–939.

(7) Faiella, M.; Roy, A.; Sommer, D.; Ghirlanda, G. *Biopolymers* **2013**, *100*, 558–571.

(8) Kries, H.; Blomberg, R.; Hilvert, D. *Curr. Opin. Chem. Biol.* **2013**, *17*, 221–228.

(9) Murphy, M. E.; Turley, S.; Adman, E. T. *J. Biol. Chem.* **1997**, *272*, 28455–28460.

(10) Boulanger, M. J.; Murphy, M. E. P. *Biochemistry* **2001**, *40*, 9132–9141.

(11) Ghosh, S.; Dey, A.; Sun, Y.; Scholes, C. P.; Solomon, E. I. *J. Am. Chem. Soc.* **2009**, *131*, 277–288.

(12) Zastrow, M. L.; Peacock, A. F. A.; Stuckey, J. A.; Pecoraro, V. L. *Nat. Chem.* **2012**, *4*, 118–123.

(13) Kataoka, K.; Furusawa, H.; Takagi, K.; Yamaguchi, K.; Suzuki, S. *J. Biochem.* **2000**, *127*, 345–350.

(14) Chufán, E. E.; Prigge, S. T.; Siebert, X.; Eipper, B. A.; Mains, R. E.; Amzel, L. M. *J. Am. Chem. Soc.* **2010**, *132*, 15565–15572.

(15) Evans, J. P.; Blackburn, N. J.; Klinman, J. P. *Biochemistry* **2006**, *45*, 15419–15429.

(16) Kline, C. D.; Mayfield, M.; Blackburn, N. J. *Biochemistry* **2013**, *52*, 2586–2596.

(17) Averill, B. A. *Chem. Rev.* **1996**, *96*, 2951–2964.

(18) Libby, E.; Averill, B. A. *Biochem. Biophys. Res. Commun.* **1992**, *187*, 1529–1535.

(19) Moura, I.; Moura, J. J. *Curr. Opin. Chem. Biol.* **2001**, *5*, 168–175.

(20) Pinho, D.; Besson, S.; Brondino, C. D.; de Castro, B.; Moura, I. *Eur. J. Biochem.* **2004**, *271*, 2361–2369.

(21) Tocheva, E. I.; Rosell, F. I.; Mauk, a G.; Murphy, M. E. P. *Science* **2004**, *304*, 867–870.

(22) Jacobson, F.; Pistorius, A.; Farkas, D.; De Grip, W.; Hansson, O.; Sjölin, L.; Neutze, R. *J. Biol. Chem.* **2007**, *282*, 6347–6355.

(23) MacPherson, I. S.; Murphy, M. E. P. *Cell. Mol. Life Sci.* **2007**, *64*, 2887–2899.

(24) Hirota, S.; Iwamoto, T.; Tanizawa, K.; Adachi, O.; Yamauchi, O. *Biochemistry* **1999**, *38*, 14256–14263.

(25) *Copper Amine Oxidases: Structures, Catalytic Mechanisms, and Role in Pathophysiology*; Floris, G.; Mondovi, B., Eds.; CRC Press, 2009.

(26) Johnson, B. J.; Cohen, J.; Welford, R. W.; Pearson, A. R.; Schulten, K.; Klinman, J. P.; Wilmot, C. M. *J. Biol. Chem.* **2007**, *282*, 17767–17776.

(27) Oka, T.; Simpson, F. J. *Biochem. Biophys. Res. Commun.* **1971**, *43*, 1–5.

(28) Steiner, R. A.; Kooter, I. M.; Dijkstra, B. W. *Biochemistry* **2002**, *41*, 7955–7962.

(29) Steiner, R. A.; Meyer-Klaucke, W.; Dijkstra, B. W. *Biochemistry* **2002**, *41*, 7963–7968.
(30) Fusetti, F.; Schro, K. H.; Steiner, R. a; Noort, P. I. Van; Pijning, T.; Rozeboom, J.; Dijkstra, B. W.; Groningen, A. G.; Noortlaan, O. Van; Schröter, K. H.; van Noort, P. I.; Rozeboom, H. J.; Kalk, K. H.; Egmond, M. R. *Structure* **2002**, *10*, 259–268.
(31) Schaab, M. R.; Barney, B. M.; Francisco, W. A. *Biochemistry* **2006**, *45*, 1009–1016.
(32) Tocheva, E. I.; Eltis, L. D.; Murphy, M. E. *Biochemistry* **2008**, *47*, 4452–4460.
(33) Mocny, C. S.; Neupane, K. P.; Pecoraro, V. L. *submitted* **2014**.
(34) Hamachi, I.; Tsukiji, S.; Shinkai, S.; Oishi, S. *J. Am. Chem. Soc.* **1999**, *121*, 5500–5506.
(35) Kitajima, N.; Moro-oka, Y. *Chem. Rev.* **1994**, *94*, 737–757.
(36) Blackman, A. G.; Tolman, W. B. In *Metal-Oxo and Metal-Peroxo Species in Catalytic Oxidations*; Springer Berlin Heidelberg, 2000; Vol. 97, pp. 179–211.
(37) Hatcher, L. Q.; Karlin, K. D. *J. Biol. Inorg. Chem.* **2004**, *9*, 669–683.
(38) Solomon, E. I.; Chen, P.; Metz, M.; Lee, S.-K.; Palmer, A. E. *Angew. Chem. Int. Ed. Engl.* **2001**, *40*, 4570–4590.
(39) Tavares, P.; Pereira, a S.; Moura, J. J. G.; Moura, I. *J. Inorg. Biochem.* **2006**, *100*, 2087–2100.
(40) Spiro, S. *Philos. Trans. R. Soc. Lond. B. Biol. Sci.* **2012**, *367*, 1213–1225.
(41) Castiglione, N.; Rinaldo, S.; Giardina, G.; Stelitano, V.; Cutruzzolà, F. *Antioxid. Redox Sign.* **2012**, *17*, 684–716.